



**HAL**  
open science

# Polarization resolved four-wave mixing microscopy: structural and vibrational read-out in molecular media

Fabiana Munhoz

► **To cite this version:**

Fabiana Munhoz. Polarization resolved four-wave mixing microscopy: structural and vibrational read-out in molecular media. Atomic Physics [physics.atom-ph]. Université Paul Cézanne - Aix-Marseille III, 2010. English. NNT: . tel-00557684

**HAL Id: tel-00557684**

**<https://theses.hal.science/tel-00557684>**

Submitted on 19 Jan 2011

**HAL** is a multi-disciplinary open access archive for the deposit and dissemination of scientific research documents, whether they are published or not. The documents may come from teaching and research institutions in France or abroad, or from public or private research centers.

L'archive ouverte pluridisciplinaire **HAL**, est destinée au dépôt et à la diffusion de documents scientifiques de niveau recherche, publiés ou non, émanant des établissements d'enseignement et de recherche français ou étrangers, des laboratoires publics ou privés.

## THÈSE

pour obtenir le grade de **Docteur en Sciences**  
de l'Université Paul Cézanne - Aix-Marseille III

**Discipline** : Optique, Photonique et Traitement d'Image

**Polarization resolved four-wave mixing microscopy: structural and  
vibrational read-out in molecular media**

(Microscopie de mélange à quatre ondes résolue en polarisation:  
lecture des symétries structurales et vibrationnelles dans les  
milieux moléculaires)

soutenue publiquement le **13 Décembre 2010** par

Fabiana Munhoz

**École Doctorale** : Physique & Sciences de la Matière

**Rapporteurs** : Dr. Herman Offerhaus  
Prof. Joseph Zyss  
**Examineurs** : Prof. Benoît Boulanger  
Prof. Peter Török  
Dr. Sophie Brasselet  
**Directeur de thèse** : Dr. Hervé Rigneault



*To my parents.*



---

# ACKNOWLEDGMENTS

In a few words, I would like to thank the people that have contributed, direct or indirectly, to the achievement of this thesis. In particular, I thank:

Claude Amra and Hugues Giovannini, former and present directors of the Fresnel Institute, for the opportunity to do my PhD at their institution during these last three years.

The members of the jury: Dr. Herman Offerhaus, Prof. Joseph Zyss, Prof. Peter Török and Prof. Benoît Boulanger for their interest and time, careful reading of this manuscript and the fruitful and encouraging remarks.

Sophie Brasselet and Hervé Rigneault, that have closely supervised this work during these last three years and to whom I express my most sincere gratitude. It is not only their scientific knowledge, which is undeniable, that has made them two brilliant researchers, but also their patience, enthusiasm and consciousness. Working with them was undoubtedly the richest and most rewarding experience of my career in science. It was thanks to the great encouragement and trust of Hervé that I regained the self-confidence lost during the first years of my life in France. It was the support and affection of Sophie that made this thesis possible: despite being extremely busy with all the projects she leads and PhD students she advises, she was always present with a fruitful idea or encouraging word, specially when things were not doing so well.

The present and former members of the Mosaic team, for the fruitful discussions and nice work atmosphere.

Dr. Mischa Bonn, for allowing me to visit his lab and to perform some multiplex CARS spectra. The students and postdocs of the AMOLF Institute, Katrin, Gianluca and James, for the very pleasant stay at Amsterdam and for all the late work that was sometimes necessary.

Il a été pour moi très enrichissant de travailler aux côtés de différentes personnes à l'Institut Fresnel. Tout d'abord je remercie Sophie Brustlein pour les nombreuses fois qu'elle est venue m'aider à régler la manip (et surtout pour les quelques fois où le problème était le cache à l'entrée du microscope). Sophie a été pour moi bien plus qu'une collègue et plus même qu'une amie... Je n'oublierai jamais toutes nos confidences échangées autour

## ACKNOWLEDGMENTS

---

d'un café et tous ses mots d'encouragement.

Je remercie Franck Billard, pour avoir développé le programme d'acquisition de données et David Gachet pour la livraison (presque hebdomadaire) d'articles scientifiques frais. Je remercie tous les deux aussi pour m'avoir formée à la manip CARS et pour avoir répondu à toutes mes questions bêtes.

Je n'oublierai pas le personnel technique et administratif de Fresnel, qui a toujours fait preuve d'efficacité. Merci Magali, Guylène et Laëticia pour tous les ordres de mission faits à l'arrache. Merci Nelly pour avoir toujours une solution. Merci Fred, Béatrice et Christophe pour les ordis réparés (merci aussi Fred pour la promenade en bateau). Merci Cynthia pour être toujours disponible. Un énorme merci à Servane Lenne, sans qui mon arrivée à Marseille aurait été beaucoup plus difficile.

Un grand merci à Jean-Yves Natoli, pour mettre autant d'effort, temps et motivation dans l'organisation des Journées de Doctorants de Fresnel.

Tous les thésards et postdocs de Fresnel, aussi bien pour la bonne ambiance au labo, que pour les nombreux apéros pris ensemble à la Plaine ou ailleurs dans Marseille: Peter, Alicja, Alla, Heykel, Pascal, Richard, Séb, Capou, Ale, Guillaume, Pierre, Dora, Nadia, Jules, Davy, Julien Savatier. Un grand merci aux expatriés Marti et Mika pour leur amitié, malgré la distance qui nous sépare maintenant. Merci à Nadine pour tout ce qu'elle a fait pour les thésards de Fresnel. Merci Cyril pour les quelques matchs de rugby regardés ensemble (même si finalement, je reste toujours accro au foot...).

Un grand merci à tous les marseillais (de naissance ou adoption) qui ont contribué pour que mon séjour à Marseille soit une de plus belles périodes de ma vie. Merci de m'avoir soutenue tout au long de cette thèse et particulièrement pendant la rédaction de ce manuscrit. Merci à Thomas, mon grand frère par adoption, l'ami de tous les moments, malgré toutes nos différences! Je n'oublierai jamais notre Noël passé ensemble au Havre, mon premier passé en France, au sein d'une famille qui m'a accueillie les bras ouverts. Merci Aurore pour être mon copilote de soirée (surtout après quelques verres), Audrey pour nos confidences échangées, des fois presque en arrivant aux larmes. Merci Séb (Gaspari) et Gaëtan pour les matchs de l'OM, Raph pour sa gentillesse, Richi pour la bouffe le lendemain des cuites. Merci Julien (Trouvé) de m'avoir invité au meilleur match de l'OM que j'ai jamais vu. Je n'aurai pas quitté Marseille sans avoir vu l'OM champion de France. Merci Soizic pour les séances de planche à voile (j'espère qu'on les reprendra). Merci François (Boisson), pour son esprit ouvert (et pour les quelques séances de psi gratuites).

Enfin, je ne serais pas arrivée jusqu'ici sans le soutien inlassable de ma famille. Eu agradeço meus pais imensamente, que sempre me apoiaram em todas as minhas decisões, desde o momento em que eu me interessei pelas ciências (na época, meu sonho era ser astrônoma... com o tempo, as escalas se inverteram um pouco). Eu agradeço minhas irmãs, a quem eu devo muito da pessoa que eu sou hoje. Vocês sempre serviram de inspiração. Agradeço meus cunhados e sobrinhos (presente e futuros) que completam essa família maravilhosa. Apesar da distância física, a presença e o carinho de vocês foi a base de tudo o que eu construí.

---

# CONTENTS

<b>Introduction</b>	<b>1</b>
<b>1 Nonlinear optics: tensorial approach</b>	<b>5</b>
1.1 The induced nonlinear polarization . . . . .	6
1.2 The susceptibility tensors . . . . .	8
1.2.1 The linear susceptibility . . . . .	8
1.2.2 The nonlinear susceptibilities . . . . .	9
1.2.3 The third order susceptibilities for coherent Raman scattering . . .	13
1.3 Role of symmetry on optical responses . . . . .	15
1.3.1 Permutation symmetry . . . . .	15
1.3.2 Spatial symmetry . . . . .	16
1.4 Vibrations and symmetry . . . . .	24
1.4.1 Representations of groups . . . . .	25
1.4.2 Character tables . . . . .	29
1.4.3 The projection operator . . . . .	31
1.4.4 Selection rules and direct products: interpreting the character tables	35
1.5 From macroscopic measurements to microscopic information . . . . .	40
1.5.1 Crystalline media . . . . .	41
1.5.2 Statistical molecular assemblies . . . . .	43
1.6 Conclusion . . . . .	50
<b>2 Experimental setup</b>	<b>51</b>
2.1 Description of the experimental setup . . . . .	51
2.1.1 The CARS setup . . . . .	51
2.1.2 The SRS setup . . . . .	53
2.2 Polarization distortions from optical reflections . . . . .	54
2.2.1 Two-photon fluorescence polarization responses in isotropic liquids .	56
2.2.2 Influence of dichroism and ellipticity on the TPF polarization responses	57

## CONTENTS

---

2.2.3	Characterization of the dichroic parameters using two-photon polarization measurements . . . . .	60
2.2.4	Characterization of the dichroic parameters by measuring the polarization states of the incident field . . . . .	64
2.3	<i>In situ</i> characterization of the sample local birefringence . . . . .	66
2.4	Conclusion . . . . .	70
<b>3</b>	<b>Polarization resolved CRS in isotropic media</b>	<b>73</b>
3.1	The third-order nonlinear susceptibility tensor for isotropic media . . . . .	74
3.1.1	The depolarization ratio . . . . .	75
3.1.2	CARS susceptibility tensor for isotropic media . . . . .	78
3.1.3	The spectral behavior of the CARS susceptibility . . . . .	78
3.1.4	SRS susceptibility tensor for isotropic media . . . . .	80
3.2	Analytical model of the induced nonlinear polarization in coherent Raman scattering . . . . .	81
3.2.1	The polarization-resolved CARS response . . . . .	81
3.2.2	Determination of the spectroscopic CARS parameters . . . . .	85
3.2.3	The polarization-resolved SRS response . . . . .	88
3.3	Experimental results: calculating the Raman depolarization ratio of liquids	90
3.3.1	Experimental polarization-resolved CARS responses . . . . .	90
3.3.2	Experimental polarization-resolved SRS responses . . . . .	95
3.4	Conclusion . . . . .	98
<b>4</b>	<b>Polarization resolved CARS signals of crystalline media</b>	<b>101</b>
4.1	The third-order nonlinear susceptibility tensor for media with cubic symmetry	102
4.1.1	The microscopic nonresonant susceptibility tensor . . . . .	102
4.1.2	The microscopic resonant susceptibility tensor . . . . .	103
4.2	The theoretical anti-Stokes signal generated by cubic crystals . . . . .	105
4.2.1	Influence of the crystal orientation on the nonresonant anti-Stokes signal . . . . .	106
4.2.2	Influence of the crystal orientation on the resonant anti-Stokes signal: theoretical study for a totally symmetric vibrational mode . . . . .	108
4.3	The sample: crystalline medium with cubic symmetry . . . . .	110
4.4	The experimental CARS signal . . . . .	111
4.4.1	The nonresonant CARS responses of a medium with cubic symmetry	111
4.4.2	The resonant CARS responses of a totally symmetric vibrational mode	114
4.4.3	The resonant CARS responses of a nontotally symmetric vibrational mode . . . . .	117
4.5	Conclusion . . . . .	120
<b>5</b>	<b>CARS responses of biomolecular assemblies</b>	<b>123</b>
5.1	The nonresonant CARS susceptibility tensor of collagen . . . . .	124
5.1.1	The molecular orientational distribution function . . . . .	127

---

5.2	Experimental nonresonant CARS responses of collagen . . . . .	128
5.2.1	Sample preparation . . . . .	128
5.2.2	Experimental Protocol . . . . .	129
5.2.3	Characterizing the orientation and symmetry order of the surface of the collagen fiber ( $Z = 0 \mu\text{m}$ ) . . . . .	129
5.3	Influence of the sample's birefringence on the polarimetric CARS responses	134
5.4	Influence of the fiber's in-plane orientation on the polarimetric CARS responses	138
5.5	Conclusion . . . . .	140
<b>Conclusion</b>		<b>142</b>
<b>A Susceptibility tensors</b>		<b>145</b>
A.1	First-order susceptibility tensor $\chi_{ij}^{(1)}(-\omega_\sigma; \omega_p)$ . . . . .	145
A.2	Second-order susceptibility tensor $\chi_{ijk}^{(2)}(-\omega_\sigma; \omega_q, \omega_p)$ . . . . .	146
A.3	Third-order susceptibility tensor $\chi_{ijkl}^{(3)}(-\omega_\sigma; \omega_r, \omega_q, \omega_p)$ . . . . .	150
<b>B Expansion of the orientational distribution function in a series of spherical harmonics</b>		<b>155</b>
<b>Published papers</b>		<b>158</b>
<b>Bibliography</b>		<b>160</b>



*“I can live with doubt, and uncertainty, and not knowing. I think it’s much more interesting living not knowing than to have answers which might be wrong.”*

Richard Feynman



---

# INTRODUCTION

In the last few decades, nonlinear optics has known a great development, becoming an essential tool in several fields of research and technology, from telecommunications and optical storage to imaging of biological systems. However, it was only after the invention of the first laser by Theodore Maiman fifty years ago, that a nonlinear optical process was observed for the first time. In 1961, the group of Franken at the University of Michigan, generated the second harmonic signal at 347.2 nm from a pulsed ruby laser emitted at 694.3 nm and transmitted through a quartz crystal [1]. Since then, nonlinear optical spectroscopy has undergone remarkable theoretical and experimental developments. It was in particular the group of Nicolaas Bloembergen at Harvard University, that has set the theoretical basis of nonlinear optical spectroscopy [2, 3, 4], by establishing general laws of reflection and refraction in the nonlinear regime. It was thanks to his works on nonlinear optics, that Bloembergen was awarded with the Nobel Prize in Physics in 1981, together with Arthur Leonard Schawlow, for “their contribution to the development of laser spectroscopy”<sup>1</sup>. Another pioneer in the field of the nonlinear optics is Sergei Akhmanov, at the Lomonosov Moscow State University, who developed the theory of parametrical oscillation and amplification [5]. In 1964, the first book in the world on nonlinear interactions of light was written by Akhmanov and Khokhlov [6].

When nonlinear optics is associated to optical microscopy, it can provide a powerful imaging system that is particularly useful for biological samples, for several reasons. First, the nonlinear nature of the light-matter interaction provides submicrometric threedimensional resolution and second, the use of near infrared excitation wavelengths allows deeper penetration into the tissues. Coherent nonlinear optics has the further advantage of providing contrast from the intrinsic properties of the studied sample, without requiring any labeling of the medium.

The first nonlinear optical microscopes go back to the 1970s, when second harmonic

---

<sup>1</sup>From the official website of the Nobel Prize <http://nobelprize.org/>. In fact, Nicolaas Bloembergen and Arthur Leonard Schawlow were awarded with half of the prize. The other half was assigned to Kai M. Siegbahn “for his contribution to the development of high-resolution electron spectroscopy”.

generation (SHG) images of non-centrosymmetric crystals were reported [7, 8]. The first application of nonlinear optics to the imaging of biological systems was only accomplished ten years later, when Freund et al. used SHG to image collagen fibers in rat-tail tendon [9]. Due to their highly oriented structure, collagen fibers have a non-centrosymmetric nature and therefore emit a very strong SHG signal. For this reason, SHG microscopy has been extensively used since the pioneer work of Freund et al. to image collagen structure and organization in tissues [10, 11, 12, 13, 14, 15]. More recently, this technique has been extended to other non-centrosymmetric biological media, such as muscles [16, 17, 18], microtubules [19] and polysaccharides [20]. SHG has also been employed in real-time measurements of membrane potential in dendritic spines [21] and ions transportation through liposome membrane [22].

Third harmonic generation (THG) is a more recent microscopy technique, whose contrast is obtained by the presence of local inhomogeneities in the sample. The first THG microscope was built in 1997 as a proof of principle of the method, applied to image transparent samples [23]. First applications to biological imaging were demonstrated in chara plant rhizoids [24] and neuron and yeast cells [25]. Recently, this technique has been applied to image the development of zebrafish embryos, until they reach about 1 mm thick [26, 27, 28].

Coherent anti-Stokes Raman scattering (CARS) was first demonstrated in 1965 by Maker and Terhune of the Ford Motor Company, that performed four-wave mixing spectroscopy experiments in liquids and crystals [29]. The name CARS, however, was only employed almost ten years later, by Begley et al. [30]. As a nonlinear optical method, CARS has the same capabilities as the previous SHG and THG techniques, with the advantage of being a vibrational resonant process, which provides chemical specificity. Compared to spontaneous Raman scattering, CARS has, in microscopy, a sensibility that is  $10^6$  times greater, due to its coherent and resonant nature. The only drawback of the CARS technique is the presence of a nonresonant background, originated from the electronic responses of the medium to the incident fields, which can eventually decrease the contrast. The first CARS microscope was built in 1982 by Duncan et al. [31], but the use of visible dye lasers resulted in a strong two-photon enhanced nonresonant background. They could however demonstrate the chemical specificity of the CARS process by imaging onion skin-cells soaked in deuterated water. Developments in the technique remained inactive until 1999, when Zumbusch and coworkers built the first CARS microscope with near infrared sources [32]. They reported CARS images of living cells (bacteria), demonstrating the capability of the method to imaging biological samples. Since then, CARS has been extensively used to image intracellular structures with different contrasts [33, 34], single lipid bilayers [35, 36] and tissues [37, 38]. More recently, another label-free imaging technique based on the stimulated Raman scattering (SRS) has allowed to image tissues and cells with chemical selectivity, without the presence of the nonresonant background [39, 40].

Combining nonlinear optics with polarimetric measurements can provide new contrast mechanisms, allowing to probe spatial symmetry properties as well as molecular organization and orientation in the samples. In 1989, Shen demonstrated that polarization-resolved second harmonic and sum-frequency generations are powerful tools to probe surface and

interface properties [41, 42]. Since then, polarization-resolved sum-frequency generation spectroscopy has been widely used to probe molecular orientations at interfaces [43, 44]. Polarimetric measurements have also been extensively employed in SHG microscopy, to probe molecular order in collagen fibers [12, 45, 46, 14, 47, 48, 49, 50], in molecular media [51, 52, 53, 54], and also to measure membrane potential in neurons [55]. More recently, the potential of polarization-resolved THG has been explored, revealing orientation of biogenic crystals [56] and anisotropic microstructures of human cornea [57].

Spectroscopic experiments using polarization-resolved coherent anti-Stokes scattering have been performed in liquids and non-centrosymmetric media since the 1970s [58, 59, 60, 61]. These measurements were able to probe the microscopic structure of the susceptibility tensors of the probed samples. Polarization-resolved CARS has also been demonstrated to be an efficient tool of modulating the nonresonant background contribution [62, 63, 64, 65], allowing to retrieve the spontaneous Raman spectrum under specific polarization configurations. Despite widespread studies in spectroscopy, polarization-resolved CARS techniques have nevertheless remained almost unexplored in microscopy applications. Only the partial potential of CARS polarization analysis has been explored, allowing to measure only qualitatively molecular orientation in anisotropic samples, such as water molecules in phospholipid bilayers [66], ordered biomolecular assemblies in tissues [67, 68], and liquid crystals [69].

In this thesis, we have explored for the first time the full potential of the polarization-resolved four-wave mixing analysis in microscopy applications and for nonisotropic samples. In our experiments, the two incident fields, called pump and Stokes, are linearly polarized and can have their polarizations controlled and tuned independently. The emitted field, called anti-Stokes, is also analyzed along two perpendicular directions. The technique was applied in three distinct samples: isotropic, crystalline and biological media. In the first two, both the resonant and nonresonant CARS signals were analyzed, providing information on the structure and orientation of the medium, together with the symmetry of the vibrational modes. In the last sample, only the nonresonant four-wave mixing signal was studied, allowing to probe order of the molecular distribution.

This manuscript is organized as follows:

- The first chapter introduces the theoretical tensorial approach of the nonlinear optics. In particular, we show how the symmetry of the medium allows to determine the structure of the susceptibility tensor. We derive both the nonresonant susceptibilities, from spatial symmetry considerations, and the resonant ones, from the symmetry properties of specific molecular modes of vibration. Then we show how to read-out microscopic information on the studied samples from the macroscopic measurements, either for media with crystalline organization or for molecular assemblies with statistical orientational distribution.
- The second chapter describes the experimental setup implemented to perform CARS and SRS measurements and depicts a calibration technique to characterize the polarization distortions introduced either by the optical apparatus or by the sample itself, when it is birefringent.

- The third chapter is an application of polarization-resolved CARS and SRS techniques to isotropic media. We first derive the expressions of the isotropic susceptibility tensors for both processes, then we measure depolarization ratios and other spectral parameters of vibrational modes with different symmetries.
- The fourth chapter uses polarization-resolved CARS analysis to probe crystals with cubic symmetry. The nonresonant CARS measurements allow to quantify departure from isotropy and the resonant responses provide a characterization of deviations from the Kleinman symmetry. For totally-symmetric vibrational modes, a comparison and spontaneous Raman scattering and CARS is provided.
- The fifth chapter studies polarization-resolved nonresonant CARS responses from collagen fibers. The analysis allow to retrieve quantitative information on orientation and symmetry order of the molecular orientational distribution in collagen fibers. An analysis of the influence of the sample's birefringence on the polarization-resolved nonresonant CARS responses is provided.

---

---

# CHAPTER 1

---

## INTRODUCTION TO THE TENSORIAL APPROACH OF THE NONLINEAR OPTICS THEORY

When light interacts with matter, the charged particles in the medium move under the action of the electrical field. This displacement induces an oscillating dipole that radiates throughout the surrounding environment. If the intensity of the incident light is sufficiently strong, the oscillation becomes anharmonic, modifying the optical properties of the medium. This anharmonic oscillation and its associated radiated fields are the very basis of nonlinear optics. In this chapter, we introduce the general theory of nonlinear optics and show briefly how to calculate the induced nonlinear polarization in the semi-classical approach. The expressions of the nonlinear susceptibility tensors can then be deduced from the induced polarization, in the formalism of the density matrix operator. Subsequently, we deal with the role of symmetry in optical responses. In particular, we introduce some tensor notations and properties that show how the molecular symmetry of the medium affects the structure of the nonlinear susceptibilities, contributing to reduce the number of independent nonvanishing tensorial components. These symmetry considerations are particularly important for high-rank tensors. Furthermore, the symmetries of the molecular modes of vibration can lead to structural changes of the susceptibility tensors at resonance. Afterward, we show how to derive the macroscopic susceptibility tensor from the molecular hyperpolarizability, either for crystalline media or molecular assemblies with statistical orientational distribution. Finally, the measured macroscopic susceptibility depends on the orientation of the sample relative to the incident field polarization, and can be determined by a 3D rotation from the sample frame to the laboratory frame.

## 1.1 The induced nonlinear polarization

The induced macroscopic polarization in a medium, resulting from the interaction of charges with a strong electrical field, can be decomposed in a power series of the incident field, where the  $p$ -order polarization is a function of order  $p$  with respect to the applied field, that writes, in SI units<sup>1</sup>:

$$\mathbf{P}^{(p)}(\omega_\sigma) = \epsilon_0 \boldsymbol{\chi}^{(p)}(-\omega_\sigma; \omega_1, \dots, \omega_p) : \mathbf{E}(\omega_1) \dots \mathbf{E}(\omega_p) \quad (1.1)$$

where  $\omega_\sigma = \omega_1 + \dots + \omega_p$ ,  $\boldsymbol{\chi}^{(p)}$  is the  $p$ -order susceptibility tensor and  $\mathbf{E}(\omega_l)$  are the spectral components of the decomposition of the electric field  $\mathbf{E}(t)$  as a combination of monochromatic coherent incident waves, according to:

$$\mathbf{E}(t) = \sum_l \mathbf{E}(\omega_l) \exp(-i\omega_l t). \quad (1.2)$$

In Cartesian coordinates, the macroscopic induced polarization writes:

$$P_{i_0}^{(p)}(\omega_\sigma) = \epsilon_0 \sum_{i_1 \dots i_p} \chi_{i_0 \dots i_p}^{(p)}(-\omega_\sigma; \omega_1, \dots, \omega_p) E_{i_1}(\omega_1) \dots E_{i_p}(\omega_p), \quad (1.3)$$

where  $i_i$  stands for one of the three coordinates,  $(x, y, z)$ .

In this section we use the density matrix formalism to calculate the induced polarization, and by consequence, the susceptibility tensor, following references [70, 71]. In this formalism, a molecule is a quantum system described by its density matrix  $\rho$  and the electrical field is treated classically. The knowledge of the density matrix allows to calculate the expectation value of any observable quantity. In order to describe the time evolution of the system, it is thus necessary to know how the density matrix operator evolves in time itself. The interest of this formalism is that it allows to take the surrounding medium into account without introducing it directly in the quantum system. We consider here a system composed of two parts: first, a quantum system with a certain number of energy eigenstates (the molecule) and second, the thermal reservoir (surrounding medium). Only the quantum system interacts with the external electrical field while the reservoir couples non-radiatively with the system, accounting for population relaxation and decoherence between atomic states. With these assumptions, the evolution in time of the component  $\rho_{nm}$  of the density matrix writes [70, 71]:

$$i\hbar \frac{d\rho_{nm}}{dt} = [\hat{H}, \hat{\rho}]_{nm} - \gamma_{nm} (\rho_{nm} - \rho_{nm}^{(\text{eq})}) \quad (1.4)$$

where  $\gamma_{nm}$  is the decay rate to the stationary value of this matrix element,  $\rho_{nm}^{(\text{eq})}$ . This rate is introduced phenomenologically in order to take in account the dissipative interaction of the molecule with its surrounding system. The Hamiltonian operator of the system,

---

<sup>1</sup>In SI units, the induced polarization is expressed in  $\text{Cm}^{-2}$  while the unit of the electrical field is the  $\text{Vm}^{-1}$ . By consequence, the dimension of the nonlinear susceptibility of order  $p$   $\boldsymbol{\chi}^{(p)}$  is  $(\text{mV}^{-1})^{p-1}$ . The linear susceptibility is thus dimensionless.

$\hat{H} = \hat{H}_0 + \hat{V}(t)$ , splits in two parts: the unperturbed Hamiltonian of the molecule  $\hat{H}_0$  and the interaction energy with the external field  $\hat{V}(t)$ . In the electric dipole approximation, the interaction energy is a function of the electric dipole operator  $\hat{\boldsymbol{\mu}}$ , as  $\hat{V}(t) = \hat{\boldsymbol{\mu}} \cdot \mathbf{E}(t)$ .

By calculating the matrix elements of the commutators  $[\hat{H}_0, \hat{\rho}]_{nm}$  and  $[\hat{V}(t), \hat{\rho}]_{nm}$  and by defining the transition angular frequency between the eigenstates of the unperturbed Hamiltonian  $|n\rangle$  and  $|m\rangle$  as  $\omega_{nm} = (E_n - E_m)/\hbar$ , the evolution equation of the elements of the density matrix operator becomes [71]:

$$\frac{d\rho_{nm}}{dt} = -i\omega_{nm}\rho_{nm} - i\hbar^{-1} \sum_{\nu} (V_{n\nu}\rho_{\nu m} - \rho_{n\nu}V_{\nu m}) - i\gamma_{nm}(\rho_{nm} - \rho_{nm}^{(\text{eq})}) \quad (1.5)$$

where  $\sum_{\nu}$  accounts for the sum over all the intermediate states  $|\nu\rangle$ . In order to solve Eq. 1.5 we develop a perturbation expansion, where the matrix element  $V_{ij}$  of the interaction Hamiltonian is replaced by  $\lambda V_{ij}$ , with  $\lambda$  accounting for the strength of the perturbation. In this approximation, the solution of the equation of motion of the density matrix can be expanded in a power series of  $\lambda$ :

$$\rho_{nm} = \rho_{nm}^{(0)} + \lambda\rho_{nm}^{(1)} + \lambda^2\rho_{nm}^{(2)} + \dots \quad (1.6)$$

Finally, by replacing Eq. (1.6) into Eq. (1.5) it is possible to obtain the set of equations of motion for each term of the perturbation expansion of the density matrix, as follows:

$$\frac{d\rho_{nm}^{(0)}}{dt} = -i\omega_{nm}\rho_{nm}^{(0)} - \gamma_{nm}(\rho_{nm}^{(0)} - \rho_{nm}^{(\text{eq})}) \quad (1.7a)$$

$$\frac{d\rho_{nm}^{(j)}}{dt} = -(i\omega_{nm} + \gamma_{nm})\rho_{nm}^{(j)} - i\hbar^{-1} [\hat{V}, \hat{\rho}^{(j-1)}]_{nm} \quad (1.7b)$$

The solution of the zeroth-order term of the perturbation expansion, given by Eq. (1.7a), corresponds to the absence of any external field, in which case, the elements of the density matrix assume their value at thermal equilibrium,  $\rho_{nm}^{(0)} = \rho_{nm}^{(\text{eq})}$ , with  $\rho_{nm}^{(\text{eq})} = 0$  when  $n \neq m$ . This last relation comes from the physical assumption that at thermal equilibrium, the excited states of the system can be populated, but thermal excitation does not contribute to any coherent superposition of molecular states. Once  $\rho_{nm}^{(0)}$  is known, all the higher-order terms in the perturbation expansion of the density matrix can be obtained by iteration. The knowledge of the matrix density allows to calculate the expectation value of any physical observable  $\hat{A}$ , through the relation  $\langle \hat{A} \rangle = \text{Tr}(\hat{\rho}\hat{A})$ . Therefore, the average induced dipole moment writes:

$$\langle \hat{\boldsymbol{\mu}}(t) \rangle = \text{Tr}(\hat{\rho}(t)\hat{\boldsymbol{\mu}}) \quad (1.8)$$

The induced macroscopic polarization is then deduced from the induced dipole moment and the  $p$ -order polarization depends on the  $p$ -order term of the density matrix operator, as follows:

$$\hat{\mathbf{P}}^{(p)}(t) = N \sum_{nm} \rho_{nm}^{(p)}(t) \boldsymbol{\mu}_{mn}, \quad (1.9)$$

where  $N$  is the number of molecules by unit volume. The induced dipole in Eq. (1.9) can be decomposed into its frequency components, and by replacing Eq. (1.9) into Eq. (1.1), the different orders of the susceptibility tensor can be calculated. In the next section we deduce the expressions for the susceptibilities tensors until the third-order of the perturbation expansion.

## 1.2 The susceptibility tensors

In this section we show the explicit expressions of the susceptibility tensors, from the linear until the third-order nonlinear susceptibilities. Here, we use the formalism developed in the previous section, but we neglect the details of the calculations, which can nevertheless be found in any specialized work in nonlinear optics[70, 72, 71].

### 1.2.1 The linear susceptibility

In order to determine the linear susceptibility, we need to calculate the density matrix in the first order of the perturbation expansion, which means to integrate Eq. (1.7b) for  $j = 1$ , once the commutator  $[\hat{V}(t), \hat{\rho}^{(0)}]_{nm}$  has been calculated. In the electric dipole approximation, this commutator is given by:

$$\begin{aligned} [\hat{V}(t), \hat{\rho}^{(0)}]_{nm} &= - \sum_{\nu} [\boldsymbol{\mu}_{n\nu} \rho_{\nu m}^{(0)} - \rho_{n\nu}^{(0)} \boldsymbol{\mu}_{\nu m}] \cdot \mathbf{E}(t) \\ &= (\rho_{mm}^{(0)} - \rho_{nn}^{(0)}) \boldsymbol{\mu}_{nm} \cdot \mathbf{E}(t), \end{aligned} \quad (1.10)$$

since  $\rho_{nm}^{(0)} = 0$  if  $n \neq m$ . If we replace Eq. (1.10) into Eq. (1.7b) for  $j = 1$  and if we integrate the last one, the expression of the density matrix element  $\rho_{nm}(t)$  in the first order of the perturbation expansion becomes:

$$\rho_{nm}^{(1)}(t) = i\hbar^{-1} (\rho_{mm}^{(0)} - \rho_{nn}^{(0)}) \boldsymbol{\mu}_{nm} \cdot \sum_l \mathbf{E}(\omega_l) e^{-(i\omega_{nm} + \gamma_{nm})t} \int_{-\infty}^t e^{[i(\omega_{nm} - \omega_l) + \gamma_{nm}]\tau} d\tau, \quad (1.11)$$

where we used Eq. (1.2) to write the electric field  $\mathbf{E}(t)$  as a discrete sum of positive and negative frequency components  $\mathbf{E}(\omega_l)$ . Finally, by solving the integral in Eq. (1.11), we can write  $\rho_{nm}^{(1)}(t)$  as:

$$\rho_{nm}^{(1)}(t) = \hbar^{-1} (\rho_{mm}^{(0)} - \rho_{nn}^{(0)}) \sum_l \frac{\boldsymbol{\mu}_{nm} \cdot \mathbf{E}(\omega_l) e^{-i\omega_l t}}{(\omega_{nm} - \omega_l) - i\gamma_{nm}}. \quad (1.12)$$

According to Eq. (1.9), the macroscopic linear polarization can be calculated by applying the density matrix operator to the induced dipole moment. By decomposing the induced polarization into its spectral components and by replacing Eq. (1.12) into Eq. (1.9), we obtain:

$$\sum_l \mathbf{P}(\omega_l) e^{-i\omega_l t} = N \sum_l \sum_{nm} \hbar^{-1} (\rho_{mm}^{(0)} - \rho_{nn}^{(0)}) \frac{\boldsymbol{\mu}_{mn} [\boldsymbol{\mu}_{nm} \cdot \mathbf{E}(\omega_l)] e^{-i\omega_l t}}{(\omega_{nm} - \omega_l) - i\gamma_{nm}}. \quad (1.13)$$

From Eq. (1.13) we can calculate the induced linear polarization  $\mathbf{P}$  at frequency  $\omega_l$ , which can be replaced into Eq. (1.1), in order to obtain the expression of the linear susceptibility tensor:

$$\boldsymbol{\chi}^{(1)}(\omega_l) = \frac{N}{\epsilon_0 \hbar} \sum_{nm} (\rho_{mm}^{(0)} - \rho_{nn}^{(0)}) \frac{\boldsymbol{\mu}_{mn} \boldsymbol{\mu}_{nm}}{(\omega_{nm} - \omega_l) - i\gamma_{nm}}. \quad (1.14)$$

In Cartesian coordinates, the linear susceptibility can be written as:

$$\chi_{ij}^{(1)}(\omega_p) = \frac{N}{\epsilon_0 \hbar} \sum_{nm} (\rho_{mm}^{(0)} - \rho_{nn}^{(0)}) \frac{\mu_{mn}^i \mu_{nm}^j}{\omega_{nm} - \omega_p - i\gamma_{nm}}. \quad (1.15)$$

Finally, the expression of the linear susceptibility can be written, after some algebraic manipulations, in a less compact form, that has a simpler physical interpretation, as follows:

$$\chi_{ij}^{(1)}(\omega_p) = \frac{N}{\epsilon_0 \hbar} \sum_{nm} \rho_{mm}^{(0)} \left[ \frac{\mu_{mn}^i \mu_{nm}^j}{\omega_{nm} - \omega_p - i\gamma_{nm}} + \frac{\mu_{nm}^i \mu_{mn}^j}{\omega_{nm} + \omega_p + i\gamma_{nm}} \right]. \quad (1.16)$$

The equation above shows that for positive frequencies ( $\omega_p > 0$ ), only the first term in brackets can become resonant. Therefore, when the incident frequency  $\omega_p$  is close to one of the molecular resonances, the second term in brackets in Eq. (1.16) can be neglected.

The absorption coefficient of a material is related to the imaginary part of the linear susceptibility  $\boldsymbol{\chi}^{(1)}$ , while its refractive index involves the real part of  $\boldsymbol{\chi}^{(1)}$ . The spontaneous Raman scattering is also associated to the linear susceptibility of the medium.

## 1.2.2 The nonlinear susceptibilities

The calculation of the higher-order susceptibilities follows the same procedure as the one developed in the case of the linear susceptibility. In this section, we show only the final expressions of the second and third-order susceptibilities, without detailing the calculations. We present here both the resonant and nonresonant expressions of the susceptibilities.

### The second-order susceptibility

The resonant second-order susceptibility  $\chi^{(2)}$  writes, in Cartesian coordinates:

$$\begin{aligned}
 \chi_{ijk}^{(2)}(-\omega_\sigma; \omega_q, \omega_p) &= \frac{N}{2\epsilon_0 \hbar^2} \sum_{lmn} \rho_{ll}^{(0)} \\
 &\times \left\{ \frac{\mu_{ln}^i \mu_{nm}^j \mu_{ml}^k}{(\omega_{nl} - \omega_p - \omega_q - i\gamma_{nl})(\omega_{ml} - \omega_p - i\gamma_{ml})} \right. \\
 &+ \frac{\mu_{ln}^i \mu_{nm}^k \mu_{ml}^j}{(\omega_{nl} - \omega_p - \omega_q - i\gamma_{nl})(\omega_{ml} - \omega_q - i\gamma_{ml})} \\
 &+ \frac{\mu_{ln}^k \mu_{nm}^i \mu_{ml}^j}{(\omega_{mn} - \omega_p - \omega_q - i\gamma_{mn})(\omega_{nl} + \omega_p - i\gamma_{nl})} \\
 &+ \frac{\mu_{ln}^j \mu_{nm}^i \mu_{ml}^k}{(\omega_{mn} - \omega_p - \omega_q - i\gamma_{mn})(\omega_{nl} + \omega_q - i\gamma_{nl})} \\
 &+ \frac{\mu_{ln}^j \mu_{nm}^i \mu_{ml}^k}{(\omega_{nm} + \omega_p + \omega_q - i\gamma_{nm})(\omega_{ml} - \omega_p - i\gamma_{ml})} \\
 &+ \frac{\mu_{ln}^k \mu_{nm}^i \mu_{ml}^j}{(\omega_{nm} + \omega_p + \omega_q - i\gamma_{nm})(\omega_{ml} - \omega_q - i\gamma_{ml})} \\
 &+ \frac{\mu_{ln}^k \mu_{nm}^j \mu_{ml}^i}{(\omega_{ml} + \omega_p + \omega_q - i\gamma_{ml})(\omega_{nl} + \omega_p - i\gamma_{nl})} \\
 &\left. + \frac{\mu_{ln}^j \mu_{nm}^k \mu_{ml}^i}{(\omega_{ml} + \omega_p + \omega_q - i\gamma_{ml})(\omega_{nl} + \omega_q - i\gamma_{nl})} \right\} \quad (1.17)
 \end{aligned}$$

with  $\omega_\sigma = \omega_p + \omega_q$ . The first important property that we can deduce from Eq. (1.17) is that the positive and negative frequency components of the susceptibility are related according to:

$$\chi_{ijk}^{(2)}(\omega_\sigma; -\omega_q, -\omega_p) = \chi_{ijk}^{(2)}(-\omega_\sigma; \omega_q, \omega_p)^*, \quad (1.18)$$

where  $*$  stands for complex conjugate. This is a direct consequence of the reality of the induced polarization and the incident electrical fields, that are physically measurable quantities. Another important property of the nonlinear susceptibilities is the intrinsic permutation symmetry. This condition states that the order of the incident fields  $E_j(\omega_q)$  and  $E_k(\omega_p)$  does not matter in the expression of the induced polarization (see Eq. (1.1)). In terms of the susceptibility tensor, this property implies that we can simultaneously interchange the last two Cartesian indices and the last two frequency arguments in Eq. (1.17):

$$\chi_{ijk}^{(2)}(-\omega_\sigma; \omega_q, \omega_p) = \chi_{ikj}^{(2)}(-\omega_\sigma; \omega_p, \omega_q) \quad (1.19)$$

When all the frequencies  $\omega_p$ ,  $\omega_q$  and  $\omega_\sigma$  are far from any molecular resonance, Eq. (1.17) can be simplified, by neglecting the imaginary contributions in the denominators. The final nonresonant second-order susceptibility is given by:

$$\begin{aligned}
 \chi_{ijk}^{(2)}(-\omega_\sigma; \omega_q, \omega_p) &= \frac{N}{2\epsilon_0 \hbar^2} \\
 &\sum_{lmn} \rho_{ll}^{(0)} \left\{ \frac{\mu_{ln}^i \mu_{nm}^j \mu_{ml}^k}{(\omega_{nl} - \omega_p - \omega_q)(\omega_{ml} - \omega_p)} + \frac{\mu_{ln}^i \mu_{nm}^k \mu_{ml}^j}{(\omega_{nl} - \omega_p - \omega_q)(\omega_{ml} - \omega_q)} \right. \\
 &+ \frac{\mu_{ln}^j \mu_{nm}^i \mu_{ml}^k}{(\omega_{nl} + \omega_q)(\omega_{ml} - \omega_p)} + \frac{\mu_{ln}^k \mu_{nm}^i \mu_{ml}^j}{(\omega_{nl} + \omega_p)(\omega_{ml} - \omega_q)} \\
 &\left. + \frac{\mu_{ln}^k \mu_{nm}^j \mu_{ml}^i}{(\omega_{ml} + \omega_p + \omega_q)(\omega_{nl} + \omega_p)} + \frac{\mu_{ln}^j \mu_{nm}^k \mu_{ml}^i}{(\omega_{ml} + \omega_p + \omega_q)(\omega_{nl} + \omega_q)} \right\} \quad (1.20)
 \end{aligned}$$

The nonresonant second-order susceptibility tensor verifies the property of full permutation symmetry. This condition allows all the frequency arguments to interchange freely, as long as the corresponding Cartesian indices are simultaneously interchanged. Therefore, the full permutation symmetry establishes that:

$$\chi_{ijk}^{(2)\text{NR}}(-\omega_\sigma; \omega_q, \omega_p) = \chi_{jki}^{(2)\text{NR}}(-\omega_q; -\omega_p, \omega_\sigma) = \chi_{kij}^{(2)\text{NR}}(-\omega_p; \omega_\sigma, -\omega_q). \quad (1.21)$$

This condition is a direct consequence of the reality of the susceptibility tensor out of resonance.

Examples of second-order nonlinear optical processes, involving the nonlinear susceptibility  $\chi^{(2)}$ , are second harmonic generation (SHG) and sum frequency generation (SFG). In the first, the incident fields have the same frequency  $\omega_q$  and  $\omega_p$  are equal ( $\omega_p = \omega_q = \omega$ ), resulting in a scattered field whose frequency is doubled ( $\omega_\sigma = 2\omega$ ). Sum frequency generation is the general case where two incident beams with distinct frequencies  $\omega_p$  and  $\omega_q$  result in a scattered field whose frequency is the sum of the incident ones ( $\omega_\sigma = \omega_p + \omega_q$ ). In spectroscopy applications, SFG is commonly used as a resonant process, where one incident infrared beam excites a molecular vibrational mode. The molecular energy-level diagram depicting these processes are shown in Fig. (1.1).

### The third-order susceptibility

In the general case of third-order nonlinear induced polarization, three distinct incident fields at angular frequencies  $\omega_p$ ,  $\omega_q$  and  $\omega_r$  combine to generate the emitted field at frequency  $\omega_\sigma = \omega_p + \omega_q + \omega_r$ . The explicit expression of the third-order susceptibility tensor  $\chi^{(3)}$  consists of 48 terms (instead of the eight terms in the case of  $\chi^{(2)}$ ). Here, in order to simplify we explicitly write only eight terms of the tensor, all the others being found by intrinsic permutations of the incident field frequencies, that are included in the permutation operator  $\mathcal{P}_I$ . In the case of a third-order nonlinear optical process, this permutation operator accounts for all the 3! permutations of the pairs  $(j, \omega_r) \rightarrow (k, \omega_q) \rightarrow (l, \omega_p)$ . The

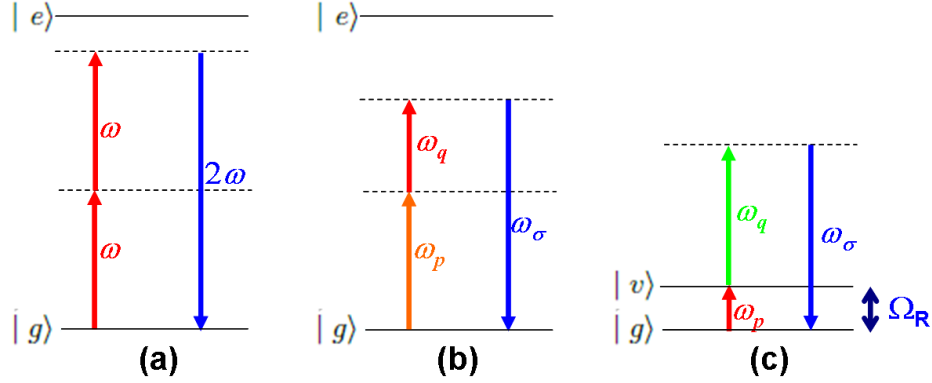


Figure 1.1: Energy diagrams depicting some second-order nonlinear optical processes: (a) second harmonic generation (SHG); (b) nonresonant sum frequency generation (SFG) and (c) resonant SFG.  $|g\rangle$  is the ground energy state,  $|v\rangle$  is one of the molecular vibrational states and  $|e\rangle$  is an electronic level. Horizontal solid lines represent real molecular states, while dashed lines correspond to virtual states.

final expression of the resonant third-order susceptibility is given by:

$$\chi_{ijkl}^{(3)}(-\omega_\sigma; \omega_r, \omega_q, \omega_p) = \frac{N}{\epsilon_0 \hbar^3} \mathcal{P}_I \sum_{\nu nml} \rho_{ll}^{(0)} \times \left\{ \frac{\mu_{l\nu}^i \mu_{\nu n}^j \mu_{nm}^k \mu_{ml}^l}{(\omega_{\nu l} - \omega_\sigma - i\gamma_{\nu l})(\omega_{nl} - \omega_p - \omega_q - i\gamma_{nl})(\omega_{ml} - \omega_p - i\gamma_{ml})} \right. \quad (1.22a)$$

$$+ \frac{\mu_{l\nu}^l \mu_{\nu n}^i \mu_{nm}^j \mu_{ml}^k}{(\omega_{n\nu} - \omega_\sigma - i\gamma_{n\nu})(\omega_{m\nu} - \omega_p - \omega_q - i\gamma_{m\nu})(\omega_{\nu l} + \omega_p + i\gamma_{\nu l})} \quad (1.22b)$$

$$+ \frac{\mu_{l\nu}^k \mu_{\nu n}^i \mu_{nm}^j \mu_{ml}^l}{(\omega_{n\nu} - \omega_\sigma - i\gamma_{n\nu})(\omega_{\nu m} + \omega_p + \omega_q + i\gamma_{\nu m})(\omega_{ml} - \omega_p - i\gamma_{ml})} \quad (1.22c)$$

$$+ \frac{\mu_{l\nu}^l \mu_{\nu n}^k \mu_{nm}^i \mu_{ml}^j}{(\omega_{mn} - \omega_\sigma - i\gamma_{mn})(\omega_{nl} + \omega_p + \omega_q + i\gamma_{nl})(\omega_{\nu l} + \omega_p + i\gamma_{\nu l})} \quad (1.22d)$$

$$+ \frac{\mu_{l\nu}^j \mu_{\nu n}^i \mu_{nm}^k \mu_{ml}^l}{(\omega_{\nu n} + \omega_\sigma + i\gamma_{\nu n})(\omega_{nl} - \omega_p - \omega_q - i\gamma_{nl})(\omega_{ml} - \omega_p - i\gamma_{ml})} \quad (1.22e)$$

$$+ \frac{\mu_{l\nu}^l \mu_{\nu n}^j \mu_{nm}^i \mu_{ml}^k}{(\omega_{nm} + \omega_\sigma + i\gamma_{nm})(\omega_{m\nu} - \omega_p - \omega_q - i\gamma_{m\nu})(\omega_{\nu l} + \omega_p + i\gamma_{\nu l})} \quad (1.22f)$$

$$+ \frac{\mu_{l\nu}^k \mu_{\nu n}^j \mu_{nm}^i \mu_{ml}^l}{(\omega_{nm} + \omega_\sigma + i\gamma_{nm})(\omega_{\nu m} + \omega_p + \omega_q + i\gamma_{\nu m})(\omega_{ml} - \omega_p - i\gamma_{ml})} \quad (1.22g)$$

$$+ \left. \frac{\mu_{l\nu}^l \mu_{\nu n}^k \mu_{nm}^j \mu_{ml}^i}{(\omega_{ml} + \omega_\sigma + i\gamma_{ml})(\omega_{nl} + \omega_p + \omega_q + i\gamma_{nl})(\omega_{\nu l} + \omega_p + i\gamma_{\nu l})} \right\} \quad (1.22h)$$

In the limit of nonresonant excitation, the imaginary contributions  $i\gamma_{\alpha\beta}$  in the denominators in Eq. (1.22) can be neglected. Both expressions for the resonant and nonresonant susceptibilities are very similar and for this reason we do not reproduce here the nonresonant tensor. As in the case of  $\chi^{(2)}$ , the nonresonant third-order susceptibility  $\chi^{(3)\text{NR}}$  also verifies the full permutation symmetry:

$$\begin{aligned}\chi_{ijkl}^{(3)\text{NR}}(-\omega_\sigma; \omega_r, \omega_q, \omega_p) &= \chi_{jkli}^{(3)\text{NR}}(-\omega_r; -\omega_q, -\omega_p, \omega_\sigma) \\ &= \chi_{klij}^{(3)\text{NR}}(-\omega_q; -\omega_p, \omega_\sigma, -\omega_r) \\ &= \chi_{lijk}^{(3)\text{NR}}(-\omega_p; \omega_\sigma, -\omega_r, -\omega_q).\end{aligned}\tag{1.23}$$

Some examples of third-order nonlinear optical processes are four-wave mixing and nonlinear coherent Raman processes, which will be detailed in the next section.

### 1.2.3 The third order susceptibilities for coherent Raman scattering

Coherent Raman scattering (CRS) processes are third-order nonlinear interactions that are resonantly enhanced by two-photon frequency difference, whose advantage is that the competing absorption processes can be neglected, once no single-photon resonances occur. CRS processes take place when two strong incident fields, called pump and Stokes, at frequencies  $\omega_p$  and  $\omega_s$  respectively, interact with a medium. By stimulated emission, this interaction can lead to the amplification of the Stokes signal (and by consequence a depletion of the pump beam) and to the emission of an anti-Stokes field (at frequency  $\omega_{as} = 2\omega_p - \omega_s$ ), under the resonant condition  $\omega_p - \omega_s = \Omega_R$ . Here,  $\Omega_R = \omega_{vg}$  corresponds to the transition frequency between the molecular ground state  $|g\rangle$  and the vibrational level  $|v\rangle$ . The two CRS processes, although concomitant, are called respectively stimulated Raman scattering (SRS) and Coherent anti-Stokes Raman scattering (CARS). The molecular energy-level diagram depicting both processes is shown in Figs. (1.2a) and (1.2b), respectively. In the case of SRS, the two complimentary processes (Stokes amplification and pump depletion) can be measured separately. When it is the amplification of the Stokes beam which is detected, the process is called stimulated Raman gain (SRG). In the other hand, we name stimulated Raman loss (SRL) the process in which the depletion of the pump field is detected. In the scope of this thesis, we are particularly interested in the CARS process, which will be developed in more detail.

In this section we propose to write explicitly the expression for the susceptibility tensor representing the resonant CARS process,  $\chi^{(3)\text{R}}(-\omega_{as}; \omega_p, \omega_p, -\omega_s)$ . For this, we start from Eq. (1.22), we replace the frequencies  $\omega_\sigma$ ,  $\omega_r$ ,  $\omega_q$  and  $\omega_p$  by the corresponding  $\omega_{as}$ ,  $\omega_p$ ,  $\omega_p$  and  $-\omega_s$  and we keep only the resonant terms, that are the ones whose denominator contain  $\Omega_R - \omega_p + \omega_s \pm i\gamma_{vg}$ . In order to simplify the calculations, we assume that the ground level energy is nondegenerate and that this is the only populated level. Mathematically, this means that  $\rho_{ll}^{(0)} = 1$  when  $l = g$  and  $\rho_{ll}^{(0)} = 0$  otherwise. By consequence, the summation

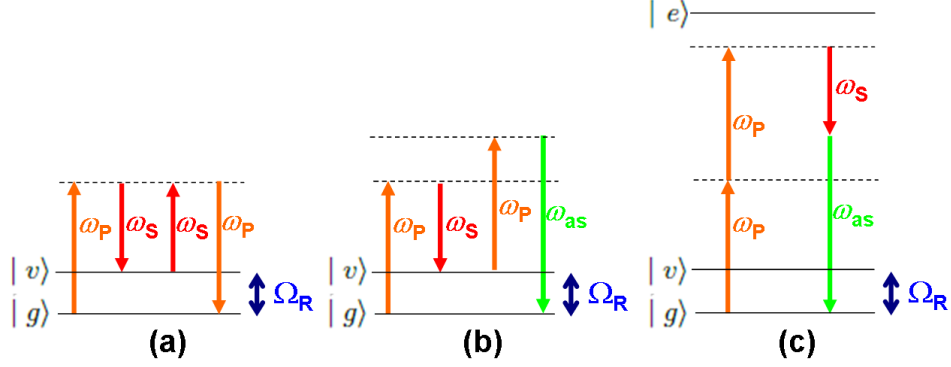


Figure 1.2: Energy diagrams depicting coherent Raman processes: (a) stimulated Raman scattering (SRS); (b) resonant coherent anti-Stokes Raman scattering (CARS) and (c) nonresonant CARS.  $|g\rangle$  is the ground energy state,  $|v\rangle$  is one of the molecular vibrational states and  $|e\rangle$  is an electronic level. All the processes depicted here occur far from any electronic resonance. The angular frequencies involved in the processes are  $\omega_p$ ,  $\omega_s$  and  $\omega_{as}$  for the pump, Stokes and anti-Stokes fields, respectively. Horizontal solid lines represent real molecular states, while dashed lines correspond to virtual states.

over  $l$  in Eq. (1.22) is done simply by replacing all the indices  $l$  by  $g$ . Therefore, the resonant condition stated above is verified in the terms (1.22a) and (1.22e) of Eq. (1.22), when  $n = v$ . Under these assumptions, the CARS susceptibility writes:

$$\begin{aligned} \chi_{ijkl}^{(3)\text{CARS}}(-\omega_{as}; \omega_p, \omega_p, -\omega_s) &= \frac{N/\epsilon_0 \hbar^3}{\Omega_R - \omega_p + \omega_s - i\gamma_{vg}} \\ \times \mathcal{P}_D \sum_{vm} \left[ \frac{\mu_{gv}^i \mu_{vv}^j \mu_{vm}^k \mu_{mg}^l}{(\omega_{vg} - \omega_{as})(\omega_{mg} + \omega_s)} + \frac{\mu_{gv}^j \mu_{vv}^i \mu_{vm}^k \mu_{mg}^l}{(\omega_{vv} + \omega_{as})(\omega_{mg} + \omega_s)} \right. \\ &\quad \left. \frac{\mu_{gv}^i \mu_{vv}^j \mu_{vm}^l \mu_{mg}^k}{(\omega_{vg} - \omega_{as})(\omega_{mg} - \omega_p)} + \frac{\mu_{gv}^j \mu_{vv}^i \mu_{vm}^l \mu_{mg}^k}{(\omega_{vv} + \omega_{as})(\omega_{mg} - \omega_p)} \right] \end{aligned} \quad (1.24)$$

In this equation we neglected all the other imaginary contributions, by assuming that neither  $\omega_p$ ,  $\omega_s$  nor  $\omega_{as}$  are close to an electronic resonance.  $\mathcal{P}_D$  is a permutation factor due to the degeneracy of the pump beams. It accounts for the four extra terms obtained by permuting  $(j, \omega_p) \rightarrow (k, \omega_p)$ .

The same development can be done for the SRS process. In this case, the third order susceptibility components have the following frequency dependence:  $\chi_{ijkl}^{(3)}(-\omega_s; \omega_p, -\omega_p, \omega_s)$  for the stimulated Raman gain and  $\chi_{ijkl}^{(3)}(-\omega_p; \omega_s, \omega_p, -\omega_s)$  for the stimulated Raman loss. The tensor elements of the susceptibilities for both SRS processes are the same, but with different spectral dependencies: the resonant denominator is  $\Omega_R - \omega_p + \omega_s + i\gamma_{vg}$  for SRG and  $\Omega_R - \omega_p + \omega_s - i\gamma_{vg}$  in the case of SRL. By consequence, the imaginary parts of the

susceptibilities change sign: in the case of amplification,  $\Im\mathbf{\chi}^{(3)} < 0$ , whereas  $\Im\mathbf{\chi}^{(3)} > 0$  for depletion of the signal. This is a mathematical verification of the physical concept that connects the gain of the Stokes field with the loss of the pump beam[73].

All the calculations developed so far in this section correspond to the frequency difference resonant CARS process. Fig. (1.2c) shows however a nonresonant third-order nonlinear process that occurs when the incident frequencies  $\omega_p$  and  $\omega_s$  generate a signal at frequency  $\omega_{as}$ . In this case, there is no enhancement of the nonlinearity by vibrational resonance and the process corresponds to the electronic response of the medium to the incident fields. This is the named nonresonant CARS process, whose susceptibility tensor is given by:

$$\chi_{ijkl}^{(3)\text{NR}}(-\omega_{as}; \omega_p, \omega_p, -\omega_s) = \frac{N}{\hbar^3 \epsilon_0} \mathcal{P}_F \sum_{\nu nm} \frac{\mu_{g\nu}^i \mu_{\nu n}^j \mu_{nm}^k \mu_{mg}^l}{(\omega_{\nu g} - \omega_{as})(\omega_{ng} - \omega_p + \omega_s)(\omega_{mg} + \omega_s)}, \quad (1.25)$$

where  $\mathcal{P}_F$  is the full permutation symmetry operator, that accounts for all permutations of the pairs  $(i, -\omega_{as})$ ,  $(j, \omega_p)$ ,  $(k, \omega_p)$  and  $(l, -\omega_s)$ . Here we used the simplifcative assumption that the ground state  $|g\rangle$  is the only populated level. The full description of the CARS process involves therefore, both the resonant and nonresonant third-order susceptibilities, given by Eqs. (1.24) and (1.25), respectively. The final susceptibility tensor corresponding to the CARS process is then given by  $\chi^{(3)\text{CARS}} = \chi^{(3)\text{R}} + \chi^{(3)\text{NR}}$ .

## 1.3 Role of symmetry on optical responses

This section concentrates on the symmetry properties of the nonlinear susceptibilities and a special attention is given to the third-order susceptibility. First, we deduce the Kleinamn symmetry rule from the full permutation symmetry and then we discuss the case of spatial symmetry. In this chapter, we give a general introduction about tensors and symmetries, and in the next chapters we will concentrate on the specific case of CARS microscopy.

In this section and the following one (section 1.4), the term susceptibility tensor and the notation  $\chi_{i_0 \dots i_p}^{(p)}$  with  $i$  one of the Cartesian coordinates  $(x, y, z)$ , will be applied to either a crystal in its unit-cell frame or to a molecule in its molecular frame defined by its principal axes. This is a simplification, since a molecular response is usually called hyperpolarizability instead of susceptibility. The formal notation will be however introduced in section 1.5.2.

### 1.3.1 Permutation symmetry

We saw in section 1.2 that the nonlinear susceptibilities involve high-rank tensors with quite complicated quantum expressions. In the case of second and third-order processes, the susceptibility tensor contain 27 and 81 components, respectively. It is therefore essential to

have a complete knowledge of the symmetry properties of these tensors in order to simplify the problems in nonlinear optics. Some of these properties have already been seen in section 1.2, in particular the ones concerning the invariance of the susceptibility when we permute simultaneously the incident frequencies and the corresponding Cartesian coordinates. In the case of the third-order susceptibility, it means that  $\chi_{ijkl}^{(3)}(-\omega_\sigma; \omega_r, \omega_q, \omega_p)$  is invariant under all permutations of the pairs  $(j, \omega_r)$ ,  $(k, \omega_q)$  and  $(l, \omega_p)$ . This property is known as intrinsic symmetry and its physical meaning is that the order of the incident fields do not matter in the interaction with the medium.

We also saw in section 1.2, that in the case of lossless media, when the susceptibility tensors are real, the susceptibilities are symmetric under the simultaneous permutation of all pairs of Cartesian indices and frequencies, including the emitted frequency. This property is called full permutation symmetry and is depicted in Eqs. (1.21) and (1.23) for the second and third-order susceptibilities, respectively. We consider now the case of the third-order susceptibility for the nonresonant CARS processes, given in Eq. (1.25). When the optical fields appearing in the denominator of this equation are much smaller than the transition frequencies  $\omega_{\nu o}$ ,  $\omega_{n o}$  and  $\omega_{m o}$  of the medium, all the angular frequencies involved in the process can be permuted freely without changing the susceptibility. This means that for nonresonant interactions, the susceptibility is independent of the frequencies and by consequence, all permutations of the Cartesian indices leave the susceptibility tensor invariant. In the case of the third-order susceptibility, this property can be expressed as:

$$\begin{aligned} \chi_{ijkl}^{(3)\text{NR}}(-\omega_\sigma; \omega_r, \omega_q, \omega_p) &= \chi_{jkli}^{(3)\text{NR}}(-\omega_\sigma; \omega_r, \omega_q, \omega_p) \\ &= \chi_{klij}^{(3)\text{NR}}(-\omega_\sigma; \omega_r, \omega_q, \omega_p) = \chi_{lij k}^{(3)\text{NR}}(-\omega_\sigma; \omega_r, \omega_q, \omega_p). \end{aligned} \quad (1.26)$$

This symmetry property is verified for all the nonresonant nonlinear susceptibilities and is known as the Kleinman symmetry. It was first reported by Kleinman in his article of 1962 for the second-order susceptibility  $\chi^{(2)}$  [74].

### 1.3.2 Spatial symmetry

In addition to the permutation symmetry properties described in section 1.3.1, the susceptibility tensors are also governed by the spatial symmetry of the medium. In this section we show how these properties allow to reduce the number of independent components of the susceptibility tensors. For this reason, in a first step, we review some of the basic mathematical concepts on tensors.

#### Tensors: basic mathematical concepts

Let us consider a set of quantities  $T_{i_1 \dots i_n \dots i_R}$  whose indices  $i_n$  may be the Cartesian coordinates  $x$ ,  $y$  or  $z$ . These quantities are the components of a tensor of rank  $R$  and the total number of components is  $3^R$ . A tensor is called symmetric with respect to the indices  $i_n$  and  $i_m$  when the permutation of these indices leave the component invariant:

$T_{i_1 \dots i_n \dots i_m \dots i_R} = T_{i_1 \dots i_m \dots i_n \dots i_R}$ . In the same way, the tensor is called antisymmetric with respect to the indices  $i_n$  and  $i_m$  when  $T_{i_1 \dots i_n \dots i_m \dots i_R} = -T_{i_1 \dots i_m \dots i_n \dots i_R}$ . A tensor is called totally symmetric when it is invariant under any permutation of the indices.

A tensorial contraction is a reduction of two tensors of different ranks into a lower order tensor. In the case of two tensors  $\mathbf{T}$  et  $\mathbf{U}$  with ranks  $R$  and  $S$ , respectively, with  $R > S$ , the resulting tensor is of rank  $R - S$ . If  $R = 4$  and  $S = 3$ , for instance, it follows:

$$\text{Tensorial contraction} \quad (\mathbf{T} : \mathbf{U})_i = \sum_{jkl} T_{ijkl} U_{jkl}.$$

When both tensors are of the same rank, their reduction is a scalar and is called tensorial scalar product. For a 4-rank tensor, it is defined as follows:

$$\text{Tensorial scalar product} \quad \mathbf{T} \cdot \mathbf{U} = \sum_{ijkl} T_{ijkl} U_{ijkl}.$$

When the tensorial scalar product is between the same tensor, it is possible to define the norm of a tensor, as follows:

$$\text{Tensor norm} \quad |\mathbf{T}| = \sqrt{\sum_{i_1 \dots i_R} T_{i_1 \dots i_R}^2}.$$

In the other hand, a tensorial product is the creation of a higher order tensor, from two tensors of the same or different ranks. If the initial tensors are  $R$ - and  $S$ -rank, then the resulting tensorial product is a  $(R + S)$ -rank tensor. As in the previous case, it follows:

$$\text{Tensorial product} \quad (\mathbf{T} \otimes \mathbf{U})_{ijklmno} = T_{ijkl} U_{mno}.$$

It is straightforward to verify that the induced nonlinear polarization  $\mathbf{P}^{(p)}$ , given in Eq. (1.1) is the result of a tensorial contraction between the susceptibility tensor  $\chi^{(p)}$  and the tensor of rank  $p - 1$  resulted from the tensorial product of the  $p - 1$  incident fields  $\mathbf{E}$ , which are 1-rank tensors.

A tensor  $\mathbf{T}$  of rank  $R$  can be decomposed into a tensorial product of the vectors that form the basis of a coordinate system. In Cartesian coordinates, the **tensor decomposition** writes:

$$\mathbf{T} = \sum_{i_1 \dots i_R} T_{i_1 \dots i_R} \mathbf{i}_1 \otimes \dots \otimes \mathbf{i}_R, \quad (1.27)$$

where the vectors  $\mathbf{i}_n$  are one of the unit vectors  $\hat{\mathbf{x}}$ ,  $\hat{\mathbf{y}}$  or  $\hat{\mathbf{z}}$  that forms the basis of the Cartesian coordinate system  $(x, y, z)$ . Therefore, the tensor properties depend on the chosen reference frame. It is then useful to define the transformation law of a tensor when we change the basis of our coordinate system (in other words, when we rotate from one coordinate system to another):

$$T'_{l_1 \dots l_n \dots l_R} = \sum_{i_1 \dots i_n \dots i_R} a_{l_1 i_1} \dots a_{l_n i_n} \dots a_{l_R i_R} T_{i_1 \dots i_n \dots i_R}. \quad (1.28)$$

Here,  $T'_{l_1 \dots l_n \dots l_R}$  and  $T_{i_1 \dots i_n \dots i_R}$  are respectively the tensor components in the new  $(x', y', z')$  and old  $(x, y, z)$  frames and  $a_{l_n i_n}$  are the matrix elements of the transformation, in other words, the rotation from  $(x, y, z)$  to  $(x', y', z')$ :

$$\begin{pmatrix} x' \\ y' \\ z' \end{pmatrix} = \begin{pmatrix} a_{x'x} & a_{x'y} & a_{x'z} \\ a_{y'x} & a_{y'y} & a_{y'z} \\ a_{z'x} & a_{z'y} & a_{z'z} \end{pmatrix} \begin{pmatrix} x \\ y \\ z \end{pmatrix} \quad (1.29)$$

### Reduction of the susceptibility tensors from spatial symmetry considerations

The structure of a susceptibility tensor depends on the vanishing of some tensor components and on the relations between the nonvanishing tensor elements. In this section, we define some rules that allow to determine the structures of the susceptibility tensors based on spatial symmetry considerations of the medium. For this purpose, the main rule is called Neumann's principle, that states that any physical property must include all the symmetry elements of the point group<sup>2</sup> of the system. In other words, Neumann's principle requires that a susceptibility tensor will be invariant under any transformation of coordinates that is governed by any symmetry operation of the medium. Mathematically, it means that, if we apply a symmetry operation to the susceptibility tensor  $\chi_{i_0 \dots i_p}^{(p)}(-\omega_\sigma; \omega_1, \dots, \omega_p)$ , the tensor in the new system of coordinates  $\chi_{l_0 \dots l_p}^{(p)' }(-\omega_\sigma; \omega_1, \dots, \omega_p)$  writes:

$$\chi_{l_0 \dots l_p}^{(p)' }(-\omega_\sigma; \omega_1, \dots, \omega_p) = \delta_{l_0 i_0} \dots \delta_{l_p i_p} \chi_{i_0 \dots i_p}^{(p)}(-\omega_\sigma; \omega_1, \dots, \omega_p). \quad (1.30)$$

The susceptibility tensor in the new coordinate system relates to the susceptibility tensor in the old coordinate system according to Eq. (1.28). Therefore, by replacing Eq. (1.28) into Eq. (1.30), we determine the set of  $3^{p+1}$  equations that must satisfy the components of any  $p$ -order (or  $p + 1$ -rank) susceptibility tensor [75]:

$$\sum_{i_0 \dots i_p} \left( a_{l_0 i_0}^j \dots a_{l_p i_p}^j - \delta_{l_0 i_0} \dots \delta_{l_p i_p} \right) \chi_{i_0 \dots i_p}^{(p)}(-\omega_\sigma; \omega_1, \dots, \omega_p) = 0. \quad (1.31)$$

Here,  $\delta_{li}$  is the Kronecker delta and the superscript  $j$  stands for the  $j^{\text{th}}$  symmetry operator of the group. These  $3^{p+1}$  equations must be verified for all matrices  $a_{li}^j$  representing all the symmetry operators of the group.

A direct consequence of Eq. (1.31) can be deduced for media with inversion operation. For this symmetry operation, the transformation matrix  $a_{li}$  is given by the opposite of the identity matrix, or  $a_{li} = -\delta_{li}$ . By replacing this relation into Eq. (1.31), it follows:

$$\begin{aligned} & [(-1)^{p+1} - 1] \chi_{i_0 \dots i_p}^{(p)}(-\omega_\sigma; \omega_1, \dots, \omega_p) = 0 \Rightarrow \\ \Rightarrow & \chi_{i_0 \dots i_p}^{(p)}(-\omega_\sigma; \omega_1, \dots, \omega_p) = \begin{cases} 0 & \text{if } p \text{ is even} \\ \forall & \text{if } p \text{ is odd} \end{cases} . \end{aligned} \quad (1.32)$$

---

<sup>2</sup>The definition of a point group is found in the paragraph "Crystal symmetry classes".

This is a very important result in nonlinear optics, stating that all the susceptibility tensors  $\chi^{(p)}$  for centrosymmetric media vanish for even-order nonlinear processes. This property explains why second order processes, in particular second harmonic and sum frequency generation, are widely used to probe interfaces and other media lacking a center of inversion.

**Crystal symmetry classes** The structure of the susceptibility tensor of a crystal in its unit-cell frame or of a molecule in its molecular frame, is strongly related to spatial symmetry considerations. According to crystallography, all crystals are divided into 32 groups, called crystallographic point groups. Most known molecules also belong to one of the 32 crystallographic point groups. These are mathematical groups containing all the symmetry operations that leave at least one point fixed and do not change the structure appearance of the crystal or molecule after the operation. The **number of symmetry operations** in a point group defines its order  $h$ . All the symmetry operations can be summarized in five types:

1. **Identity**: a trivial operation, represented by the letter  $E$ .
2.  $n$ -fold **rotation**  $C_n$ : the crystal is symmetric under rotations by  $360^\circ/n$ .
3. **Reflection** in a plane  $\sigma$ . The reflection plane is labeled either  $\sigma_v$  or  $\sigma_d$  if it contains the main axis of rotation  $C_n$ , or  $\sigma_h$  if it is perpendicular to  $C_n$ .
4. **Inversion**  $i$ : the crystal is symmetric under inversion of the space in respect to the origin of the coordinate system.
5. **Rotation-reflection** (or improper rotation)  $S$ : the crystal is symmetric under a rotation by  $360^\circ/n$  followed by a reflection in a plane perpendicular to the rotation axis.

For a crystalline medium, determining the structure of the  $p$ -order susceptibility tensor  $\chi^{(p)}$  in its crystallographic frame  $(x, y, z)$ , consists of solving the system of  $3^{p+1}$  linear equations (1.31) for all the  $h$  symmetry operations of the group, which results in a total of  $h3^{p+1}$  equations. It is well known from group theory, however, that only a limited number of basic symmetry operations are sufficient to derive all the symmetry operations[75, 76]. Therefore, knowing the transformation matrices corresponding to these basic symmetry operations, allows to reduce the system of linear equations to be solved in order to determine the susceptibility tensor components. These transformation matrices are called “**generating matrices**” and are summarized in table 1.1. In this table, we do not show the explicit expression of the generating matrices, but instead, the result of the transformation  $\mathbf{x}' = \mathbf{M}\mathbf{x}$ .

The 32 crystallographic point groups and their main symmetry operations are listed in table 1.2, divided into seven crystal systems. Here, we use the *Schönflies notation*, that is widely employed among chemists and spectroscopists. Some authors prefer to use the *Hermann-Mauguin notation*, that is the current labeling among crystallographers. As

Table 1.1: Generating transformation matrices  $\mathbf{x}' = \mathbf{M}\mathbf{x}$  [76].

	<b>Transformation <math>\mathbf{x}' = \mathbf{M}\mathbf{x}</math></b>	<b>Physical interpretation</b>
$M_0$	$(x, y, z) \rightarrow (x, y, z)$	Identity
$M_1$	$(x, y, z) \rightarrow (-x, -y, -z)$	Inversion
$M_2$	$(x, y, z) \rightarrow (-x, -y, z)$	Two-fold rotation about $z$ axis
$M_3$	$(x, y, z) \rightarrow (x, y, -z)$	Reflection in the $xy$ plane
$M_4$	$(x, y, z) \rightarrow (x, -y, z)$	Two-fold rotation about $x$ axis
$M_5$	$(x, y, z) \rightarrow (-x, y, z)$	Reflection in the $yz$ plane
$M_6$	$(x, y, z) \rightarrow (x, -y, z)$	Reflection in the $xz$ plane
$M_7$	$(x, y, z) \rightarrow (y, -x, z)$	Four-fold rotation about $z$ axis
$M_8$	$(x, y, z) \rightarrow (-y, x, -z)$	Four-fold inversion-rotation about $z$ axis
$M_9$	$(x, y, z) \rightarrow \left(-\frac{x}{2} - \frac{\sqrt{3}y}{2}, \frac{\sqrt{3}x}{2} - \frac{y}{2}, z\right)$	Three-fold rotation about $z$ axis
$M_{10}$	$(x, y, z) \rightarrow \left(\frac{x}{2} - \frac{\sqrt{3}y}{2}, \frac{\sqrt{3}x}{2} + \frac{y}{2}, -z\right)$	Three-fold inversion-rotation about $z$ axis
$M_{11}$	$(x, y, z) \rightarrow \left(\frac{x}{2} - \frac{\sqrt{3}y}{2}, \frac{\sqrt{3}x}{2} + \frac{y}{2}, z\right)$	Six-fold rotation about $z$ axis
$M_{12}$	$(x, y, z) \rightarrow \left(-\frac{x}{2} - \frac{\sqrt{3}y}{2}, \frac{\sqrt{3}x}{2} - \frac{y}{2}, -z\right)$	Six-fold inversion-rotation about $z$ axis
$M_{13}$	$(x, y, z) \rightarrow (z, x, y)$	Three-fold rotation about [111] direction
$M_{14}$	$(x, y, z) \rightarrow (-y, -z, -x)$	Three-fold inversion-rotation about [111] direction

we are not concerned with calculating the transformation matrices to all the symmetry operations, we list in table 1.2 the generating matrices for each crystallographic point group. These transformation matrices are valid only for a specific coordinate system, which is specified in the last column of table 1.1. The orthonormal Cartesian coordinate system  $(x, y, z)$  defined by the “right-hand” rule is the most widely used. Here, we adopt the convention that the main axis of symmetry is oriented along the  $z$  direction.

**Direct inspection method** The direct inspection, or Fumi’s method, is the simplest way of analyzing the invariance equation (1.31). According to this method, the different

Table 1.2: List of the 32 crystallographic point groups, divided into seven crystal systems, with their respective symmetry operations and generating matrices.

Crystal system	Point group	Symmetry operation	Group order $h$	Generating matrices
Triclinic	$C_1$	$E$	1	$M_0$
	$C_i$	$E, i$	1	$M_1$
Monoclinic	$C_2$	$E, C_2$	1	$M_2$
	$C_s$	$E, \sigma$	1	$M_3$
	$C_{2h}$	$E, C_2, \sigma, i$	4	$M_2, M_3$
Orthorhombic	$D_2$	$E, C_2$	4	$M_4, M_2$
	$C_{2v}$	$E, C_2, \sigma$	4	$M_5, M_2$
	$D_{2h}$	$E, C_2, \sigma, i$	8	$M_6, M_5, M_3$
Trigonal	$C_3$	$E, C_3$	3	$M_9$
	$S_6$	$E, C_3, S_6, i$	6	$M_{10}$
	$D_3$	$E, C_3, C_2$	6	$M_9, M_4$
	$C_{3v}$	$E, C_3, \sigma$	6	$M_9, M_5$
	$D_{3d}$	$E, C_3, C_2, \sigma, i, S_6$	12	$M_{10}, M_5$
Hexagonal	$C_6$	$E, C_6$	6	$M_{11}$
	$C_{3h}$	$E, C_3, \sigma, S_3$	6	$M_{12}$
	$C_{6h}$	$E, C_6, C_3, C_2, i, S_3, S_6, \sigma$	12	$M_{12}, M_5$
	$D_6$	$E, C_6, C_3, C_2$	12	$M_{11}, M_4$
	$C_{6v}$	$E, C_6, C_3, C_2, \sigma$	12	$M_{11}, M_5$
	$D_{3h}$	$E, C_3, C_2, \sigma, S_3$	12	$M_{11}, M_3$
	$D_{6h}$	$E, C_6, C_3, C_2, \sigma, S_3, S_6, i$	24	$M_{11}, M_5, M_3$
Tetragonal	$C_4$	$E, C_4$	4	$M_7$
	$S_4$	$E, S_4, C_2$	4	$M_8$
	$C_{4h}$	$E, C_4, C_2, i, S_4, \sigma$	8	$M_7, M_3$
	$D_4$	$E, C_4, C_2$	8	$M_7, M_3$
	$C_{4v}$	$E, C_4, C_2, \sigma$	8	$M_7, M_5$
	$D_{2d}$	$E, S_4, C_2, \sigma$	8	$M_8, M_4$
	$D_{4h}$	$E, C_4, C_2, i, S_4, \sigma$	16	$M_7, M_3, M_5$
	Cubic	$T$	$E, C_3, C_2$	12
$T_h$		$E, C_3, C_2, i, S_6, \sigma$	24	$M_{14}, M_2$
$O$		$E, C_4, C_3, C_2$	24	$M_{13}, M_7$
$T_d$		$E, C_3, C_2, S_4, \sigma$	24	$M_{13}, M_8$
$O_h$		$E, C_4, C_3, C_2, i, S_4, S_6, \sigma$	48	$M_{14}, M_7$

symmetry operations for a certain number of crystallographic point groups, when applied to the  $h3^{p+1}$  set of equations (1.31), result only in intermixing of the indices and/or change in the sign of the tensorial components. Mathematically, it is equivalent to:

$$\chi_{l_0 \dots l_p}^{(p)}(-\omega_\sigma; \omega_1, \dots, \omega_p) = \pm \chi_{i_0 \dots i_p}^{(p)}(-\omega_\sigma; \omega_1, \dots, \omega_p). \quad (1.33)$$

This method can be applied to all point groups belonging to the monoclinic, orthorhombic, tetragonal and cubic systems. They correspond to the crystal systems whose generating matrices include  $M_1$  to  $M_8$ ,  $M_{13}$  and  $M_{14}$ . These transformation matrices only transform one coordinate into another or change their signs. They do not include transformations in which the final coordinate is a linear combination of the initial ones.

From the tensor decomposition rule in Eq. (1.27), a  $p$ -order ( $(p+1)$ -rank) tensor behaves as the  $(p+1)$  tensorial product of the unit vectors  $\hat{\mathbf{x}}$ ,  $\hat{\mathbf{y}}$  and  $\hat{\mathbf{z}}$  that form the basis of the Cartesian coordinate system. Therefore, a  $(p+1)$ -rank tensor behaves as a  $(p+1)$ -rank polynomial build from the product of indexes  $x$ ,  $y$  and  $z$ . The component  $\chi_{xxyy}^{(3)}(-\omega_\sigma; \omega_r, \omega_q, \omega_p)$ , for instance, behaves like the polynomial  $xxyy$ . Note that the order of the indexes in the polynomial is very important and must be respected. Consequently, from Eq. (1.33), the direct inspection of the coordinates before and after transformation is sufficient to determine the structure of the susceptibility tensor. If a polynomial is equal to itself but with the opposite sign, then the corresponding component vanishes. All the other elements of the tensor can be deduced by the relations between the polynomials.

As an example, we consider the case of the linear susceptibility  $\chi^{(1)}$  of a crystal with cubic symmetry, belonging to the  $O_h$  point group. According to table 1.2, it is necessary to inspect two generating matrices,  $M_7$  and  $M_{14}$ , in order to determine the tensorial structure of the crystal. As the linear susceptibility  $\chi^{(1)}$  is a 2-rank tensor of a linear optical process ( $p=1$ ), for each generating matrix we have to solve a system of  $3^{p+1} = 9$  equations. Therefore, for both transformations  $M_7$  and  $M_{14}$  the system to be solved consists of 18 polynomial equations. From table 1.1, these transformations are (from  $M_{14}$  in the left and  $M_7$  in the right):

$$\begin{array}{ll} (1) & xx \rightarrow yy \\ (2) & xy \rightarrow yz \\ (3) & xz \rightarrow yx \\ (4) & yx \rightarrow zy \\ (5) & yy \rightarrow zz \\ (6) & yz \rightarrow zx \\ (7) & zx \rightarrow xy \\ (8) & zy \rightarrow xz \\ (9) & zz \rightarrow xx \\ (10) & xx \rightarrow yy \\ (11) & xy \rightarrow -yx \\ (12) & xz \rightarrow yz \\ (13) & yx \rightarrow -xy \\ (14) & yy \rightarrow xx \\ (15) & yz \rightarrow -xz \\ (16) & zx \rightarrow zy \\ (17) & zy \rightarrow -zx \\ (18) & zz \rightarrow zz. \end{array}$$

From (12) and (15),  $xz = yz = 0$ . In the same way, from (16) and (17),  $zx = zy = 0$ . From (10) and (14),  $xx = yy$  and from (11),  $xy = -yx$ . But, from the relations given by  $M_{14}$ , like (2) for instance,  $xy = yz$ , which means  $xy = yx = 0$ . Finally, from (5) or (9),  $xx = yy = zz$ . In conclusion, for a crystal that belongs to the  $O_h$  crystallographic

point group, the linear susceptibility has only three nonvanishing components, that are furthermore mutually equal:  $\chi_{xx}^{(1)} = \chi_{yy}^{(1)} = \chi_{zz}^{(1)}$ . All the other terms vanish:  $\chi_{ij}^{(1)} = 0$  for  $i \neq j$ . The same procedure allows to show that these relations stand for all crystals with cubic symmetry. This structure also corresponds to the linear susceptibility for an isotropic material. Therefore, linear optics does not allow to differentiate between isotropy and cubic symmetry. A more detailed discussion is done in chapter 3.

Finally, the structure of the susceptibility tensors determined by direct inspection, can be further modified if we take into account additional permutation symmetry of the tensor. For instance, when Kleinman symmetry is observed, some additional components may vanish or become equal.

The direct inspection method and by consequence Eq. (1.33) are not valid for crystals and molecules belonging to the trigonal and hexagonal systems. In these cases, the three- or six-fold rotations lead to transformation matrices that change one coordinate into a linear combination of coordinates, as we show in table 1.1. For these crystals, determining the structure of the susceptibility tensors, requires to solve the whole system of equations (1.31). Some methods, as the method of cyclic coordinates described in [75], make it easier the determination of the structures of high-rank susceptibilities. The description of this method however, is beyond the scope of this manuscript. Here, we are mainly concerned with calculating susceptibility tensors until the fourth-rank (third order nonlinear processes,  $p = 3$ ). In the most complex case, corresponding to the  $D_{6h}$  point group in the hexagonal crystal system, determining the structure of the third order susceptibility tensor  $\chi^{(3)}$ , requires to solve  $3^{p+1} = 81$  linear equations for each of the three generating matrices, resulting in a system of  $3 \cdot 3^{p+1} = 243$  equations.

As an example, let us use Eq. (1.31) to determine the linear susceptibility  $\chi^{(1)}$  of a crystal belonging to the  $C_3$  crystallographic point group. The only generating matrix for this point group is  $M_9$ , listed in table 1.1. Consequently, the tensor structure of the linear susceptibility is determined by solving a system of  $1 \cdot 3^{p+1} = 9$  equations:

$$(11) \quad -\frac{3}{4}(\chi_{xx}^{(1)} - \chi_{yy}^{(1)}) + \frac{\sqrt{3}}{4}(\chi_{xy}^{(1)} + \chi_{yx}^{(1)}) = 0$$

$$(12) \quad -\frac{\sqrt{3}}{4}(\chi_{xx}^{(1)} - \chi_{yy}^{(1)}) - \frac{3}{4}(\chi_{xy}^{(1)} + \chi_{yx}^{(1)}) = 0$$

$$(13) \quad -\frac{3}{2}\chi_{xz}^{(1)} - \frac{\sqrt{3}}{2}\chi_{yz}^{(1)} = 0$$

$$(21) \quad -\frac{\sqrt{3}}{4}(\chi_{xx}^{(1)} - \chi_{yy}^{(1)}) - \frac{3}{4}(\chi_{xy}^{(1)} + \chi_{yx}^{(1)}) = 0$$

$$(22) \quad \frac{3}{4}(\chi_{xx}^{(1)} - \chi_{yy}^{(1)}) - \frac{\sqrt{3}}{4}(\chi_{xy}^{(1)} + \chi_{yx}^{(1)}) = 0$$

$$(23) \quad \frac{\sqrt{3}}{2}\chi_{xz}^{(1)} - \frac{3}{2}\chi_{yz}^{(1)} = 0$$

$$(31) \quad -\frac{3}{2}\chi_{zx}^{(1)} - \frac{\sqrt{3}}{2}\chi_{zy}^{(1)} = 0$$

$$(32) \quad \frac{\sqrt{3}}{2}\chi_{zx}^{(1)} - \frac{3}{2}\chi_{zy}^{(1)} = 0$$

$$(33) \quad 0\chi_{zz}^{(1)} = 0,$$

where the indices in brackets refer to the tensor components after transformation. From (11) and (12) or (21) and (22) we deduce that  $\chi_{xx}^{(1)} = \chi_{yy}^{(1)}$  and  $\chi_{xy}^{(1)} = -\chi_{yx}^{(1)}$ . It has been demonstrated however, that the linear susceptibility is totally symmetric [72, 77], which leads to  $\chi_{xy}^{(1)} = \chi_{yx}^{(1)} = 0$ . From (13) and (23), we show  $\chi_{xz}^{(1)} = \chi_{yz}^{(1)} = 0$  and (31) and (32) imply that  $\chi_{zx}^{(1)} = \chi_{zy}^{(1)} = 0$ . Finally, (33) indicates that  $\chi_{zz}^{(1)}$  is independent and can have any value. In conclusion, for a crystal that possesses a three-fold symmetry axis, the linear susceptibility has only three nonvanishing components,  $\chi_{xx}^{(1)}$ ,  $\chi_{yy}^{(1)}$  and  $\chi_{zz}^{(1)}$ , two of which are independent ( $\chi_{xx}^{(1)} = \chi_{yy}^{(1)}$ ).

In appendix A we show the first-, second- and third-order susceptibility tensors, for all the 32 crystallographic point groups. In the case of linear optical processes, only five different tensor structures can be found. Indeed, the linear susceptibility tensors of crystals belonging to the tetragonal, trigonal and hexagonal systems have the same structures, as well as the susceptibilities of cubic crystals and isotropic media. In appendix A, the tensor structures for the second-order susceptibilities are listed only for the 21 crystallographic point groups that have no center of inversion.

## 1.4 Vibrations and symmetry

In the previous section (1.3.2), we studied how the structure of the susceptibility tensor depends on the spatial symmetry of the crystal or the molecule. In this section, we will use symmetry considerations to investigate the tensorial structure of the normal modes of

crystal and molecular vibration. A polyatomic molecule composed of  $n$  atoms, possesses  $3n$  degrees of freedom of motion, because any of its atoms can move along the three directions of a Cartesian coordinate system. The motions of a molecule can be either rotations, translations or vibrations. Molecules can have  $3n - 5$  or  $3n - 6$  normal modes of vibration, depending on whether they have linear<sup>3</sup> or nonlinear<sup>4</sup> geometries, respectively. If we suppose that the atoms move as harmonic oscillators, then the normal modes of vibration are independent of each other. According to group theory considerations [78], molecular vibrational modes are classified into the irreducible representations of the point group of the molecule. In order to study molecular vibration, it is therefore necessary to introduce some basic concepts of group theory, including, representations and the character table of a point group.

### 1.4.1 Representations of groups

Group representations allow to manipulate group theory using linear algebra, which is particularly useful when dealing with the effects of symmetry on the solutions of equations describing a system such as a molecule.

In mathematics, a group is a set  $G$  with an operation, called group law and denoted with the symbol  $\bullet$ , which combines two elements of the group  $g$  and  $g'$  to form another element  $g \bullet g'$ , of the same group. Every group has an identity element  $e$ , for which  $g \bullet e = e \bullet g = g$ . For every element in the group we associate an inverse element. It means that, if  $g'$  is the inverse element of  $g$ , then  $g \bullet g' = g' \bullet g = e$ .

A group representation is a linear transformation which corresponds to an action of the group  $G$  on a vector space  $V$ . In the particular case of the theory of molecular vibrations, representations of the point groups are sets of square matrices, so that the group operations can be represented by matrix multiplication. In this way, if  $\Gamma$  is a representation of the group  $G$ , for every two group elements  $g$  and  $g'$ , we associate the matrices  $\Gamma(g)$  and  $\Gamma(g')$ , that satisfy the group operation  $\Gamma(g)\Gamma(g') = \Gamma(g \bullet g')$ . The **dimensionality** of the representation corresponds to the number of rows or columns in the matrix.

A **similarity transformation** relates two elements  $g$  and  $g'$  of the group  $G$ . We say that  $g$  and  $g'$  are similar when there is an element  $h$  of the group  $G$  for each the following relation is satisfied:

$$h^{-1} \bullet g \bullet h = g'. \quad (1.34)$$

The notation  $h^{-1}$  stands for the inverse element of  $h$ .

When it is possible to reduce the matrices representing all the elements of the group to block form, with the same block structure and by the same similarity transformation, then the representation is said to be reducible. If this cannot be done, the representation

<sup>3</sup>In linear molecules, the bond angles between atoms are  $180^\circ$ . Carbon dioxide ( $\text{CO}_2$ ) is an example of linear molecule.

<sup>4</sup>In water molecule  $\text{H}_2\text{O}$ , the bonding angle between hydrogens is  $104.45^\circ$ , which characterizes a non-linear molecule.

is irreducible. An *irreducible representation* is the simplest and most fundamental representation of a group.

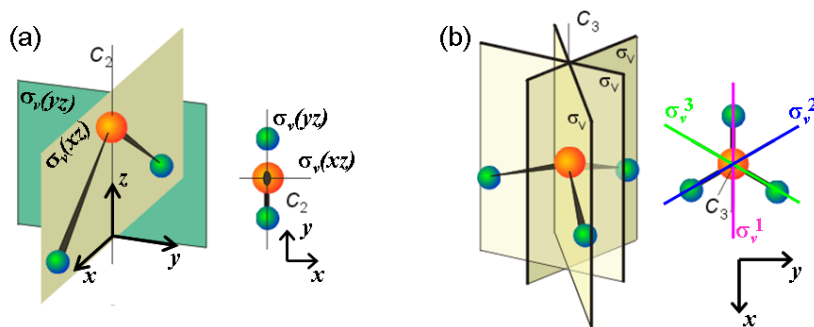


Figure 1.3: Scheme of the symmetry elements in the molecular frame for (a) a water molecule, that has  $C_{2v}$  symmetry and (b) an ammonia molecule, that belongs to the  $C_{3v}$  point group. In both cases we depict the symmetry elements in the 3D-space together with their projection in the  $xy$  plane (the molecule is seen from the top, the  $z$  axis pointing towards the reader). Reproduced from <http://www-linux.gsi.de/~wolle/TELEKOLLEG/KERN/PPT/NH3-symmetry1.ppt>.

As an example, let us consider the point group  $C_{2v}$ . This group has four elements: identity  $E$ , two-fold rotation  $C_2$  and two vertical reflection planes  $\sigma_v(xz)$  and  $\sigma_v(yz)$ , as depicted in Fig. (1.3a). The  $3 \times 3$  matrices corresponding to the transformation of the cartesian coordinate system  $(x, y, z)$  under each one of the four group operations are listed in table 1.3. The set of all four matrices together is a representation of dimension 3 of the group  $C_{2v}$ . We name this representation  $\Gamma_r$ . All four  $3 \times 3$  matrices of the representation  $\Gamma_r$  of the group  $C_{2v}$  are diagonal and have thus the same block structure. It means that  $\Gamma_r$  is a reducible representation that can be decomposed in 3 irreducible representations of  $C_{2v}$ , that we name  $\Gamma_r^1$ ,  $\Gamma_r^2$  and  $\Gamma_r^3$ . These are one-dimensional representations and they correspond to the diagonal elements of  $\Gamma_r$ , as listed in table 1.4.

Another example is the  $C_{3v}$  group, that has 6 symmetry elements: the identity  $E$ , two three-fold axes that we note  $C_3$  for a rotation of  $120^\circ$  and  $C_3^2$  for a rotation of  $240^\circ$ , and three vertical reflection planes that we note  $\sigma_v^1$ ,  $\sigma_v^2$  and  $\sigma_v^3$ . These symmetry elements are depicted in Fig. (1.3b). The  $3 \times 3$  matrices corresponding to the transformation of the cartesian coordinate system  $(x, y, z)$  under each one of the six operations are showed in table 1.5. The set of all six matrices together is a representation of dimension 3 of the group  $C_{3v}$ . This representation is named  $\Gamma_m$ . Two of the six  $3 \times 3$  matrices,  $\Gamma_m(E)$  and  $\Gamma_m(\sigma_v^1)$ , of the representation  $\Gamma_m$  are diagonal while four matrices,  $\Gamma_m(C_3)$ ,  $\Gamma_m(C_3^2)$ ,  $\Gamma_m(\sigma_v^2)$  and  $\Gamma_m(\sigma_v^3)$ , are block-diagonalizable with two blocks: the first one consisting of  $2 \times 2$  matrices, corresponding to the first two rows and columns and the second one composed by the element in the third row and third column of the matrices in  $\Gamma_m$ . This block structure is also present in a diagonal matrix, which means that  $\Gamma_m$  is a reducible representation that

Table 1.3: One reducible representation of the  $C_{2v}$  point group.

$C_{2v}$	$E$	$C_2$	$\sigma_v(xz)$	$\sigma_v(yz)$
$\Gamma_r$	$\begin{pmatrix} 1 & 0 & 0 \\ 0 & 1 & 0 \\ 0 & 0 & 1 \end{pmatrix}$	$\begin{pmatrix} -1 & 0 & 0 \\ 0 & -1 & 0 \\ 0 & 0 & 1 \end{pmatrix}$	$\begin{pmatrix} 1 & 0 & 0 \\ 0 & -1 & 0 \\ 0 & 0 & 1 \end{pmatrix}$	$\begin{pmatrix} -1 & 0 & 0 \\ 0 & 1 & 0 \\ 0 & 0 & 1 \end{pmatrix}$

Table 1.4: Some irreducible representations of the  $C_{2v}$  point group.

$C_{2v}$	$E$	$C_2$	$\sigma_v(xz)$	$\sigma_v(yz)$
$\Gamma_r^1$	1	-1	1	-1
$\Gamma_r^2$	1	-1	-1	1
$\Gamma_r^3$	1	1	1	1

can be decomposed in 2 irreducible representations of  $C_{3v}$ , that we name  $\Gamma_m^1$  and  $\Gamma_m^2$ . They are listed in table 1.6.

Table 1.5: One reducible representation of the  $C_{3v}$  point group.

$C_{3v}$	$E$	$C_3$	$C_3^2$	$\sigma_v^1$	$\sigma_v^2$	$\sigma_v^3$
$\Gamma_m$	$\begin{pmatrix} 1 & 0 & 0 \\ 0 & 1 & 0 \\ 0 & 0 & 1 \end{pmatrix}$	$\frac{1}{2} \begin{pmatrix} -1 & -\sqrt{3} & 0 \\ \sqrt{3} & -1 & 0 \\ 0 & 0 & 2 \end{pmatrix}$	$\frac{1}{2} \begin{pmatrix} -1 & \sqrt{3} & 0 \\ -\sqrt{3} & -1 & 0 \\ 0 & 0 & 2 \end{pmatrix}$	$\begin{pmatrix} 1 & 0 & 0 \\ 0 & -1 & 0 \\ 0 & 0 & 1 \end{pmatrix}$	$\frac{1}{2} \begin{pmatrix} -1 & -\sqrt{3} & 0 \\ -\sqrt{3} & 1 & 0 \\ 0 & 0 & 2 \end{pmatrix}$	$\frac{1}{2} \begin{pmatrix} -1 & \sqrt{3} & 0 \\ \sqrt{3} & 1 & 0 \\ 0 & 0 & 2 \end{pmatrix}$

Table 1.6: Some irreducible representations of the  $C_{3v}$  point group.

$C_{3v}$	$E$	$C_3$	$C_3^2$	$\sigma_v^1$	$\sigma_v^2$	$\sigma_v^3$
$\Gamma_m^1$	$\begin{pmatrix} 1 & 0 \\ 0 & 1 \end{pmatrix}$	$\frac{1}{2} \begin{pmatrix} -1 & -\sqrt{3} \\ \sqrt{3} & -1 \end{pmatrix}$	$\frac{1}{2} \begin{pmatrix} -1 & \sqrt{3} \\ -\sqrt{3} & -1 \end{pmatrix}$	$\begin{pmatrix} 1 & 0 \\ 0 & -1 \end{pmatrix}$	$\frac{1}{2} \begin{pmatrix} -1 & -\sqrt{3} \\ -\sqrt{3} & 1 \end{pmatrix}$	$\frac{1}{2} \begin{pmatrix} -1 & \sqrt{3} \\ \sqrt{3} & 1 \end{pmatrix}$
$\Gamma_m^2$	1	1	1	1	1	1

The representation  $\Gamma_m^1$  has dimension 2 while the representation  $\Gamma_m^2$  is one-dimensional.

The irreducible representations of a group satisfy the **great orthogonality theorem**, that establishes the following relation:

$$\sum_g \Gamma^{(i)}(g)_{\mu\nu}^* \Gamma^{(j)}(g)_{\alpha\beta} = \frac{h}{l_i} \delta_{ij} \delta_{\mu\alpha} \delta_{\nu\beta} \quad (1.35)$$

where  $*$  denotes the complex conjugate and  $\Gamma^{(i)}$  and  $\Gamma^{(j)}$  are inequivalent and irreducible representations of a group with  $h$  elements. Here, the summation over  $g$  runs over all the group elements and  $l_i$  is the dimensionality of the representation  $\Gamma^{(i)}$ . The subscripts  $\mu$  and  $\nu$  stand for the element in the  $\mu^{\text{th}}$  line and  $\nu^{\text{th}}$  column of the matrix  $\Gamma^{(i)}(g)$  (subscripts  $\alpha$  and  $\beta$  have the same role in the matrix  $\Gamma^{(j)}(g)$ ). It can be shown [78] that  $\sum_i l_i^2 = h$ , where the sum runs over all the inequivalent irreducible representations of the group. This relation is called the **dimensionality theorem** and is essential for working out the irreducible representations of any group.

All the matrix representations that are related to each other through unitary transformations are equivalent and therefore, there is a large degree of arbitrariness in the definition of the irreducible representations. The traces of matrices are, however, invariant under such transformations and by consequence, they can be used as characterizers of these representations. For this purpose, we define the *character* of the group element  $g$  in the  $j^{\text{th}}$  representation as<sup>5</sup>:

$$\chi_c^{(j)}(g) = \text{Tr}[\Gamma^{(j)}(g)], \quad (1.36)$$

where  $\Gamma^{(j)}(g)$  is the matrix corresponding to the element  $g$  in the representation  $\Gamma^{(j)}$ . When the irreducible representation is one-dimensional, the character of  $\Gamma^{(j)}(g)$  is  $\Gamma^{(j)}(g)$  itself, as a consequence of Eq. (1.36).

It is straightforward to prove that the characters form a set of orthogonal vectors in the group-element space, by replacing Eq. (1.36) into the relation established by the great orthogonality theorem (1.35) and by using in addition the dimensionality theorem. This leads to:

$$\sum_g \chi^{(i)}(g)^* \chi^{(j)}(g) = h \delta_{ij}. \quad (1.37)$$

The group elements can be classified into classes. Two symmetry operations are in the same class when they can be converted into one another by changing the coordinate system through application of some symmetry operation of the group. Mathematically, it means that two group elements  $g$  and  $g'$  are in the same class if they can transform into one another through a similarity transformation given by Eq. (1.34). For instance, in the group  $C_{3v}$  the two three-fold rotations  $C_3$  (rotation of  $120^\circ$  about the main axis) and  $C_3^2$  (rotation of  $240^\circ$ ) belong to the same class. In the same way, the three vertical mirror planes  $\sigma_v$ , containing the main axis of symmetry, belong also to the same class.

Matrices representing group elements of the same class have the same traces (in the  $C_{3v}$  group  $\text{Tr}[\Gamma_m^1(C_3)] = \text{Tr}[\Gamma_m^1(C_3^2)]$  and  $\text{Tr}[\Gamma_m^1(\sigma_v^1)] = \text{Tr}[\Gamma_m^1(\sigma_v^2)] = \text{Tr}[\Gamma_m^1(\sigma_v^3)]$ ). Matrices with the same trace have the same character and therefore, Eq. (1.37) can be rewritten in terms of classes, instead of group elements, according to:

---

<sup>5</sup>In general, a character is denoted  $\chi^{(j)}(g)$ . In this manuscript, we added the subscript  $c$  in order to discriminate the character  $\chi_c^{(j)}(g)$  from the  $p$ -order susceptibility tensor  $\chi^{(p)}$ .

Table 1.7: Character table of the  $C_{2v}$  point group.

$C_{2v}$	$E$	$C_2$	$\sigma_v(xz)$	$\sigma'_v(yz)$
$A_1$	1	1	1	1
$A_2$	1	1	-1	-1
$B_1$	1	-1	1	-1
$B_2$	1	-1	-1	1

Table 1.8: Character table of the  $C_{3v}$  point group.

$C_{3v}$	$E$	$2C_3$	$3\sigma_v$
$A_1$	1	1	1
$A_2$	1	1	-1
$E$	2	-1	0

$$\sum_k \chi_c^{(i)}(\mathcal{C}_k)^* \chi_c^{(j)}(\mathcal{C}_k) N_k = h \delta_{ij}, \quad (1.38)$$

where  $N_k$  is the number of elements in the class  $\mathcal{C}_k$  and the sum runs over classes and not group elements.

It can be shown [78], finally, that **the number of irreducible representations is equal to the number of classes** of a group.

## 1.4.2 Character tables

The *character tables* are a convenient way of displaying the characters of the classes in the different irreducible representations of a group. In these tables, the columns are labeled with the different classes of the group and the rows correspond to the irreducible representations. The entries are the character  $\chi_c^{(j)}(\mathcal{C}_k)$  of the class  $\mathcal{C}_k$  in the  $j^{\text{th}}$  irreducible representation. Tables 1.7 and 1.8 show the character table for the groups  $C_{2v}$  and  $C_{3v}$ , respectively.

The first row of a character table lists all the classes of the group, that are labeled according to the Schönflies notation. Each class is preceded by the number  $N_k$  of symmetry elements in the class. The first column of a character table lists all the irreducible representations of the group, that are labeled according to the Mulikan symbols. The number of rows and columns in a character table are the same, which is a consequence of the fact that the number of classes in a group is equal to the number of its irreducible representations.

The one-dimensional representations ( $l_i = 1$ ) are said to be nondegenerate and they are labeled with the symbols  $A$  or  $B$  in the Mulikan notation. Representations with dimension 2 ( $l_i = 2$ ) or 3 ( $l_i = 3$ ) are called doubly or triply degenerate and they are labeled  $E$  or  $T$ ,

respectively. All point groups with principal axes greater than two-fold (principal rotation less than  $180^\circ$ ) have degenerate representations.

The rules on how to interpret a character table are the following:

- If the irreducible representation is labeled  $A$ , then it is symmetric with respect to the principal rotation. By consequence, any  $A$  representation has always a character  $+1$  for the principal axis  $C_n$ . In the case of the point groups  $C_{2v}$  and  $C_{3v}$  the principal axes are respectively  $C_2$  and  $C_3$ , which have characters  $+1$  when the irreducible representation is  $A$ , according to tables 1.7 and 1.8.
- If the irreducible representation is labeled  $B$ , then its is antisymmetric with respect to the main axis of rotation. Therefore, any  $B$  representation has the character  $-1$  for the principal rotation  $C_n$ .
- One-dimensional representations,  $A$  and  $B$ , can only have characters  $\pm 1$ .
- The first listed symmetry operation is always the identity operation and its character gives the dimensionality of the irreducible representation. Consequently, in  $A$  and  $B$  representations the character of the element  $E$  is always 1, in  $E$  representations the character of the identity element is always 2 and in  $T$  representations the character of the  $E$  element is always 3.
- The first listed irreducible representation in a character table is always the totally symmetric representation of the group, labeled  $A_1$ , and it is composed of characters  $+1$  for all the symmetry operations.
- In centrosymmetric groups (i.e. groups with a center of inversion), the subscript  $g$  indicates symmetry with respect to inversion, whereas  $u$  stands for antisymmetry. For instance if an irreducible representation is labeled  $A_g$ , it is symmetric with respect to the principal rotation and also to inversion. Therefore, the characters of the main axis  $C_n$  and the inversion  $i$  are both  $+1$ .

According to these rules, we can identify the irreducible representations  $\Gamma_r^3$  of  $C_{2v}$  and  $\Gamma_m^2$  of  $C_{3v}$  in tables 1.4 and 1.6, to the totally symmetric representation  $A_1$ . In the same way, the irreducible representations  $\Gamma_r^1$  and  $\Gamma_r^2$  of  $C_{2v}$  (table 1.4) are identified as  $B$  representations, since they are antisymmetric with respect to the  $C_2$  axis. According to the character table of the group  $C_{2v}$  (table 1.7), we associate  $\Gamma_r^1$  to the  $B_1$  representation and  $\Gamma_r^2$  to  $B_2$ . The irreducible representation  $\Gamma_m^1$  of  $C_{3v}$  (table 1.6) is two-dimensional and it corresponds thus to the doubly-degenerate representation  $E$ . Note that  $\text{Tr}[\Gamma_m^1(E)] = 2$ , which corresponds to the dimensionality of the representation. Furthermore,  $\text{Tr}[\Gamma_m^1(C_3)] = \text{Tr}[\Gamma_m^1(C_3^2)] = 1$ , which corresponds to the character of the class  $C_3$  for the irreducible representation  $E$  in table 1.8, and  $\text{Tr}[\Gamma_m^1(\sigma_v^1)] = \text{Tr}[\Gamma_m^1(\sigma_v^2)] = \text{Tr}[\Gamma_m^1(\sigma_v^3)] = 0$ , which is the character of the class  $\sigma_v$  in the character table of the group  $C_{3v}$ .

### 1.4.3 The projection operator

It can be shown [78] that degenerate vibrational modes transform according to the irreducible representations of dimensionality greater than 1 and nondegenerate modes correspond to one-dimensional representations of the molecular point group. In order to determine the resonant susceptibility tensor (either linear, for spontaneous Raman scattering, third-order, for CRS processes or higher-order, for hyper-Raman effects) of a vibrational mode of a crystal or molecule belonging to some point group, one convenient way is to use the projection operator. This operator is a consequence of the great orthogonality theorem, stated in Eq. (1.35) and it allows to find the transformation properties of the susceptibility tensor of a specific vibrational mode, by projecting it into the irreducible representation that corresponds to the normal mode of vibration of the resonance. The projection operator to the  $j^{\text{th}}$  irreducible representation of a point group is given by [78, 79]:

$$\mathcal{P}^{(j)} = \frac{l_j}{h} \sum_g \chi_c^{(j)}(g)^{*} \mathbf{a}(g), \quad (1.39)$$

where  $\chi_c^{(j)}(g)$  is the character of the  $j^{\text{th}}$  irreducible representation,  $*$  stands for the complex conjugate and  $\mathbf{a}(g)$  is the transformation operator that corresponds to the action of the symmetry element  $g$  on the molecular frame  $(x, y, z)$ . In other words,  $\mathbf{a}(g)$  is the matrix that transforms  $(x, y, z)$  into  $(x', y', z')$  under the action of the group element  $g$ . The sum runs over all the symmetry operations of the group. The  $p$ -order susceptibility tensors for a given normal mode of vibration corresponding to the  $j^{\text{th}}$  irreducible representation of the group can be deduced from the projection operator as:

$$\chi^{(p)j} = \mathcal{P}^{(j)} \chi^{(p)}, \quad (1.40)$$

where  $\chi^{(p)}$  is the  $p$ -order susceptibility tensor in the molecular frame and  $\chi^{(p)j}$  is its “transformation” by the projection operator associated to the  $j^{\text{th}}$  irreducible representation of the group. By replacing Eq. (1.39) into Eq. (1.40) and from the fact that a tensor transforms according to Eq. (1.28), we can write:

$$\chi_{l_0 \dots l_p}^{(p)j} = \frac{l_j}{h} \sum_g \sum_{i_0 \dots i_p} \chi_c^{(j)}(g)^{*} a_{l_0 i_0}(g) \dots a_{l_p i_p}(g) \chi_{i_0 \dots i_p}^{(p)}, \quad (1.41)$$

with  $a_{li}(g)$  the element in the  $l^{\text{th}}$  row and  $i^{\text{th}}$  column of the matrix transformation corresponding the element  $g$  of the group. Furthermore, the susceptibility tensor must remain invariant under the application of the projection operator, which means that  $\chi_{l_0 \dots l_p}^{(p)j} = \delta_{l_0 i_0} \dots \delta_{l_p i_p} \chi_{i_0 \dots i_p}^{(p)}$ , according to Eq. (1.30).

For the group  $C_{2v}$ , the operators  $\mathbf{a}(g)$  are the  $3 \times 3$  matrices corresponding to the transformation of the cartesian coordinate system  $(x, y, z)$  that we depicted in table 1.3. Therefore,  $\mathbf{a}(E) = \Gamma_r(E)$  for the identity operator,  $\mathbf{a}(C_2) = \Gamma_r(C_2)$  for the two-fold rotation,  $\mathbf{a}(\sigma_v(xz)) = \Gamma_r(\sigma_v(xz))$  for the reflection plane  $xz$  and  $\mathbf{a}(\sigma_v(yz)) = \Gamma_r(\sigma_v(yz))$  for the reflection plane  $yz$ . As an example, we can calculate from the projection operator in Eq.

(1.41), the resonant linear susceptibility tensor  $\chi^{(1)}$  of a Raman process for a molecule in the group  $C_{2v}$ .

In order to determine the Raman susceptibility tensor of a totally symmetric vibrational mode, we have to project the susceptibility tensor  $\chi^{(1)}$  into the irreducible representation  $A_1$ . If the medium has  $C_{2v}$  symmetry, the component  $\chi_{lm}^{(1)A_1}$  for the totally symmetric resonance writes, according to Eq.(1.41):

$$\begin{aligned} \chi_{lm}^{(1)A_1} = & \frac{1}{4} \sum_{ij} \chi_{ij}^{(1)} [\chi_c^{A_1}(E)a_{li}(E)a_{mj}(E) + \chi_c^{A_1}(C_2)a_{li}(C_2)a_{mj}(C_2) \\ & + \chi_c^{A_1}(\sigma_v(xz))a_{li}(\sigma_v(xz))a_{mj}(\sigma_v(xz)) + \chi_c^{A_1}(\sigma_v(yz))a_{li}(\sigma_v(yz))a_{mj}(\sigma_v(yz))] \end{aligned} \quad (1.42)$$

where we used the fact that the dimensionality of the irreducible representation  $A_1$  is  $l_{A_1} = 1$  and the order of the group  $C_{2v}$  is  $h = 4$ .  $\chi_c^{A_1}(E)$  are the characters of the group elements in this representation and they are given in table 1.7. The transformation matrices  $\mathbf{a}$  are listed in table 1.3. By performing the calculations in Eq. (1.42), and by imposing the invariance of the the linear susceptibility tensor under the application of the projection operator, the linear susceptibility of a totally symmetric vibrational mode writes:

$$\begin{aligned} & \chi_{xx}^{(1)}; \quad \chi_{yy}^{(1)}; \quad \chi_{zz}^{(1)} \\ \chi_{xy}^{(1)} = \chi_{xz}^{(1)} = \chi_{yx}^{(1)} = \chi_{yz}^{(1)} = \chi_{zx}^{(1)} = \chi_{zy}^{(1)} = 0 \quad . \end{aligned} \quad (1.43)$$

Therefore, the linear susceptibility tensor of a totally symmetric vibrational mode of a medium with  $C_{2v}$  symmetry has only three nonvanishing components,  $\chi_{xx}^{(1)}$ ,  $\chi_{yy}^{(1)}$  and  $\chi_{zz}^{(1)}$ , that are all independent from each other.

The linear susceptibility tensors of the other vibrational modes of the  $C_{2v}$  group can be determined in the same way as for the totally symmetric vibration. Following, we list the structures of the linear susceptibility tensor for all the irreducible representations of the group  $C_{2v}$ , without considering the calculations:

- $A_2$  vibrational mode: all the tensor components vanish, except  $\chi_{xy}^{(1)}$  and  $\chi_{yx}^{(1)}$ . Since the linear susceptibility is a symmetric tensor, the two nonvanishing elements are equal, and  $\chi^{(1)A_2}$  is completely characterized by  $\chi_{xy}^{(1)} = \chi_{yx}^{(1)}$ .
- $B_1$  vibrational mode: the linear susceptibility has only two nonvanishing components that are equal due to the symmetric nature of the tensor. These components are  $\chi_{xz}^{(1)} = \chi_{zx}^{(1)}$ .
- $B_2$  vibrational mode: the only two nonvanishing components of the linear susceptibility are  $\chi_{yz}^{(1)} = \chi_{zy}^{(1)}$ .

The same procedure can be employed to calculate the Raman susceptibility for a molecule in the group  $C_{3v}$ . In this case, the operators  $\mathbf{a}(g)$  are the  $3 \times 3$  matrices corresponding to the transformation of the cartesian coordinate system  $(x, y, z)$  that we depicted in table 1.5:  $\mathbf{a}(E) = \Gamma_m(E)$  for the identity operator,  $\mathbf{a}(C_3) = \Gamma_m(C_3)$  for the three-fold rotation of  $120^\circ$ ,  $\mathbf{a}(C_3^2) = \Gamma_m(C_3^2)$  for three-fold rotation of  $240^\circ$ ,  $\mathbf{a}(\sigma_v^1) = \Gamma_m(\sigma_v^1)$ ,

$\mathbf{a}(\sigma_v^2) = \Gamma_m(\sigma_v^2)$  and  $\mathbf{a}(\sigma_v^3) = \Gamma_m(\sigma_v^3)$  for the three reflection planes. Here, we detail the calculations of the structure of the linear susceptibility tensor of a degenerate vibrational mode  $E$ . From Eq. (1.41), the component  $\chi_{lm}^{(1)E}$  writes:

$$\begin{aligned} \chi_{lm}^{(1)E} = & \frac{2}{6} \sum_{ij} \chi_{ij}^{(1)} \{2a_{li}(E)a_{mj}(E) - 1[a_{li}(C_3)a_{mj}(C_3) + a_{li}(C_3^2)a_{mj}(C_3^2)] \\ & + 0[a_{li}(\sigma_v^1)a_{mj}(\sigma_v^1) + a_{li}(\sigma_v^2)a_{mj}(\sigma_v^2) + a_{li}(\sigma_v^3)a_{mj}(\sigma_v^3)]\}, \end{aligned} \quad (1.44)$$

where we used the fact that the dimensionality of the irreducible representation  $E$  is  $l_E = 2$  and the order of the group  $C_{3v}$  is  $h = 6$ . The numbers multiplying the sums correspond to the characters of the group elements in this representation, according to table 1.8. The transformation matrices  $\mathbf{a}$  are listed in table 1.5. Eq. (1.44), together with the invariance of the susceptibility tensor under the application of the projection operator, leads to the following linear susceptibility of a degenerate vibrational mode  $E$  of a molecule with  $C_{3v}$  symmetry:

$$\chi_{xx}^{(1)} = \frac{1}{2} (\chi_{xx}^{(1)} - \chi_{yy}^{(1)}) \quad (1.45a)$$

$$\chi_{xy}^{(1)} = \frac{1}{2} (\chi_{xy}^{(1)} + \chi_{yx}^{(1)}) \quad (1.45b)$$

$$\chi_{xz}^{(1)} = \chi_{xz}^{(1)} \quad (1.45c)$$

$$\chi_{yy}^{(1)} = -\frac{1}{2} (\chi_{xx}^{(1)} - \chi_{yy}^{(1)}) \quad (1.45d)$$

$$\chi_{yz}^{(1)} = \chi_{yz}^{(1)} \quad (1.45e)$$

$$\chi_{zz}^{(1)} = 0 \quad (1.45f)$$

It follows from Eq. (1.45) that the linear susceptibility tensor of a degenerate vibrational mode  $E$  of the  $C_{3v}$  point group has only one vanishing component,  $\chi_{zz}^{(1)}$ . All the others are nonvanishing, and they are related to each other as follows: from Eqs. (1.45a) and (1.45d),  $\chi_{xx}^{(1)} = -\chi_{yy}^{(1)}$ ; from Eq. (1.45b)  $\chi_{xy}^{(1)} = \chi_{yx}^{(1)}$ ; from the symmetric nature of the linear susceptibility,  $\chi_{xz}^{(1)} = \chi_{zx}^{(1)}$  and  $\chi_{yz}^{(1)} = \chi_{zy}^{(1)}$ .

The same procedure can be applied to determine the linear susceptibility tensors of the other vibrational modes of the  $C_{3v}$  group:

- Totally symmetric vibrational mode  $A_1$ : the linear susceptibility has three nonvanishing components:  $\chi_{xx}^{(1)}$ ,  $\chi_{yy}^{(1)}$  and  $\chi_{zz}^{(1)}$ , from which only  $\chi_{zz}^{(1)}$  is independent. The other two nonvanishing tensor components are equal ( $\chi_{xx}^{(1)} = \chi_{yy}^{(1)}$ ).
- $A_2$  vibrational mode: the linear susceptibility tensor vanishes. It means that  $A_2$  normal modes of vibration can not be probed by spontaneous Raman scattering. We say that this mode is Raman inactive.

Table 1.9: Complete character table of the  $C_{2v}$  point group [80].

$C_{2v}$	$E$	$C_2$	$\sigma_v(xz)$	$\sigma'_v(yz)$	Unit vectors (IR)	Binary direct products (Raman)
$A_1$	1	1	1	1	$z$	$x^2, y^2, z^2$
$A_2$	1	1	-1	-1	$R_z$	$xy$
$B_1$	1	-1	1	-1	$x, R_y$	$xz$
$B_2$	1	-1	-1	1	$y, R_x$	$yz$

 Table 1.10: Complete character table of the  $C_{3v}$  point group [80].

$C_{3v}$	$E$	$2C_3$	$3\sigma_v$	Unit vectors (IR)	Binary direct products (Raman)
$A_1$	1	1	1	$z$	$x^2 + y^2, z^2$
$A_2$	1	1	-1	$R_z$	
$E$	2	-1	0	$(x, y), (R_x, R_y)$	$(x^2 - y^2, xy), (xz, yz)$

We have seen in section 1.3.2 that a  $(p + 1)$ -rank tensor behaves as a  $(p + 1)$ -rank polynomial, which is a consequence of the tensor decomposition in Eq. (1.27). Therefore, the susceptibility tensors deduced from the application of the projection operators can be written as polynomials, which are listed in the two last columns of the character tables (polynomials of rank 1 and 2 are depicted in the penultimate and last column of the character table, respectively). As an example, the complete character tables of the groups  $C_{2v}$  and  $C_{3v}$  are reproduced in tables 1.9 and 1.10, respectively.

In the case of the  $C_{2v}$  point group, the polynomial bases listed in the last column of the character table (see table (1.9)) come from the decomposition of the linear susceptibility tensors of the different vibrational modes, obtained from the projection operators. In the case of a totally symmetric vibration, from the structure of the linear susceptibility depicted in Eq. (1.43),  $\chi^{(1)A_1}$  decomposes as:

$$\chi^{(1)A_1} = \chi_{xx}^{(1)} \hat{\mathbf{x}} \otimes \hat{\mathbf{x}} + \chi_{yy}^{(1)} \hat{\mathbf{y}} \otimes \hat{\mathbf{y}} + \chi_{zz}^{(1)} \hat{\mathbf{z}} \otimes \hat{\mathbf{z}}.$$

By consequence, the three nonvanishing and independent components,  $\chi_{xx}^{(1)}$ ,  $\chi_{yy}^{(1)}$  and  $\chi_{zz}^{(1)}$  of the totally symmetric vibration ( $A_1$ ) correspond to the polynomials  $x^2$ ,  $y^2$  and  $z^2$  listed in the character table. The same analysis can be done for the other irreducible representations of the group.

The same reasoning applies to the  $C_{3v}$  point group. In the case of the  $A_1$  irreducible representation, we have seen that the linear susceptibility has three nonvanishing components,  $\chi_{xx}^{(1)} = \chi_{yy}^{(1)}$  and  $\chi_{zz}^{(1)A_1}$ . It means that the decomposition of the susceptibility tensor of a totally symmetric vibrational mode writes:

$$\begin{aligned}\chi^{(1)A_1} &= \chi_{xx}^{(1)}\hat{\mathbf{x}} \otimes \hat{\mathbf{x}} + \chi_{yy}^{(1)}\hat{\mathbf{y}} \otimes \hat{\mathbf{y}} + \chi_{zz}^{(1)}\hat{\mathbf{z}} \otimes \hat{\mathbf{z}} \\ &= \chi_{xx}^{(1)}(\hat{\mathbf{x}} \otimes \hat{\mathbf{x}} + \hat{\mathbf{y}} \otimes \hat{\mathbf{y}}) + \chi_{zz}^{(1)}\hat{\mathbf{z}} \otimes \hat{\mathbf{z}},\end{aligned}$$

Consequently, the two tensor components that are equal to each other,  $\chi_{xx}^{(1)}$  and  $\chi_{yy}^{(1)}$  correspond to the polynomial  $x^2+y^2$  and while  $\chi_{zz}^{(1)}$  is associated to  $z^2$ . These are the polynomials that are listed in the first row (corresponding to the  $A_1$  irreducible representation) in the last column of the character table of the group  $C_{3v}$  (see table 1.10).

The same procedure applied to the irreducible representation  $E$  of the point group  $C_{3v}$  leads to the following polynomials [see Eq. (1.45)]:  $x^2 - y^2$ , corresponding to the tensor components  $\chi_{xx}^{(1)} = -\chi_{yy}^{(1)}$  and  $xy$ ,  $xz$  and  $yz$  associated to the tensor elements  $\chi_{xy}^{(1)}$ ,  $\chi_{xz}^{(1)}$  and  $\chi_{yz}^{(1)}$ , respectively. These polynomials are listed in the line corresponding to the degenerate irreducible representation  $E$  in the last column of the character table of the  $C_{3v}$  group (see table 1.10). The brackets in the table, combining the polynomials as  $(x^2 - y^2, xy)$  and  $(xz, yz)$ , come from the fact that  $(x, y)$  are degenerated in couple, as we will see in next section (1.4.4).

Finally, even though we have calculated only linear susceptibilities in our examples, the projection operator technique can be applied to susceptibility tensors of any order. Therefore, the structures of the third order susceptibilities  $\chi^{(3)}$  of specific vibrational modes can be determined from the projections operators. This has already been done in reference [77], where the susceptibilities for all the irreducible representations of all the crystallographic point groups are listed, including linear, second and third-order susceptibilities.

#### 1.4.4 Selection rules and direct products: interpreting the character tables

In the previous section (sec. 1.4.3) we showed how to determine resonant susceptibility tensors for specific vibrational modes and how the tensor components are related to the polynomials listed in the last column of the character tables. A more straightforward way of obtaining the structures of the susceptibility tensors at resonance can be achieved in some particular cases by direct inspection of the character tables. These particular cases are dipole moments (infrared absorption) and linear susceptibilities (Raman scattering) at resonance. Higher-order susceptibilities are also included in the particular cases when the normal mode of vibration of the resonance is nondegenerate.

Linear unit vectors are the unit vectors  $\hat{\mathbf{x}}$ ,  $\hat{\mathbf{y}}$  and  $\hat{\mathbf{z}}$  that form the basis of the Cartesian coordinate system. A rotational unit vector is a vector with norm 1 that represents a rotation about one axis of the coordinate system. Accordingly,  $\mathbf{R}_x$ ,  $\mathbf{R}_y$  and  $\mathbf{R}_z$  are rotations about the  $x$ ,  $y$  and  $z$  axes, respectively. Finally, binary direct product of linear unit vectors corresponds to the tensorial product of these vectors. The result is a rank-2 tensor (a matrix) that can be decomposed according to the tensor decomposition rule in Eq. (1.27), as we showed in the previous section (1.4.3).

The penultimate column of the character table implies linear and rotational unit vectors: it shows how they transform under the symmetry operations of the group. If one coordinate  $x$ ,  $y$  or  $z$  features in one row of the character table, it means that the corresponding unit vector transforms according to this irreducible representation under the symmetry operations of the group. In vibrational spectroscopy, selection rules state that vibrational modes that transform as the linear unit vectors are infrared (IR) active (it means that they can be observed in the infrared spectrum) [78, 80]. By consequence, IR active modes can be easily identified from the character tables.

In the case of the  $C_{2v}$  point group (see table 1.9), the linear vectors  $\hat{z}$ ,  $\hat{x}$  and  $\hat{y}$  transform as the irreducible representations  $A_1$ ,  $B_1$  and  $B_2$ , respectively. It means that  $\hat{z}$  is invariant under all the symmetry operations of the group;  $\hat{x}$  remains itself under the identity operation and a reflection through the plane  $\sigma_v(xz)$  while it changes its direction (it becomes  $-\hat{x}$ ) under the two-fold rotation and the reflection through the plane  $\sigma_v(yz)$ ;  $\hat{y}$  is unaltered under the identity and reflection through  $\sigma_v(yz)$  but it changes its direction after a two-fold rotation or a reflection through  $\sigma_v(xz)$ .

For the  $C_{3v}$  point group (see table 1.10), the unit vector  $\hat{z}$  transforms following the totally symmetric representation  $A_1$ . It means that  $\hat{z}$  remains invariant under all the symmetry operations of the group. In the row of the degenerate representation  $E$  we observe the notation  $(x, y)$ . This indicates that the unit vectors  $\hat{x}$  and  $\hat{y}$  transform as a degenerate pair and by consequence, there is no difference in symmetry between the  $x$  and  $y$  directions, that must be treated as equivalent and indistinguishable.

The last column of the character table lists the transformation properties of the binary direct products of linear vectors. Selection rules state that normal modes of vibration transforming as the binary direct products of linear vectors are Raman active [80, 78]. By consequence, Raman active vibrations can be easily identified from the molecule's character table and the structure of the Raman susceptibility tensor can be inferred from the analysis of the last column of the character table, according to section 1.4.3.

In a similar way, the analysis of the character tables can lead to the tensor structure of nonlinear Raman processes. When it is not possible to determine the tensor structure directly from the character tables, which is the case for point groups with degenerate irreducible representations, it is necessary to use projection operators. However, the character tables can give at least some useful information on the vibrational modes. The end of this section is devoted to the study of the character tables in order to obtain information on the resonant nonlinear optical processes of higher-order.

Vibrational modes that are active in nonlinear Raman processes of order  $p$  transform as the  $(p + 1)$ -nary direct product of unit linear vectors. Therefore, in the case of normal modes active in CARS or SRS (third-order nonlinear optical processes with  $p = 3$ ), they transform as the quaternary direct product of linear unit vectors. The main selection rules for CARS and SRS, as third order nonlinear processes, are: (1) in centrosymmetric molecules, only vibrational modes that are symmetric with respect to the inversion will be allowed as transitions from the ground state, and (2) all Raman active modes are CARS and SRS active [81]. The reciprocal of the second condition is not necessarily true, and some vibrational modes active in CARS or SRS may be inactive in Raman.

In order to identify which normal modes are CARS active, from the inspection of the character tables, it is necessary to enumerate some rules to calculate direct products. Note that direct products of unit linear vectors imply the direct products of the corresponding irreducible representations<sup>6</sup>. The rules are listed below.

1. Any direct product of two or more irreducible representations of a group results in a representation of the group. The character and dimension of the resulting representation will be the multiplication of the characters and dimensions, respectively, of the irreducible representations present in the direct product.
2. The direct product of nondegenerate irreducible representations will also be a nondegenerate representation.
3. The product of a nondegenerate with a degenerate irreducible representation is a degenerate representation.
4. The direct product of any representation with the totally symmetric representation is the representation itself.
5. The direct product of an irreducible representation with itself is or contains the totally symmetric representation.
6. The direct product of two or more degenerate representations is a reducible representation  $\Gamma_r$ . The later can be reduced into the irreducible representations of the group  $\Gamma_i$ . The number of times  $n_i$  each irreducible representation  $\Gamma_i$  occurs in the reducible representation  $\Gamma_r$  is given by the relation:

$$n_i = \frac{1}{h} \sum_k N_k \chi_c^{(r)}(\mathcal{C}_k) \chi_c^{(i)}(\mathcal{C}_k), \quad (1.46)$$

where  $\chi_c^{(r)}(\mathcal{C}_k)$  and  $\chi_c^{(i)}(\mathcal{C}_k)$  are the characters of the class  $\mathcal{C}_k$  in the reducible and irreducible representations respectively, and  $h$  is the number of elements of the group. The sum runs over the classes of operations  $\mathcal{C}_k$  and  $N_k$  is the number of elements in the class.

In the case of the  $C_{2v}$  point group, these relations allow indeed to build the last column of the character table, according to:

- The unit vector  $\hat{\mathbf{z}}$  transforms as the totally symmetric irreducible representation  $A_1$ . By consequence, its binary direct product  $\hat{\mathbf{z}} \otimes \hat{\mathbf{z}}$  also transforms as the irreducible representation  $A_1$ .

---

<sup>6</sup>Here, we are not concerned with formal mathematical definitions. Readers interested in the mathematical formalism of group theory can read [82].

- According to the rules stated above, the direct product of the irreducible representation  $B_1$  with itself is the totally symmetric irreducible representation  $A_1$ . By consequence,  $\hat{\mathbf{x}} \otimes \hat{\mathbf{x}}$  transforms as  $A_1$ . The same is true for the representation  $B_2$  which implies that  $\hat{\mathbf{y}} \otimes \hat{\mathbf{y}}$  transforms as the totally symmetric irreducible representation.
- $B_1 \otimes A_1 = B_1$  and  $B_2 \otimes A_1 = B_2$ . By consequence,  $\hat{\mathbf{x}} \otimes \hat{\mathbf{z}}$  transforms as  $B_1$  and  $\hat{\mathbf{y}} \otimes \hat{\mathbf{z}}$  transforms as  $B_2$ .
- $B_1 \otimes B_2 = A_2$  which means that  $\hat{\mathbf{x}} \otimes \hat{\mathbf{y}}$  transforms as  $A_2$ .

In the same way, we can calculate the quaternary direct products of linear vectors in order to obtain the vibrational modes active in CARS or SRS. This corresponds to calculating the binary direct product of the binary direct product of unit linear vectors. In other words, the tensor structures of the resonant susceptibilities in a CARS or SRS process is obtained by calculating the direct product of the last column of the character table with itself. The result for the  $C_{2v}$  point group is listed below (in order to lighten the notation, we write the direct products as polynomials; for instance, we note  $x^2y^2$  instead of  $\hat{\mathbf{x}} \otimes \hat{\mathbf{x}} \otimes \hat{\mathbf{y}} \otimes \hat{\mathbf{y}}$ ):

$$\begin{aligned}
 A_1 \otimes A_1 &= A_1 \rightarrow x^4, y^4, z^4, x^2y^2, x^2z^2, y^2z^2 \\
 A_1 \otimes A_2 &= A_2 \rightarrow x^3y, xy^3, xyz^2 \\
 A_1 \otimes B_1 &= B_1 \rightarrow x^3z, xy^2z, xz^3 \\
 A_1 \otimes B_2 &= B_2 \rightarrow x^2yz, y^3z, yz^3 \\
 \left. \begin{aligned}
 A_2 \otimes A_2 &= A_1 \rightarrow x^2y^2 \\
 B_1 \otimes B_1 &= A_1 \rightarrow x^2z^2 \\
 B_2 \otimes B_2 &= A_1 \rightarrow y^2z^2
 \end{aligned} \right\} & \text{already obtained from } A_1 \otimes A_1 \\
 A_2 \otimes B_1 &= B_2 \rightarrow x^2yz & \text{already obtained from } A_1 \otimes B_2 \\
 A_2 \otimes B_2 &= B_1 \rightarrow xy^2z & \text{already obtained from } A_1 \otimes B_1 \\
 B_1 \otimes B_2 &= A_2 \rightarrow xyz^2 & \text{already obtained from } A_1 \otimes A_2. \quad (1.47)
 \end{aligned}$$

From Eq. (1.47) we can determine the structure of the CARS susceptibility of a medium with  $C_{2v}$  symmetry for any of the irreducible representations of the group. Let us consider the totally symmetric irreducible representation  $A_1$ . From the tensor decomposition rule in Eq. (1.27) and the polynomials listed in Eq. (1.47), the CARS susceptibility tensor of a totally symmetric resonance decomposes according to:

$$\begin{aligned}
 \chi^{(3)A_1} &= \chi_{xxxx}^{(3)} \hat{\mathbf{x}} \otimes \hat{\mathbf{x}} \otimes \hat{\mathbf{x}} \otimes \hat{\mathbf{x}} + \chi_{yyyy}^{(3)} \hat{\mathbf{y}} \otimes \hat{\mathbf{y}} \otimes \hat{\mathbf{y}} \otimes \hat{\mathbf{y}} + \chi_{zzzz}^{(3)} \hat{\mathbf{z}} \otimes \hat{\mathbf{z}} \otimes \hat{\mathbf{z}} \otimes \hat{\mathbf{z}} \\
 &+ \chi_{xxyy}^{(3)} \hat{\mathbf{x}} \otimes \hat{\mathbf{x}} \otimes \hat{\mathbf{y}} \otimes \hat{\mathbf{y}} + \chi_{xxzz}^{(3)} \hat{\mathbf{x}} \otimes \hat{\mathbf{x}} \otimes \hat{\mathbf{z}} \otimes \hat{\mathbf{z}} + \chi_{yyzz}^{(3)} \hat{\mathbf{y}} \otimes \hat{\mathbf{y}} \otimes \hat{\mathbf{z}} \otimes \hat{\mathbf{z}}.
 \end{aligned}$$

This leads to the following nonvanishing and independent components of the third-order susceptibility tensor of a totally symmetric resonance of a medium with  $C_{2v}$  symmetry:

$\chi_{xxxx}^{(3)}$ ,  $\chi_{yyyy}^{(3)}$ ,  $\chi_{zzzz}^{(3)}$ ,  $\chi_{xxyy}^{(3)}$ ,  $\chi_{xxzz}^{(3)}$  and  $\chi_{yyzz}^{(3)}$ . In a point group with only nondegenerate irreducible representations, the inconvenience of the direct product method compared to the projection operator is that in the first, the resulting susceptibility tensor is always symmetric under indexes permutation. This is a crude approximation at resonance, where Kleinman symmetry does not apply and indexes permutation are not authorized.

The same procedure can be applied to the  $C_{3v}$  point group. In this case however, this technique has an addition limitation because it does not allow to determine explicitly the direct products of linear vectors that correspond to degenerate irreducible representations. From the rules of direct products, we can nevertheless extract some information from the character tables. First, concerning the binary direct products of unit vectors, we can infer that:

$$\begin{aligned} A_1 \otimes A_1 &= A_1 \rightarrow z^2 \\ A_1 \otimes E &= E \rightarrow (xz, yz) \\ E \otimes E &= A_1 + A_2 + E \rightarrow ? \end{aligned} \tag{1.48}$$

The decomposition of the direct product  $E \otimes E$  is obtained from Eq. (1.46) and from the rules of the direct products stated above. First, we know that  $E \otimes E$  results in a reducible representation  $\Gamma_r$  of the group  $C_{3v}$  whose characters are:  $\chi_c^{(r)}(E) = \chi_c^{(E)}(E)\chi_c^{(E)}(E) = 4$ ,  $\chi_c^{(r)}(C_3) = \chi_c^{(E)}(C_3)\chi_c^{(E)}(C_3) = 1$  and  $\chi_c^{(r)}(\sigma_v) = \chi_c^{(E)}(\sigma_v)\chi_c^{(E)}(\sigma_v) = 0$ . Then, we decompose the representation  $\Gamma_r$  into the irreducible representations of the  $C_{3v}$  point group  $A_1$ ,  $A_2$  and  $E$  by using Eq. (1.46). This leads to  $n_{A_1} = n_{A_2} = n_E = 1$ , which means that each irreducible representation of the group occurs once in the reducible representation  $\Gamma_r$ . The inspection of the character table allows to find the decomposition into irreducible representations of the direct product  $E \otimes E$ , but it does not allow to determine the direct products of the linear unit vectors, which are now degenerated in couples. This is the reason of the question mark in Eq. (1.48).

In the case of CARS and SRS, the binary direct products of the binary direct products of linear vectors, give the normal modes that are active in CARS. When the direct product involves at least one nondegenerate representation of the  $C_{3v}$  group, it can be calculated directly from the character table, depicted in table 1.10. This leads to:

$$A_1 \otimes A_1 = A_1 \rightarrow z^4, x^2z^2 + y^2z^2, x^4 + 2x^2y^2 + y^4 \tag{1.49a}$$

$$\begin{aligned} A_1 \otimes E = E &\rightarrow (x^2z^2 - y^2z^2, xyz^2), (xz^3, yz^3), (x^4 - y^4, x^3y + xy^3), \\ &(x^3z + xy^2z, x^2yz + y^3z) \end{aligned} \tag{1.49b}$$

Note that  $E \otimes E = A_1 + A_2 + E$ , which means that Eq. (1.49) does not contain all the possible 4-nary direct products, but only the ones obtained when a nondegenerate irreducible representation is implied in the direct product. It means that the method of the direct product does not allow to determine the whole structure of the susceptibility

tensor when the point group has degenerate irreducible representations. This can only be done by applying the projection operator, as we showed in section 1.4.3.

## 1.5 From macroscopic measurements to microscopic information

We showed in sections 1.3 and 1.4 that the structure of the microscopic susceptibility tensor contains rich information on the symmetries, either structural or vibrational, of crystals or molecules in their proper frame. In polarimetric nonlinear optics experiments, however, the incident electrical fields that probe the macroscopic susceptibility tensor of the medium, are controlled and expressed in the macroscopic frame. In order to extract molecular or microscopic information on the studied sample it is thus necessary to relate the macroscopic and microscopic susceptibilities. In this section, we are particularly interested in two kinds of media: (1) crystalline and (2) molecular assemblies with an orientational statistical distribution.

Eq. (1.9) shows that the macroscopic nonlinear polarization  $\mathbf{P}^{(p)}$  is expressed as a function of the expectation values of the induced microscopic dipole moments and the number of polarizable units by unit volume. Here, we use an “additive model”, where the macroscopic polarization is calculated by summing over all molecular dipole moments. In this model, we assume that the interaction volume between the macroscopic incident field  $\mathbf{E}(\omega)$  and the medium is large enough to contain a large number of molecules but small enough so that  $\mathbf{E}(\omega)$  is uniform within it. In this way, we do not account for local fields or interactions between molecules. This model has shown its robustness in distinct situations, including crystals [83].

In this section, we define three distinct coordinate systems at different scales: molecular, microscopic and macroscopic. The first one is labeled  $(u, v, w)$  and it corresponds to the proper frame of one single molecule [see Fig. (1.4a)]. The local molecular dipole moment induced by the electrical field depends on the molecular hyperpolarizability, that we note  $\gamma_{\nu_0 \dots \nu_p}^{(p)}$ . The microscopic coordinate system is labeled  $(x, y, z)$  and it is defined either by the frame of a crystal unit-cell in a crystalline medium, or by the frame of the molecular distribution in the case of an assembly of molecules, as shown in Fig. (1.4b). The microscopic susceptibility is denoted  $\chi_{i_0 \dots i_p}^{(p)}$  and it is associated with the molecular hyperpolarizability by the relation  $\gamma_{\nu_0 \dots \nu_p}^{(p)} = \chi_{i_0 \dots i_p}^{(p)} / N$ , with  $N$  the number of crystal unit cells or molecules by unit volume<sup>7</sup>. Finally, the macroscopic coordinate system is labeled  $(X, Y, Z)$  [Fig. (1.4c)] and it corresponds to the laboratory frame where the electrical field components are defined. The  $p$ -order macroscopic susceptibility is represented by  $\chi_{I_0 \dots I_p}^{(p)}$ .

---

<sup>7</sup>The lowest-order hyperpolarizabilities are commonly labeled:  $\alpha_{uv}(-\omega; \omega)$ ,  $\beta_{uvw}(-\omega_\sigma; \omega_1, \omega_2)$  and  $\gamma_{uvvw}(-\omega_\sigma; \omega_1, \omega_2, \omega_3)$ , for  $p = 1, 2$  and  $3$ , respectively. In SI units they are expressed in  $\text{m}^3(\text{mV}^{-1})^{n-1}$ .

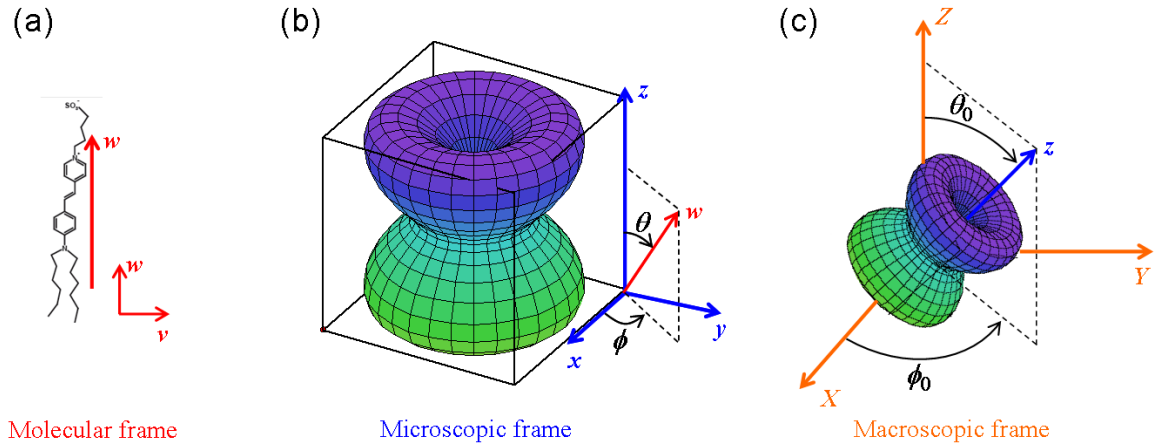


Figure 1.4: Definition of the coordinate systems at the three distinct scales of a molecular assembly: (a) the molecular frame  $(u, v, w)$  (the  $u$  points towards the reader); (b) the microscopic frame  $(x, y, z)$ , defined by the principal axis of the molecular distribution (see section 1.5.2) and (c) the macroscopic (or laboratory) frame.

### 1.5.1 Crystalline media

A crystal is a 3D spatial translational-repetition of a unit cell that contains all the information on the crystal symmetry. The unit cell is an assembly of atoms, ions or molecules defining a fixed structure with a given crystalline symmetry. The unit cells for all crystals must belong to one of the 32 crystallographic point groups defined in section 1.3.2. Therefore, the microscopic susceptibility tensors of crystalline media are deduced from the symmetry considerations discussed above. For a single crystal, the macroscopic susceptibility tensor depends on the orientation of the unit-cell. Thus, the nonlinear optical response for a given input polarization depends on both the symmetry and orientation of the unit cell. Fig. (1.5) shows a crystal of sodium chloride as an example. The chloride and sodium ions arrange themselves in a unit-cell with face-centered cubic symmetry. The translational-repetition of the unit-cells give raise to the macroscopic crystal.

The orientation of the crystal unit-cell in the 3D space is defined by the Euler angles  $\Omega_0 = (\theta_0, \phi_0, \psi_0)$ . These angles represent a composition of three elementary rotations, each one around a single axis, that allow to transform from a coordinate system to another. According to the definitions established in the introduction of this section, we chose the macroscopic frame as the coordinate system in which the incident electrical field polarizations are defined. This coordinate system is fixed as the reference frame and is called laboratory frame. The orientation of the microscopic (crystal) frame in relation to the reference coordinate system is obtained by three successive uniaxial rotations: first, a counterclockwise rotation of  $\phi_0$  around the  $z$  axis, followed by a clockwise rotation of  $\theta_0$  around the new  $y'$  axis and finally a counterclockwise rotation of  $\psi_0$  around the new  $z''$  axis.

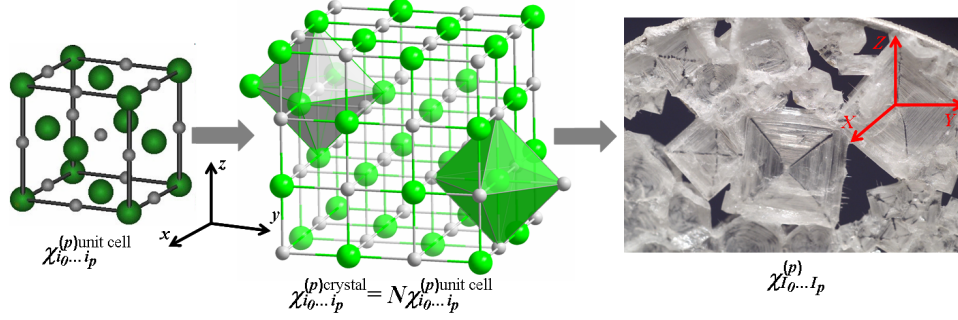


Figure 1.5: Sodium chloride crystal, composed of chloride (green) and sodium (grey) ions. The unit-cell is shown at left. Each ion is surrounded by six of the other type, which are located at the vertices of a regular octahedron. The macroscopic crystal structure, shown in the center, is obtained by translational-repetition of the unit-cell. Images of the crystal are shown at right.

The coordinate systems together with the defined Euler angles are depicted in Fig. (1.6). Following this convention, macroscopic susceptibility tensor  $\chi_{I_0 \dots I_p}^{(p)}$  can be obtained from the microscopic susceptibility  $\chi_{i_0 \dots i_p}^{(p)}$ , through a transformation such as the one described in Eq. (1.28), with the Euler transformation matrix  $a$  given by:

$$a = \begin{pmatrix} \cos \phi_0 \cos \theta_0 \cos \psi_0 - \sin \phi_0 \sin \psi_0 & -\cos \phi_0 \cos \theta_0 \sin \psi_0 - \sin \phi_0 \cos \psi_0 & \cos \phi_0 \sin \theta_0 \\ \sin \phi_0 \cos \theta_0 \cos \psi_0 + \cos \phi_0 \sin \psi_0 & -\sin \phi_0 \cos \theta_0 \sin \psi_0 + \cos \phi_0 \cos \psi_0 & \sin \phi_0 \sin \theta_0 \\ -\cos \psi_0 \sin \theta_0 & \sin \psi_0 \sin \theta_0 & \cos \theta_0 \end{pmatrix}. \quad (1.50)$$

This matrix transforms from the microscopic to the laboratory frame. Therefore, it is equal to the inverse of the matrix obtained by the three successive rotations by the angles  $(\theta_0, \phi_0, \psi_0)$  described above. If the microscopic frame is rotated by an angle  $\Omega_0$  in respect to the macroscopic frame, the final expression of the macroscopic susceptibility tensor writes, after transformation by Eq. (1.28):

$$\chi_{I_0 \dots I_p}^{(p)}(-\omega_\sigma; \omega_1, \dots, \omega_p) = \sum_{i_0 \dots i_p} a_{I_0 i_0}(\Omega_0) \dots a_{I_p i_p}(\Omega_0) \chi_{i_0 \dots i_p}^{(p)}(-\omega_\sigma; \omega_1, \dots, \omega_p), \quad (1.51)$$

where the capital and lowercase subscripts correspond respectively to the columns and lines of the transformation matrix  $a$  and  $\chi_{i_0 \dots i_p}^{(p)}$  is the susceptibility tensor in the crystal unit cell frame. The number of crystal unit cells by unit volume is included in the microscopic susceptibility. Since a crystal is defined as a translational-repetition of an unit cell, the frame for one or  $N$  unit cells is the same.

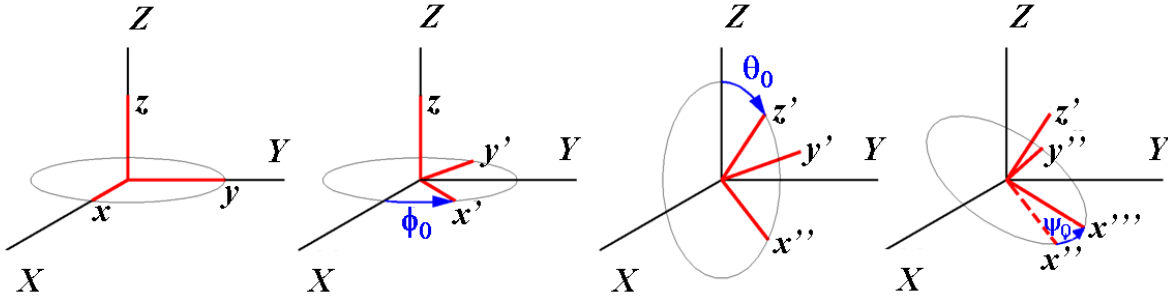


Figure 1.6: Euler angles  $(\theta_0, \phi_0, \psi_0)$  allowing to orient the crystal frame  $(x, y, z)$ , in red, in relation to the macroscopic coordinate system  $(X, Y, Z)$ , in black. The three successive rotations are depicted in the figure. First, a rotation of  $\phi$  around  $z$ , followed by a clockwise rotation of  $\theta$  around the new axis  $y'$  and finally, a rotation of  $\psi$  around the  $z$  axis.

## 1.5.2 Statistical molecular assemblies

When the electric field interacts with one molecule, it induces a local molecular dipole moment, that depends on the molecular hyperpolarizability  $\gamma_{\nu_0 \dots \nu_p}^{(p)}$ , whose structure is determined from the vibrational and structural symmetries of the molecule, as we showed in sections 1.3.2 and 1.4.

Molecules can aggregate in non-crystalline structures, with a certain degree of organization, such as polymers, membranes and proteins. Probing the molecular order and orientation of these structures is a great challenge for biologists and can bring important information on the functioning of biological entities. Molecular ensembles can be described as an assemblage of molecules with a probability  $f(\Omega)$  of being oriented between  $\Omega$  and  $\Omega + d\Omega$ , where  $\Omega = (\theta, \phi, \psi)$  are the Euler angles defined in section 1.5.1. The function  $f(\Omega)$  is named an orientational distribution function.

The  $p$ -order microscopic induced polarization of a molecular assembly is an orientational average of the molecular dipole moments  $p_{\text{mol}_i}^{(p)}$  in the frame  $(x, y, z)$  of the distribution function, defined by its principal axis of symmetry, as we show in Fig. (1.4b). It follows that:

$$p_i^{(p)} = \langle p_{\text{mol}_i}^{(p)}(\Omega) \rangle_{\Omega} = \int p_{\text{mol}_i}^{(p)}(\Omega) dN(\Omega), \quad (1.52)$$

where  $dN(\Omega) = Nf(\Omega)d\Omega$  is the number of molecules by unit volume with orientation between  $\Omega$  and  $\Omega + d\Omega$ . The molecular polarization in the microscopic frame  $(x, y, z)$  is a function of the orientation angle  $\Omega = (\theta, \phi, \psi)$  and of the molecular hyperpolarizability  $\gamma^{(p)}$ , according to:

$$p_{\text{mol}i_0}^{(p)}(\Omega) = \sum_{i_1 \dots i_p} \left[ \sum_{\nu_0 \dots \nu_p} a_{i_0 \nu_0} \dots a_{i_p \nu_p} \gamma_{\nu_0 \dots \nu_p}^{(p)} \right] E_{i_1} \dots E_{i_p}, \quad (1.53)$$

where the term in brackets corresponds to the molecular hyperpolarizability in the microscopic frame,  $\gamma_{\nu_0 \dots \nu_p}^{(p)}$  is the molecular hyperpolarizability in the molecular frame ( $u, v, w$ ) and  $a_{i\nu}$  is the transformation matrix from the molecular to the microscopic frame, given in Eq. (1.50). If we replace Eq. (1.53) into Eq. (1.52), the microscopic polarization induced in the sample is given by:

$$\chi_{i_0 \dots i_p}^{(p)}(-\omega_\sigma; \omega_1, \dots, \omega_p) = N \int \sum_{\nu_0 \dots \nu_p} \left[ a_{i_0 \nu_0}(\Omega) \dots a_{i_p \nu_p}(\Omega) \gamma_{\nu_0 \dots \nu_p}^{(p)}(-\omega_\sigma; \omega_1, \dots, \omega_p) \right] f(\Omega) d\Omega. \quad (1.54)$$

The macroscopic susceptibility  $\chi_{I_0 \dots I_p}^{(p)}$  can be obtained from a tensorial rotation of the microscopic susceptibility given in Eq. (1.54). If  $\Omega_0$  is the orientation of the distribution function in the macroscopic frame, as we show in Fig. (1.4c), then:

$$\chi_{I_0 \dots I_p}^{(p)}(-\omega_\sigma; \omega_1, \dots, \omega_p) = \sum_{I_0 \dots I_p} a_{I_0 i_0}(\Omega_0) \dots a_{I_p i_p}(\Omega_0) \chi_{i_0 \dots i_p}^{(p)}(-\omega_\sigma; \omega_1, \dots, \omega_p), \quad (1.55)$$

with  $a_{I_i}$  the rotation matrix from the microscopic to the macroscopic frame, given in Eq. (1.50). Therefore, the macroscopic susceptibility depends on the following microscopic information on the sample: (1) the molecular hyperpolarizability  $\gamma_{\nu_0 \dots \nu_p}^{(p)}$ , (2) the orientational distribution function  $f(\Omega)$  of the molecular assembly and (3) the orientation  $\Omega_0$  of the distribution function in relation to the macroscopic frame. The structure of the molecular hyperpolarizability can be determine from the analysis developed in sections 1.3.2 and 1.4. In order to characterize completely the macroscopic susceptibility, it is thus necessary to define the orientational distribution function.

## The orientational distribution function

**Orientational distribution functions with a known shape** The distribution function is unknown in general, but under some simplificative assumptions, we can suppose that its shape is known. This approach is usually applied in biological media, for which the orientational distribution function is most often defined with gaussian or cone shape [18, 84, 48, 50]. In a cone model, the orientational distribution function is depicted in Fig. (1.7a), and it is defined as:

$$f(\theta, \phi) = \begin{cases} \frac{1}{4\pi\xi} & \text{if } |\theta| \leq \xi \\ 0 & \text{otherwise,} \end{cases} \quad (1.56)$$

where  $\xi$  is the cone aperture. We have further supposed that the molecules are uniaxial, which is the reason why the orientational distribution function  $f(\theta, \phi)$  does not depend on

$\psi$ . We assume that the main axis of the cone lies in the  $XY$  plane, which means that the orientation of the cone in the macroscopic frame is completely specified by the angle  $\phi_0$ , as we show in Fig. (1.7). With these assumptions, the polarimetric nonlinear measurements give access to three microscopic parameters:

- the orientation of the molecules in the conical distribution, characterized by the cone aperture  $\xi$ ,
- the orientation of the cone in the macroscopic frame, characterized by the angle  $\phi_0$  in the  $XY$  plane,
- the component  $\gamma_{w\dots w}^{(p)}$  of the hyperpolarizability, which is the only one nonvanishing in uniaxial molecules.

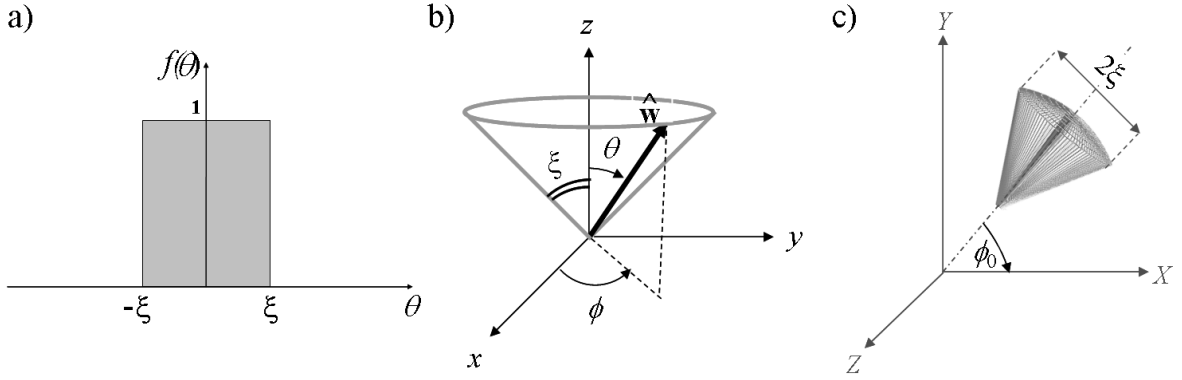


Figure 1.7: (a) FWHM of the function of a cone with aperture  $\xi$ , represented on the  $\theta$ -dependent section. (b) Scheme of the distribution in the microscopic frame  $(x, y, z)$ :  $\xi$  is the cone aperture of the distribution function and  $(\theta, \phi)$  defines the orientation of the molecular frame in the cone frame. (c) In the macroscopic frame, the main axis of the cone lays in the sample  $(XY)$  plane. The angle  $\phi_0$  specifies the orientation of the cone.

If the orientational distribution function is a discrete distribution  $\delta(\Omega - \Omega_0)$ , as we would expect for a crystal whose lattice is oriented at  $\Omega_0$  in respect to the laboratory frame, Eq. (1.54) becomes:

$$\begin{aligned} \chi_{I_0 \dots I_p}^{(p)}(-\omega_\sigma; \omega_1, \dots, \omega_p) &= N \int \sum_{i_0 \dots i_p} a_{I_0 i_0}(\Omega) \dots a_{I_p i_p}(\Omega) \chi_{i_0 \dots i_p}^{(p) \text{unit cell}}(-\omega_\sigma; \omega_1, \dots, \omega_p) \delta(\Omega - \Omega_0) d\Omega \\ &= N \int \sum_{i_0 \dots i_p} a_{I_0 i_0}(\Omega_0) \dots a_{I_p i_p}(\Omega_0) \chi_{i_0 \dots i_p}^{(p) \text{unit cell}}(-\omega_\sigma; \omega_1, \dots, \omega_p) \end{aligned}$$

that is equivalent to Eq. (1.51), if  $\chi_{i_0 \dots i_p}^{(p)\text{unit cell}} = \chi_{i_0 \dots i_p}^{(p)}/N$ . Note that in a crystal, we consider the distribution of unit cells in the macroscopic frame, which is defined by the orientation  $\Omega_0$ . This is why we used the microscopic susceptibility of one unit cell  $\chi_{i_0 \dots i_p}^{(p)\text{unit cell}}$ , instead of the molecular hyperpolarizability. This means that the approaches developed for crystals and molecular assemblies with angular statistical distributions is the same, the only difference being the angular distribution function.

**Unknown orientational distribution functions** If the shape of the orientational distribution function is unknown, we can decompose it in a series of orthogonal functions that are dependent on  $\Omega = (\theta, \phi, \psi)$ . Let us begin with some simplifivative assumptions: first, the molecules are uniaxial, which means that the orientational distribution function  $f(\theta, \phi)$  does not depend on  $\psi$  and the molecular hyperpolarizability in the molecular frame has only one nonvanishing component  $\gamma_{w \dots w}^{(p)}$ . Second, we state that the orientational distribution function is positive and normalized, following:

$$\begin{cases} f(\theta, \phi) \geq 0 & \forall(\theta, \phi) \\ \int_0^{2\pi} \int_0^\pi f(\theta, \phi) \sin \theta d\phi d\theta = 1. \end{cases} \quad (1.57)$$

which guarantees the possibility of decomposing the function in a series of orthogonal function.

It is well known that the functions named *spherical harmonics* form a complete orthonormal set for the functions defined in  $S^2$ , where  $S^2 \subset \mathbb{R}^3$  is the sphere of unit radius centered in the origin of the Cartesian coordinate system. Therefore, the orientational distribution function can be decomposed according to:

$$f(\theta, \phi) = \sum_{J=0}^{\infty} \sum_{m=-J}^{m=J} f_m^J Y_m^J(\theta, \phi), \quad (1.58)$$

where  $Y_m^J(\theta, \phi)$  is the spherical harmonics of order  $J$ , with  $J \in \mathbb{N}$  and  $|m| \leq J$ . The zero-order term of the decomposition,  $Y_0^0$  is isotropic and the degree of order becomes higher when  $J$  increases. The coefficients  $f_m^J$  are called *order parameters* [85] and they correspond to the weights of the function  $Y_m^J$  in the decomposition. Here, we list the first-order spherical harmonics ( $J = 1$ ), that will be necessary for the following of this section:

$$Y_{-1}^1(\theta, \phi) = \frac{1}{2} \sqrt{\frac{3}{2\pi}} \sin \theta e^{-i\phi} \quad Y_0^1(\theta, \phi) = \frac{1}{2} \sqrt{\frac{3}{\pi}} \cos \theta \quad Y_1^1(\theta, \phi) = -\frac{1}{2} \sqrt{\frac{3}{2\pi}} \sin \theta e^{i\phi}. \quad (1.59)$$

An important property of the spherical harmonics is the orthogonality relation, that establishes that:

$$\int_0^{2\pi} \int_0^\pi Y_m^{J*}(\theta, \phi) Y_{m'}^{J'}(\theta, \phi) \sin \theta d\theta d\phi = \delta_{JJ'} \delta_{mm'} \quad (1.60)$$

where  $\delta_{JJ'}$  is the Kronecker delta and  $*$  stands for the complex conjugate. It can be shown that  $Y_m^{J*}(\theta, \phi) = (-1)^m Y_{-m}^J(\theta, \phi)$ .

The product of two spherical harmonics of order  $J$  and  $J'$  results:

$$Y_{m_1}^{J_1}(\theta, \phi) Y_{m_2}^{J_2}(\theta, \phi) = \sum_{J=|J_1-J_2|}^{|J_1+J_2|} \sum_{m=-J}^J \sqrt{\frac{(2J_1+1)(2J_2+1)(2J+1)}{4\pi}} \times \begin{pmatrix} J_1 & J_2 & J \\ 0 & 0 & 0 \end{pmatrix} \begin{pmatrix} J_1 & J_2 & J \\ m_1 & m_2 & m \end{pmatrix} Y_m^{J*}(\theta, \phi), \quad (1.61)$$

where  $\begin{pmatrix} J_1 & J_2 & J \\ m_1 & m_2 & m \end{pmatrix}$  are the Wigner 3  $j$ -symbols, that are related to the Clebsch-Gordan coefficients [86]. These symbols are integers or half-integers that verify the following properties:

1.  $-|J_1| \leq m_1 \leq |J_1|$ ,  $-|J_2| \leq m_2 \leq |J_2|$  and  $-|J| \leq m \leq |J|$
2.  $m_1 + m_2 = m$
3.  $J_1 + J_2 + J$  is an integer
4. the triangular inequalities  $|J_1 - J_2| \leq J \leq |J_1 + J_2|$
5.  $\begin{pmatrix} J_1 & J_2 & J \\ 0 & 0 & 0 \end{pmatrix} = 0$  if  $J_1 + J_2 + J$  is odd.

Consequently, the products of two spherical harmonics will follow the selections rules of the Wigner 3  $j$ -symbols.

We have so far expanded the orientational distribution function  $f(\theta, \phi)$  in a series of spherical harmonics and we have stated some important properties and rules for the spherical harmonics. Now, we will show how to use these rules so that we can extract order information from the microscopic susceptibility tensor  $\chi_{i_0 \dots i_p}^{(p)}$ , given in Eq. (1.54).

First, as stated above, the hypothesis adopted here is that the molecules are uniaxial. This means that the only nonvanishing component of the  $p$ -order molecular hyperpolarizability is  $\gamma_{w \dots w}^{(p)}$ . In this case, the sum in Eq. (1.54), that corresponds to the tensor rotation from the molecular frame to the microscopic frame (of the orientational distribution), has only one term,  $a_{i_0 w} \dots a_{i_p w} \gamma_{w \dots w}^{(p)}$ , where  $a$  is the rotation matrix given in Eq. (1.50) with  $\psi = 0^\circ$ . We note that the only matrix components that are involved in the theoretical microscopic  $p$ -order susceptibilities, are the ones in the third column of the rotation matrix  $a$ , that we reproduce here:

$$a_{xw} = \cos \phi \sin \theta, \quad a_{yw} = \sin \phi \sin \theta, \quad a_{zw} = \cos \theta.$$

From the expressions of the first-order spherical harmonics, given in Eq. (1.59), we can write the components  $a_{iw}$  of the rotation matrix as a linear combination of the functions  $Y_m^1$ , according to:

$$\begin{aligned}
 a_{xw} &= \sin \theta \cos \phi = \sqrt{\frac{2\pi}{3}}(Y_{-1}^1 - Y_1^1) \\
 a_{yw} &= \sin \theta \sin \phi = i\sqrt{\frac{2\pi}{3}}(Y_{-1}^1 + Y_1^1) \\
 a_{zw} &= \cos \theta = 2\sqrt{\frac{\pi}{3}}Y_0^1.
 \end{aligned} \tag{1.62}$$

As a consequence, the microscopic susceptibility in Eq. (1.54) can be written in function of the spherical harmonics, following:

$$\begin{aligned}
 \chi_{i_0 \dots i_p}^{(p)}(-\omega_\sigma; \omega_1, \dots, \omega_p) &\propto N\gamma_{w \dots w}^{(p)}(-\omega_\sigma; \omega_1, \dots, \omega_p) \int_0^\pi \int_0^{2\pi} Y_{m_0}^1(\theta, \phi) \dots Y_{m_p}^1(\theta, \phi) \\
 &\times \sum_{J=0}^\infty \sum_{m=-J}^{m=J} f_m^J Y_m^J(\theta, \phi) \sin \theta d\theta d\phi,
 \end{aligned} \tag{1.63}$$

with -1, 0 or 1 being all the possibilities for  $m_0 \dots m_p$ .

From the product rule of spherical harmonics, in Eq. (1.61), we can write:

$$Y_{m_0}^1(\theta, \phi) \dots Y_{m_p}^1 \propto \sum_{J=0}^{J=p+1} \sum_{m=-J}^J C_m^J Y_m^{J*}(\theta, \phi), \tag{1.64}$$

where  $p$  is the order of the nonlinear optical process and the proportionality signal omits all the Wigner 3  $j$ -symbols from the successive products  $Y_{m_i}^1 Y_{m_{i+1}}^1$  (detailed calculations for a third-order nonlinear optical process ( $p = 3$ ) are shown in appendix B). From the selection rules of the Wigner 3  $j$ -symbols,  $J + 1 \times (p + 1)$  must be even so that the product does not vanish. Therefore, the order  $J$  of the resulting spherical harmonics must have the same parity as  $p + 1$ <sup>8</sup>. Furthermore, as a consequence of the triangular inequalities,  $0 \leq J \leq p + 1$ . By replacing Eq. (1.64) into Eq. (1.63), the microscopic susceptibility writes:

---

<sup>8</sup>Note that this property arises only when the order of the spherical harmonics in the product is indiscernible. If it is not the case (such as for resonant processes, where it is not possible to permute the  $Y_m^J$  in the product), a different formalism should be used, and this property does not hold [87].

$$\begin{aligned}
 \chi_{i_0 \dots i_p}^{(p)} &\propto N \gamma_{w \dots w}^{(p)} \sum_{J=0}^{\infty} \sum_{m=-J}^J \sum_{J'=p+1}^{J'} \sum_{m'=-J'}^{J'} f_m^J C_{m'}^{J'} \int_0^\pi \int_0^{2\pi} Y_{m'}^{J'*}(\theta, \phi) Y_m^J(\theta, \phi) \sin \theta d\theta d\phi, \\
 &\propto N \gamma_{w \dots w}^{(p)} \sum_{J=0}^{\infty} \sum_{m=-J}^J \sum_{J'=p+1}^{J'} \sum_{m'=-J'}^{J'} C_{m'}^{J'} f_m^J \delta_{JJ'} \delta_{mm'}.
 \end{aligned} \tag{1.65}$$

where we have omitted the frequency arguments of the susceptibility. The last proportionality comes from the orthogonality property of the spherical harmonics, in Eq. (1.60). As  $J'$  has the same parity as  $p + 1$  and  $0 \leq J' \leq p + 1$ , the orthogonality of the spherical harmonics implies that the  $p$ -order theoretical microscopic susceptibility vanishes when  $J > p + 1$  or if the parities of  $J$  and  $p + 1$  are not the same. Consequently, the theoretical  $\chi_{i_0 \dots i_p}^{(p)}$  depends only on the terms of the expansion of the orientational distribution function whose orders  $J$  are lower than  $p + 1$  and with the same parity. Therefore, for even-order nonlinear optical processes, only the odd order terms of the series expansion of the distribution function contribute to the theoretical expression of the microscopic susceptibility. In the contrary, in the case of odd-order processes, only the even terms of the series expansion are taken into account.

The macroscopic susceptibility tensor is finally obtained by rotating the microscopic  $\chi_{i_0 \dots i_p}^{(p)}$  in the laboratory frame, as in Eq. (1.55). By consequence, the microscopic parameters that can be read-out from a  $p$ -order nonlinear optical process are the following:

- The nonvanishing component of molecular hyperpolarizability  $\gamma_{w \dots w}^{(p)}$ .
- The order parameters  $f_m^J$  of the spherical harmonics expansion of the orientational distribution function. If  $p$  is even (respectively odd), only the parameters with  $J$  odd (respectively even) can be determined.
- The orientation  $(\theta_0, \phi_0)$  of the orientational distribution function in the macroscopic frame.

In the case of a third-order nonlinear process, such as CARS or SRS, the only order parameters that can be read-out from the polarimetric measurements in the nonresonant regime are the zero, second and fourth order,  $f_m^0$ ,  $f_m^2$  and  $f_m^4$ , respectively. Note that for each order  $J$  the number of parameters to be determined is  $2J + 1$ , since  $|m| \leq J$ .

We have assumed in this paragraph that the molecules are uniaxial and by consequence, the orientational distribution function does not depend on  $\psi$ . If we add the assumption that the orientational distribution function has cylindrical symmetry, then it does not depend on  $\phi$  and the decomposition is done in a series of the Legendre polynomials  $P^J(\cos \theta)$ . They can be obtained from the spherical harmonic functions through the relation  $Y_0^J(\theta, \phi) = [(2J + 1)/4\pi]^{1/2} P^J(\cos \theta)$ . The expansion of the orientational distribution function in a series of the Legendre polynomials is detailed in chapter 5.

In the other hand, if we do not suppose any *a priori* information on the symmetry of the medium, the orientational distribution function can also be expanded in a series of orthogonal functions, called the Wigner functions, that depend on the three Euler angles  $(\theta, \phi, \psi)$ . In this case, the decomposition of the distribution function writes:

$$f(\theta, \phi, \psi) = \sum_{m', m, J} f_{m'm}^J D_{m'm}^J(\theta, \phi, \psi), \quad (1.66)$$

where the coefficients  $f_{m'm}^J$  are the order parameters and  $-J \leq m, m' \leq J$ , with  $J \in \mathbb{N}$ . The Wigner functions relate to the spherical harmonics according to  $D_{m0}^J(\theta, \phi, \psi) = \sqrt{4\pi/(2J+1)} Y_m^J(\theta, \phi)$ . They satisfy the following orthogonality property:

$$\int_0^{2\pi} \int_0^\pi \int_0^{2\pi} D_{m'_1 m_1}^{J_1*}(\theta, \phi, \psi) D_{m'_2 m_2}^{J_2}(\theta, \phi, \psi) \sin \theta d\theta d\phi d\psi = \frac{8\pi^2}{2J_1 + 1} \delta_{J_1 J_2} \delta_{m_1 m_2} \delta_{m'_1 m'_2}. \quad (1.67)$$

In the general case, where no assumption is made on the distribution function, the calculations when the molecular assembly depends on the three Euler angles  $(\theta, \phi, \psi)$  become more complex, since the number of order parameters to be determined increases.

## 1.6 Conclusion

In this chapter, we developed the basis of nonlinear optics from a semi-classical approach. First, we were able to write the expressions of the susceptibility tensors from the density matrix formalism. Then we deduced some of the symmetry properties of the susceptibilities, that could be intrinsic permutation symmetries or arise from spatial considerations. In the case of vibrational resonances, we showed how the symmetry of the normal mode of the molecular vibration changes the structure of the associated susceptibilities. Next, we studied the macroscopic nonlinear optical responses from crystals and molecular assemblies with statistical orientational distribution. In the case of crystals, nonlinear polarimetric measurements allow to retrieve the symmetry of the unit cell and its orientation in the macroscopic frame. In the case of molecular assemblies, if the orientational distribution function is unknown, it can be expanded in a series of orthonormal functions, that characterize the order of the molecular assembly. Finally, polarimetric measurements on this kind of sample allow to determine the symmetry of the molecular hyperpolarizability and of the distribution function, together with its orientation in the macroscopic frame. The symmetry properties discussed in this chapter will be exploited throughout this manuscript, in order to analyze molecular and biological samples.

---

---

## CHAPTER 2

---

# THE POLARIZATION RESOLVED CRS SETUP: DESCRIPTION AND CHARACTERIZATION

As we demonstrated in chapter 1, molecular symmetry and macroscopic distribution read-out of the susceptibility tensor is possible with polarization dependence monitoring. In this section we describe the experimental setup used in order to perform polarization resolved CARS and SRS measurements. Special attention must be paid to the incident polarization distortions that may introduce the optical apparatus. These distortions can lead to misleading extraction of molecular order information from polarimetric measurements. Here, we describe a model accounting for these effects and develop a calibration technique for the determination of polarization parameters in the sample plane using either two-photon fluorescence polarimetry in liquids or polarimetric analysis of the incident beam itself. Finally, some samples can be highly birefringent, which can also affect the incident and emitted polarizations. In this chapter, we depict a model that allows measuring the anisotropy of a thick sample and accounting for this effect in nonlinear polarization resolved experiments.

## 2.1 Description of the experimental setup

### 2.1.1 The CARS setup

The experimental CARS setup is depicted in Fig. (2.1). The incident pump and Stokes pulse trains are delivered by two picosecond tunable mode-locked lasers (Coherent Mira 900, 76 MHz, 3 ps), pumped by a Nd:Vanadate laser (Coherent verdi). The lasers are electronically synchronized (Coherent SychroLock System) and are externally pulse-picked (APE pulse Picker) to reduce their rate to 3.8 MHz. Both beams are linearly polarized and achromatic half-waveplates mounted in a step rotation motor, allow to rotate the incident

## EXPERIMENTAL SETUP

polarizations independently. The beams are spatially recombined through a dichroic filter, injected into a commercial inverted microscope (Zeiss Axiovert 200 M) and focused in the sample through a low numerical aperture microscope objective (Olympus LUCPLFLN 40X, NA = 0.6), in order to avoid any contribution from the  $Z$ -polarized component of the excitation field in the experiment [88]. In microscopy configuration, the sample is placed in a  $XYZ$  piezoelectric plate (Physike Instrument), in order to allow 3D scanning. In spectroscopy configuration (liquid sample), the sample is placed in a fixed plate. The generated signal is either collected forward (fwd-CARS) by another microscope objective (Olympus LMPLFLN 50X, NA = 0.5) or backward by the excitation objective (epi-CARS). Then, it is filtered by two dichroic filters (a lowpass filter to reject the incident lasers and a bandpass filter spectrally centered at the wavelength of the emitted anti-Stokes beam). The signal is split by a broadband polarizing cube beamsplitter (Newport) and the two resulting perpendicularly polarized beams are finally detected by two avalanche photodiodes (Perkin Elmer SPCM-AQR-14) used in photon counting mode.

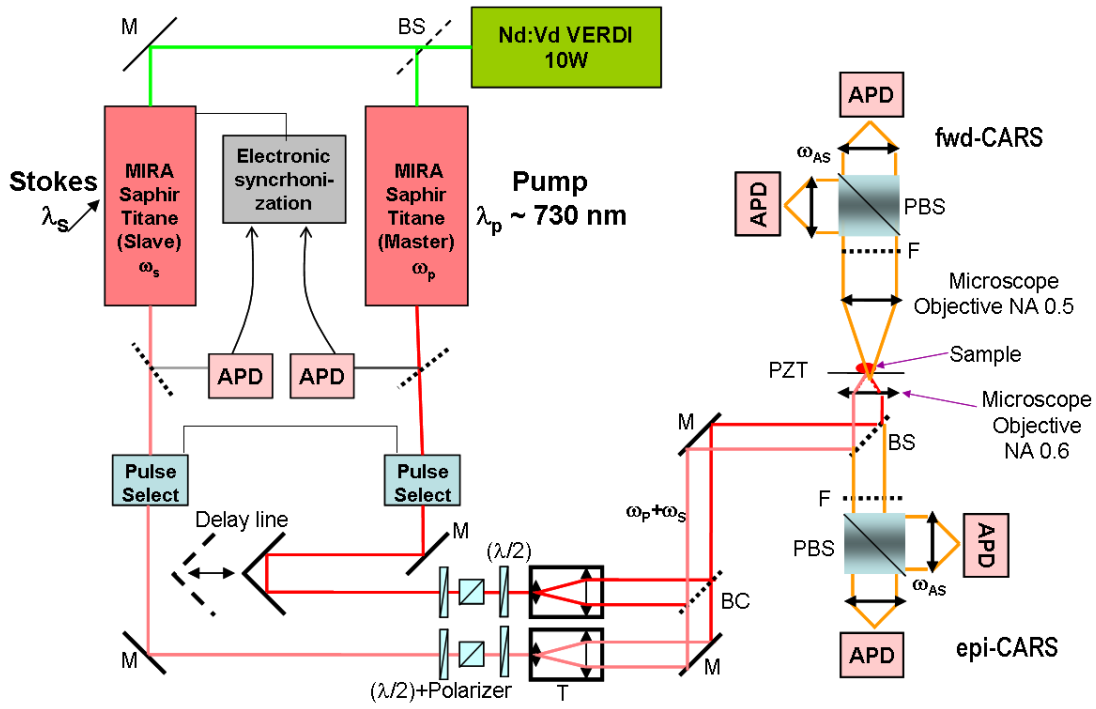


Figure 2.1: Scheme of the polarization resolved CARS setup. APD: avalanche photodiode; M: mirror; BC and BS: beam combiner and beamsplitter, respectively (dichroic filters); F: lowpass or bandpass filters; PZT: translational  $XYZ$  piezoelectric plate; PBS: polarizing beamsplitter; T: telescope;  $\lambda/2$ : half-wave plates.

The incident wavelengths are tunable in order to probe different vibrational resonances of the several studied samples. Here, the adopted protocol is to set the wavelength of the

pump beam  $\lambda_p \approx 730$  nm and to adjust the wavelength of the Stokes field according to the targeted resonance. In this work, we perform a complete polarimetric CARS analysis, where three different schemes of polarization tuning are feasible: either the polarization of the Stokes (respectively pump) is fixed along the  $X$  axis and the polarization of the pump (respectively Stokes) rotates from  $0^\circ$  to  $360^\circ$ , or both input polarizations rotate simultaneously. The three polarization configurations are called P, S and PS, respectively. The step of the incident polarization tuning is  $5^\circ$ , except when noted otherwise. For each pair of incident field directions,  $(\mathbf{E}(\alpha_p), \mathbf{E}(\alpha_s))$ , the intensity of the emitted anti-Stokes signal is detected either along the  $X$  or the  $Y$  axes. In the following of this manuscript, we note  $\alpha_{p,s}$  the incident polarization angles relative to the  $X$  axis. Fig. (2.2) shows the three possible polarization configurations, with a closeup on the detection scheme. The linear incident polarizations lay in the  $XY$  plane, which corresponds to the sample plane.

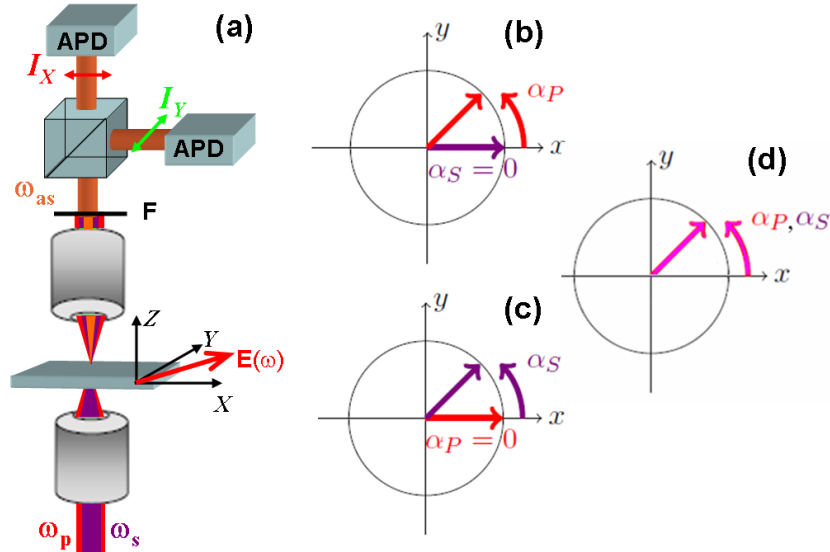


Figure 2.2: The three schemes of polarization tuning used in this work. (a) Closeup of the detection setup. The incident polarizations lay in the sample plane and the intensity of the emitted signal is detected either along  $X$  or  $Y$ . (b) Polarization configuration P: the Stokes polarization is fixed along  $X$  ( $\alpha_s = 0^\circ$ ) whereas the pump polarization  $\alpha_p$  rotates between  $0^\circ$  and  $360^\circ$ , in the sample plane. (c) Polarization configuration S:  $\alpha_p = 0^\circ$  and  $\alpha_s$  rotates from  $0^\circ$  to  $360^\circ$ . (d) Polarization configuration PS: both incident polarization rotate simultaneously in the sample plane between  $0^\circ$  and  $360^\circ$ .

### 2.1.2 The SRS setup

The SRS experiment is based on the stimulated Raman loss process (SRL), in which we detect the decrease of the pump intensity due to stimulated Raman emission. The setup for performing SRS measurements is showed in Fig. (2.3a) and it has been developed according

to the principles described in references [40, 39]. It is based on the CARS experiment, with some significant modifications. First, the laser beams are not pulse-picked and they operate with their standard repetition rate of 76 MHz. Second, the Stokes beam is modulated at 1 MHz with an acousto-optic modulator. Due to the stimulated Raman scattering, the pump beam transmitted through the sample is modulated at the same frequency as the Stokes field, according to Fig. (2.3b). The pump field is then collected in the forward direction by the same collection objective as in the CARS setup, filtered by a short-pass filter, projected into the  $X$  or  $Y$  directions by a polarizer and detected by a high-speed photodiode (Thorlabs DET10A/M). The SRL signal, which is the modulation of the pump intensity, is measured by a lock-in amplifier (Signal Recovery 7280).

The polarimetric SRS analysis is performed by tuning independently the incident linear polarizations of the pump and Stokes beams. However, an important feature of the SRL signal is that it is always projected along the polarization of the pump field ( $\mathbf{E}_p(\omega_p)$ ). A more formal demonstration will be developed in chapter 3. Therefore, in the SRL experiment we perform the S polarization configuration, where the Stokes linear polarization  $\alpha_s$  rotates from  $0^\circ$  to  $360^\circ$  and the pump field is linearly polarized along an fixed direction  $\alpha_p$ . The SRL signal is detected along the  $X$  and  $Y$  directions and the polarimetric measurements are repeated for different orientations  $\alpha_p$  of the pump beam.

## 2.2 Characterizing the polarization distortions from optical reflection

The accuracy of the polarization resolved nonlinear optical technique requires the control of the incident polarization states at the focal spot of the objective, which can be very delicate. Through their optical path, the incident beams are successively reflected on mirrors and dichroic filters, that can introduce several perturbations on their polarization states. These distortions may lead to serious misinterpretations of the measured signals. In inverted microscopy, where the polarization gets fixed at the entrance of the microscope, there are two sources of these distortions: reflection optics and high numerical aperture focusing. In the scope of this thesis, we are mostly concerned with the first source of distortions, because we are not dealing with high numerical aperture focusing, as we stated in the previous section. A detailed analysis of the effect of focusing the incident beams on the emitted nonlinear optical signal can be found in [89], where it was shown that polarization nonlinear microscopy is affected by high numerical aperture of the objective when  $NA > 0.8$ . The polarization distortions arise from the reflections of the beam at mirrors and dichroic beam splitters, which are made of multilayer dielectric thin films usually well controlled for the field amplitudes but not for their phases. In the latter they can be strongly frequency dependent, especially as one approaches the cutoff frequency that separates the reflective and transmissive spectral regions of the dichroic. Another source of polarization distortions which we were confronted during this work, is the sample itself, when it is anisotropic and therefore potentially birefringent. This is frequently observed in

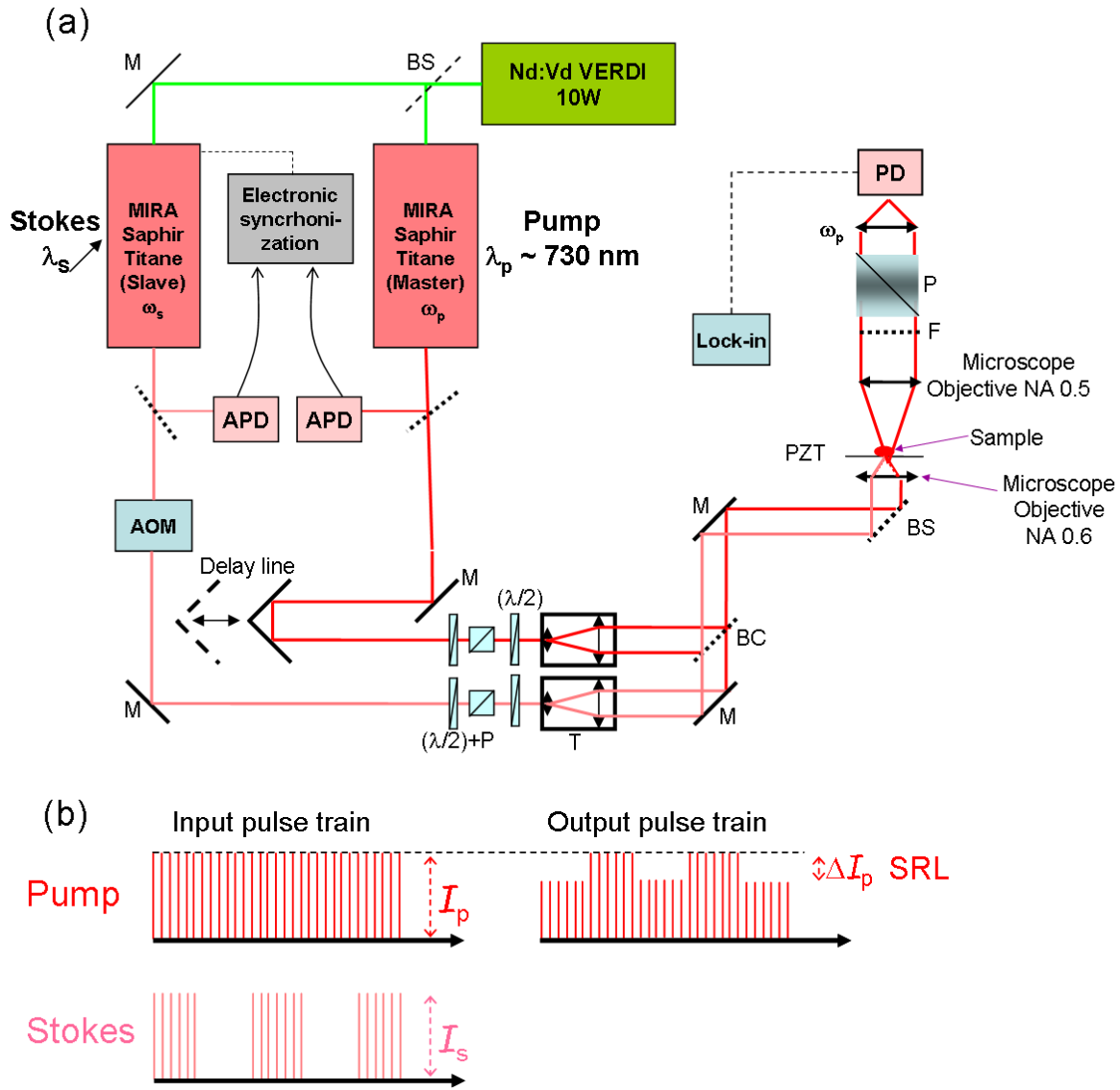


Figure 2.3: Polarization resolved SRS experiment, based on the SRL detection. (a) Experimental setup. AOM: acousto-optic modulator. PD: photodiode; M: mirror; BC and BS: beam combiner and beamsplitter, respectively (dichroic filters); F: short-pass filter; PZT: translational  $XYZ$  piezoelectric plate; P: polarizer; T: telescope;  $\lambda/2$ : half-wave plates. (b) Principle of the SRL detection scheme: the modulation of the Stokes amplitude results in the modulation of the pump intensity due to stimulated Raman scattering (reproduced from [40]).

crystals belonging to certain crystallographic point groups and in thick biological samples, such as tissues.

In this section, we present two simple and powerful techniques to retrieve the dichroism and ellipticity in the sample plane of a nonlinear microscope. The first is based on the effects of reflection optics on two-photon fluorescence polarization responses of model samples and can be used either in epi or fwd-detection configuration. The second consists of a polarimetric analysis of either the incident beam itself when no sample is present in the focal volume, or the field transmitted through the object when it is not birefringent. This technique can be performed in fwd-detection scheme.

### 2.2.1 Two-photon fluorescence polarization responses in isotropic liquids

In this section we analyze the features of two-photon fluorescence (TPF) polarimetry under a linearly tunable incident polarization at the entrance of the microscope, accounting for experimental factors inducing polarization distortions.

The fluorescence intensity analyzed along a given polarization direction  $\mathcal{I}$  is proportional to the two-photon absorption probability multiplied by the probability of emission in that direction, which, in a molecular ensemble, can be written as [53]:

$$\mathcal{I}_I(\alpha) \propto \int \int \int \int \int \overline{|\boldsymbol{\mu}_{abs}(\Omega, \mathbf{r}) \cdot \mathbf{E}(\alpha, \mathbf{r})|^4} |\mathbf{E}_{em}(\Omega', \mathbf{r}', \mathbf{k}) \cdot \mathbf{u}_I|^2 f(\Omega, \Omega') d\Omega d\Omega' d\mathbf{r} d\mathbf{r}' d\mathbf{k}, \quad (2.1)$$

where  $\overline{\dots}$  accounts for time average. The fluorescence signal for a field propagating along  $Z$  is detected along the direction  $I = (X, Y)$ . The incident electric field  $\mathbf{E}(\alpha, \mathbf{r})$  interacts at position  $\mathbf{r}$  with the absorption dipole  $\boldsymbol{\mu}_{abs}(\Omega, \mathbf{r})$  whose orientation is given by the solid angle  $\Omega$ . The far field  $\mathbf{E}_{em}(\Omega', \mathbf{r}', \mathbf{k})$  is radiated by the emission dipole  $\boldsymbol{\mu}_{em}(\Omega', \mathbf{r}')$  in the propagation direction  $\mathbf{k}$ , with  $\mathbf{E}_{em}(\Omega', \mathbf{r}', \mathbf{k}) \propto \mathbf{k} \times [\mathbf{k} \times \boldsymbol{\mu}_{em}(\Omega', \mathbf{r}')]$ .  $\mathbf{u}_I$  is a normalized vector in the analysis direction  $I$ .  $f(\Omega, \Omega')$  is the normalized molecular orientation distribution function for the absorption and emission dipole orientations  $\Omega = (\theta, \phi)$  and  $\Omega' = (\theta', \phi')$ , respectively. The incoherent summation of the fluorescence signal from individual molecules over all their positions and orientations is denoted by  $d\Omega d\Omega' d\mathbf{r} d\mathbf{r}'$ , while  $d\mathbf{k}$  describes the integration over the emission propagation angles within the collection aperture. The proportionality sign in Eq. (2.1) allows omitting efficiency and collection factors that do not come into play in a relative polarization measurement which is the case in our studies.

For an isotropic liquid under two-photon excitation, the rotational diffusion time of the molecules is shorter than their typical fluorescence lifetimes. Therefore, the orientations of the emission dipoles are decorrelated from those of the absorption dipoles, which leads to  $f(\Omega, \Omega') = f(\Omega)f(\Omega')$ . Moreover, the orientation distribution function for isotropic liquids is  $f(\Omega) = f(\Omega') = 1/(4\pi^2)$  and Eq. (2.1) can then be written as:

$$\mathcal{I}_I(\alpha) \propto \int \int \overline{|\boldsymbol{\mu}_{abs}(\Omega, \mathbf{r}) \cdot \mathbf{E}(\alpha, \mathbf{r})|^4} d\Omega d\mathbf{r} \int \int \int |\mathbf{E}_{em}(\Omega', \mathbf{r}', \mathbf{k}) \cdot \mathbf{u}_I|^2 d\Omega' d\mathbf{r}' d\mathbf{k}, \quad (2.2)$$

where the absorption and emission dipoles  $\boldsymbol{\mu}_{abs}(\Omega, \mathbf{r})$  and  $\boldsymbol{\mu}_{em}(\Omega', \mathbf{r}')$  are now completely independent. The emission probability does not depend on the incident polarization and as a consequence, contributes only as a multiplicative constant when this polarization is tuned. Consequently, the collection aperture has no effect on the polarimetric response of the emitted signal and only affects its global efficiency. The study of the polarization response of the fluorescence emission depends therefore only on the absorption probability and Eq. (2.2) can be simplified according to:

$$\mathcal{I}_I(\alpha) \propto C_I \int \int |\boldsymbol{\mu}_{abs}(\Omega, \mathbf{r}) \cdot \mathbf{E}(\alpha, \mathbf{r})|^4 d\Omega d\mathbf{r}, \quad (2.3)$$

where  $C_I$  contains the emitted field radiation factor and may vary for different analyzing directions due to different efficiencies along  $X$  and  $Y$ .

As the emission and excitation dependencies can be totally decoupled in isotropic liquids, the result is not affected by correlation-related issues such as fluorescence energy transfer or angles between the absorption and emission dipoles in the used molecules, contrary to isotropic materials made of fixed molecules such as in a polymer matrix [53]. As a consequence, in the case of isotropic liquids, the fluorescence signal is independent on the molecules and their concentrations.

### 2.2.2 Influence of dichroism and ellipticity on the TPF polarization responses

When the incident linear polarization is rotated, the excitation field  $\mathbf{E}(\alpha)$  can be affected by polarizations distortions, characterized by a degree of ellipticity and dichroism. The incident amplitude of the field at the entrance of the objective can be written as [90]:

$$\mathbf{E}(\alpha, \delta, \gamma) \propto \frac{E}{\sqrt{1 + (1 - \gamma^2)}} \begin{pmatrix} \cos \alpha \\ (1 - \gamma) \sin \alpha e^{i\delta} \\ 0 \end{pmatrix}, \quad (2.4)$$

where  $\gamma$  is the amplitude factor (dichroism) and  $\delta$  is the phase difference (ellipticity) between the two perpendicular polarization states  $s$  and  $p$ , defined by  $\alpha = 0$  and  $\alpha = \frac{\pi}{2}$ , corresponding to the  $X$  and  $Y$  directions in the sample plane. Note that when the field is polarized along  $X$  or  $Y$ , it is not affected by ellipticity and the polarization is kept linear for any dichroism and ellipticity factors. By consequence, only the intermediate polarizations are affected by these distortions. For any  $\alpha$  between 0 and  $\pi/2$ , the polarization remains linear along  $\alpha$  for  $\delta = 0$ , but it becomes elliptical around  $\alpha$  when  $\delta$  increases up to  $\frac{\pi}{2}$ . At this value, the field can even become circularly polarized when  $\alpha = \frac{\pi}{4}$ . For  $\pi/2 \leq \delta \leq \pi$ , the ellipticity decreases, but the ellipse becomes oriented along  $\pi - \alpha$ . At  $\delta = \pi$  the field is linear again, but along  $\pi - \alpha$ . The effect of the ellipticity on the incident polarization is depicted in Fig. 2.4. Dichroism only plays a role on the relative amplitudes between  $X$  and  $Y$  components of the electrical field. When  $\gamma > 0$ , the fields becomes stronger in  $X$  relative to  $Y$ , and the opposite occurs when  $\gamma < 0$ .

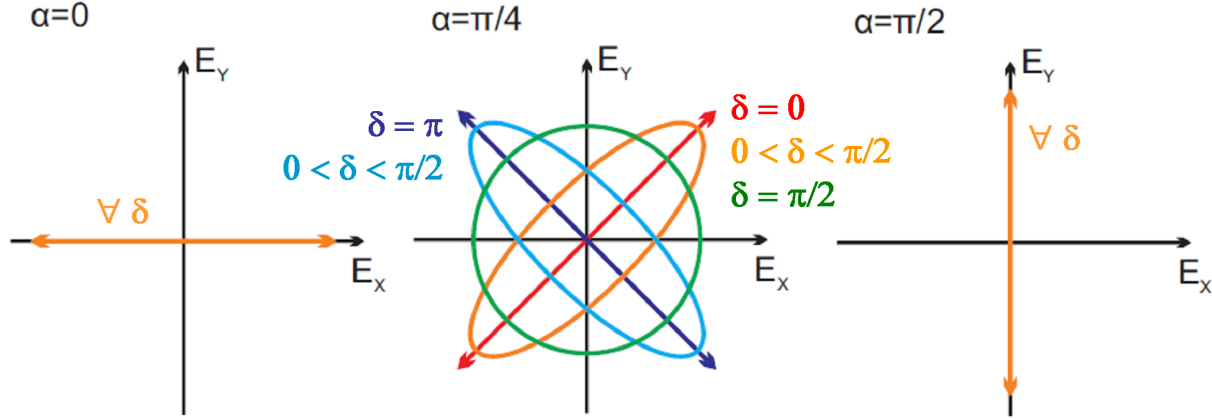


Figure 2.4: Effect of ellipticity  $\delta$  on the polarization of the electric field for, different polarization angles  $\alpha$ . At left,  $\alpha = 0$ : the polarization remains linear along  $X$  for any  $\delta$ . in the middle,  $\alpha = \frac{\pi}{4}$ : the polarization is greatly affected by  $\delta$ . Ellipticity increases with  $\delta$  until  $\delta = \pi/2$  and decreases for  $\pi/2 \leq \delta \leq \pi$ , but the ellipse switches its orientation. At right,  $\alpha = \frac{\pi}{2}$ : the polarization remains linear along  $Y$  for any  $\delta$ .

Eq. (2.4) represents the expression of the amplitude of the electric field in the plane wave approximation. When the field is focused, a small  $Z$ -component, which increases with the numerical aperture, appears along the propagation direction of the field. In this case, Eq. (2.4) is not valid anymore to characterize the incident electrical field. It is shown however that, in a solution where the excitation process is randomized, the fluorescence polarimetric response is independent on the objective's numerical aperture both in the excitation and collection modes. An example is shown in Fig. (2.5), where we depict theoretical curves of the TPF signal resolved in polarization for excitation objectives with different numerical apertures. The detail of the calculations is reported elsewhere [89]. For the case of strong focusing ( $NA = 1.2$ ), numerical simulations were carried out in a volume of  $0.8 \mu\text{m}$  in the lateral directions ( $X$  and  $Y$ ) and  $1.6 \mu\text{m}$  in the axial direction ( $Z$ ), homogeneously filled with  $160 \times 160 \times 320$  dipoles. The weaker focusing case ( $NA = 0.9$ ) is based on a focal volume of  $1 \times 1 \times 2 \mu\text{m}^3$  with  $200 \times 200 \times 400$  dipoles. Both intensities along the  $X$  and  $Y$  directions are conserved, since the fluorescence emission does not depend on the analysis direction. The plane wave approximation is therefore adequate to study the polarization state distortions brought by the reflection optics.

By replacing the expression of the electric field (2.4) into Eq. (2.3), it is possible to study the effect of the ellipticity  $\delta$  and the amplitude factor  $\gamma$  on the polarization response of the fluorescence intensity in an isotropic solution. The results are shown in Figs. (2.6a) and (b). They show a polar representation of the fluorescence intensity as a function of the polarization angle  $\alpha$ . When no ellipticity and dichroism are present, the response does not depend on  $\alpha$ , as expected from an isotropic solution. At intermediate polarizations ( $\alpha \neq 0^\circ$  or  $90^\circ$ ), the ellipticity  $\delta$  decreases the excitation efficiency, whose minimum occurs

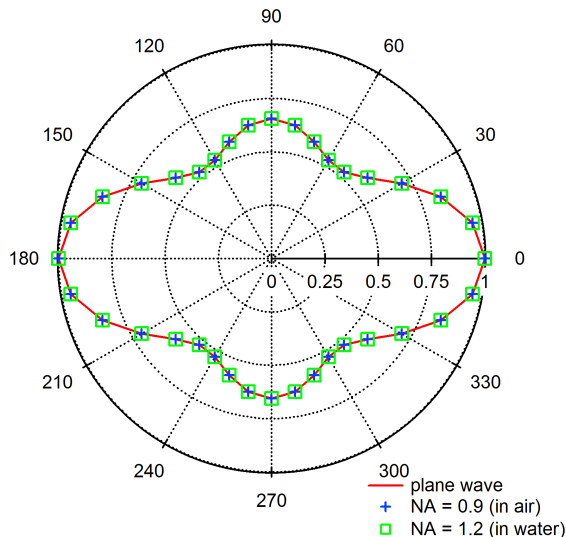


Figure 2.5: Polarization resolved TPF responses of an isotropic solution for different numerical apertures of the excitation objective. Three cases are simulated: very strong focusing (NA = 1.2 - green squares), medium focusing (NA = 0.9 - blue crosses) and plane wave illumination (NA = 0 - red line). Dichroic parameters:  $\gamma = 0.1$  and  $\delta = \frac{\pi}{2}$ . All calculations are performed for an excitation wavelength of 800 nm.

at  $\alpha = \pi/4$  modulo  $\pi/2$ . Contrary to  $\delta$ , the amplitude factor  $\gamma$  affects mostly the intensities in the  $X$  and  $Y$  polarization directions: when it is positive (resp. negative) the fluorescence is the most efficient for an incident polarization parallel to the  $X$  (resp.  $Y$ ) axis. For an isotropic solution, the effect of the ellipticity  $\delta$  on the fluorescence polarization response has a period of  $\pi/2$ : the polar plots for  $0 \leq \delta \leq \pi/2$  or  $\pi/2 \leq \delta \leq \pi$  are ambiguous. This is a consequence of the fact that in the isotropic summation of Eq. (2.3), the detected fluorescence signal is dependent on  $|\cos(2\delta)|$ . Therefore, only polarization responses from nonisotropic molecular angular distributions will be able to raise the ambiguity on  $\delta$ . This is illustrated in Fig. (2.6c) where the polarization fluorescence responses of a fixed 1D fluorescent crystal has been modeled with an in-plane orientation of  $2\pi/9$  ( $40^\circ$ ) in respect to the  $X$  axis. In this case, the orientation distribution for the absorption dipoles in Eq. (2.4) is a discrete function  $f(\Omega) = \delta(\Omega - \Omega_0)$ . The emitted fluorescence signal is then calculated by taking  $\Omega_0$  as the orientation of the crystal:  $\Omega_0 = (\phi_0, \theta_0) = (2\pi/9, \pi/2)$ . In this situation, the TPF polarization response is strongly dependent on the polarization parameters of the dichroic used, as depicted in Fig. (2.6c). When there is no ellipticity, the polarization response is anisotropic in the  $2\pi/9$  direction, as expected from the 1D symmetry of the sample. As  $\delta$  increases, the polarization response changes its direction, until it reaches another quadrant for  $\delta > \pi/2$ . Therefore, this is an efficient technique to remove the ambiguity on the range of the ellipticity: if the TPF polarization response is in the quadrant of the sample orientation, then  $0 \leq \delta \leq \pi/2$ ; otherwise, when the polarization response reaches the next quadrant,  $\pi/2 \leq \delta \leq \pi$ . This example emphasizes

the detrimental influence of in-plane polarization ellipticity when performing polarimetric measurements, the response being indeed strongly distorted for high ellipticities.

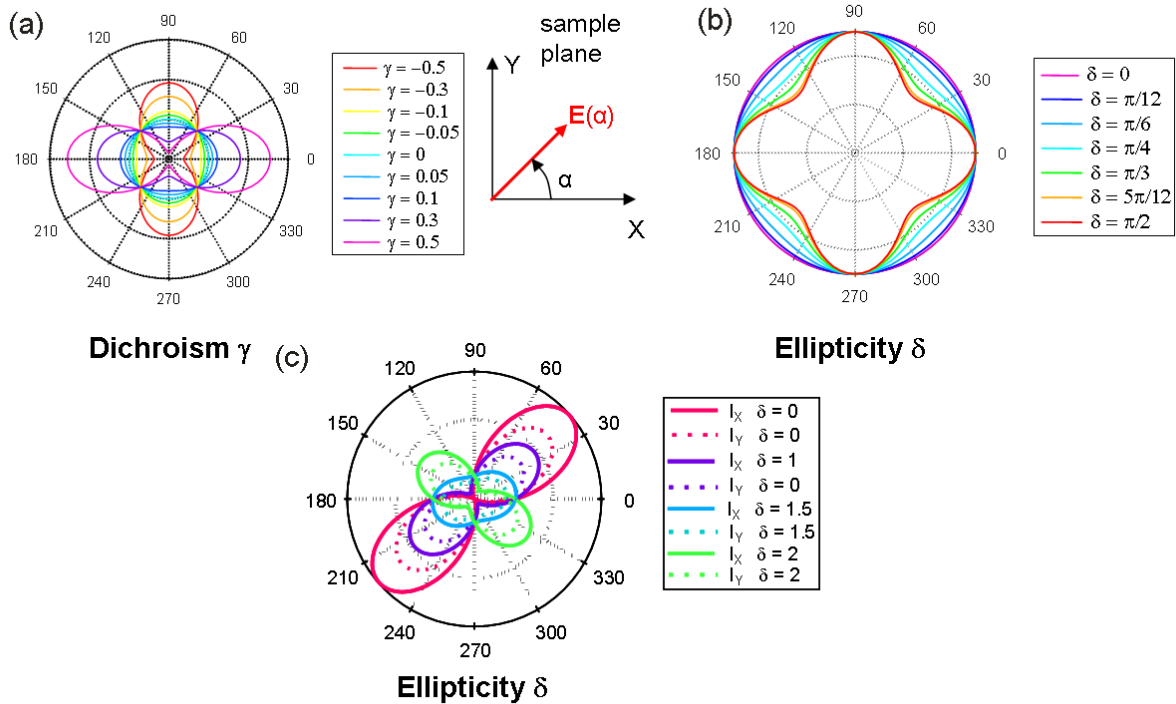


Figure 2.6: Effect of the ellipticity ( $\delta$  in rad) and dichroic ( $\gamma$ ) parameters on the TPF polarization response for a solution of Rhodamine6G (a,b) and an 1D fluorescent sample oriented at  $(\phi_0, \theta_0) = (2\pi/9, \pi/2)$  (c). (a) Influence of the amplitude factor  $\gamma$  for  $\delta = 0$ . (b,c) Influence of the ellipticity  $\delta$  when  $\gamma = 0$ . In the isotropic case, the polar plots are expected to be identical for the signal detected along X and Y directions. The polarization responses are normalized to a maximum value of 1.

### 2.2.3 Characterization of the dichroic parameters using two-photon polarization measurements

In the previous section (2.2.2), we showed that the characterization of the polarization perturbations induced by the dichroic beamsplitter is possible by performing polarization resolved two photon fluorescence on an isotropic liquid, by continuously rotating the incident polarization. Actually, the determination of  $(\gamma, \delta)$  requires only the measurements of the TPF intensities at three incident polarizations:  $\alpha = 0, \pi/4$  and  $\pi/2$ . This is shown in Fig. (2.7), representing the cartographies of the ratios  $\mathcal{I}_I(\pi/2)/\mathcal{I}_I(0)$  and  $\mathcal{I}_I(\pi/4)/\mathcal{I}_I(0)$  in a  $(\gamma, \delta)$  coordinates map. Fig. (2.7a) shows that a given value of the ratio  $\mathcal{I}_I(\pi/2)/\mathcal{I}_I(0)$

corresponds to a vertical line in the  $(\gamma, \delta)$ -map, this ratio being independent on the ellipticity of the dichroic beamsplitter, whereas Fig. (2.7b) indicates that a given value of the ratio  $\mathcal{I}_I(\pi/4)/\mathcal{I}_I(0)$  corresponds to a curve that is  $(\gamma, \delta)$ -dependent. The interception between both curves is therefore a single point in the  $(\gamma, \delta)$ -diagram, proving that the solution  $(\gamma, \delta)$  is unique with only three incident polarizations. Taking into account typical experimental uncertainties, the solution space for each ratio will no longer be a single line but a band with certain error-width, as shown in Fig. (2.7c). For a better experimental estimation we do not measure the TPF intensity for only three incident polarizations, but instead, we continuously rotate the incident polarization between  $0^\circ$  and  $360^\circ$ . In this case, a fit of the polarization dependent TPF-signal should be considered.

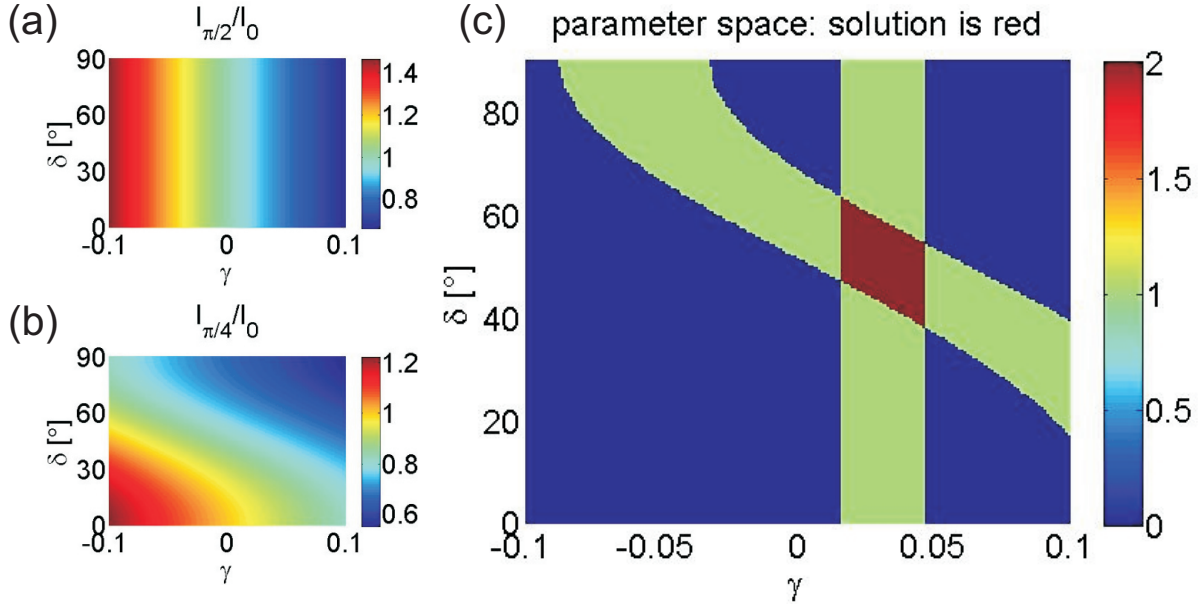


Figure 2.7:  $(\gamma, \delta)$  cartography of the two-photon fluorescence ratios ( $\delta$  in deg): (a)  $\mathcal{I}_I(\pi/2)/\mathcal{I}_I(0)$  and (b)  $\mathcal{I}_I(\pi/4)/\mathcal{I}_I(0)$ . (c) Typical solution (red space) including experimental error margins for a three-point fit.

The measurement of the polarization resolved TPF signal is made in the same setup where the CARS or the SRS experiments are done. Polarimetric TPF is therefore employed as an *in situ* calibration step before any polarization resolved measurements are performed. The isotropic liquid used to perform the TPF experiments is a solution of free Rhodamine 6G (Rh6G) diluted in water. As the performance of all reflection optics and in particular the dichroic mirror is wavelength-dependent, the calibration procedure has to be carried out at different  $\lambda$ . In particular, in the case of CRS experiments, the parameters  $(\gamma, \delta)$  must be determined for both incident fields, at angular frequencies pump and Stokes.

In order to determine the dichroic parameters  $(\gamma, \delta)$  with accuracy, a fit procedure is developed. For this purpose, theoretical curves, based on Eqs. (2.3) and (2.4), were

calculated for a large variety of  $(\gamma, \delta)$ -values and compared with the experimental data. The concordance between theoretical and experimental curves is evaluated by the mean square error method, in which the indicator is the sum of mean squares:

$$\chi^2(\gamma, \delta) = \frac{1}{N} \sum_{\alpha} [\mathcal{I}_{exp}(\alpha) - \mathcal{I}_{theo}(\alpha, \gamma, \delta)]^2, \quad (2.5)$$

where  $N$  is the number of incident polarizations  $\alpha$ . Fig. (2.8a) shows the dependence of  $\chi^2$  on  $\gamma$  and  $\delta$  for a TPF measurement of Rh6G solution at  $\lambda_p = 730$  nm. Only one minimum exists, corresponding to the region surrounded by the red ellipse in the  $(\gamma, \delta)$  cartography in Fig. (2.8a), which proves that the solution is unique. The same is true for all other tested cases. This allows the use of a fitting procedure starting at an arbitrary point within the  $(\gamma, \delta)$ -space that minimizes  $\chi^2$  by alternately varying both parameters until a stable minimum is found. The best fit for the presented case is depicted in Fig. (2.8b) and it corresponds to  $\gamma = 0.08$  and  $\delta = \pi/5$  rad ( $36^\circ$ ).

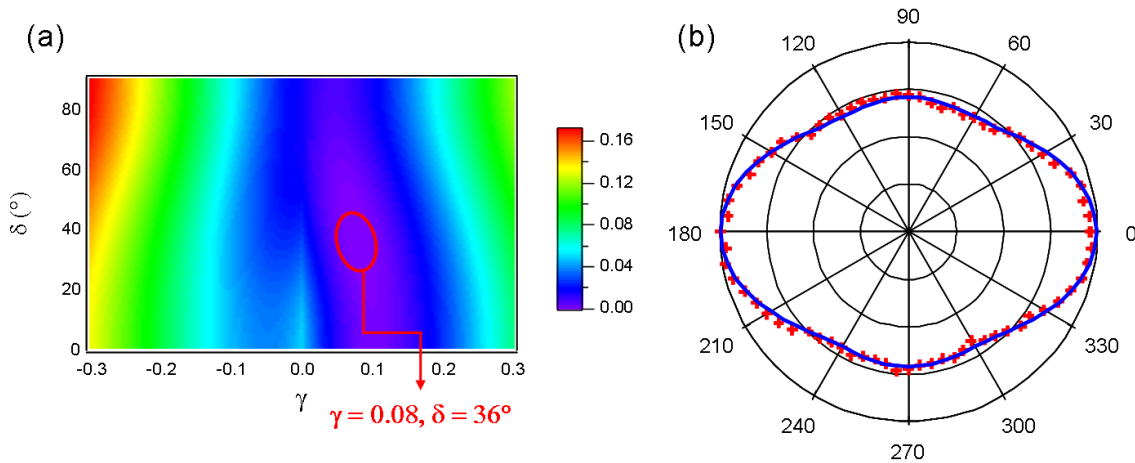


Figure 2.8: Experimental polarization resolved TPF response from a Rh6G solution excited at  $\lambda = 730$  nm. (a)  $\chi^2$  cartography for a range of  $(\gamma, \delta)$  ( $\delta$  in deg). The red ellipse indicates the region in the map where the mean square error is minimum. (b) Experimental points (red markers) and corresponding best fit (blue solid line) given by  $(\gamma, \delta) = (0.08, 36^\circ)$ .

As we stated in the previous section (2.2.2), polarization resolved TPF response from isotropic liquids does not allow to determine if the ellipticity is in the range  $[0, \pi/2]$  or  $[\pi/2, \pi]$ . To remove this ambiguity, it is necessary to perform measurements on anisotropic samples. For this purpose, we carried out TPF polarimetric experiments on a 1D fluorescent sample made of oriented fluorescent molecules along a macroscopic crystal axis, which macroscopic orientation can be identified visually. This sample is a Perhydrotriphenylene (PHTP)-4-Dimethylamino-40-nitrostilbene (DANS) co-crystal characterized in a previous

work [91], oriented at an angle close to  $150^\circ$  in the plane of the sample. This can be verified in Fig. (2.9a), where we show a white light image of the crystal detected in a CCD camera. The corresponding polarization resolved TPF signal is depicted in Fig. (2.9b). As the orientation of the crystal and of the experimental curve depicted in the polar plot are not in the same quadrant, it means that  $\pi/2 \leq \delta \leq \pi$  and the value found in the rhodamine fit is not the one of the real ellipticity. This is given by  $\delta = \pi - \delta'$ , with  $\delta'$  the ellipticity fitted by the rhodamine solution. This means that the dichroic parameters for the pump beam at  $\lambda_p = 730$  nm are  $\gamma = 0.08$  and  $\delta = 4\pi/5$  ( $144^\circ$ ).

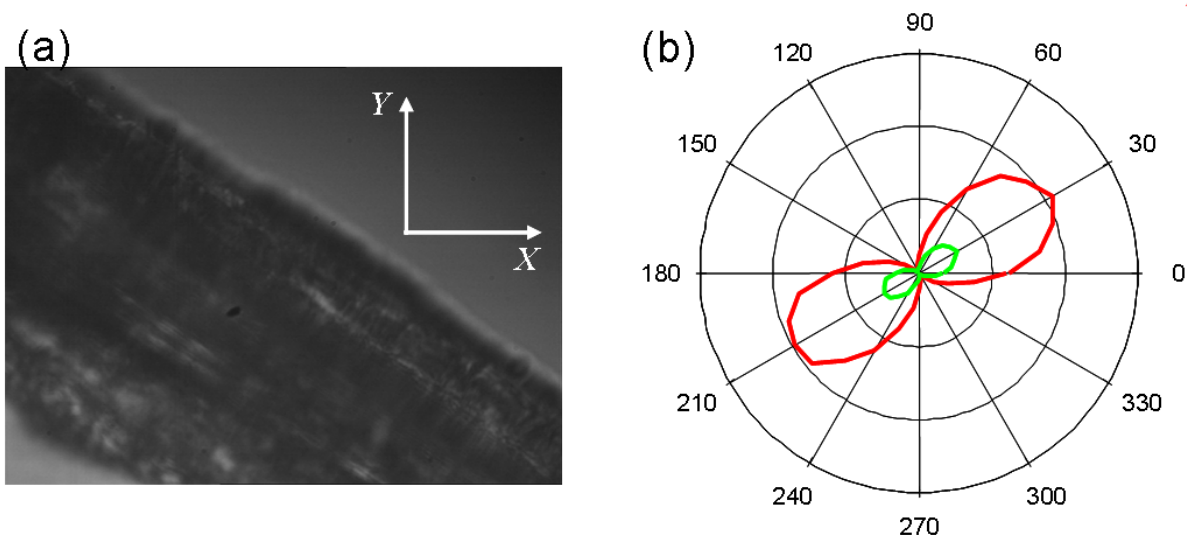


Figure 2.9: TPF polarization response of a 1D crystalline fluorescence sample made of DANS molecules in a PHTP crystalline host, excited at  $\lambda = 730$  nm. (a) White light image of the crystal, showing its orientation in the sample plane. (b) Experimental polar plots: the curves in red and green correspond to signal detected along X and Y axes, respectively.

Finally, the performance of the dichroic mirror is wavelength-dependent. In the case of the Stokes beam, whose wavelength is tuned in spectroscopic measurements, it is important to characterize the polarization distortions introduced by the dichroic mirror for a large range of  $\lambda_s$ . Some examples are shown in Fig. (2.10), for  $\lambda_s$  varying between 780 and 830 nm. Both the ellipticity and dichroic factors are very sensitive to the incident wavelength, as indicated in the figure. Big absolute value of  $\gamma$  at  $\lambda_s \approx 780$  nm ( $\gamma = -0.185$ ) is due to the fact that this wavelength is not far from the cutoff frequency that separates the reflective and transmissive spectral regions of the dichroic beamsplitter, where high amplitude factors are expected. The polarization resolved TPF experiments on 1D crystal, with the same in-plane orientation as in Fig. (2.9a) shows that  $0 \leq \delta \leq \pi/2$  in the wavelength range studied here.

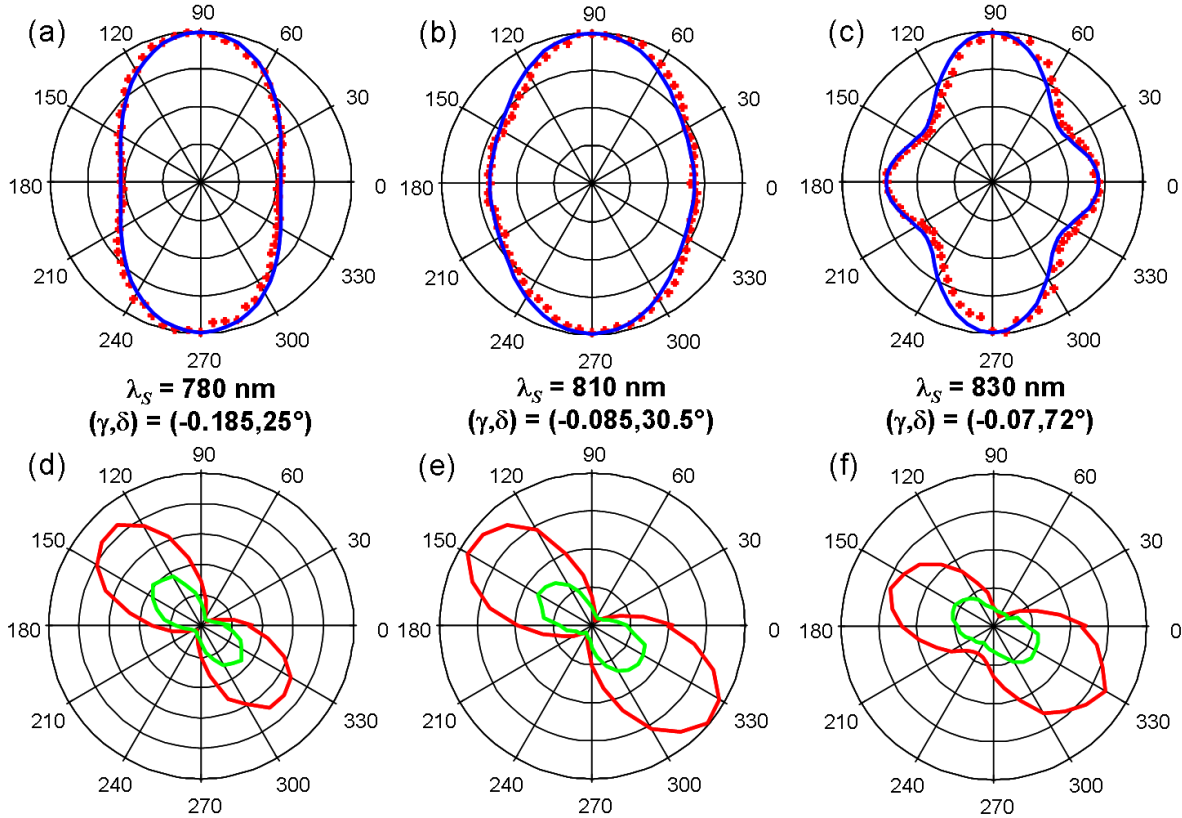


Figure 2.10: TPF polarization responses for excitations varying from  $\lambda_s = 780$  to  $830$  nm. (a-c) Measurements on a Rh6G solution; red marks correspond to the experimental data, while the blue solid lines show the fitted curves. (d-f) Measurements on an 1D crystalline fluorescent sample made of DANS molecules in a PHTP crystalline host; red and green curves correspond to the signal detected along  $X$  and  $Y$  axes respectively.

## 2.2.4 Characterization of the dichroic parameters by measuring the polarization states of the incident field

The method described in section 2.2.3, that uses TPF polarimetric measurements to characterize the polarization distortions introduced by the experimental setup, can be used either in the fwd- or epi-CARS detection schemes. This method had been initially implemented in a setup where only the epi-detection geometry was available. However, when performing experiments based on the forward detection of the emitted signal, a more straightforward way of measuring these polarization aberrations is to carry out polarimetric measurements on the excitation field itself. According to section 2.2.3, when the incident linear polarization is rotated, the amplitude of the electric field  $\mathbf{E}(\alpha)$  is affected by ellipticity and dichroism according to Eq. (2.4). If this field is projected along a particular direction  $\alpha_{\text{det}}$ ,

the intensity detected along this direction is given by:

$$\begin{aligned} \mathcal{I}(\alpha, \alpha_{\text{det}}, \gamma, \delta) = & \frac{E^2}{1 + (1 - \gamma^2)} \left[ \cos^2 \alpha \cos^2 \alpha_{\text{det}} + (1 - \gamma)^2 \sin^2 \alpha \sin^2 \alpha_{\text{det}} \right. \\ & \left. + 2(1 - \gamma) \cos \delta \cos \alpha \cos \alpha_{\text{det}} \sin \alpha \sin \alpha_{\text{det}} \right], \end{aligned} \quad (2.6)$$

where  $\alpha$  is the incident polarization and  $\gamma$  and  $\delta$  are the dichroism and ellipticity, respectively. Note that when the detection is along  $X$  or  $Y$ , the intensity does not depend on the ellipticity. Therefore, in order to estimate both dichroic parameters  $\delta$  and  $\gamma$ , it is necessary that the detection direction be at an intermediate angle  $\alpha_{\text{det}} \neq 0^\circ$  or  $90^\circ$ .

Fig. (2.11) shows the effect of the ellipticity  $\delta$  [Fig. (2.11)a] and the amplitude factor  $\gamma$  [Fig. (2.11)b] on the polarization response of the intensity of the incident field, in a polar representation. The detection direction is set at  $\alpha_{\text{det}} = 30^\circ$  and the theoretical intensities are calculated as a function of the incident polarization  $\alpha$ , according to Eq. (2.6). When no ellipticity and dichroism are present, the polarization response has a two-lobe shape dependent on  $\cos^2(\alpha - \alpha_{\text{det}})$ , with the maximum intensity along the direction of analysis. When ellipticity is present, these two-lobe shapes tend to open (no extinction occurring at  $\alpha = \alpha_{\text{det}} + 90^\circ$ ) and rotate progressively when  $\delta$  increases, until they reach a dependence on  $\cos^2(\alpha + \alpha_{\text{det}})$  when  $\delta = \pi$  ( $180^\circ$ ). The effect of the amplitude factor is less significant and its contribution only slightly rotates the polar plots and increases or decreases their maximum intensity if  $\gamma < 0$  or  $\gamma > 0$ , respectively.

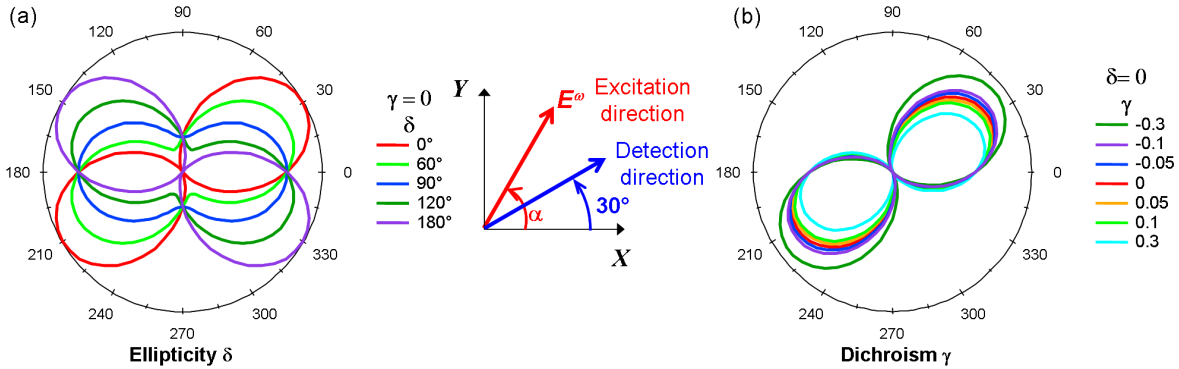


Figure 2.11: Effect of the ellipticity ( $\delta$  in deg) and dichroic parameters ( $\gamma$ ) on the polarization response of the detected intensity of the incident field. (a) Influence of the ellipticity  $\delta$  when  $\gamma = 0$ . (b) Influence of the amplitude factor  $\gamma$  for  $\delta = 0^\circ$ . Here,  $\alpha_{\text{det}}$  is set at  $30^\circ$ .

We perform this technique in order to measure the dichroic parameters of the pump beam at  $\lambda_p = 730$  nm. For this purpose, we rotate the incident polarization  $\alpha$  from  $0^\circ$  to  $360^\circ$  and we detect the intensity of the excitation field along four different directions:  $\alpha_{\text{det}} = 0^\circ, 30^\circ, 60^\circ$  and  $90^\circ$ . The results are shown in Fig. (2.12). The fit procedure is

analogous to the one proposed in section 2.2.3, but here all the detection orientations are fitted simultaneously, which leads to the following mean square error function:

$$\chi^2(\gamma, \delta) = \frac{1}{N} \sum_{\alpha, \alpha_{\text{det}}} [\mathcal{I}_{\text{exp}}(\alpha, \alpha_{\text{det}}) - \mathcal{I}_{\text{theo}}(\alpha, \alpha_{\text{det}}, \gamma, \delta)]^2. \quad (2.7)$$

The values of the dichroic parameters that minimize the mean square error  $\chi^2$  are  $\gamma = 0.09$  and  $\delta = 5\pi/6$  ( $150^\circ$ ), which are in good agreement with the ones found in section 2.2.3. The theoretical intensities resulted from the fit are superimposed to the experimental curves in Fig. (2.12).

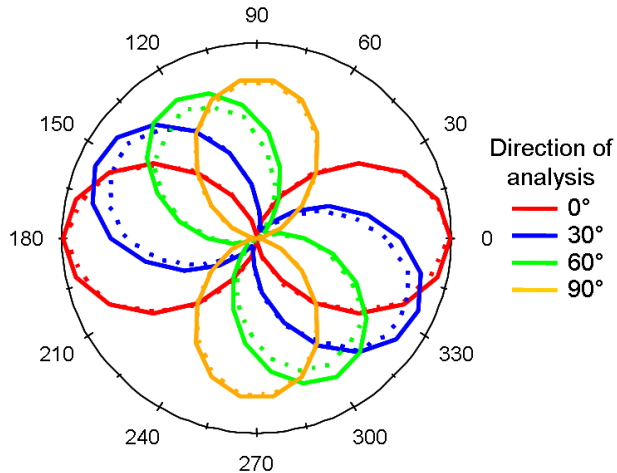


Figure 2.12: Experimental intensities of the pump excitation field at  $\lambda_s = 730$  nm resolved in polarization. The intensities are detected along four different directions:  $\alpha_{\text{det}} = 0^\circ$  (red),  $30^\circ$  (blue),  $60^\circ$  (green) and  $90^\circ$  (yellow). Dotted and solid lines correspond to the experimental and theoretical curves, respectively. The fitted parameters are  $(\gamma, \delta) = (0.09, 150^\circ)$ .

Once these measurements are done, we can focus the incident beams in the sample in order to determine its birefringence, through a technique that is presented in the next section.

## 2.3 *In situ* characterization of the sample local birefringence

In anisotropic samples, the incident field undergoes a birefringence retardation and its expression must be rewritten in order to account for the consequent polarization distortions.

In this work, we consider that the object projection in the  $(X, Y)$  plane is uniaxial, which is consistent with a cylindrical-symmetry distribution lying in the  $(X, Y)$  plane, and is relevant in most of the systems imaged in nonlinear microscopy. Following [92], we denote  $\Theta_b$  the angle between the macroscopic  $X$  axis and the fast optical axis of the object  $x_b$ , as shown in Fig. (2.13a), and  $\Phi_b$  the phase shift between its fast and slow optical axes, after a propagation distance  $d$  in the sample. The optical field polarization state at the focal depth distance  $d$  can be obtained in three steps. First, by performing a rotation of  $\Theta_b$ , we calculate the projection of the electric field along the optical axes of the sample at the object surface ( $Z = 0$ ) [Fig. (2.13b)]:

$$\begin{bmatrix} E_{x_b}^0(\alpha) \\ E_{y_b}^0(\alpha) \end{bmatrix} = \begin{bmatrix} \cos \Theta_b & -\sin \Theta_b \\ \sin \Theta_b & \cos \Theta_b \end{bmatrix} \cdot \begin{bmatrix} E_X^0(\alpha) \\ E_Y^0(\alpha) \end{bmatrix},$$

Then, as the electric field propagates a distance  $d$  in the sample, its component along the slow axis undergoes a phase shift of  $\Phi_b(d)$  relative to the component parallel to the fast axis. The new electric field writes:

$$\begin{bmatrix} E_{x_b}^d(\alpha) \\ E_{y_b}^d(\alpha) \end{bmatrix} = \begin{bmatrix} E_{x_b}^0(\alpha) \\ E_{y_b}^0(\alpha) \exp[i\Phi_b(d)] \end{bmatrix}.$$

Finally, the electric field in the laboratory frame can be obtained by performing a rotation of  $-\Theta_b$ , following:

$$\begin{bmatrix} E_X^d(\alpha) \\ E_Y^d(\alpha) \end{bmatrix} = \begin{bmatrix} \cos \Theta_b & \sin \Theta_b \\ -\sin \Theta_b & \cos \Theta_b \end{bmatrix} \cdot \begin{bmatrix} E_{x_b}^d(\alpha) \\ E_{y_b}^d(\alpha) \end{bmatrix}.$$

Putting all three steps together, the optical field polarization state at the focal depth distance  $d$  in the laboratory frame is given by:

$$\begin{bmatrix} E_X(Z = d) \\ E_Y(Z = d) \end{bmatrix} = \begin{bmatrix} \cos \Theta_b & \sin \Theta_b \\ -\sin \Theta_b & \cos \Theta_b \end{bmatrix} \cdot \begin{bmatrix} \cos \Theta_b & -\sin \Theta_b \\ \sin \Theta_b \exp(i\Phi_b(d)) & \cos \Theta_b \exp(i\Phi_b(d)) \end{bmatrix} \cdot \begin{bmatrix} E_X^0(\alpha) \\ E_Y^0(\alpha) \end{bmatrix}, \quad (2.8)$$

where  $E_{X,Y}^0(\alpha)$  is the optical field polarization components in the macroscopic  $(X, Y)$  frame at the sample surface ( $Z = 0$ ) [Fig. (2.13b)], given by Eq. (2.4). The phase shift  $\Phi_b$  is given by  $\Phi_b = \frac{2\pi}{\lambda} \Delta n d$ , with  $\lambda$  the incident wavelength and  $\Delta n$  the refractive index difference between the fast and slow axes of the object in the sample plane.

In addition to this effect on the incident field, birefringence also affects the detected signal at anti-stokes frequency, which propagates through the sample in the forward direction. A similar approach as the one described above can be implemented to account for this effect, assuming that the same  $\Delta n$  applies to both incident and emitted wavelengths. In this work, we suppose that the refractive index difference between the fast and slow axes of the sample is the same for the three wavelengths involved in the CARS process,  $\lambda_p$ ,  $\lambda_s$  and  $\lambda_{as}$ . We will show in chapter 5 the influence of birefringence on the CARS signal, when focusing at different depths in the sample volume. We consider that only the emitted signal is affected by the birefringence when focusing at the surface of the sample

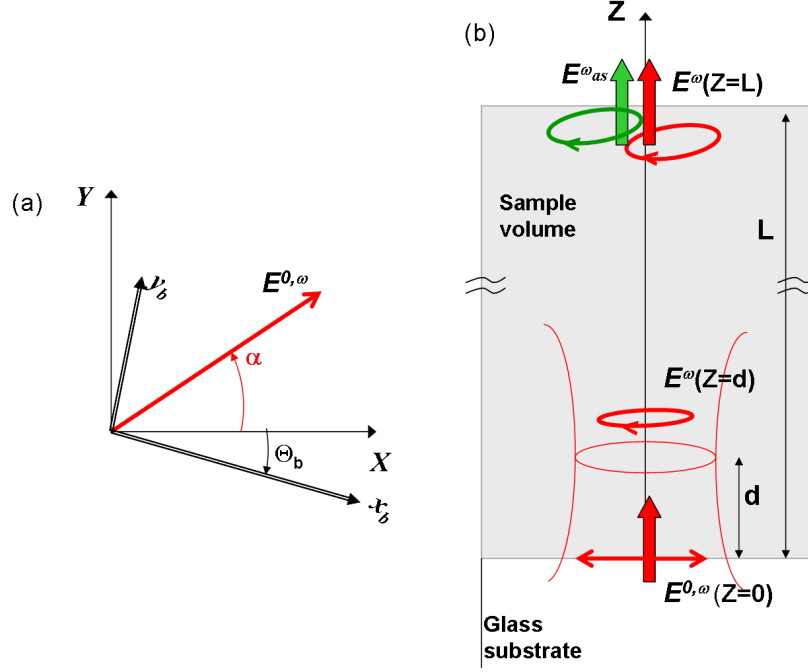


Figure 2.13: (a) Definition of the input polarization angle  $\alpha$  and the birefringence fast optical axis direction  $x_b$  in the macroscopic frame of the sample plane  $(X, Y)$ . (b) Experimental configuration in the sample volume: a linearly polarized field at frequency  $\omega$  is focused at a distance  $d$  from the sample bottom surface along the optical axis direction  $Z$ . The transmitted field at  $\omega$ , that propagates through the whole thickness of the medium  $L$ , is elliptical if the sample is birefringent.

( $Z = 0$ ), if forward detection is applied (this means that we neglect the fact that birefringence can have an effect over the focusing volume in the sample). Alternatively, when we focus at  $Z = L$ , the upper surface of the sample, only the incident fields are affected by birefringence. Finally, at intermediate focusing depths  $Z = d$ , we make the approximative assumption that the incident fields propagate through a distance  $d$  in the sample, while the emitted field propagates through the remaining distance  $L - d$ . This latter case is taken into account in our calculations through a simple cross-multiplication. We define two phase shifts  $\Phi_{b_{inc}}$  and  $\Phi_{b_{as}}$ , characterizing the birefringence affecting the incident and emitted fields, respectively and by cross-multiplication, we impose that  $\Phi_{b_{inc}} = \frac{d}{L}\Phi_b(\lambda_{inc})$  and  $\Phi_{b_{as}} = \left(1 - \frac{d}{L}\right)\Phi_b(\lambda_{as})$ .

The sample birefringence parameters can be deduced from a polarimetric measurement similar to the one described in section 2.2.4, where the intensity of the field at frequency  $\omega_p$  propagating through the sample is detected for various angles  $\alpha$  of the incident polarization  $\mathbf{E}^{\omega_p}(\alpha)$ . In this configuration, the field propagates through the whole thickness of the sample  $L$  and therefore the measured phase shift is  $\Phi_b(L)$  at  $\lambda_{inc} = \lambda_p$ . Here, in order to

determine the parameters  $(\Theta_b, \Phi_b)$ , we employ a fit procedure similar to the one described in Eq. (2.5), where  $I_{theo}$  in this case is calculated from Eq. (2.8). A polar representation of the theoretical polarimetric responses of the transmitted intensity  $I_X^{\omega p}(\alpha)$  is depicted in Fig. (2.14a). The figure shows the effect of different birefringence phase shifts when varying the incoming polarization  $\alpha$ , for a sample which optical axis  $x_b$  is oriented at  $\Theta_b = 30^\circ$  in respect to the macroscopic  $X$  axis. If no birefringence is present in the sample, the polarization response presents a two-lobe pattern dependent on  $\cos^2 \alpha$  with a maximum intensity along  $X$  and vanishing intensity along the  $Y$  axis. In the presence of birefringence, this pattern tends to open (no extinction occurring along the  $Y$  axis) and rotates progressively when  $\Phi_b$  increases. A similar behavior is expected for the intensity detected along the  $Y$  axis.

Fig. (2.14b) shows the polarization resolved intensity of the transmitted field calculated from Eq. (2.8) for a given couple of birefringence parameters  $(\Theta_b, \Phi_b) = (44^\circ, 97^\circ)$ , when no polarization distortions are introduced ( $\gamma$  and  $\delta$  are zero). The  $(\Theta_b, \Phi_b)$  cartography of the mean square error ( $\chi^2$ ) for this theoretical solution is shown in Fig. (2.14c). We observe that the solution is unique, but with a certain periodicity: the minima of the mean square error can be found for the given value of  $\Theta_b$  with a  $\pi/2$  periodicity and for each  $\Theta_b$  two solutions for the phase shift are possible, with  $\Phi_{b1}(L) + \Phi_{b2}(L) = 2\pi$ . The periodicity observed for both  $\Theta_b$  and  $\Phi_b$  is consistent with the fact that this technique does not discriminate the fast and slow axes of the system. When we account for the ellipticity  $\delta$  and dichroism  $\gamma$  introduced by the reflection optics on the optical path, the theoretical polar plots present a completely different behavior, as shown in Fig. (2.14d). Changes are also observed for the mean square error cartography, according to Fig. (2.14e). Here, the theoretical solution is built with the same birefringence parameters  $(\Theta_b, \Phi_b) = (44^\circ, 97^\circ)$  as the previous case, but with the introduction of ellipticity and dichroism  $(\gamma, \delta) = (0.043, 55^\circ)$ . Both Figs. (2.14d) and (e) show that accounting for the instrumental polarization distortions is crucial before any data analysis. The main effect of the dichroic parameters is to introduce a new solution  $(\Theta_b, \Phi_b)$ , corresponding to the gray ellipses in Fig. (2.14e), that is independent from the expected result. This means that the solution is not unique when the incident polarizations are distorted by the effect of reflection optics. Besides, the  $\pi/2$  periodicity observed for  $\Theta_b$ ,  $\Theta_{b2} = \Theta_{b1} + \pi/2$ , leads necessarily to a new value of  $\Phi_b$ , that follows the relation  $\Phi_{b2}(L) + \Phi_{b1}(L) = 2\pi$ .

This technique is applied to a collagen type I fiber oriented at around  $50^\circ$  relative to the  $X$  axis, as can be seen in Fig. (2.15a), which shows a white light image of the fiber. The experimental curves representing the polarimetric responses of the transmitted intensities detected along the  $X$  and  $Y$  axes, from a given position of the fiber, are depicted in Fig. (2.15b). The corresponding  $(\Theta_b, \Phi_b)$  cartography of the mean square error is reproduced in Fig. (2.15c). It presents the same pattern as the theoretical  $(\Theta_b, \Phi_b)$  map where the incident polarization is affected by ellipticity and dichroism [see Fig. (2.14e)], with eight solutions when both  $\Theta_b$  and  $\Phi_b$  are in the range  $[0^\circ, 360^\circ]$ . From the eight possible solutions, only two are independent and their values are:  $(\Theta_b, \Phi_b) = (44^\circ, 263^\circ)$  and  $(65^\circ, 204^\circ)$ . Both values fitted for  $\Theta_b$  lie roughly along the observed collagen fiber orientation that is depicted Fig. (2.15a). In chapter 5, we will study the polarization resolved CARS responses of collagen fibers. The determination of the birefringence parameters  $(\Theta_b, \Phi_b)$  is crucial for

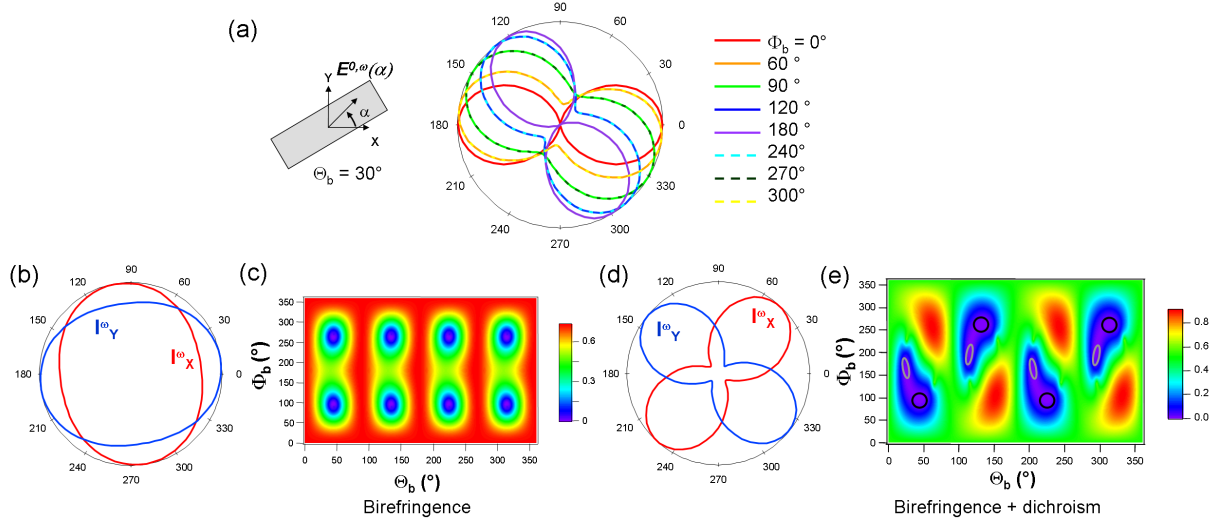


Figure 2.14: (a) Theoretical polarization-resolved intensities of the transmitted field at frequency  $\omega$  detected along the  $X$  axis ( $\mathcal{I}_X^\omega$ ). The optical axis of the sample is fixed at  $\Theta_b = 30^\circ$  and the curves show the influence of the phase shift  $\Phi_b$  on the polarimetric measurements. (b,d) Theoretical polarization responses  $\mathcal{I}_{X,Y}^\omega$  from a sample whose birefringence parameters are  $(\Theta_b, \Phi_b) = (44^\circ, 97^\circ)$ . (c,e) Theoretical  $(\Theta_b, \Phi_b)$  cartographies of the mean square error. In (b,c) no polarization distortions are introduced whereas in (d,e) the polarization distortions are  $\gamma = 0.043$  and  $\delta = 55^\circ$ . Dark and gray circles in (d) depict all the possible solutions. Different colors indicate that the solutions are independent.

an accurate interpretation of the experimental data and a more detailed study will be developed therein. Note however that the method presented here allows only calculating the average birefringence parameters over the whole thickness of the sample and does not account for inhomogeneities of the sample along the optical axis  $Z$ .

## 2.4 Conclusion

In this chapter, we described the experimental setup used to perform polarization resolved CARS and SRS microscopies. In this setup, the two incident fields at frequencies  $\omega_p$  and  $\omega_s$  can have their linear polarizations tuned independently and continuously. Furthermore, the emitted anti-Stokes signal, at frequency  $\omega_{as} = 2\omega_p - \omega_s$ , or the SRL signal, at frequency  $\omega_p$ , are detected along the two perpendicular polarizations  $X$  and  $Y$ . We showed that the characterization of the polarization distortions introduced either by the reflection optics in the optical path or by birefringence of the sample, is crucial to an accurate interpretation of the experimental data. Finally, we proposed different models allowing to characterize these polarization distortions. The first one enables the determination of the dichroic and ellipticity parameters introduced by the dichroic beamsplitter. The second allows to estimate

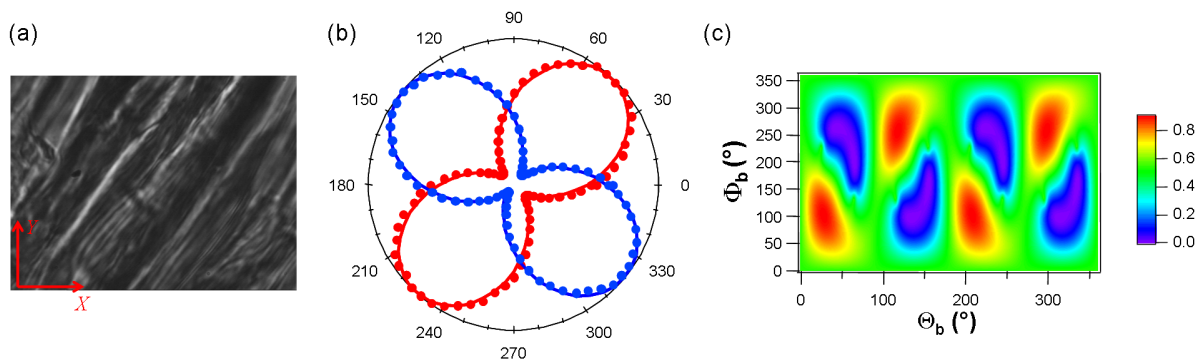


Figure 2.15: Experimental polarization-resolved intensities when the incident field is transmitted through a collagen fiber oriented at around  $50^\circ$ . (a) White light image of the fiber. (b) Experimental polar plots (dots) and corresponding best fits (solid line). Curves in red and blue depict the intensities detected along the  $X$  and  $Y$  axes, respectively. (c)  $(\Theta_b, \Phi_b)$  cartography of the mean square error. Best fit solutions are:  $(\Theta_b, \Phi_b) = (44^\circ, 263^\circ)$  and  $(65^\circ, 204^\circ)$

the birefringence parameters of the sample, defined by the orientation of the optical axis of the object in the macroscopic frame  $(X, Y)$  and the phase shift between the fast and slow axes of the sample. These methods are a good calibration of the polarimetric setup and must be executed before performing polarization resolved nonlinear optical experiments.



---

---

## CHAPTER 3

---

# POLARIZATION RESOLVED COHERENT RAMAN SCATTERING IN ISOTROPIC MEDIA

In this chapter, we use polarization resolved CARS and SRS spectroscopies in order to measure depolarization ratios in isotropic media, away from electronic resonances. This quantity measures the depolarization of the scattered field in relation to the incident field, when a particular molecular vibrational mode is addressed and characterizes the molecular symmetry of liquids and solutions. Pioneer work in polarization-resolved CARS spectroscopy has been developed in the late seventies and early eighties [93, 60, 62, 61] as a powerful alternative tool to spontaneous Raman spectroscopy, allowing the detection of weak Raman bands and the discrimination of individual lines in congested spectra. Moreover, this technique makes it possible to measure tensor invariants, such as the Raman depolarization ratio, as well as the spectral features of the Raman lines. Finally, the control of the incident polarizations combined with a heterodyne detection, where the nonresonant signal plays the role of the local oscillator, allows to remove the nonresonant background [93, 62]. More recently, these polarization analysis have been applied in the determination of depolarization ratios by using multiplex coherent Raman scattering, either in the absence of resonance enhancement [64, 94, 65] or under electronic resonant conditions [95, 96, 63].

Our approach consists in a more general coherent Raman scattering polarization scheme, as we showed in chapter 2. In the case of CARS spectroscopy, we do not seek to remove the nonresonant background but instead, to probe differences in polarimetric signatures between the resonant and nonresonant signal. In order to find polarimetric signatures of vibrational modes in coherent Raman spectroscopy, we first deduce the isotropic third-order susceptibility tensor from the theoretical considerations developed in chapter 1. Then, we develop an analytical model for both the polarized CARS and SRS signals, based on the

plane wave approximation for the incident fields. Finally, we show how to extract the Raman depolarization ratio of a given vibrational mode, from the analytical model. In the case of CARS, a spectroscopic study around the resonance allows to obtain all the spectroscopic parameters of a Raman band: the resonance frequency of the Raman mode, the linewidth (HWHM) of the band and resonant versus nonresonant contribution. In the case of SRS, we can access directly the Raman depolarization ratio, without any spectroscopic consideration, except the knowledge of the Raman resonance frequency.

### 3.1 The third-order nonlinear susceptibility tensor for isotropic media

Isotropy is the characteristic of a medium that is invariant under any rotation of the coordinate system. In the term rotation, we also include inversion and reflection operations. As we showed in chapter 1, the even-order susceptibility tensors vanish for isotropic media and by consequence, the lowest nonlinear optical process capable of probing isotropic samples is the third-order. Here, we use the direct inspection method, described in section 1.3.2, to deduce the nonvanishing and independent components of the susceptibility tensor  $\chi^{(3)}$  for isotropic media. In particular, we follow the procedure adopted in reference [72]. This is not the formal mathematical method of determining the structure of an isotropic tensor, but is a very intuitive way, that has the advantage of using some of the concepts introduced in chapter 1. As we saw in section 1.3.2, inversion operation does not impose any constraint on the  $\chi^{(3)}$  tensor, but instead, it tells only that it does not vanish when the object is isotropic. Let us then consider a reflection through the plane  $YZ$ . In an isotropic medium, it means that  $XJKL \rightarrow -XJKL$  and  $XXXXL \rightarrow -XXXXL$ , with  $JKL \neq X$  and including all indexes permutations. Therefore, according to Fumi's method described in section 1.3.2, this symmetry operation implies that all tensor components containing an odd number of  $X$  indexes vanish. The same is verified for the indexes  $Y$  and  $Z$  when we consider reflections through the planes  $XZ$  and  $XY$ , respectively. By consequence, all the tensor components in which one of the indexes  $X, Y$ , or  $Z$  appears an odd number of times, vanish for an isotropic medium. Therefore, only the remaining 21 components are nonvanishing. It remains now to find which of these components are independent and which relationships exist between dependent tensor elements.

Consider now a four-fold rotation about the  $Z$  axis. This operation corresponds to the transformation  $M_7$  in table 1.1 and implies that  $\chi_{XXXX}^{(3)} = \chi_{YYYY}^{(3)}$ ,  $\chi_{XXYY}^{(3)} = \chi_{YYXX}^{(3)}$ ,  $\chi_{XYXY}^{(3)} = \chi_{YXYX}^{(3)}$  and  $\chi_{XYYX}^{(3)} = \chi_{YXXY}^{(3)}$ . Here, we omit the frequency arguments in order to lighten the writing. Similar relations are obtained for four-fold rotations about the  $X$  and  $Y$  axes and we conclude that:

$$\begin{aligned}
 \chi_{XXXX}^{(3)} &= \chi_{YYYY}^{(3)} = \chi_{ZZZZ}^{(3)} \\
 \chi_{XXYY}^{(3)} &= \chi_{XXZZ}^{(3)} = \chi_{YYXX}^{(3)} = \chi_{YYZZ}^{(3)} = \chi_{ZZXX}^{(3)} = \chi_{ZZYY}^{(3)} \\
 \chi_{XYXY}^{(3)} &= \chi_{XZZX}^{(3)} = \chi_{YXYX}^{(3)} = \chi_{YZYZ}^{(3)} = \chi_{ZXXZ}^{(3)} = \chi_{ZYYZ}^{(3)} \\
 \chi_{XY YX}^{(3)} &= \chi_{XZZX}^{(3)} = \chi_{YXYX}^{(3)} = \chi_{YZYZ}^{(3)} = \chi_{ZXXZ}^{(3)} = \chi_{ZYYZ}^{(3)} \quad .
 \end{aligned} \tag{3.1}$$

Finally, consider a general rotation of an angle  $\theta$  about the  $Z$  axis. In this case, as we showed in section 1.3.2, the direction inspection method is not applicable, but instead, we can find linear combinations between the tensor components. In this case, the tensor transformation law, given in Eq. (1.28), when applied to the component  $\chi_{XXXX}^{(3)}$ , together with the relations established in Eq. (3.1) results in:

$$\chi_{XXXX}^{(3)} = (\cos^4 \theta + \sin^4 \theta) \chi_{XXXX}^{(3)} + 2 \cos^2 \theta \sin^2 \theta \left( \chi_{XXYY}^{(3)} + \chi_{XYXY}^{(3)} + \chi_{XY YX}^{(3)} \right). \tag{3.2}$$

Applying the basic rule of trigonometry,  $\cos^2 \theta + \sin^2 \theta = 1$ , into Eq. (3.2), it can be shown that for an arbitrary angle  $\theta$ , the relation  $\chi_{XXXX}^{(3)} = \chi_{XXYY}^{(3)} + \chi_{XYXY}^{(3)} + \chi_{XY YX}^{(3)}$  is always verified. This completes the proof that the third-order susceptibility tensor for an isotropic medium has 21 nonvanishing components, from which three are independent. Finally, from the results obtained above, it is possible to write the  $\chi^{(3)}$  elements in a compact form, following:

$$\chi_{IJKL}^{(3)} = \delta_{IJ} \delta_{KL} \chi_{XXYY}^{(3)} + \delta_{IK} \delta_{JL} \chi_{XYXY}^{(3)} + \delta_{IL} \delta_{JK} \chi_{XY YX}^{(3)}, \tag{3.3}$$

where  $\delta$  is the Kronecker delta function.

### 3.1.1 The depolarization ratio

In spontaneous Raman scattering, the depolarization ratio measures the degree of depolarization of the scattered field in respect to the incident field, when a molecular normal mode of vibration is excited. It is defined as:

$$\rho_{\text{SR}} = \frac{I_{\perp}^{\text{SR}}}{I_{\parallel}^{\text{SR}}}, \tag{3.4}$$

where  $I^{\text{SR}}$  is the intensity of the scattered light, that can be polarized either parallel or perpendicularly to the incident field polarization. A scheme of this definition is shown in Fig. (3.1). This ratio can be expressed in terms of the invariant components of the Raman polarizability tensor [97].

$$\rho_{\text{SR}} = \frac{5\gamma_a^2 + 3\gamma_s^2}{45\alpha^2 + 4\gamma_s^2}, \tag{3.5}$$

where  $\alpha$  and  $\gamma$  are respectively the isotropic and anisotropic components of the invariant decomposition of the polarizability tensor<sup>1</sup> (note that the  $\gamma$  term introduced here is different from the third-order molecular hyperpolarizability  $\gamma$ ). The subscripts  $s$  and  $a$  stand for the symmetric and anti-symmetric contributions of the  $\gamma$  term. As we are dealing with electronically non-resonant scattering, the polarizability tensor is totally symmetric and the anti-symmetric component  $\gamma_a^2$  vanishes. A polarized band corresponds to a totally symmetric vibrational mode and it is characterized by  $0 \leq \rho_{\text{SR}} < 0.75$ . Usually, for highly symmetric molecules,  $\rho_{\text{SR}} \approx 0$  [80], in which case the anisotropic component of the polarizability  $\gamma_s^2$ , vanishes. A depolarized band characterizes a non-totally symmetric normal mode of vibration and it exists when the isotropic component of the polarizability  $\alpha^2$  vanishes, which corresponds to  $\rho_{\text{SR}} = 0.75$ .

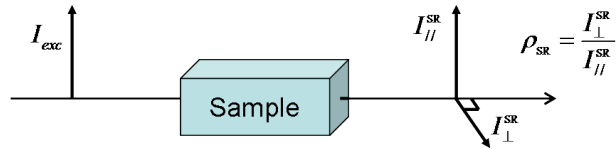


Figure 3.1: Definition of the depolarization ratio in spontaneous Raman scattering.  $I_{\parallel}^{\text{SR}}$  and  $I_{\perp}^{\text{SR}}$  are the intensities scattered by Raman effect polarized, respectively, parallel and perpendicularly to the incident polarization.

By analogy, it is possible to define a depolarization ratio for coherent Raman scattering. As the third-order susceptibility tensor has three independent components for an isotropic medium, we can define up to three CRS depolarization ratios, that can be expressed as functions of the invariants of the Raman polarizability tensor [95], according to:

$$\bar{\rho}_{\text{CRS}} = \frac{\chi_{XXYY}^{(3)\text{R}}}{\chi_{XXXX}^{(3)\text{R}}} = \frac{45\bar{\alpha}^2 - 2\bar{\gamma}_s^2}{45\bar{\alpha}^2 + 4\bar{\gamma}_s^2} \quad (3.6a)$$

$$\bar{\rho}_{\text{CRS}} = \frac{\chi_{XYXY}^{(3)\text{R}}}{\chi_{XXXX}^{(3)\text{R}}} = \frac{5\bar{\gamma}_a^2 + 3\bar{\gamma}_s^2}{45\bar{\alpha}^2 + 4\bar{\gamma}_s^2} \quad (3.6b)$$

$$\rho_{\text{CRS}} = \frac{\chi_{XYX}^{(3)\text{R}}}{\chi_{XXXX}^{(3)\text{R}}} = \frac{-5\bar{\gamma}_a^2 + 3\bar{\gamma}_s^2}{45\bar{\alpha}^2 + 4\bar{\gamma}_s^2} \quad (3.6c)$$

with  $\bar{\bar{\rho}}_{\text{CRS}} + \bar{\rho}_{\text{CRS}} + \rho_{\text{CRS}} = 1$ , which is a consequence from Eq. (3.3). The terms  $\bar{\alpha}$  and  $\bar{\gamma}$  are similar to the  $\alpha$  and  $\gamma$  introduced above, except that they are written as elements of the CRS tensor and therefore involve different resonance properties [97]. The main difference between Raman and CRS depolarization ratios is that the former is a ratio of intensities whether the second is a ratio of susceptibility tensor components. By consequence, in the

<sup>1</sup> $\alpha$  is the trace of the Raman polarizability  $\sum_i \alpha_{ii}$ , while  $\gamma$  contains the terms  $(\alpha_{ii} - \alpha_{jj})$  and  $\alpha_{ij}$ , with  $i \neq j$  [97].

case of spontaneous Raman scattering, the depolarization ratio is always a positive and real number whereas it can assume a complex and negative value in CRS. However, if one-photon absorption is not allowed at frequencies  $\omega_p$  and  $\omega_s$ , the anti-symmetric term  $\bar{\gamma}_a^2$  vanishes and Eqs. (3.6b) and (3.6c) are equivalent. Moreover, under this condition, it has been shown [63] that the remaining invariants are the same as the ones in spontaneous Raman scattering ( $\bar{\alpha} = \alpha$ ) and ( $\bar{\gamma}_s = \gamma_s$ ). Consequently, the depolarization ratios  $\bar{\rho}_{\text{CRS}}$  and  $\rho_{\text{CRS}}$  in coherent Raman scattering and  $\rho_{\text{SR}}$  in spontaneous Raman scattering are equivalent.

This definition of the depolarization ratio for the CRS processes can be rather intuitive. In the case of CARS, the susceptibility tensor, including the frequency arguments, writes  $\chi_{IJKL}^{(3)\text{R}}(-\omega_{as}; \omega_p, \omega_p, -\omega_s)$ . The  $\chi_{YXXY}^{(3)\text{R}}$  component represents the polarization state where the anti-Stokes and Stokes fields are polarized perpendicularly to the pump polarization. In the other hand, the  $\chi_{XXXX}^{(3)\text{R}}$  component accounts for the polarization state where all the fields are parallelly polarized. Their ratio measures therefore how a vibrational mode that is excited by stimulated emission depolarizes the scattered field. In this way, as  $\chi_{YXXY}^{(3)\text{R}} = \chi_{XYXY}^{(3)\text{R}}$  from Eq. (3.1), we associate  $\rho_{\text{CRS}}$  in Eq. (3.6c) to the CARS depolarization ratio. In the same way, we can define the depolarization ratios for SRS. In the case of stimulated raman gain, the susceptibility tensor writes  $\chi_{IJKL}^{(3)\text{SRG}}(-\omega_s; \omega_p, -\omega_p, \omega_s)$  and we can associate to this scattering the same depolarization ratio as for the CARS process. The susceptibility tensor for the stimulated Raman loss scattering is given by  $\chi_{IJKL}^{(3)\text{SRL}}(-\omega_p; \omega_s, \omega_p, -\omega_s)$ , which can be associated to  $\bar{\rho}_{\text{CRS}}$  in Eq. (3.6b).

In conclusion, we can define two depolarization ratios for CARS and SRS processes, that are equivalent to the spontaneous Raman depolarization ratio, under the condition that no electronically resonance is addressed. Eq. (3.7) summarizes the expressions of the depolarization ratios in CRS processes:

$$\rho_{\text{CARS}} = \rho_{\text{SRG}} = \frac{\chi_{XYXY}^{(3)\text{R}}}{\chi_{XXXX}^{(3)\text{R}}} = \rho_{\text{SR}} \quad (3.7a)$$

$$\rho_{\text{SRL}} = \frac{\chi_{XYXY}^{(3)\text{R}}}{\chi_{XXXX}^{(3)\text{R}}} = \rho_{\text{SR}} \quad (3.7b)$$

Since the medium concerned here is isotropic, it appears that  $\rho_{\text{SR}}$  will only depend on the structure of the molecular hyperpolarizability  $\gamma$  ( $\chi_{IJKL}^{(3)}$  is indeed constructed from an isotropic average of the molecular hyperpolarizabilities  $\gamma$ , as seen in chapter 1). Therefore, the depolarization ratio  $\rho_{\text{SR}}$  will strongly depend on the symmetry of the molecular vibration, which determines the structure of the  $\gamma$  tensor (distinct molecular modes of vibration imply different hyperpolarizability structures, resulting in different values of the depolarization ratio  $\rho_{\text{SR}}$ ).

In the CARS process, the susceptibility tensor has also a nonresonant contribution, that accounts for the electronic responses of the medium. In this case, since it is a nonresonant scattering, Kleinman symmetry applies and as a consequence,  $\chi_{XYXY}^{(3)\text{NR}} = \chi_{XXYY}^{(3)\text{NR}} = \chi_{XYXY}^{(3)\text{NR}}$ .

From Eq. (3.3) we can deduce that they are equal to  $\chi_{XXXX}^{(3)\text{NR}}/3$ . It is then possible to define a nonresonant depolarization ratio  $\rho_{\text{NR}}$  that, from Eq. (3.7a), is equal to 1/3.

### 3.1.2 CARS susceptibility tensor for isotropic media

From the general expression of the third-order susceptibility for isotropic media, given by Eq. (3.3) together with the expression of the CARS polarization ratio (Eq. [3.7a]), we can deduce the CARS susceptibility, as a function of  $\rho_{\text{SR}}$ . In order to do this, we need first to take into account the degeneracy of the  $\chi^{(3)\text{CARS}}$  in respect to the frequency of the pump field, which implicates that  $\chi_{XXYY}^{(3)\text{R}} = \chi_{XYXY}^{(3)\text{R}}$ . Replacing this relation and Eq. (3.7a) into Eq. (3.3), we can write the resonant CARS susceptibility as:

$$\chi_{IJKL}^{(3)\text{R}} = \chi_{\text{R}} \left( \delta_{IJ}\delta_{KL} + \delta_{IK}\delta_{JL} + \frac{2\rho_{\text{SR}}}{1 - \rho_{\text{SR}}}\delta_{IL}\delta_{JK} \right). \quad (3.8)$$

where  $\chi_{\text{R}}$  is an alleged notation for the susceptibility component  $\chi_{XXYY}^{(3)\text{R}}$ . The nonresonant CARS susceptibility is given by Eq. (3.3) when Kleinman symmetry condition is verified. If we sum the resonant contribution, given by Eq. (3.8), with the nonresonant one, we can deduce the total CARS susceptibility tensor, as following:

$$\begin{aligned} \chi^{(3)\text{CARS}} &= \chi^{(3)\text{NR}} + \chi^{(3)\text{R}} & (3.9a) \\ \Rightarrow \chi_{IJKL}^{(3)\text{CARS}} &= \chi_{\text{NR}} (\delta_{IJ}\delta_{KL} + \delta_{IK}\delta_{JL} + \delta_{IL}\delta_{JK}) \\ &+ \chi_{\text{R}} \left( \delta_{IJ}\delta_{KL} + \delta_{IK}\delta_{JL} + \frac{2\rho_{\text{SR}}}{1 - \rho_{\text{SR}}}\delta_{IL}\delta_{JK} \right), & (3.9b) \end{aligned}$$

where  $\chi_{\text{NR}}$  is the notation to refer to the nonresonant tensor component  $\chi_{XXYY}^{(3)\text{NR}}$ . This term has a real value and does not depend on the incident frequencies,  $\omega_p$  and  $\omega_s$  [58, 98]. On the other hand, the resonant term  $\chi_{\text{R}}$  is a complex number and presents a lorentzian spectral dependency, given by

$$\chi_{\text{R}}(\delta\omega) = \frac{a}{(\delta\omega - \Omega_{\text{R}}) + i\Gamma}, \quad (3.10)$$

according to section 1.2.3. The formalism developed therein establishes that the coefficient  $a$ , characterizing the oscillator strength, has a strictly negative value.  $\Omega_{\text{R}}$  is the resonance angular frequency,  $\delta\omega = \omega_p - \omega_s$  is the angular frequency difference between the pump and Stokes fields and  $\Gamma$  is the half width at half maximum (HWHM) of the probed Raman line, which represents the damping factor  $\gamma_{vg}$  between the molecular excited vibrational level and the ground state, as we saw in Eq. (1.24), in section 1.2.3.

### 3.1.3 The spectral behavior of the CARS susceptibility

The far field anti-Stokes field detected in a position  $\mathbf{R}'$  in the space results from a linear contribution of the nonlinear polarization  $\mathbf{P}^{(3)}$  induced at all positions  $\mathbf{R}$  in the sample. By

consequence, the CARS intensity is proportional to the modulus square of  $\mathbf{P}^{(3)}$  and therefore, from Eq. (1.1), to the modulus square of the CARS susceptibility tensor  $\chi^{(3)\text{CARS}}(\mathbf{R})$ , according to:

$$\mathcal{I}_{\text{CARS}}(\mathbf{R}') = |\mathbf{E}_{as}(\mathbf{R}')|^2 \propto |\mathbf{P}^{(3)}(\mathbf{R})|^2 \propto |\chi^{(3)\text{CARS}}(\mathbf{R})|^2 \quad (3.11)$$

As we saw in the previous section, the CARS susceptibility tensor has two different contributions: one that is resonant and originates from the excitation of the molecular vibrational mode and another one that is nonresonant and arises from the electronically response of the medium. If we replace Eq. (3.9a) into Eq. (3.11), the latter becomes:

$$\mathcal{I}_{\text{CARS}}(\mathbf{R}') \propto |\chi^{(3)\text{R}}(\mathbf{R})|^2 + |\chi^{(3)\text{NR}}(\mathbf{R})|^2 + 2\Re[\chi^{(3)\text{R}}(\mathbf{R}) \cdot \chi^{(3)\text{NR}*}(\mathbf{R})]. \quad (3.12)$$

Even for an isotropic material, Eq. (3.12) is very complicated because it holds the tensorial and spectral dependency of the medium. In a first step, we are interested only in the spectral behavior of the medium, in such a way that we neglect its tensorial structure. This can be done simply by replacing the tensors in Eq. (3.12) by scalars that keep their spectral dependency. This crude approximation corresponds to the physical situation where both terms in brackets in (Eq. 3.9b), corresponding to nonresonant and resonant tensor structures, are equal to each other. This can be achieved, for instance, in a vibrational mode with depolarization ratio equal to 1/3, when all the incident and emitted polarizations are parallel to each other. With this simplifications, and omitting the arguments  $\mathbf{R}$  and  $\mathbf{R}'$  in order to shorten the notation, Eq. (3.11) writes

$$\mathcal{I}_{\text{CARS}} \propto |\chi_{\text{R}}|^2 + \chi_{\text{NR}}^2 + 2\chi_{\text{NR}}\Re(\chi_{\text{R}}). \quad (3.13)$$

The CARS intensity is the superposition of three contributions called, in the order they appear in Eq. (3.13), “resonant”, “nonresonant” and “heterodyne”, respectively. The resonant term holds all the spectral information on the addressed vibrational mode, according to Eq. (3.10). The nonresonant term is constant and does not contain any spectral information. Finally, the heterodyne contribution is proportional to the real part of the resonant term. In this way, the CARS signal can be interpreted as being the result of the interference between two spectral waves, where the interference term is carried by the heterodyne component. In Fig. (3.2) we plot the typical CARS spectrum for an isotropic medium, together with the three contributions: resonant, nonresonant and heterodyne. The spectrum was built with the following spectral parameters:  $a = -5$ ,  $\Gamma = 3 \text{ cm}^{-1}$ , for the resonant contribution, and  $\chi_{\text{NR}} = 1$  for the nonresonant term.

Fig. (3.2) shows the typical CARS spectrum of a molecular vibrational mode in an isotropic medium. Without the simplificative assumptions applied earlier in this section, the spectrum will vary according to the different polarization configurations, but it will keep the same characteristic patterns. The major changes of the CARS spectrum compared to the Raman spectrum arise from the presence of the heterodyne term. This term is proportional to the real part of the resonant term, expressed as the lorentzian function

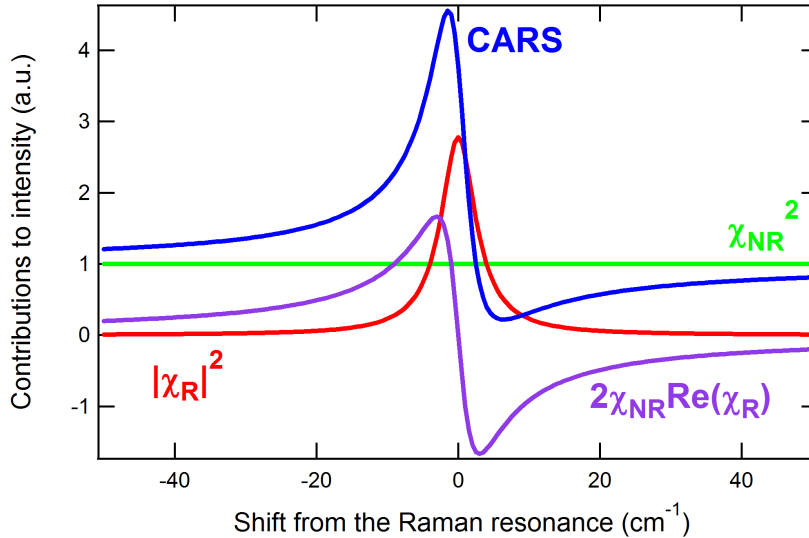


Figure 3.2: Typical CARS spectrum for an isotropic medium (in blue), together with the contributions of the resonant (in red), nonresonant (in green) and heterodyne (in purple) terms.

in Eq. (3.10), and is therefore antisymmetric in relation to the resonance frequency  $\Omega_R$ . This is the reason why the heterodyne contribution reaches a maximum intensity when the frequency shift from the Raman resonance is negative ( $\delta\omega - \Omega_R < 0$ ) and a minimum intensity when this shift is positive ( $\delta\omega - \Omega_R > 0$ ). Therefore, when we sum the heterodyne contribution with the resonant and nonresonant terms, the resulting CARS spectrum also presents a maximum and a minimum. These intensities are named respectively peak and dip [35]. Moreover, the peak is shifted towards the lower frequencies, compared to the peak of the Raman spectrum. Finally, the presence of the heterodyne contribution makes the CARS band wider than the Raman line. When the medium is not isotropic, however, the CARS spectrum can present different features from the ones presented here, depending on the symmetry of the medium and on the polarization configuration. An example will be shown in chapter 4, in the case of a crystal with cubic symmetry.

### 3.1.4 SRS susceptibility tensor for isotropic media

We can determine the expression of the SRS susceptibility tensor, either for the stimulated Raman gain or loss scattering. As in our experimental setup we are only concerned in detecting the depletion of the pump field resulted from the stimulated emission, we are only interested in the  $\chi^{(3)}$  tensor for the SRL process. In this case, the degeneracy in the Stokes frequency implies that  $\chi_{XXYY}^{(3)\text{SRL}} = \chi_{XYXX}^{(3)\text{SRL}}$ . To this relation, we add the expression of the SRL depolarization ratio, given by Eq. (3.7b), and from Eq. (3.3), we determine the SRL susceptibility tensor for isotropic media, as:

$$\chi_{IJKL}^{(3)\text{SRL}} = \chi_R \left( \delta_{IJ}\delta_{KL} + \delta_{IL}\delta_{KJ} + \frac{2\rho_{\text{SR}}}{1 - \rho_{\text{SR}}}\delta_{IK}\delta_{JL} \right), \quad (3.14)$$

where  $\chi_R = \chi_{XXYY}^{(3)\text{SRL}}$ . This term has a complex value and is frequency dependent according to the Lorentzian function in Eq. (3.10). Eqs. (3.8) and (3.14) show that the resonant isotropic tensor is not the same for different coherent Raman scattering processes and therefore care must be taken when manipulating the tensorial indexes and the frequency arguments.

## 3.2 Analytical model of the induced nonlinear polarization in coherent Raman scattering

### 3.2.1 The polarization-resolved CARS response

In chapter 1, we showed that the  $p$ -order macroscopic induced polarization results from the coupling of the susceptibility tensor  $\chi^{(p)}$  with the exciting electromagnetic fields. In the case of CARS, the third-order nonlinear induced polarization writes:

$$P_I^{(3)}(\omega_{as}) = \epsilon_0 \sum_{IJKL} \chi_{IJKL}^{(3)\text{CARS}}(-\omega_{as}; \omega_p, \omega_p, -\omega_s) E_{PJ}(\omega_p) E_{PK}(\omega_p) E_{sL}^*(\omega_s), \quad (3.15)$$

where  $\mathbf{E}_p$  and  $\mathbf{E}_s$  are the pump and Stokes incident fields at angular frequencies  $\omega_p$  and  $\omega_s$ , respectively and  $\omega_{as} = 2\omega_p - \omega_s$  is the angular frequency of the emitted anti-Stokes field.

The analytic model of the polarization-resolved CARS emission for an isotropic medium follows the work described in [99]. It is developed from the tensor structure introduced in Eq. (3.9) and under some additional simplificative assumptions. First, following the polarization schemes described in chapter 2, the pump and Stokes fields are linearly polarized with polarization angles  $\alpha_p$  and  $\alpha_s$ , respectively, with respect to the  $X$  direction. Second, as we are focusing with a low numerical aperture objective (NA=0.6), we assume that the incident fields are plane waves propagating in the  $Z$  direction and therefore, we neglect the field components  $E_{pz}$  and  $E_{sz}$ , that can contribute up to 20% of the field amplitudes, as showed in chapter 2. Nevertheless, we will show in section 3.3.1 that for the case of nonresonant CARS responses, the experimental and theoretical intensities are in very good agreement, which justifies the simplification adopted here. Under these assumptions, the  $X$  and  $Y$  components of the CARS signal polarization can be determined by introducing Eq. (3.9) into Eq. (3.15), following:

$$P_X^{(3)} = \epsilon_0 \chi_{X\text{eff}}^{(3)} E_p^2 E_s^* \quad (3.16a)$$

$$P_Y^{(3)} = \epsilon_0 \chi_{Y\text{eff}}^{(3)} E_p^2 E_s^* \quad (3.16b)$$

where  $E_p$  and  $E_s$  are the peak amplitudes of the incident fields and the effective susceptibilities  $\chi_{X_{\text{eff}}}^{(3)}$  and  $\chi_{Y_{\text{eff}}}^{(3)}$  are defined as:

$$\chi_{X_{\text{eff}}}^{(3)} = \chi_{\text{NR}} \left( 2 \cos \alpha_p \sin \alpha_p \sin \alpha_s + \sin^2 \alpha_p \cos \alpha_s + 3 \cos^2 \alpha_p \cos \alpha_s \right) + 2\chi_{\text{R}} \times \left( \cos \alpha_p \sin \alpha_p \sin \alpha_s + \frac{\rho_{\text{SR}}}{1 - \rho_{\text{SR}}} \sin^2 \alpha_p \cos \alpha_s + \frac{1}{1 - \rho_{\text{SR}}} \cos^2 \alpha_p \cos \alpha_s \right) \quad (3.17a)$$

$$\chi_{Y_{\text{eff}}}^{(3)} = \chi_{\text{NR}} \left( 2 \cos \alpha_p \sin \alpha_p \cos \alpha_s + \cos^2 \alpha_p \sin \alpha_s + 3 \sin^2 \alpha_p \sin \alpha_s \right) + 2\chi_{\text{R}} \times \left( \cos \alpha_p \sin \alpha_p \cos \alpha_s + \frac{\rho_{\text{SR}}}{1 - \rho_{\text{SR}}} \cos^2 \alpha_p \sin \alpha_s + \frac{1}{1 - \rho_{\text{SR}}} \sin^2 \alpha_p \sin \alpha_s \right). \quad (3.17b)$$

By manipulating the  $\cos \alpha$  and  $\sin \alpha$  with the standard trigonometric relations, Eq. (3.17) can be recast under:

$$\chi_{X_{\text{eff}}}^{(3)} = \chi_{\text{NR}} [2 \cos \alpha_s + \cos(2\alpha_p - \alpha_s)] + \frac{a}{(\delta\omega - \Omega_{\text{R}}) + i\Gamma} \left[ \frac{1 + \rho_{\text{SR}}}{1 - \rho_{\text{SR}}} \cos \alpha_s + \cos(2\alpha_p - \alpha_s) \right] \quad (3.18a)$$

$$\chi_{Y_{\text{eff}}}^{(3)} = \chi_{\text{NR}} [2 \sin \alpha_s + \sin(2\alpha_p - \alpha_s)] + \frac{a}{(\delta\omega - \Omega_{\text{R}}) + i\Gamma} \left[ \frac{1 + \rho_{\text{SR}}}{1 - \rho_{\text{SR}}} \sin \alpha_s + \sin(2\alpha_p - \alpha_s) \right], \quad (3.18b)$$

where  $\chi_{\text{R}}$  was replaced by its expression given by Eq. (3.10). From Eq. (3.18), both expressions of  $\chi_{X_{\text{eff}}}^{(3)}$  and  $\chi_{Y_{\text{eff}}}^{(3)}$  have a nonresonant term that only depends on the incident polarization direction and a resonant contribution that depends also on the spectral shift and the Raman depolarization ratio.

In order to simplify the expression of the effective CARS susceptibility, in Eq. (3.18), let us first define the functions

$$G_X(\alpha_p, \alpha_s) = \chi_{\text{NR}} [2 \cos \alpha_s + \cos(2\alpha_p - \alpha_s)] \quad (3.19a)$$

$$G_Y(\alpha_p, \alpha_s) = \chi_{\text{NR}} [2 \sin \alpha_s + \sin(2\alpha_p - \alpha_s)], \quad (3.19b)$$

that correspond to the nonresonant terms in Eqs. (3.18a) and (3.18b), respectively. Then, we can define a normalized spectral shift from the Raman resonance as

$$\zeta = \frac{\delta\omega - \Omega_{\text{R}}}{\Gamma}. \quad (3.20)$$

By replacing Eqs. (3.19) and (3.20) into Eq. (3.18) the effective susceptibilities become

$$\chi_{X(Y)\text{eff}}^{(3)}(\alpha_p, \alpha_s, \zeta, \rho_{\text{SR}}) = G_{X(Y)} \times \left[ 1 + \frac{a}{\chi_{\text{NR}}\Gamma(\zeta + i)} \frac{1}{2 + \beta_{X(Y)}} \left( \frac{1 + \rho_{\text{SR}}}{1 - \rho_{\text{SR}}} + \beta_{X(Y)} \right) \right]. \quad (3.21)$$

where the angular dependency in the functions  $G$  and  $\beta$  are omitted in order to shorten the notation. The latter, is a function of the incident polarizations  $\alpha_p$  and  $\alpha_s$ , defined as

$$\beta_X(\alpha_p, \alpha_s) = \frac{\cos(2\alpha_p - \alpha_s)}{\cos(\alpha_s)} \quad \text{and} \quad \beta_Y(\alpha_p, \alpha_s) = \frac{\sin(2\alpha_p - \alpha_s)}{\sin(\alpha_s)}. \quad (3.22)$$

By analogy with [100], we define a function  $\eta_{X(Y)} = -2\Gamma\chi_{\text{NR}}/(aF_{X(Y)})$  that characterizes the strength of the nonresonant over the resonant CARS signal. Here, the function  $F_{X(Y)}$  expresses the polarization-dependent term of the resonant contribution, as follows

$$F_{X(Y)}(\alpha_s, \alpha_s, \rho_{\text{SR}}) = \frac{1}{2 + \beta_{X(Y)}} \left( \frac{1 + \rho_{\text{SR}}}{1 - \rho_{\text{SR}}} + \beta_{X(Y)} \right). \quad (3.23)$$

After some algebraic manipulations, that we do not detail here, Eq. (3.21) can be recast under a polar form, according to the formalism developed in [100]:

$$\chi_{X(Y)\text{eff}}^{(3)}(\alpha_p, \alpha_s, \zeta, \rho_{\text{SR}}) = \frac{G_{X(Y)}}{\eta_{X(Y)}(\zeta^2 + 1)} [\eta_{X(Y)}(\zeta^2 + 1) - 2\zeta + 2i], \quad (3.24)$$

$$\propto \sqrt{\mathcal{I}_{X(Y)}} \exp(i\phi)$$

where  $\mathcal{I}$  corresponds to a CARS intensity analyzed along the  $X$  or the  $Y$  directions. The proportionality in Eq. (3.24) is a crude simplification that does not take into account the far field structure and its relation to the spatial dependent susceptibility  $\chi^{(3)}$ . Nevertheless we know that the total emitted CARS intensity is proportional to the modulus square of the susceptibility, which is expressed here on a simple plane wave basis. From Eq. (3.24), the CARS intensity  $\mathcal{I}$  and the phase of the effective susceptibility  $\phi$  write

$$\mathcal{I}_{X(Y)}(\alpha_p, \alpha_s, \zeta, \rho_{\text{SR}}) \propto G_{X(Y)}^2 \left[ 1 + 4 \frac{\frac{1}{\eta_{X(Y)}} - \zeta}{\eta_{X(Y)}(\zeta^2 + 1)} \right], \quad (3.25a)$$

$$\tan \phi_{X(Y)}(\alpha_p, \alpha_s, \zeta, \rho_{\text{SR}}) = \frac{2}{\eta_{X(Y)}(\zeta^2 + 1) - 2\zeta}. \quad (3.25b)$$

When the pump and Stokes fields are fixed, the term  $\epsilon_0 E_p^2 E_s^*$  in Eq. (3.16) acts only as a multiplicative constant and does not contribute in Eqs. (3.25a) and (3.25b). Finally, Eq. (3.25a) includes any linear polarization states of the pump and Stokes beams together with the spectral dispersion associated with the Raman line.

### The nonresonant polarization-resolved CARS response

When the incident frequencies  $\omega_p$  and  $\omega_s$  are tuned away from the resonance frequency of a molecular vibrational mode, the CARS process is purely nonresonant and the second term in brackets in Eq. (3.25a) vanishes, leading to  $\mathcal{I}_{X(Y)}(\alpha_p, \alpha_s) \propto G_{X(Y)}^2$ <sup>2</sup>. Therefore, the CARS intensities depend only on the incident polarizations and we can study the theoretical polarization-responses of the nonresonant CARS signal for the three polarization configurations stated in section 2.1. The results are depicted in Fig. (3.3). In (a), the Stokes polarization is fixed along the  $X$  axis ( $\alpha_s = 0^\circ$ ) and the CARS intensities are plotted as a function of the pump polarization (P configuration), whereas in (b)  $\alpha_p = 0^\circ$  and the CARS intensities vary according to  $\alpha_s$  (S configuration). In both cases the CARS signal is emitted essentially along the  $X$  axis, except for  $\alpha_p = 90^\circ$  and  $\alpha_s = 0^\circ$ , when the  $\mathcal{I}_X$  vanishes. In Fig. (3.3c) (PS configuration), the incident polarizations rotate simultaneously and the polar plots show the typical emission pattern of an isotropic medium, where the intensity of the total emitted signal does not depend on the incident polarization, ie,  $(\mathcal{I}_X + \mathcal{I}_Y)(\alpha_p = \alpha_s) = C$ .

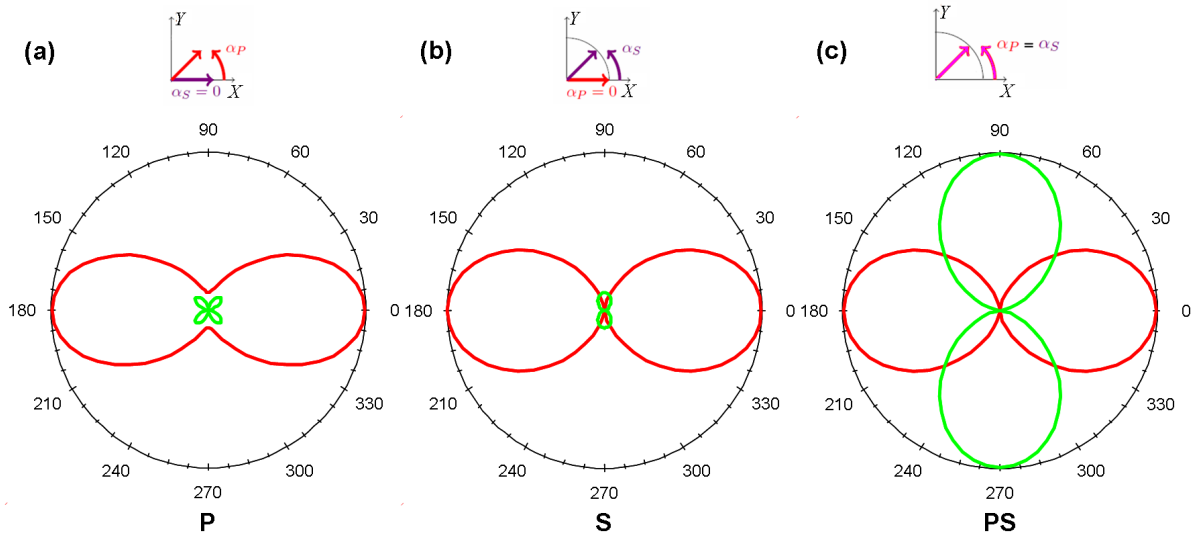


Figure 3.3: Theoretical polarization-resolved nonresonant CARS intensities. (a)  $\alpha_s = 0^\circ$  and  $\alpha_p$  rotates from  $0^\circ$  to  $360^\circ$  (P polarization configuration). (b)  $\alpha_p = 0^\circ$  and  $\alpha_s$  rotates (S polarization configuration). (c) Both polarizations rotate simultaneously (PS polarization scheme). Red and green curves depict the CARS intensities along the  $X$  and  $Y$  axes, respectively.

It is worth noticing that, in the PS polarization configuration, the polar plots representing the CARS intensities have always the same shape, even when a molecular vibrational

<sup>2</sup>This is not surprising, since the function  $G_{X(Y)}$  is by definition the nonresonant contribution to the CARS signal.

mode is addressed. This fact can be verified from the expressions of the effective susceptibilities in Eq. (3.18). If we put  $\alpha_p = \alpha_s = \alpha$ , then these susceptibilities become:

$$\begin{aligned}\chi_{X\text{eff}}^{(3)} &= \left[ 3\chi_{\text{NR}} + \frac{2a}{[(\delta\omega - \Omega_{\text{R}}) + i\Gamma](1 - \rho_{\text{SR}})} \right] \cos \alpha \\ \chi_{Y\text{eff}}^{(3)} &= \left[ 3\chi_{\text{NR}} + \frac{a}{[(\delta\omega - \Omega_{\text{R}}) + i\Gamma](1 - \rho_{\text{SR}})} \right] \sin \alpha.\end{aligned}$$

The CARS intensities along the  $X$  and  $Y$  directions are therefore proportional to  $\cos^2 \alpha$  and  $\sin^2 \alpha$ , respectively, with the same proportionality constant. By consequence, the total intensity  $\mathcal{I}_X + \mathcal{I}_Y$  does not depend on the polarization angle  $\alpha$  and the shapes of the polar plots are the same as in the nonresonant case. In conclusion, the PS polarization scheme brings no additional information on the medium, beyond the fact that it is isotropic, and can be consequently, discarded when studying isotropic samples.

### 3.2.2 Determination of the spectroscopic CARS parameters

In this section, we propose a simple method to determine the Raman depolarization ratio and the strength of the resonant over the nonresonant amplitudes  $a/\chi_{\text{NR}}$  of an isotropic medium, together with its spectral parameters  $\Omega_{\text{R}}$  and  $\Gamma$ . For this purpose, we derive the expressions of the polarized CARS intensities at the two spectral positions defined earlier in section 3.1.3, the peak and dip. The choice of these specific spectral positions comes from the fact that they are convenient to determine experimentally. In order to derive theoretical expressions for these intensities, the first step is to calculate the spectral shifts  $\zeta_{P_{X(Y)}}$  and  $\zeta_{D_{X(Y)}}$ , where  $P$  and  $D$  stand respectively for peak and dip, for which the CARS intensity in Eq. (3.25a) is maximum or minimum. This is done by canceling the first derivative of the CARS intensities with respect to  $\zeta$ . The spectral shifts found by this method are

$$\zeta_{P_{X(Y)}} = \frac{1 - \sqrt{1 + \eta_{X(Y)}^2}}{\eta_{X(Y)}} \quad \text{and} \quad \zeta_{D_{X(Y)}} = \frac{1 + \sqrt{1 + \eta_{X(Y)}^2}}{\eta_{X(Y)}}. \quad (3.26)$$

This operation requires some caution because Eq. (3.26) is not valid when  $G_{X(Y)} = 0$  or  $\eta_{X(Y)}$  tends to infinity: in both situations the derivative of the intensity with respect to  $\zeta$  vanishes for any value of  $\zeta$ . The polarization configuration that verifies  $G_X = 0$  correspond to  $\alpha_p = 0^\circ$  and  $\alpha_s = 90^\circ$  modulo  $180^\circ$ . Two polarization settings satisfy  $G_Y = 0$ : either  $\alpha_s = 0^\circ$  and  $\alpha_p = 0^\circ$  modulo  $90^\circ$ , or  $\alpha_p = 0^\circ$  and  $\alpha_s = 0^\circ$  modulo  $180^\circ$ .  $\eta_{X(Y)}$  can tend to infinity only when  $\rho_{\text{SR}} = 0$  and  $\beta_{X(Y)} = -1$ .

Replacing Eq. (3.26) into Eq. (3.25a) leads to the final expressions for the CARS peak and dip intensities:

$$\mathcal{I}_{P_{X(Y)}} \propto G_{X(Y)}^2 \frac{\sqrt{1 + \eta_{X(Y)}^2} + 1}{\sqrt{1 + \eta_{X(Y)}^2} - 1} \text{ and } \mathcal{I}_{D_{x(y)}} \propto G_{X(Y)}^2 \frac{\sqrt{1 + \eta_{X(Y)}^2} - 1}{\sqrt{1 + \eta_{X(Y)}^2} + 1}. \quad (3.27)$$

Both expressions are very similar except for the fact that they interchange  $(-)$  and  $(+)$  signals. Consequently, if we sum them up, we obtain a simple quadratic function of  $\eta_{X(Y)}$  and therefore of  $\rho_{\text{SR}}$  and  $a/(\chi_{\text{NR}}\Gamma)$ . Moreover, multiplying  $\mathcal{I}_{P_{X(Y)}}$  by  $\mathcal{I}_{D_{X(Y)}}$  results in the nonresonant contribution  $G_{X(Y)}^4$ . From these observations, we can define the ratio  $S_{\text{PD}}$  as

$$S_{\text{PD}_{X(Y)}}(\alpha_p, \alpha_s, \rho_{\text{SR}}) = \frac{\mathcal{I}_{P_{X(Y)}} + \mathcal{I}_{D_{X(Y)}}}{\sqrt{\mathcal{I}_{P_{X(Y)}}\mathcal{I}_{D_{X(Y)}}}} = 2 + \left(\frac{a}{\chi_{\text{NR}}\Gamma}\right)^2 F_{X(Y)}^2, \quad (3.28)$$

where  $F_{X(Y)}$  is given by Eq. (3.23) and the normalization factor  $(\mathcal{I}_{P_{X(Y)}}\mathcal{I}_{D_{X(Y)}})^{1/2}$  was chosen to eliminate the nonresonant contribution of  $G_{X(Y)}$ . When  $\alpha_s = 0^\circ$ ,  $\beta_Y$  tends to infinity for any value of  $\alpha_p$  and by consequence  $F_Y$  tends to 1 (see Eq. (3.23)) and  $S_{\text{PD}_Y}$  does not depend on the Raman depolarization ratio. As a result, measuring the  $Y$  component of the peak and dip CARS intensities allows to retrieve the ratio  $a/(\chi_{\text{NR}}\Gamma)$ , following

$$\frac{a}{\chi_{\text{NR}}\Gamma} = -\sqrt{S_{\text{PD}_Y}(\alpha_s = 0^\circ) - 2}. \quad (3.29)$$

When  $\alpha_s = 0^\circ$ , this expression is valid for any value of the pump polarization, except when they cancel  $G_Y$ . In particular, Eq. (3.29) is verified when  $\alpha_p = 45^\circ$ , the pump polarization that maximizes the CARS intensity along the  $Y$  direction, as shown in Fig. (3.3a) for the nonresonant case. By setting the incident polarizations  $\alpha_s = 0^\circ$  and  $\alpha_p = 45^\circ$  and inserting Eq. (3.29) into the expression of  $S_{\text{PD}_X}$  given by Eq. (3.28), the Raman depolarization ratio can be calculated as

$$\rho_{\text{SR}} = \frac{2\sqrt{\frac{S_{\text{PD}_X}(\alpha_p = 45^\circ, \alpha_s = 0^\circ) - 2}{S_{\text{PD}_Y}(\alpha_p = 45^\circ, \alpha_s = 0^\circ) - 2}} - 1}{2\sqrt{\frac{S_{\text{PD}_X}(\alpha_p = 45^\circ, \alpha_s = 0^\circ) - 2}{S_{\text{PD}_Y}(\alpha_p = 45^\circ, \alpha_s = 0^\circ) - 2}} + 1}. \quad (3.30)$$

As Eq. (3.28) is quadratic on  $\rho_{\text{SR}}$ , another solution is also possible and is given by the same expression as Eq. (3.30) but with the  $(-)$  and  $(+)$  signs interchanged. However, this leads to a solution where  $\rho_{\text{SR}} > 1$  which is not acceptable since  $0 \leq \rho_{\text{R}} \leq 3/4$  for non electronically resonant excitation and linear incident polarizations, as we saw in section 3.1.1. The scheme described above permits therefore to measure  $\rho_{\text{SR}}$  and  $a/(\chi_{\text{NR}}\Gamma)$  for any pump polarization angle different from  $0^\circ$  modulo  $90^\circ$ , but one specific polarization configuration, namely  $\alpha_s = 0^\circ$  and  $\alpha_p = 45^\circ$ , is chosen in order to maximize the signal to noise ratio in the  $Y$  direction.

It is also possible to determine  $\rho_{\text{SR}}$  and  $a/(\chi_{\text{NR}}\Gamma)$  by recording the  $X$  component of the peak and dip CARS intensities for several pump polarization angles, in the  $P$  polarization

### 3.2. Analytical model of the induced nonlinear polarization in coherent Raman scattering

configuration ( $\alpha_s = 0^\circ$  and  $\alpha_p$  rotates from  $0^\circ$  to  $360^\circ$ ). We can then search for the set of parameters ( $a/(\chi_{\text{NR}}\Gamma), \rho_{\text{SR}}$ ) that best fits the experimental data to the analytic expression of  $S_{\text{PD}_X}$  given by Eq. (3.28), using the least square method. We can thus build an indicator of the fit quality,  $\chi^2(a/(\chi_{\text{NR}}\Gamma), \rho_{\text{SR}})$ , following

$$\chi^2(a/(\chi_{\text{NR}}\Gamma), \rho_{\text{SR}}) = \frac{1}{N} \sum_{\alpha_p} [S_{\text{PD}_X}^{\text{exp}}(\alpha_p) - S_{\text{PD}_X}^{\text{theo}}(\alpha_p, a/(\chi_{\text{NR}}\Gamma), \rho_{\text{SR}})]^2, \quad (3.31)$$

where we have used the same notation as in Eq. (2.5) in section 2.2.2. The interest of this method is that the behavior of  $S_{\text{PD}_X}$  changes dramatically for different values of the Raman depolarization ratio, as we show in Fig. (3.4). This can be explained by the fact that, according to Eq. (3.28),  $S_{\text{PD}_X}$  depends quadratically on  $F_X$ , whose behavior with respect to  $\beta_X$  varies for different values of  $\rho_{\text{SR}}$ . From Eq. (3.23),  $F_X$  is an increasing function of  $\beta_X$  for  $\rho_{\text{SR}} < 1/3$ , it is constant for  $\rho_{\text{SR}} = 1/3$  and a decreasing function of  $\beta_X$  for  $\rho_{\text{SR}} > 1/3$ . Unlike the first method that uses only one pump polarization  $\alpha_p = 45^\circ$ , this fitting method uses several pump polarization angles in order to determine  $\rho_{\text{SR}}$  and  $a/(\chi_{\text{NR}}\Gamma)$ , which can be more accurate for a medium where the signal to noise ratio is too low.

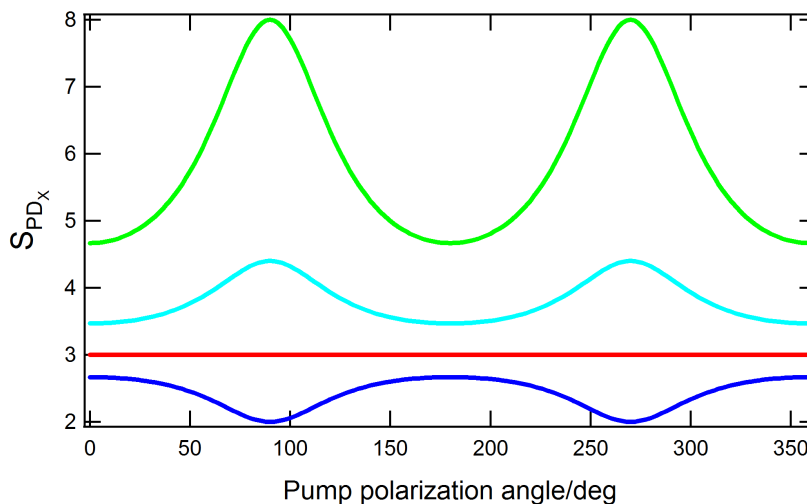


Figure 3.4: Theoretical  $S_{\text{PD}_X}$  ratios as a function of the pump polarization angle when  $\alpha_s = 0^\circ$ , for different depolarization ratios: 0 (blue),  $1/3$  (red), 0.55 (light blue) and 0.75 (green). The ratio  $a/(\chi_{\text{NR}}\Gamma)$  is fixed and equal to -1.

The Raman frequency  $\Omega_{\text{R}}$  and its half width at half-maximum  $\Gamma$  can be determined by solving the two-equation system  $\zeta_{\text{P(D)}} = (\delta\omega_{\text{P(D)}} - \Omega_{\text{R}})/\Gamma$ . The two unknown can be then written as

$$\Gamma = \frac{\delta\omega_{\text{D}} - \delta\omega_{\text{P}}}{\zeta_{\text{P}} - \zeta_{\text{D}}} \quad \text{and} \quad \Omega_{\text{R}} = \frac{\zeta_{\text{D}}\delta\omega_{\text{P}} - \zeta_{\text{P}}\delta\omega_{\text{D}}}{\zeta_{\text{D}} - \zeta_{\text{P}}}, \quad (3.32)$$

where the values of the normalized spectral shift  $\zeta_P$  and  $\zeta_D$  are calculated from Eq. (3.26).

### 3.2.3 The polarization-resolved SRS response

In the SRS process, the signal detected is either the increase of the Stokes intensity or the decrease of the pump intensity due to the stimulated Raman emission, when a molecular vibrational mode is addressed. Here, we are interested in the stimulated Raman loss process (SRL) in which we quantify the depletion undergone by the pump field (see section 1.2.3). In this case, the detected SRL signal can be interpreted as the interference between the incident field at frequency  $\omega_p$ ,  $\mathbf{E}_p(\omega_p)$ , and the field generated by stimulated Raman effect in the interaction length  $L$ ,  $\mathbf{E}^{\text{SRL}}(\omega_p, L)$ , according to:

$$\mathcal{I}_p(\omega_p, L) \propto |\mathbf{E}_p(\omega_p) + \mathbf{E}^{\text{SRL}}(\omega_p, L)|^2. \quad (3.33)$$

The field  $\mathbf{E}^{\text{SRL}}(\omega_p, L)$  is generated by the four-wave mixing process and is proportional to the third-order nonlinear polarization induced in the sample, given by Eq. (1.1). The signal measured in the lock-in detection is the variation of the pump intensity. In the limit where the SRL field is weak compared to the pump field ( $\mathbf{E}^{\text{SRL}} \ll \mathbf{E}_p$ ), the detected signal corresponds to the interference term between both electric fields,  $\mathbf{E}_p(\omega_p)$  and  $\mathbf{E}^{\text{SRL}}(\omega_p, L)$ , following:

$$\begin{aligned} \Delta\mathcal{I}_p(\omega_p, L) &= \mathcal{I}_p(\omega_p, L) - \mathcal{I}_p(\omega_p) = \mathbf{E}_p^*(\omega_p) \cdot \mathbf{E}^{\text{SRL}}(\omega_p, L) + c.c. \\ &= \sum_I E_{pI}^*(\omega_p) E_I^{\text{SRL}}(\omega_p, L) + c.c. \end{aligned} \quad (3.34)$$

where *c.c.* stands for complex conjugate. If we replace the Eq. (1.3) into Eq. (3.34) and if we omit the propagation of the field through the interaction length  $L$ , the SRL signal detected along the direction  $I = (X, Y)$  writes:

$$\mathcal{I}_I^{\text{SRL}} \Delta\mathcal{I}_{pI}(\omega_p) \propto \epsilon_0 \sum_{JKL} \chi_{IJKL}^{(3)\text{SRL}}(-\omega_p; \omega_s, \omega_p, -\omega_s) E_{pI}^*(\omega_p) E_{sI}(\omega_s) E_{pJ}(\omega_p) E_{sK}^*(\omega_s), \quad (3.35)$$

where the signal measured is denoted  $\mathcal{I}_I^{\text{SRL}}$ , by analogy with the notation used in the CARS process.

Contrary to the CARS process, which is proportional to the modulus square of the susceptibility and consequently to the square of the molecular concentration, the SRS process is linear with the susceptibility and by consequence, with the number of molecules by unit volume. By analogy with Eq. (3.16), we can replace the expression of the SRL susceptibility tensor, given by Eq. (3.14), into Eq. (3.35) and by using the plane wave approximation for the incident fields, we can write the SRL intensity along the  $X$  or the  $Y$  axes as:

$$\mathcal{I}_{X(Y)}^{\text{SRL}} \propto \epsilon_0 \chi_{X(Y)\text{eff}}^{(3)\text{SRL}} \mathcal{I}_p \mathcal{I}_s, \quad (3.36)$$

### 3.2. Analytical model of the induced nonlinear polarization in coherent Raman scattering

where  $\mathcal{I}_p = |\mathbf{E}_p|^2$  and  $\mathcal{I}_s = |\mathbf{E}_s|^2$  are the intensities of the pump and Stokes fields, respectively, and the effective susceptibilities are given by:

$$\begin{aligned} \chi_{X_{\text{eff}}}^{(3)\text{SRL}}(\alpha_p, \alpha_s, \rho_{\text{SR}}) &\propto \Im(\chi_{\text{R}}) \left[ \cos^2 \alpha_p \left( \frac{\rho_{\text{SR}}}{1 - \rho_{\text{SR}}} + \cos^2 \alpha_s \right) \right. \\ &\quad \left. + \cos \alpha_p \sin \alpha_p \cos \alpha_s \sin \alpha_s \right] \end{aligned} \quad (3.37a)$$

$$\begin{aligned} \chi_{Y_{\text{eff}}}^{(3)\text{SRL}}(\alpha_p, \alpha_s, \rho_{\text{SR}}) &\propto \Im(\chi_{\text{R}}) \left[ \sin^2 \alpha_p \left( \frac{\rho_{\text{SR}}}{1 - \rho_{\text{SR}}} + \sin^2 \alpha_s \right) \right. \\ &\quad \left. + \cos \alpha_p \sin \alpha_p \cos \alpha_s \sin \alpha_s \right]. \end{aligned} \quad (3.37b)$$

The proportionality symbol accounts for the omission of some constants, which are the same in both directions  $X$  and  $Y$  and thus do not contribute to the analysis developed here. We do not demonstrate that the spectral term is equal to the imaginary part of the third-order susceptibility. This can be done by calculating the wave propagation equation in the nonlinear regime, which is not in the scope of this manuscript, but is very well presented in references [73, 72]. By consequence, as the SRL is proportional to  $\Im(\chi^{(3)})$ , it is not affected by any nonresonant contribution from the electronic response of the medium, for which,  $\chi_{\text{NR}}^{(3)}$  is real. As a consequence, the expressions of the effective susceptibilities, given by Eq. (3.37), are much simpler than in the CARS process [see Eq. (3.18)]. Therefore, SRS allows direct access to the depolarization ratio without any *a priori* spectral knowledge, except the position of the Raman peak. Moreover, its spectrum coincides with the spectrum of the spontaneous Raman scattering, also proportional to  $\Im(\chi_{\text{R}})$ . On the other hand, a polarimetric study of the SRL signal in the peak of the Raman band does not allow to determine any other spectral parameter of the Raman band.

The first consequence of Eq. (3.37) is that there is no SRL signal along the  $X$  or the  $Y$  direction if the pump polarization is along the  $Y$  or the  $X$  axis, respectively. This comes from the fact that the SRL scattering results from an interferometric process with the pump field and by consequence, no signal is generated perpendicular to the pump polarization. The depolarization ratio can be extracted from Eq. (3.37a), for different polarization configurations. In particular, if we set  $\alpha_p = 0^\circ$  and we measure the SRL signal along  $X$ , at two different Stokes polarizations,  $\alpha_s = 0^\circ$  and  $\alpha_s = 90^\circ$ , we obtain:

$$\left. \begin{aligned} \mathcal{I}_X^{\text{SRL}}(\alpha_p = 0^\circ, \alpha_s = 0^\circ) &= \frac{1}{1 - \rho_{\text{SR}}} \\ \mathcal{I}_X^{\text{SRL}}(\alpha_p = 0^\circ, \alpha_s = 90^\circ) &= \frac{\rho_{\text{SR}}}{1 - \rho_{\text{SR}}} \end{aligned} \right\} \Rightarrow \rho_{\text{SR}} = \frac{\mathcal{I}_X^{\text{SRL}}(\alpha_p = 0^\circ, \alpha_s = 90^\circ)}{\mathcal{I}_X^{\text{SRL}}(\alpha_p = 0^\circ, \alpha_s = 0^\circ)} \quad (3.38)$$

which is actually the definition of the depolarization ratio showed in Eq. (3.7b). Note that we omitted the spectral contribution in Eq. (3.38). In fact, this term acts only as a multiplicative factor that is constant for any polarization configuration, and is canceled when performing the ratio  $\mathcal{I}_X^{\text{SRL}}(\alpha_p = 0^\circ, \alpha_s = 90^\circ)/\mathcal{I}_X^{\text{SRL}}(\alpha_p = 0^\circ, \alpha_s = 0^\circ)$ . The inconvenience of this method of calculating the Raman depolarization ratio, specially when working in

a microscopy setup, is that it is necessary to perform two measurements at two distinct Stokes polarizations. Consider then the case where the Stokes polarization is fixed along the  $X$  axis, which leads to:

$$\mathcal{I}_X^{\text{SRL}}(\alpha_p, \alpha_s = 0^\circ) = \cos^2 \alpha_p \frac{1}{1 - \rho_{\text{SR}}} \quad \text{and} \quad \mathcal{I}_Y^{\text{SRL}}(\alpha_p, \alpha_s = 0^\circ) = \sin^2 \alpha_p \frac{\rho_{\text{SR}}}{1 - \rho_{\text{SR}}}.$$

If besides, we set  $\alpha_p = 45^\circ$ , then we can determine the Raman depolarization ratio by recording simultaneously the SRL signal along the  $X$  and  $Y$  axes, for only one incident polarization configuration,  $\alpha_p = 45^\circ, \alpha_s = 0^\circ$ , following:

$$\rho_{\text{SR}} = \frac{\mathcal{I}_Y^{\text{SRL}}(\alpha_p = 45^\circ, \alpha_s = 0^\circ)}{\mathcal{I}_X^{\text{SRL}}(\alpha_p = 45^\circ, \alpha_s = 0^\circ)}. \quad (3.39)$$

### 3.3 Experimental results: calculating the Raman depolarization ratio of liquids

#### 3.3.1 Experimental polarization-resolved CARS responses

##### The nonresonant response

We first present the CARS polarization responses of a pure nonresonant medium, here water, for the two polarization configurations P and S. In the first, the Stokes polarization angle is fixed to zero ( $\alpha_s = 0^\circ$ ) while the pump linear polarization rotates from  $0^\circ$  to  $360^\circ$ . In the second, it is the pump polarization that is fixed along  $X$  while the Stokes polarization rotates. Pump and Stokes wavelengths are fixed to 724.5 nm and 797.0 nm, which corresponds to a frequency shift  $\delta\omega = 1236.5 \text{ cm}^{-1}$ , that is far from any resonance frequency of pure water. The average powers are 2 mW and 1 mW for pump and Stokes, respectively. The results are shown in Fig. 3.5, where we plot the experimental CARS intensities together with the theoretical ones, calculated as the modulus square of the function  $G_{X(Y)}$ , given in Eq. (3.19). It is important to note here that the theoretical approach developed in this chapter does not take in account possible polarization distortions from optical reflections. The good agreement observed between the uncorrected theoretical intensities and the experimental data, in the nonresonant case for both polarization configurations, shows that the effects of dichroism and ellipticity can be neglected. This is only true for an isotropic medium probed with the same wavelengths as in the nonresonant case. As the wavelength of the pump is fixed (or varies slightly), we can always neglect the polarization distortions in the P configuration, for an isotropic medium. In the S polarization scheme, however, the wavelength of the Stokes field can have distinct values, according to the resonance frequency of the probed vibrational mode. As we showed in section 2.2.3, the polarization distortions are very sensitive to the incident wavelength and therefore, in the S polarization configuration, it is necessary to verify the dichroism and ellipticity introduced by the optical reflections for each Stokes frequency. Nevertheless,

the two fit methods for the CARS intensities proposed in this chapter are performed in the P polarization scheme and by consequence, we are not concerned with polarization distortions affecting the Stokes field.

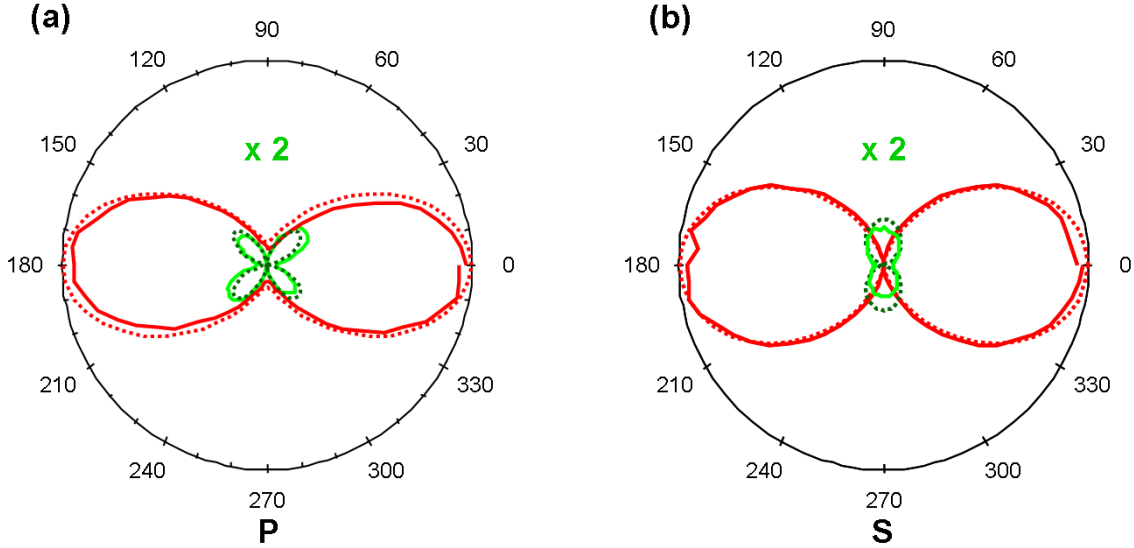


Figure 3.5: CARS polarization responses  $\mathcal{I}_X$  (in red) and  $\mathcal{I}_Y$  (in green), for pure water, with the respective theoretical nonresonant intensities (dotted lines). (a) Stokes polarization  $\alpha_s$  is set parallel to the  $X$  axis and the pump  $\alpha_p$  polarization rotates from  $0^\circ$  to  $360^\circ$ . (b)  $\alpha_p = 0^\circ$  and  $\alpha_s$  rotates.  $\mathcal{I}_Y$  are magnified by a factor of 2 for clarity.

### The resonant response

We now focus on the resonant polarization-resolved CARS responses of some liquids, in order to determine their spectroscopic parameters, in particular, the Raman depolarization ratio. The experiments are carried out on toluene and cyclohexane, at two vibrational modes with different symmetries. In the case of toluene, we concentrate on the polarized Raman band at  $787\text{ cm}^{-1}$  corresponding to the  $A_1$  vibration [101]. The corresponding CARS peak arises at  $776\text{ cm}^{-1}$  which is addressed with pump and Stokes wavelengths at  $730.26\text{ nm}$  and  $774.15\text{ nm}$ , respectively and average power  $300\text{ }\mu\text{W}$  for each beam. For cyclohexane, we focus on the depolarized Raman line at  $1267\text{ cm}^{-1}$  corresponding to the  $E_g$   $\text{CH}_2$  wagging vibration [102]. In this case, the corresponding CARS peak arises at  $1256\text{ cm}^{-1}$  and is addressed with pump and Stokes wavelengths at  $724.5\text{ nm}$  and  $797.0\text{ nm}$  and average powers  $2\text{ mW}$  and  $1\text{ mW}$ , respectively. In this section, the words “toluene” and “cyclohexane” will refer exclusively to these two bands.

We first acquire the CARS spectra of toluene and cyclohexane with both incident polarizations parallel to the  $X$  axis ( $\alpha_p = \alpha_s = 0^\circ$ ), in order to determine their peak and

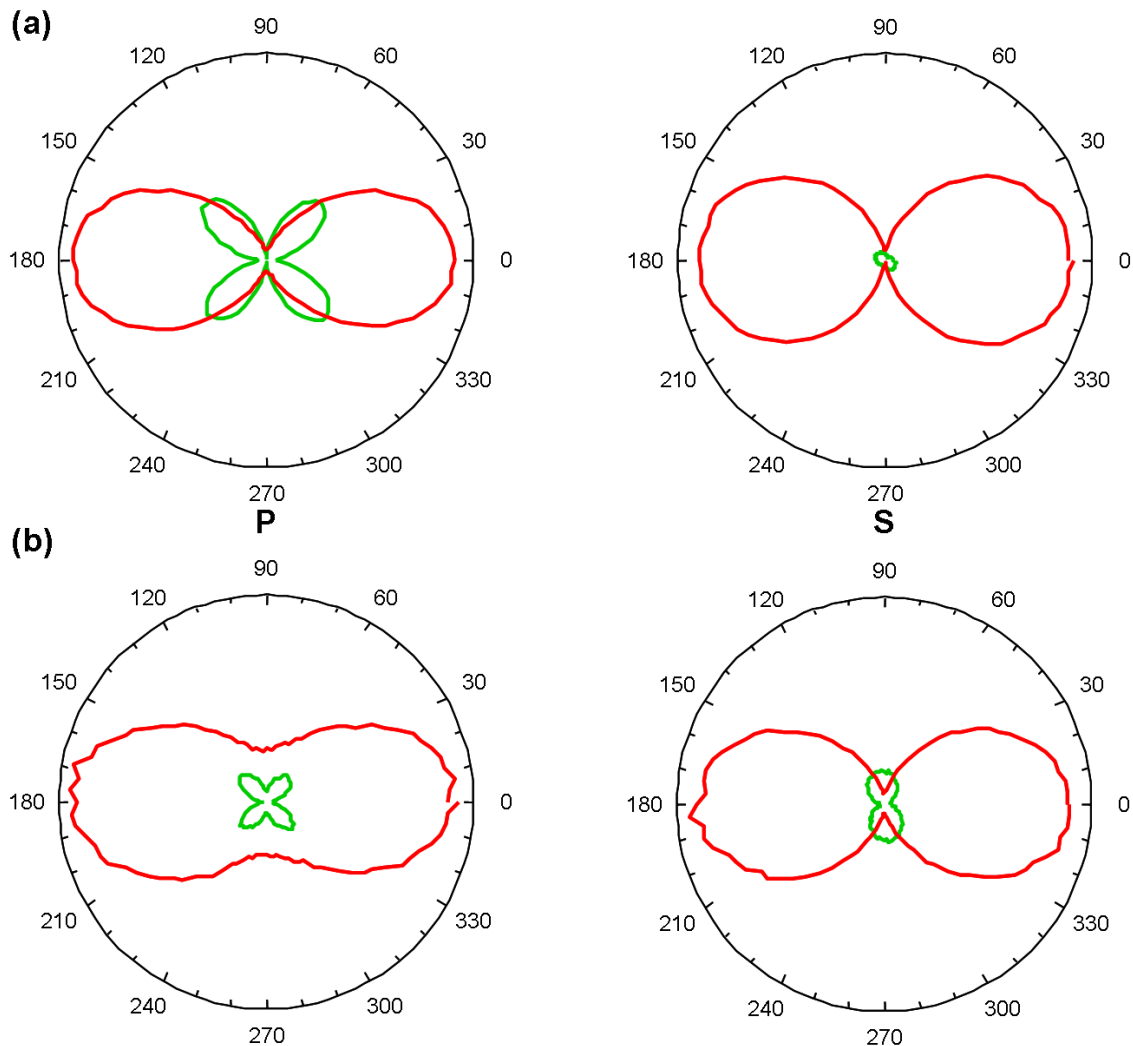


Figure 3.6: Experimental CARS polarization responses  $I_X$  (in red) and  $I_Y$  (in green), for toluene, in the two polarization configurations, P (left) and S (right). (a) Intensities acquired at the peak of the CARS spectrum. (b) Polarimetric measurements at the dip.

dip wavenumbers. As we work with two picosecond lasers, the CARS spectra are obtained by fixing the wavelength of the pump field and by acquiring the CARS intensity along the  $X$  direction for different values of the Stokes wavelength. The peak and dip wavenumbers are determined within an experimental accuracy of  $\pm 4 \text{ cm}^{-1}$ .

The CARS polarization responses are shown in Fig. 3.6 for toluene and Fig. 3.7 for cyclohexane, for both polarization configurations P and S. In Figs. (3.6a) and (3.7a), we depict the CARS signal recorded at the peak of the considered Raman bands, while in (b) we show the intensities at the dip of the spectrum. At first sight, a comparison between the

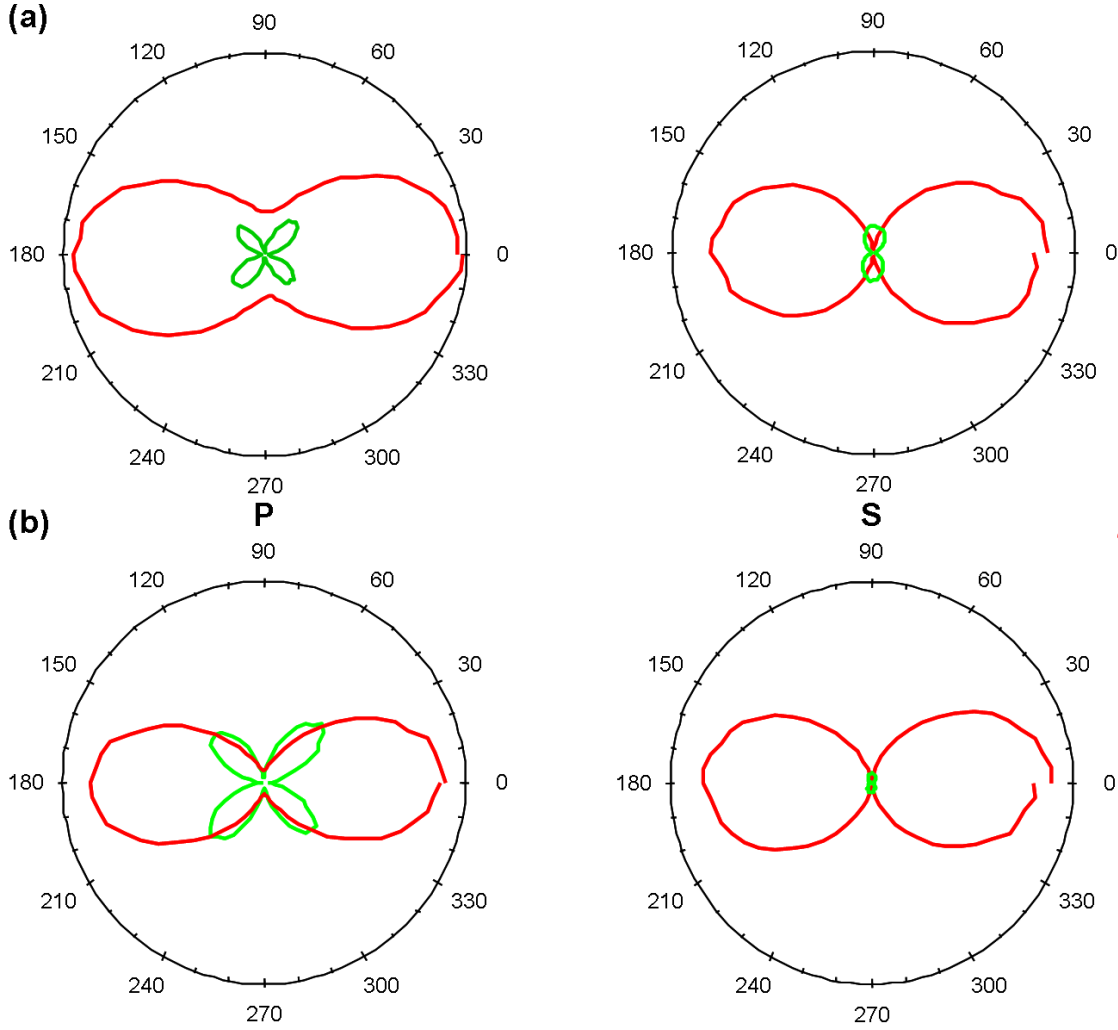


Figure 3.7: Experimental CARS polarization responses  $\mathcal{I}_X$  (in red) and  $\mathcal{I}_Y$  (in green), for cyclohexane, in the two polarization configurations, P (left) and S (right). (a) Intensities acquired at the peak of the CARS spectrum. (b) Polarimetric measurements at the dip.

resonant polar plots [Figs. (3.6) and (3.7)] and the nonresonant ones (Fig. [3.5]) depict very similar curve shapes, showing that the polarization-resolved CARS signal is dominated by the nonresonant response of the considered medium. Nevertheless, a careful observation shows that the signature of the spectral resonance is the ratio of the two perpendicularly polarized CARS intensities,  $\mathcal{I}_X$  and  $\mathcal{I}_Y$ . For both polarization configurations at the CARS peak and dip, the ratio of  $\mathcal{I}_Y$  to  $\mathcal{I}_X$  is indeed strongly dependent on the Raman line depolarization ratio. At the peak of the spectrum, the ratio  $\mathcal{I}_Y/\mathcal{I}_X$  for  $\alpha_s = 0^\circ$  and  $\alpha_p = 45^\circ$ , is close to unity in a polarized band, as toluene, and it decreases to less than

1/2 in a depolarized band, as in cyclohexane. At the dip of the spectrum, the polarized and depolarized band present the opposite behavior in respect to the ratio  $\mathcal{I}_Y/\mathcal{I}_X$ : in this case, when  $\alpha_s = 0^\circ$  and  $\alpha_p = 45^\circ$ , the ratio tends to unity for a depolarized line. In the S polarization scheme, the relative intensities between the CARS signals along  $X$  and  $Y$  is also a signature of the vibrational resonance.

Table 3.1: Raman depolarization ratios and spectral parameters calculated for toluene and cyclohexane.

Sample	$\frac{a}{\chi_{\text{NR}}^{(3)}\Gamma}$	$\rho_{\text{R}}$	$\Gamma$ (cm $^{-1}$ )	$\Omega_{\text{R}}$ (cm $^{-1}$ )	Method
Toluene	$-1.301\pm 0.003$	$0.037\pm 0.002$	$6.5\pm 1.5$	$779\pm 3$	1
	$-1.24\pm 0.03$	$0.04\pm 0.01$	$6.1\pm 1.4$	$779\pm 3$	2
Cyclohexane	$-0.154\pm 0.009$	$0.78\pm 0.01$	$10.9\pm 2.0$	$1266\pm 3$	1
	$-0.12\pm 0.02$	$0.82\pm 0.03$	$10.9\pm 2.0$	$1267\pm 3$	2

From the acquired CARS intensities, we calculate the ratio  $S_{\text{PD}_{X(Y)}}$  (for  $\alpha_s = 0^\circ$ ,  $\alpha_p = 45^\circ$  - referred as method 1) and then we use Eqs. (3.29) and (3.30) to obtain respectively the factor  $a/(\chi_{\text{NR}}\Gamma)$  and the Raman depolarization ratio  $\rho_{\text{SR}}$ . The results are shown in table 3.1, under the label method 1. The uncertainties were derived from the experimental uncertainties of  $\mathcal{I}_{X(Y)}$ . The same CARS spectroscopic coefficients were also deduced from fitting the analytic expression of  $S_{\text{PD}_X}$  in Eq. (3.28) to the experimental data (for  $\alpha_p$  in the range  $[0^\circ, 360^\circ]$  and  $\alpha_s = 0^\circ$  - referred as method 2). The results are shown in table 3.1, under the label method 2. For method 2, the retained solution is the couple  $(a/(\chi_{\text{NR}}\Gamma), \rho_{\text{SR}})$  that minimizes the mean square error function given by Eq. (3.31). Fig. (3.8) plots the cartography of the mean square error  $\chi^2(a/(\chi_{\text{NR}}\Gamma), \rho_{\text{SR}})$ , for toluene (a) and cyclohexane (b). As both surfaces have only one and well defined global minimum, we demonstrate here the unicity of the solution, for different depolarization ratios. Fig. (3.9) shows the experimental ratio  $S_{\text{PD}_X}$  for toluene and cyclohexane and the best fit to Eq. (3.28) as a function of the pump polarization angle  $\alpha_p$ . We observe that  $S_{\text{PD}_X}$  for toluene and cyclohexane exhibit very different behaviors, as expected from Eqs. (3.28) and (3.23) for polarized and depolarized lines. We finally calculate  $\Gamma$  and  $\Omega_{\text{R}}$ , as explained in section 3.2.2 for both methods (see table 3.1, methods 1 and 2).

From table 3.1, both methods allow recovering the degree of polarization of the toluene and cyclohexane bands ( $\rho_{\text{SR}} \approx 0$  and  $\rho_{\text{SR}} \approx 3/4$  respectively). Furthermore, the ratio of the resonant to the nonresonant contribution ( $a/\chi_{\text{NR}}$ ), the spectral line position and its HWHM are obtained within an acceptable agreement between methods 1 and 2. The advantage of method 1 lies in its increased simplicity in an experimental setup: only one polarization configuration at two specific spectral positions (peak and dip) is required to obtain the CARS spectroscopic parameters. Results are also comparable with Raman measurements reported elsewhere for toluene [101] and cyclohexane [64]. The Raman depolarization ratio bigger than 3/4 for the depolarized band of the cyclohexane can be attributed to possible remaining ellipticity introduced by the dichroic filter to the incident

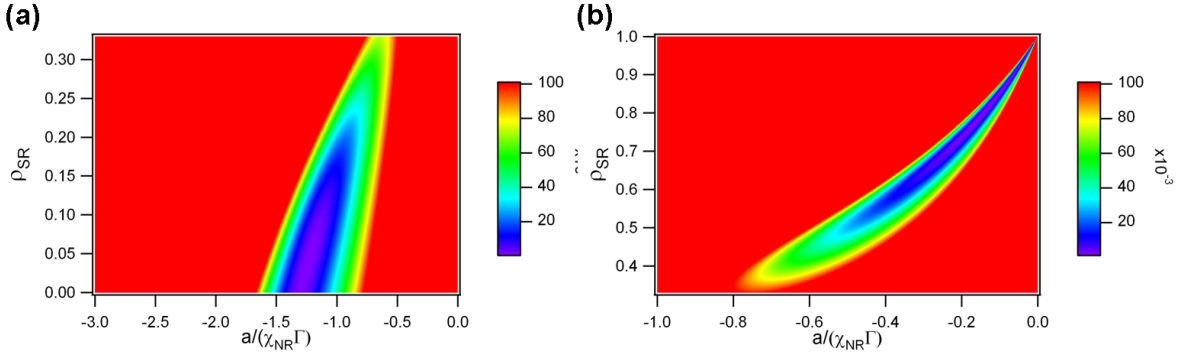


Figure 3.8: Cartography of the mean square error  $\chi^2(a/(\chi_{NR}\Gamma), \rho_{SR})$  for toluene (a) and cyclohexane (b). The retained solution in each case is the couple  $(a/(\chi_{NR}\Gamma), \rho_{SR})$  that minimizes  $\chi^2$ .

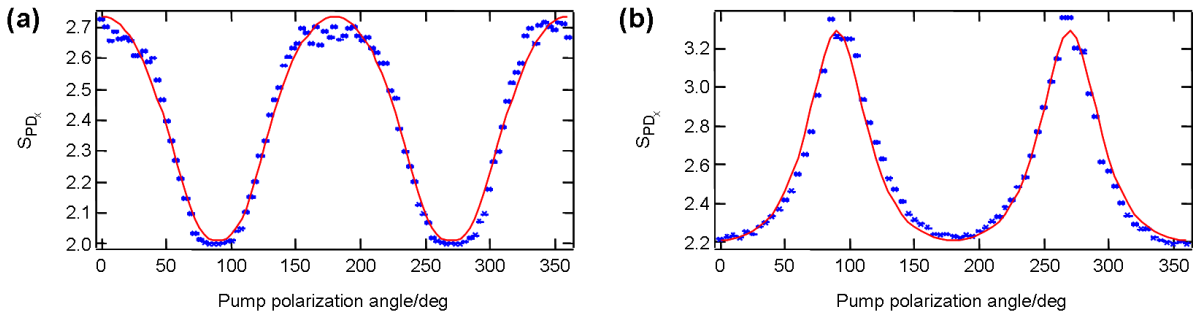


Figure 3.9: Experimental  $S_{PD_X}$  and their best fit as a function of the pump polarization angle  $\alpha_p$  for toluene (a) and cyclohexane (b).

pump polarization. In order to verify the consistency of the parameters fitted in this section, we build a theoretical CARS spectrum for toluene and compare it with the experimental one. The result is shown in Fig. (3.10). The CARS intensity is calculated as the modulus square of the effective susceptibility  $\chi_{X_{eff}}^{(3)}$ , given in Eq. (3.18), with  $\alpha_p = \alpha_s = 0^\circ$  and the spectroscopic parameters given in table 3.1 (we chose to take the mean values between method 1 and 2). Both theoretical and experimental spectra are in good agreement, which shows that despite its simplified assumptions, our analytic model can estimate satisfyingly the CARS spectroscopic parameters for isotropic media.

### 3.3.2 Experimental polarization-resolved SRS responses

The SRS experiments were carried out only on cyclohexane, at two distinct vibrational modes with different symmetries. The first is the polarized Raman band at  $802 \text{ cm}^{-1}$ , corresponding to the totally symmetric ( $A_{1g}$ ) vibration of the carbon ring [102]. This

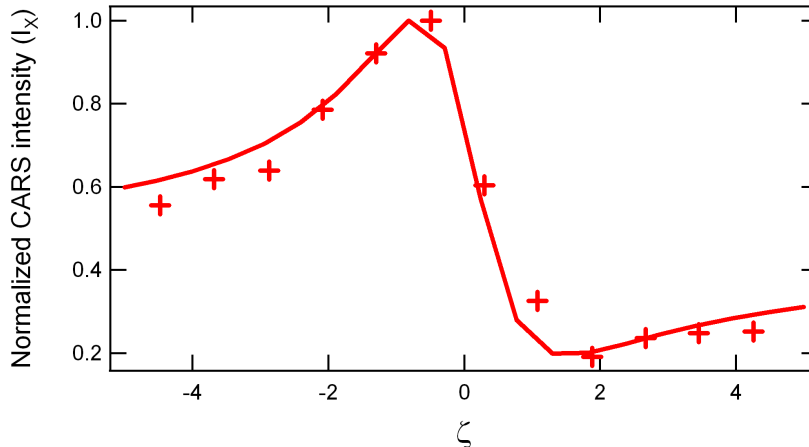


Figure 3.10: Experimental spectrum of toluene (markers) for  $\alpha_p = \alpha_s = 0^\circ$  detected along the  $X$  axis, together with the theoretical spectrum (solid line), calculated with the spectral parameters determined by the analytic model. The intensities are normalized so that they are equal to one at the peak. Spectra are plotted as a function of the normalized spectral shift  $\zeta$ .

resonance is addressed with pump and Stokes wavelengths at 730.26 nm and 775.47 nm, respectively. The second resonance is the same as in the CARS experiment i.e., the depolarized Raman line at  $1267 \text{ cm}^{-1}$  corresponding to the  $E_g$   $\text{CH}_2$  wagging vibration [102]. In this case, the peak is addressed with pump and Stokes wavelengths at 724.5 nm and 797.66 nm. The average powers are 10 mW for each beam.

In the SRS experiments, the pump polarization is fixed along a given direction and we rotate the Stokes linear polarization. For each Stokes wavelength, it is therefore necessary to characterize the ellipticity and dichroism introduced by the dichroic mirror and to correct the theoretical curves by these factors, by accounting them into the incident fields. It is worth noticing, however, that ellipticity does not affect the value of the depolarization ratio, as a consequence of the fact that in the calculations, we only take into account the Stokes intensities acquired along the  $X$  or  $Y$  axes, as showed in Eqs. (3.38) and (3.39). Indeed, according to section 2.2.2, the incident polarization remains linear when it is parallel the  $X$  or the  $Y$  axis. When we use Eq. (3.39) to calculate  $\rho_{\text{SR}}$ , the pump is polarized along  $\alpha_p = 45^\circ$ , direction that can present high ellipticity. However, as the depolarization ratio is calculated by dividing two intensities acquired at the same polarization  $\alpha_p = 45^\circ$ , then this ellipticity does not affect the result.

Here, we perform two distinct polarization-resolved experiments for each vibrational mode. In the first, the pump polarization is fixed along the  $X$  axis and the Stokes polarization rotates from  $0^\circ$  to  $360^\circ$ . In the second, the pump beam has a fixed linear polarization along an intermediate direction ( $\alpha_p \neq 0^\circ$  or  $90^\circ$ ) and the Stokes polarization is tuned as in the first configuration. For the  $A_{1g}$  mode, we chose to fix  $\alpha_p = 150^\circ$ , whereas for the  $E_g$  mode we set  $\alpha_p = 30^\circ$ . In both schemes, we detect the SRL signal along the  $X$  and  $Y$  directions. With the first polarization configuration ( $\alpha_p = 0^\circ$ ), we calculate

the Raman depolarization ratio by using Eq. (3.38). Then, we verify that the theoretical SRL intensities, calculated by replacing the value of  $\rho_{\text{SR}}$  into Eq. (3.37) with the appropriate polarization angles, agree with the intensities acquired in the second polarization configuration ( $\alpha_p \neq 0^\circ$ ).

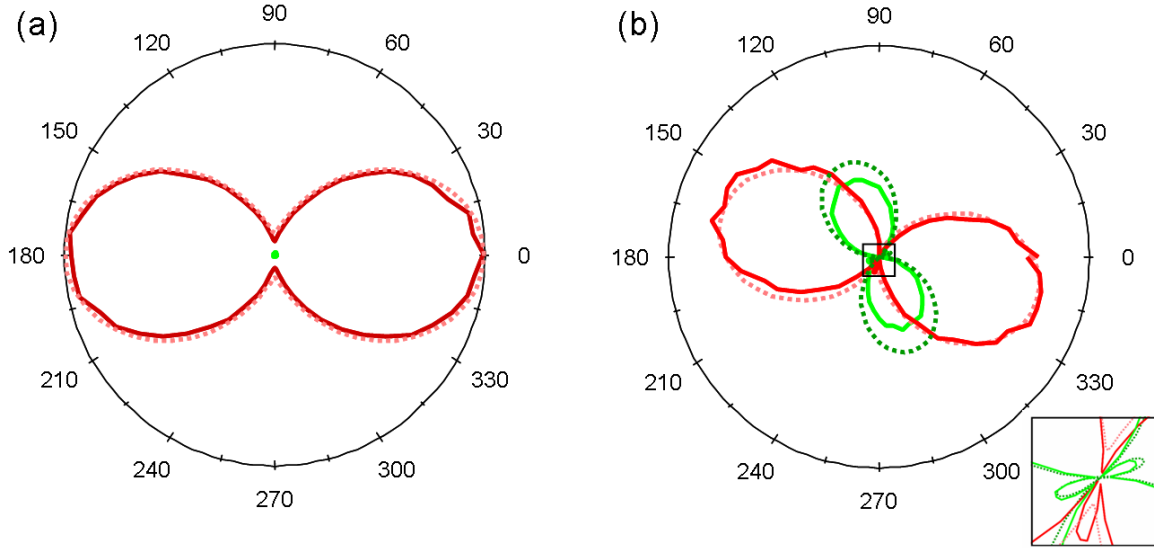


Figure 3.11: Polarization-resolved SRL responses  $\mathcal{I}_X$  (in red) and  $\mathcal{I}_Y$  (in green), for the  $A_{1g}$  vibrational mode of cyclohexane. Solid lines correspond to the experimental data and dotted lines represent the theoretical intensities. (a)  $\alpha_p = 0^\circ$  and  $\alpha_s$  rotates from  $0^\circ$  to  $360^\circ$ . (b)  $\alpha_p = 150^\circ$  and  $\alpha_s$  rotates from  $0^\circ$  to  $360^\circ$ . Inset: Zoom into small intensities: the lobes correspond to negative values of the SRL signal.

The results are shown in Fig. (3.11) for the  $A_{1g}$  mode and Fig. (3.12) for the  $E_g$  mode. In both figures, (a) corresponds to the case for which  $\alpha_p = 0^\circ$  and (b) depicts the polar plots obtained for the intermediate linear polarization  $\alpha_p$ . The curves are normalized so that the maximum of the total intensity ( $\mathcal{I}_X + \mathcal{I}_Y$ ) is equal to 1. As expected, when  $\alpha_p = 0^\circ$ , no SRL signal is detected in the  $Y$  direction, for both vibrational modes (the small intensities depicted in the polar plots correspond to the noise of the detector). Moreover, the shapes of the polarization-resolved intensities along  $X$  are good signatures of the Raman depolarization ratio. For a polarized band [Fig. (3.11)] we observe a two-lobe shape that is almost closed when  $\alpha_s = 90^\circ$ , which points out that  $\rho_{\text{SR}}$  is close to zero. For a depolarized band [Fig. (3.12)], the shape of the polar plot becomes more isotropic, indicating that  $\rho_{\text{SR}}$  is close to 0.75.

The values of depolarization ratios found are  $0.063 \pm 0.006$  for the  $A_{1g}$  mode and  $0.743 \pm 0.014$  for the  $E_g$  mode, which is in agreement with values found in the literature [64]. In Fig. (3.12b), we can observe that the experimental curve corresponding to the  $\mathcal{I}_X$  SRL intensity is tilted in relation to the theoretical one. This can be an effect of small

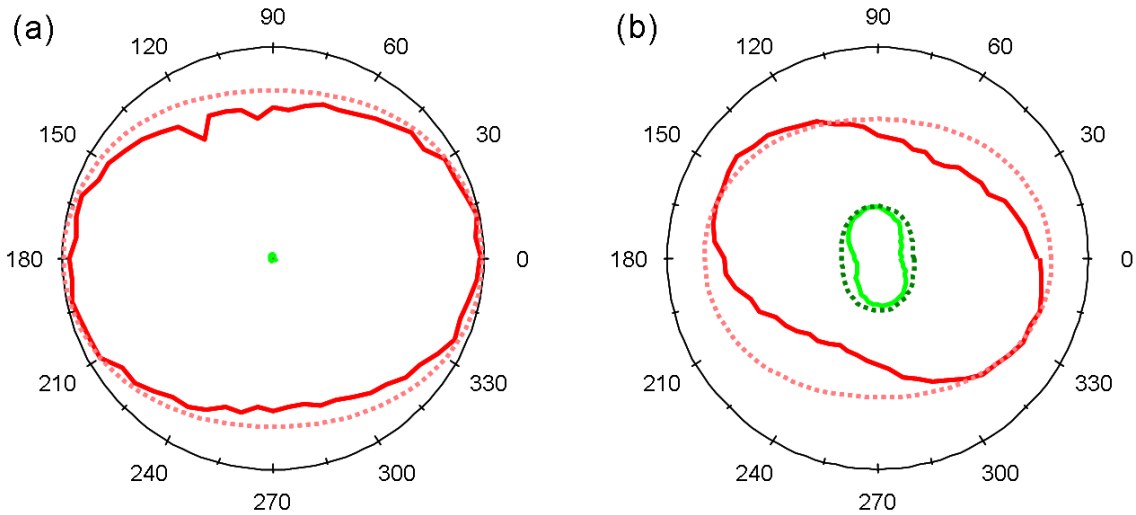


Figure 3.12: Polarization-resolved SRL responses  $\mathcal{I}_X$  (in red) and  $\mathcal{I}_Y$  (in green), for the  $E_g$  vibrational mode of cyclohexane. Solid lines correspond to the experimental data and dotted lines represent the theoretical intensities. (a)  $\alpha_p = 0^\circ$  and  $\alpha_s$  rotates from  $0^\circ$  to  $360^\circ$ . (b)  $\alpha_p = 30^\circ$  and  $\alpha_s$  rotates from  $0^\circ$  to  $360^\circ$ .

misalignments in the experimental setup. Our results seem to show however that these misalignments are negligible when the pump field is linearly polarized along  $X$  but they become crucial when the pump is polarized along an intermediate direction.

Finally, the inset in Fig. (3.11b) shows small lobes in the SRL intensities appearing when  $\alpha_s \approx 240^\circ$  for  $\mathcal{I}_X$  and  $\alpha_s \approx 30^\circ$  and  $150^\circ$ , for  $\mathcal{I}_Y$ . In fact, these lobes correspond to negative values of the SRL signal, which means that at these particular polarization configurations, the component  $X$  or  $Y$  of the pump field is not depleted but stimulated. Note however that the total intensity of the pump beam always decreases in a SRL process (the sum of the SRL signal along the  $X$  and  $Y$  axes is always positive). Moreover, these effect is only observed in polarized bands.

### 3.4 Conclusion

In this chapter, we have developed analytic models for the linear polarization CARS and SRS spectroscopies applied to isotropic media without electronic resonances. In the case of SRS we were particularly interested in the stimulated Raman loss effect, that accounts for the decrease of intensity of the pump field. These models give simple expressions for the perpendicularly polarized CARS and SRS intensities  $\mathcal{I}_X$  and  $\mathcal{I}_Y$  as a function of the incident pump and Stokes polarization angles. In the case of CARS, the access to the depolarization

ratios is less direct than in SRS, due to the presence, in the former, of the nonresonant response of the medium. We have shown that the influence of the depolarization ratio in the CARS signal, and thus of the resonant response, can be observed in the ratio of  $\mathcal{I}_X$  to  $\mathcal{I}_Y$ , although the general shape of these plots are dominated by the nonresonant response.

The CARS analytic model allowed us to calculate analytic expressions of the CARS signal at the spectral peak and dip. Two different methods were then proposed to determine the CARS spectroscopic parameters (depolarization ratio, ratio of the resonant to the nonresonant components  $a/\chi_{\text{NR}}$ , spectral position of the Raman band and its half width at half-maximum). The first method uses only one polarization configuration, where the Stokes beam is polarized parallel to the  $X$  axis and the pump polarization angle is fixed at  $45^\circ$  with respect to the same axis. The second method keeps the Stokes field polarized parallel to the  $X$  axis whereas the pump polarization angle rotates from  $0^\circ$  to  $360^\circ$ .

In the SRS analytic model, we can calculate the Raman depolarization ratio without any *a priori* spectral information, with the exception of the resonance frequency of the vibrational mode. When the pump field is polarized along  $X$ , the depolarization ratio is given simply by the ratio of the SRS intensities  $\mathcal{I}_X$  detected when the Stokes polarization is  $\alpha_s = 90^\circ$  and  $\alpha_s = 0^\circ$ . Another way of determining  $\rho_{\text{SR}}$  in the SRS model consists of fixing  $\alpha_s$  along  $X$  and  $\alpha_p$  at  $45^\circ$  and calculating the ratio of the SRS intensities  $\mathcal{I}_Y/\mathcal{I}_X$ . Satisfying results for the CARS and SRS analytic methods were found for toluene and cyclohexane solutions. Here, we have considered species with well separated spectral lines. In congested spectra, the methods developed here could be in principle applicable, not without some additional difficulties, particularly in the case of CARS, where it can be difficult to identify spectral peaks and dips.



---

---

## CHAPTER 4

---

# POLARIZATION RESOLVED CARS SIGNALS OF CRYSTALLINE MEDIA

In the previous chapter, we studied the polarization-resolved CARS and SRS responses in isotropic media. The main application of the study was to measure depolarization ratios of liquids, that characterize the symmetry of the addressed vibrational modes. Here, we extend some of the concepts developed in chapter 3 to crystalline media. We concentrate our analysis in the case of the CARS process.

In the case of ordered media with crystalline organization, the polarization-resolved CARS study is based on the *a priori* knowledge of the crystallographic point group of the crystal. According to chapter 1, this information allows to retrieve the structure of the susceptibility tensor of the medium. In nonisotropic samples, the polarimetric CARS study must be done in two steps. First, we analyze the nonresonant response of the medium, in order to determine the orientation of the crystal lattice in the macroscopic coordinate system and also the nonresonant tensor components in the microscopic frame. Here, we are not interested in finding the absolute values of these tensor elements but instead, we calculate relative values to one particular component, that act as generalized structural depolarization ratios. Second, we study the resonant responses of the medium to one particular vibrational mode, whose symmetry is also known *a priori*. As we showed in chapter 1, the tensor structure of a vibrational mode can be different from the one of the bulk, unless the addressed resonance is the totally symmetric mode. In the resonant case, we study departures from the Kleinman symmetry and we try to calculate the new microscopic elements of the susceptibility tensor .

In this chapter, we apply polarization-resolved CARS analysis to crystals with cubic symmetry. As these are centrosymmetric media, there is no nonlinear process of lower order that can occur in the sample. Moreover, these high order symmetry crystals are seen as isotropic in spontaneous Raman scattering. By consequence, CARS is the lowest order optical process capable of probing the susceptibility tensor structure of cubic systems. In

our approach, we use the polarization-resolved nonresonant CARS responses to quantify departure from isotropy and the resonant responses to characterize, or even quantify in the particular case of totally symmetric vibrations, deviations from the Kleinman symmetry. The work reported in this chapter is based on reference [103].

## 4.1 The third-order nonlinear susceptibility tensor for media with cubic symmetry

In nonisotropic samples, the CARS susceptibility tensor has a more complex structure than for isotropic media. First, the nonresonant CARS signal generated by the electronic response of the medium to the incident fields is not isotropic. Second, each resonance has its own symmetry specificity, which is characterized by a tensor whose structure can be different from the nonresonant one. The complexity of the susceptibility tensor is further increased at resonance, where Kleinman symmetry conditions do not apply [74]. In this section, we develop the expressions of the microscopic CARS susceptibility tensor for a medium with cubic symmetry, belonging to the  $O_h$  crystallographic point group. First, we describe the nonresonant tensor and then the resonant susceptibility for two different vibrational modes: the totally symmetric resonance  $A_{1g}$  and the degenerate mode  $E_g$ .

### 4.1.1 The microscopic nonresonant susceptibility tensor

Appendix A presents the structures of the third-order susceptibility tensors for all 32 crystallographic point groups. In particular, crystals with cubic symmetry have the same 21 nonvanishing components as an isotropic medium. In the specific case of crystals belonging to the  $O_h$  crystallographic point group, only four tensor elements are independent, which leads to the following  $\chi^{(3)}$  structure:

$$\chi_{xxxx}^{(3)} = \chi_{yyyy}^{(3)} = \chi_{zzzz}^{(3)} \quad (4.1a)$$

$$\chi_{xyxy}^{(3)} = \chi_{xzzz}^{(3)} = \chi_{yxyx}^{(3)} = \chi_{yzyz}^{(3)} = \chi_{zxzx}^{(3)} = \chi_{zyzy}^{(3)} \quad (4.1b)$$

$$\chi_{xxyy}^{(3)} = \chi_{xxzz}^{(3)} = \chi_{yyxx}^{(3)} = \chi_{yyzz}^{(3)} = \chi_{zzxx}^{(3)} = \chi_{zzyy}^{(3)} \quad (4.1c)$$

$$\chi_{xyyx}^{(3)} = \chi_{xzzx}^{(3)} = \chi_{yxxy}^{(3)} = \chi_{yzzx}^{(3)} = \chi_{zxzx}^{(3)} = \chi_{zyyz}^{(3)} \quad (4.1d)$$

where the frequency arguments are omitted in order to shorten the notation. Lowercase indexes  $x, y, z$  indicate that we are dealing with the microscopic susceptibility tensor in the crystal frame. In the nonresonant regime, Kleinman symmetry applies and the nonresonant  $\chi^{(3)\text{NR}}$  has only two independent components, following:

$$\begin{cases} \chi_{xxxx}^{(3)\text{NR}} = \chi_{yyyy}^{(3)\text{NR}} = \chi_{zzzz}^{(3)\text{NR}} \\ \chi_{xxyy}^{(3)\text{NR}} = \chi_{xzzz}^{(3)\text{NR}} = \chi_{yyzz}^{(3)\text{NR}} \end{cases} \quad (4.2)$$

with all index permutations allowed. The aim of our polarimetric study is not to calculate absolute values of tensor elements, but to determine some important ratios between components, that allow to characterize the symmetries of the medium or its resonances, as we did in the isotropic case. For this purpose, in analogy with an isotropic medium, we define a generalized nonresonant depolarization ratio,

$$\rho_{\text{NR}} = \frac{\chi_{xyyx}^{(3)\text{NR}}}{\chi_{xxxx}^{(3)\text{NR}}} \quad (4.3)$$

that characterizes completely the whole microscopic susceptibility tensor of a crystal that belongs to the  $O_h$  point group. From Eq. (3.3), this ratio is equal to 1/3 in the isotropic case. In a crystal with cubic symmetry,  $\rho_{\text{NR}}$  can have any arbitrary value and it quantifies the departure from isotropy. Note that this simplification is only possible in the case of the  $O_h$  point group and a more complex symmetry would involve more than one depolarization ratio.

#### 4.1.2 The microscopic resonant susceptibility tensor

In the vicinity of vibrational resonances, the CARS susceptibility tensor takes a more complex expression including the Lorentzian spectral resonant contribution, given by Eq. (3.10), leading to the following expression for  $\chi^{(3)}$ :

$$\chi^{(3)} = \chi_{xxxx}^{(3)\text{NR}} \left( \frac{\chi^{(3)\text{NR}}}{\chi_{xxxx}^{(3)\text{NR}}} + \frac{A}{(\delta\omega - \Omega_{\text{R}}) + i\Gamma} \frac{\chi^{(3)\text{R}}}{\chi_{xxxx}^{(3)\text{R}}} \right) \quad (4.4)$$

with  $\Omega_{\text{R}}$  the frequency of the addressed vibrational mode,  $A = \chi_{xxxx}^{(3)\text{R}}/\chi_{xxxx}^{(3)\text{NR}}$  the ratio of the strength of the resonant over the nonresonant contributions, and  $\Gamma$  the Raman line width (HWHM). We chose to normalize the whole tensor by the component  $\chi_{xxxx}^{(3)\text{NR}}$ , so the first term in brackets in Eq. 4.4 corresponds exactly to the nonresonant tensor in section 4.1.1. The tensor structure of the resonant contribution  $\chi^{(3)\text{R}}$ , which can differ from that of  $\chi^{(3)\text{NR}}$ , depends on the symmetry of the vibrational mode and is deduced from the analysis of the corresponding irreducible representation, as we showed in section 1.4. It is therefore expected that the CARS spectral behavior will considerably depend on the polarization settings for both pump and Stokes fields, especially for nontotally symmetric modes that exhibit different symmetry properties than the nonresonant background.

#### The totally symmetric vibrational mode

A totally symmetric vibrational mode,  $A_{1g}$ , exhibits a similar symmetry structure as the crystal point group. The only difference between the nonresonant and resonant cases is the antisymmetric nature of the tensor at resonance, due to the departure from Kleinman symmetry conditions which imposes  $\chi_{iijj}^{(3)\text{R}} \neq \chi_{ijij}^{(3)\text{R}} \neq \chi_{ijji}^{(3)\text{R}}$ , with  $i, j = (x, y, z)$  and  $i \neq j$ . Consequently, the resonant CARS tensor for a totally symmetric vibration has three

independent components that are, from Eq. (4.1) and taking into account the degeneracy with respect to the pump field,

$$\left\{ \begin{array}{l} \chi_{xxxx}^{(3)\text{R}}(-\omega_{as}; \omega_p, \omega_p, -\omega_s) \\ \chi_{xxyy}^{(3)\text{R}}(-\omega_{as}; \omega_p, \omega_p, -\omega_s) = \chi_{xyxy}^{(3)\text{R}}(-\omega_{as}; \omega_p, \omega_p, -\omega_s) \\ \chi_{xyyx}^{(3)\text{R}}(-\omega_{as}; \omega_p, \omega_p, -\omega_s). \end{array} \right. \quad (4.5)$$

Here we explicit the frequency arguments in order to show the degeneracy of the tensor with respect to the second and third indexes. All components obtained by interchanging the indexes  $x \rightarrow y \rightarrow z$  are equal. By analogy with the nonresonant case, for a totally symmetric vibrational resonance of a crystal belonging to the  $O_h$  point group, we can define two depolarization ratios, that characterize the whole resonant tensor:

$$\rho_{A_1}^{\text{R}} = \frac{\chi_{xyyx}^{(3)\text{R}}}{\chi_{xxxx}^{(3)\text{R}}} \text{ and } \rho_{A_2}^{\text{R}} = \frac{\chi_{xxyy}^{(3)\text{R}}}{\chi_{xxxx}^{(3)\text{R}}}. \quad (4.6)$$

When  $\rho_{A_1}^{\text{R}} = \rho_{A_2}^{\text{R}}$ , Kleinman symmetry is verified and the tensor is totally symmetric. When this is not the case, the ratio between the two depolarization ratios quantifies the departure from Kleinman symmetry at resonance.

### Nontotally symmetric resonance: the degenerate $E_g$ mode

In a crystal with cubic symmetry, the tensorial structure of the third-order susceptibility of a degenerate vibrational mode  $E_g$  is very different from the nonresonant or the totally symmetric resonant tensors, mainly because in the former, the  $z$  dependent components become nondegenerate. According to section 1.4, the tensor structure of a degenerate mode can be determined by the method of the projection operators. Here, we use the results tabulated in reference [77], where we can find the selection rules for linear up to third-order nonlinear Raman effects. According to this reference, the quaternary direct products transforming as the  $E_g$  irreducible representation of the  $O_h$  crystallographic point-group are:

$$\begin{aligned} & (x^4 - y^4, x^4 + y^4 - 2z^4) \\ & (y^2z^2 - z^2x^2, y^2z^2 + z^2x^2 - 2x^2y^2) \quad . \end{aligned}$$

From section 1.4.4, we know that the third order susceptibility tensor can be decomposed, in Cartesian coordinates, in a linear combination of the quaternary direct products, following:

$$\begin{aligned}
\chi_{E_g}^{(3)R} &= \alpha (x^4 - y^4) + \beta (x^4 + y^4 - 2z^4) + \gamma (y^2 z^2 - z^2 x^2) + \delta (y^2 z^2 + z^2 x^2 - 2x^2 y^2) \\
&= (\alpha + \beta)x^4 + (-\alpha + \beta)y^4 - 2\beta z^4 + (\gamma + \delta)y^2 z^2 + (-\gamma + \delta)z^2 x^2 - 2\delta x^2 y^2 \\
&= \chi_{xxxx}^{(3)R} x^4 + \chi_{yyyy}^{(3)R} y^4 + \chi_{zzzz}^{(3)R} z^4 + \chi_{y^2 z^2}^{(3)R} y^2 z^2 + \chi_{zzxx}^{(3)R} z^2 x^2 + \chi_{xxyy}^{(3)R} x^2 y^2
\end{aligned}$$

where the polynomials  $i^4$  and  $i^2 j^2$  are lightened notations for the fourth-order tensorial product of unit vectors,  $\hat{\mathbf{i}} \otimes \hat{\mathbf{i}} \otimes \hat{\mathbf{i}} \otimes \hat{\mathbf{i}}$  and  $\hat{\mathbf{i}} \otimes \hat{\mathbf{i}} \otimes \hat{\mathbf{j}} \otimes \hat{\mathbf{j}}$ , respectively. The resulting susceptibility tensor structure of an  $E_g$  vibrational mode is:

$$\begin{cases} \chi_{zzzz}^{(3)R} = - \left( \chi_{xxxx}^{(3)R} + \chi_{yyyy}^{(3)R} \right) & \text{with } \chi_{xxxx}^{(3)R} \neq \chi_{yyyy}^{(3)R} \\ \chi_{xxyy}^{(3)R} = - \left( \chi_{xxzz}^{(3)R} + \chi_{yyzz}^{(3)R} \right) & \text{with } \chi_{xxzz}^{(3)R} \neq \chi_{yyzz}^{(3)R}. \end{cases} \quad (4.7)$$

If we suppose that Kleinman symmetry applies, which is a crude approximation due to the resonant nature of the process but reduces considerably the number of independent tensor components, then we can define three depolarization ratios that characterize the whole structure of the susceptibility tensor, following:

$$\rho_{E1}^R = \frac{\chi_{yyyy}^{(3)R}}{\chi_{xxxx}^{(3)R}}, \quad \rho_{E2}^R = \frac{\chi_{yyzz}^{(3)R}}{\chi_{xxxx}^{(3)R}} \quad \text{and} \quad \rho_{E3}^R = \frac{\chi_{zzxx}^{(3)R}}{\chi_{xxxx}^{(3)R}}. \quad (4.8)$$

## 4.2 The theoretical anti-Stokes signal generated by cubic crystals

According to Eq.(1.1), the third-order nonlinear polarization induced in the sample results from the coupling of the linearly polarized incident fields pump and Stokes with the macroscopic susceptibility tensor of the medium  $\chi^{(3)}$ . The emitted anti-Stokes intensity is proportional to the induced polarization and is given by:

$$\begin{aligned}
\mathcal{I}_I(\omega_{as}, \alpha_p, \alpha_s) &\propto \\
&\left| \chi_{IJKL}^{(3)}(-\omega_{as}, \omega_p, \omega_p, -\omega_s) E_{pJ}(\omega_p, \alpha_p) E_{pK}(\omega_p, \alpha_p) E_{sL}^*(\omega_s, \alpha_s) \right|^2, \quad (4.9)
\end{aligned}$$

with  $I, J, K, L$  standing for the macroscopic axes  $X, Y,$  or  $Z$ . In section 4.1 we reported the microscopic nonresonant and resonant susceptibility tensors  $\chi^{(3)}$  in the crystal frame. In order to obtain the macroscopic susceptibility, in the frame where the incident polarizations are defined, it is necessary to apply the tensor transformation relation, given in Eq. (1.51), which we reproduce here for the case of a third-order nonlinear process:

$$\chi_{IJKL}^{(3)}(-\omega_{as}; \omega_p, \omega_p, -\omega_s) = \sum_{ijkl} a_{Ii} a_{Jj} a_{Kk} a_{Ll}(\Omega) \chi_{ijkl}^{(3)}(-\omega_{as}; \omega_p, \omega_p, -\omega_s). \quad (4.10)$$

The orientation of the crystal unit-cell in the 3D space is defined by the Euler angles  $\Omega = (\theta, \phi, \psi)$  and  $a_{Ii}$  are the rotation matrix components between the macroscopic and microscopic frames, given by Eq. (1.50). Contrary to the isotropic case, the CARS signal emitted by a crystal with cubic symmetry depends on the orientation of the crystal lattice. One feasible approach to retrieve the orientation of the crystal unit-cell would be to study the polarization responses of the nonresonant CARS signal. In this case the anti-Stokes intensity is not affected by any vibrational resonance and the microscopic susceptibility tensor is very simple, depending only on the depolarization ratio  $\rho_{NR}$ .

#### 4.2.1 Influence of the crystal orientation on the nonresonant anti-Stokes signal

The nonresonant CARS signal emitted by a medium with cubic symmetry depends on the 3D orientation of the crystal lattice, characterized by the Euler angles  $\Omega = (\theta, \phi, \psi)$  that were introduced on section 1.5, and on the nonresonant depolarization ratio  $\rho_{NR}$ , defined in Eq. (4.3). Figs. (4.1) and (4.2) show the influence of the crystal orientation on the theoretical nonresonant anti-Stokes intensities resolved in polarization, for  $\rho_{NR} = 0.75$ .

Fig. (4.1) shows the theoretical CARS intensities along the  $X$  and  $Y$  directions, as a function of the tuning incident polarization, in the three polarization configurations, P, S and PS, for different values of the Euler angle  $\phi$ . The curves are normalized so that the maximum of the total intensity  $\mathcal{I}_X + \mathcal{I}_Y$  is equal to 1. The polarimetric CARS responses in the three polarization configurations, P, S and PS are very sensitive to  $\phi$ , when  $\theta$  and  $\psi$  are  $0^\circ$ . The only exception is observed for the curves of  $\mathcal{I}_X$  in the S polarization scheme, for which the only effect of  $\phi$  is to tilt slightly the polar plots around the  $X$  axis, without modifying their two-lobe shapes. A prominent feature in the polar graphs is that the curves obtained for  $\phi$  modulo  $45^\circ$  are related to each other by a rotation of the polar plots in the  $XY$  plane. This is a result of the cubic symmetry of the medium but is only verified when  $\theta = 0^\circ$ . Another consequence of the cubic symmetry of the medium, is that the polarimetric responses are equivalent for  $\phi = 0^\circ$  and  $\phi = 90^\circ$ . This is observed because the main axis of symmetry is a four-fold axis. Finally, the theoretical curves presented in Fig. (4.1) were built for  $\psi = 0^\circ$  but the same results would have been found for  $\phi = 0^\circ$ . In fact, when the microscopic axis  $z$  is aligned with the macroscopic  $Z$  ( $\theta = 0^\circ$ ),  $\phi$  and  $\psi$  have equivalent roles. This means that the theoretical polar plots obtained for  $\phi = 0^\circ$ ,  $\psi = 30^\circ$  or  $\phi = 30^\circ$ ,  $\psi = 0^\circ$ , for instance, are the same. Moreover, the rotation  $\phi + \psi = 30^\circ$  is equivalent to  $\phi = 0^\circ$ ,  $\psi = 30^\circ$  or  $\phi = 30^\circ$ ,  $\psi = 0^\circ$ .

The same study can be done to verify the influence of  $\theta$  on the polarimetric CARS responses. The results are shown in Fig. (4.2), for the three polarization configurations, P, S and PS, with  $\phi = \psi = 0^\circ$ . Again, the anti-Stokes intensities resolved in polarization

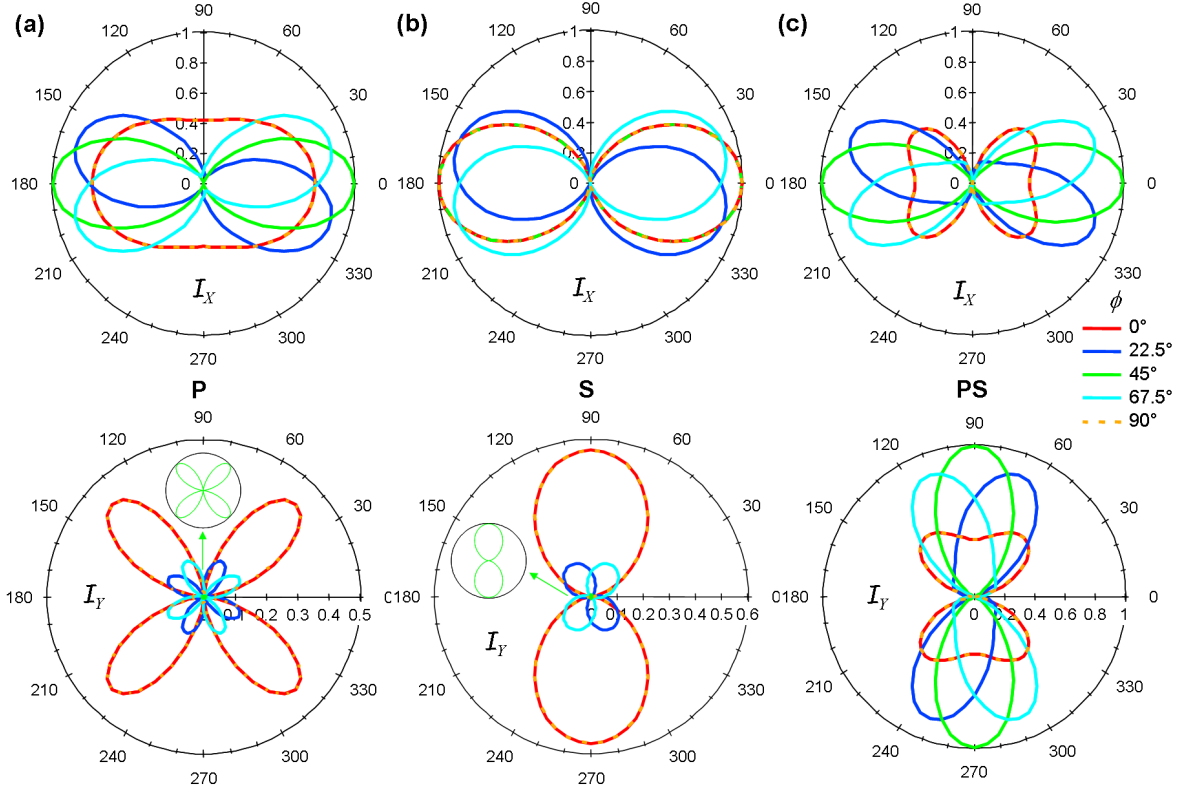


Figure 4.1: Theoretical nonresonant CARS intensities resolved in polarization, for a medium with cubic symmetry and depolarization ratio  $\rho_{\text{NR}} = 0.75$ . The Euler angles  $\theta$  and  $\psi$  are set to  $0^\circ$  and  $\phi$  varies from  $0^\circ$  to  $90^\circ$ . (a) P polarization configuration:  $\alpha_s = 0^\circ$  and  $\alpha_p$  rotates from  $0^\circ$  to  $360^\circ$ . (b) S polarization scheme:  $\alpha_p = 0^\circ$  and  $\alpha_s$  rotates. (c) PS polarization configuration: both incident polarizations rotate simultaneously. Polar plots on the top row depict the CARS intensities along the  $X$  axis  $\mathcal{I}_X$ , while the ones on the bottom show  $\mathcal{I}_Y$ . Insets show the curves enlarged for clarity. Curves are normalized so that the maximum of the total intensity ( $\mathcal{I}_X + \mathcal{I}_Y$ ) is equal to 1. Curves in the insets were enlarged for clarity.

are sensitive to  $\theta$ , with the only exception of  $\mathcal{I}_X$  in the S polarization scheme, where no dependence on  $\theta$  is observed. The curves obtained for  $\theta$  modulo  $45^\circ$  are equal to each other, which is a consequence of the cubic symmetry of the medium but only verified when  $\phi = \psi = 0^\circ$ .

The study developed in this section is valid for any depolarization ratio, except for  $\rho_{\text{NR}} = 1/3$ . In this case,  $\chi_{xxyy}^{(3)\text{NR}} + \chi_{xyxy}^{(3)\text{NR}} + \chi_{yyxx}^{(3)\text{NR}} = \chi_{xxxx}^{(3)\text{NR}}$ , according to Eq. (4.1), which is the characterization of an isotropic medium, as we showed in Eq. (3.3). By consequence, the polarization resolved nonresonant CARS responses of a cubic crystal for which  $\rho_{\text{NR}} = 1/3$ , do not depend on the orientation of the crystal lattice.

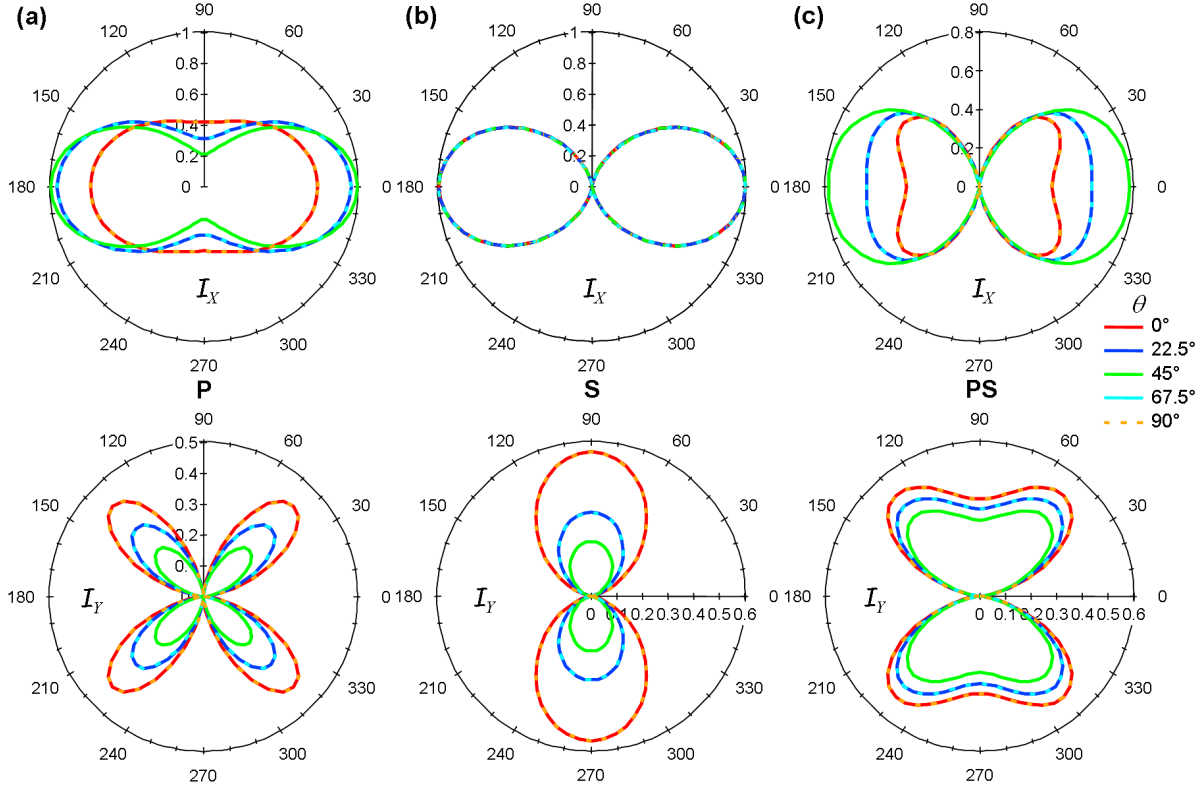


Figure 4.2: Theoretical nonresonant CARS intensities resolved in polarization, for a medium with cubic symmetry and depolarization ratio  $\rho_{\text{NR}} = 0.75$ . The Euler angles  $\phi$  and  $\psi$  are set to  $0^\circ$  and  $\theta$  varies from  $0^\circ$  to  $90^\circ$ . (a) P polarization configuration:  $\alpha_s = 0^\circ$  and  $\alpha_p$  rotates from  $0^\circ$  to  $360^\circ$ . (b) S polarization scheme:  $\alpha_p = 0^\circ$  and  $\alpha_s$  rotates. (c) PS polarization configuration: both incident polarizations rotate simultaneously. Polar plots on the top row depict the CARS intensities along the  $X$  axis  $\mathcal{I}_X$ , while the ones on the bottom show  $\mathcal{I}_Y$ . Curves are normalized so that the maximum of the total intensity ( $\mathcal{I}_X + \mathcal{I}_Y$ ) is equal to 1.

#### 4.2.2 Influence of the crystal orientation on the resonant anti-Stokes signal: theoretical study for a totally symmetric vibrational mode

We can extend the analysis done in the previous section to the resonant CARS signal. In particular, we are interested in the anti-Stokes field emitted when a totally symmetric vibrational mode is addressed. In this case, the resonant susceptibility tensor has the same structure as the nonresonant one, but it is completely characterized by two depolarization ratios, as we showed in Eq. (4.6). Fig. (4.3) shows how the orientation of the crystal lattice affects the polarization resolved CARS intensities. Here, we concentrate on the PS

polarization configuration, where we tune both incident polarizations simultaneously. The theoretical curves were built for  $\rho_{\text{NR}} = 0.38$ ,  $\rho_{\text{A1}}^{\text{R}} = 2.5$  and  $\rho_{\text{A12}}^{\text{R}} = 1.5$ .

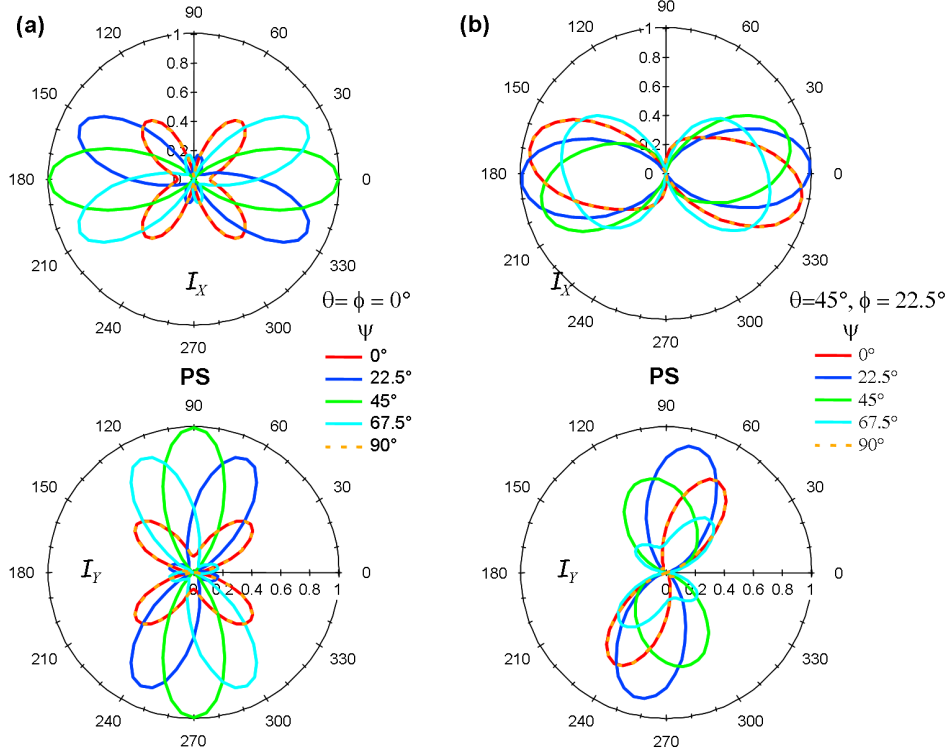


Figure 4.3: Theoretical resonant CARS intensities resolved in polarization, for the totally symmetric vibrational mode of a medium with cubic symmetry. Depolarization ratios:  $\rho_{\text{NR}} = 0.38$ ,  $\rho_{\text{A1}}^{\text{R}} = 2.5$  and  $\rho_{\text{A12}}^{\text{R}} = 1.5$ . The polar plots correspond to the PS polarization configuration. Different curves depict different values of  $\psi$  from  $0^\circ$  to  $90^\circ$ . The other Euler angles are set to:  $\theta = \phi = 0^\circ$  in (a) and  $\theta = 45^\circ$ ,  $\phi = 22.5^\circ$  in (b). Polar plots on the top row depict the CARS intensities along the X axis  $\mathcal{I}_X$ , while the ones on the bottom show  $\mathcal{I}_Y$ . Curves are normalized so that the maximum of the total intensity ( $\mathcal{I}_X + \mathcal{I}_Y$ ) is equal to 1.

Fig. (4.3a) displays very similar features to Fig. (4.1c) and the same analysis developed in the previous section for the nonresonant case is also valid for the totally symmetric resonance. Fig. (4.3b) shows that when  $\theta$  and  $\phi$  are different from  $0^\circ$ , the polar plots do not have any periodicity on  $45^\circ$  but the  $90^\circ$ - periodicity, that is intrinsic to a medium with cubic symmetry, is always observed, even at resonance.

When  $\rho_{\text{NR}} = 1/3$  and  $\rho_{\text{A1}}^{\text{R}} + 2\rho_{\text{A2}}^{\text{R}} = 1$  the susceptibility tensor has the same structure as for an isotropic medium and no influence of the crystal lattice orientation is expected to be observed.

At this level, it is interesting to compare, for a totally symmetric vibrational mode,

the polarization responses of the anti-Stokes signal emitted by the CARS process, which is a third-order nonlinear scattering, to the Stokes signal emitted by spontaneous Raman scattering, which is a linear optical process. As we showed in section 1.3.2, the linear susceptibility  $\chi^{(1)}$  of a medium with cubic symmetry has the same structure as an isotropic object: only three nonzero components equal to each other,  $\chi_{xx}^{(1)} = \chi_{yy}^{(1)} = \chi_{zz}^{(1)}$ . This tensor, which has the same structure at resonance when the vibrational mode is totally symmetric, is thus invariant under the transformation by the rotation matrix  $aIi$  given by Eq. (1.50), for any Euler angle  $\Omega$ . Therefore, the macroscopic linear susceptibility  $\chi_{IJ}^{(1)}$  of a crystal with cubic symmetry does not depend on the orientation of the crystal lattice in the macroscopic frame. Consequently, in spontaneous Raman scattering, if the incident field is linearly polarized, the intensity of the scattered Stokes field is:

$$\begin{aligned}\mathcal{I}_X^s &= (\chi_{xx}^{(1)})^2 \cos^2(\alpha_p) \mathcal{I}_{pX} \\ \mathcal{I}_Y^s &= (\chi_{xx}^{(1)})^2 \sin^2(\alpha_p) \mathcal{I}_{pY},\end{aligned}\tag{4.11}$$

where  $\alpha_p$  and  $\mathcal{I}_p$  are the polarization and intensity of the incident field, respectively. The total Raman intensity  $\mathcal{I}_X + \mathcal{I}_Y$  is hence constant for whatever  $\alpha_p$ , which proofs that spontaneous Raman scattering does not differentiate between cubic symmetry and isotropy. Note that this is only true for a totally symmetric resonance, whose susceptibility tensor structure is the same as the crystal point group. In the case of nontotally symmetric vibrational modes, the structure of the first-order resonant susceptibility can become different from the nonresonant tensor structure, making it possible to distinguish between isotropy and cubic symmetry through spontaneous Raman scattering.

Fig. (4.3) shows that in the case of the CARS process, contrary to spontaneous Raman scattering, the polarization resolved intensities emitted when a totally symmetric vibrational mode is addressed are highly sensitive to the orientation of the crystal lattice. It means that the CARS process allows to distinguish between an isotropic medium and an object with cubic symmetry. Therefore, nonlinear optical process are necessary to characterize high-order symmetries.

### 4.3 The sample: crystalline medium with cubic symmetry

The sample studied in this work is an octahydrosilasesquioxane (HT8)  $\text{H}_8\text{Si}_8\text{O}_{12}$  crystal, that has cubic symmetry and belongs to the  $O_h$  crystallographic point group [104]. The elementary molecular component is shown in Fig. (4.4a). The investigated crystals are of millimetric size and their in-plane orientation can be easily visualized from their rectangular shape using white light transmission imaging, as we show in Fig. (4.4b). From this image, we can deduce that the main axis of the crystal is oriented at  $49^\circ$  relative to the  $X$  axis and therefore,  $\phi = 49^\circ$ . Fig. (4.4c) shows a scheme of the 3D orientation of the crystal lattice in the macroscopic frame, with the definition of the respective Euler angles. As the

principal axis of the crystal  $z$  lays in the  $XY$  plane, the angle  $\theta$  is known and fixed to  $90^\circ$ . The remaining Euler angle  $\psi$  can not be deduced from direct macroscopic observation of the sample and is one of the parameters that we try to determine from the polarimetric CARS measurements.

Despite their cubic symmetry, these crystals are found to be birefringent. This behavior has already been reported for other cubic crystals [105]. It is important to notice that this anisotropy only affects the polarization of the incident or emitted light and does not have any influence on the susceptibility tensor structure of the medium. This birefringence can be characterized by the method that we proposed in section 2.3. However, in order to minimize these effects in our measurements, we chose to align the fast optical axis of the crystal to the macroscopic  $X$  axis. This is why we set  $\phi = 49^\circ$ . Furthermore, if we focus the incident beams on the bottom surface of the crystal [position  $Z = 0 \mu\text{m}$  in Fig. (2.13)], only the polarization of the emitted anti-Stokes field is distorted by birefringence. As the optical axis of the sample is aligned to the macroscopic coordinate system, Eq. (2.8) shows that the only consequence of the sample's birefringence is to introduce a phase shift between the  $X$  and  $Y$  components of the anti-Stokes field. As we detect the intensities of the CARS signal, this dephasing is not measured and by consequence, our results are not affected by birefringence.

In this work, we explore the polarized CARS responses of the HT8 crystal at three distinct spectral positions, that are pointed out in the Raman spectrum depicted in Fig. (4.4d). First, we study the nonresonant response at  $\approx 1380 \text{ cm}^{-1}$ ; second, the totally symmetric  $A_{1g}$  vibrational mode, corresponding to the Si-H stretching at  $2302 \text{ cm}^{-1}$ , and third, the degenerate  $E_g$  mode of the O-Si-H bending at  $932 \text{ cm}^{-1}$ . In order to address these different vibrational modes we set the pump wavelength at  $\lambda_p = 724.49 \text{ nm}$  and we tune the Stokes wavelength  $\lambda_s$ . The polarization measurements are performed following the three different polarization schemes described in section 2.1: P, when the pump polarization is tuned; S, when the Stokes polarization rotates and PS when both incident polarizations are rotated simultaneously.

## 4.4 The experimental CARS signal

### 4.4.1 The nonresonant CARS responses of a medium with cubic symmetry

The microscopic nonresonant susceptibility tensor of a medium with cubic symmetry is given by Eq. (4.2) and it depends only on the nonresonant depolarization ratio  $\rho_{\text{NR}}$ , defined in Eq. (4.3). The emitted anti-Stokes signal is given by Eq. (4.9) and it is a function of the macroscopic nonresonant CARS susceptibility, which can be obtained from the microscopic tensor, by a 3D rotation of the Euler angles  $\Omega = (\theta, \phi, \psi)$ . According to section 4.3, two Euler angles  $\phi$  and  $\theta$  are deduced by the macroscopic observation of the crystal. Consequently, only two unknowns are involved in the nonresonant experiment,  $\psi$  and  $\rho_{\text{NR}}$ , and they can be considered as free parameters in a data fitting method. The

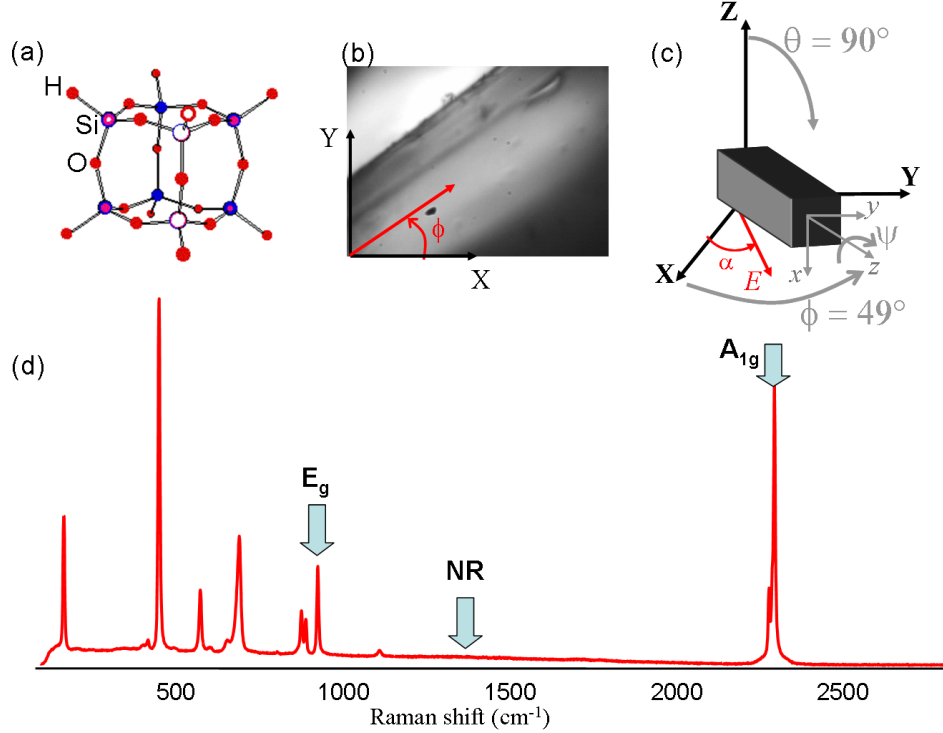


Figure 4.4: (a) Molecular structure of the H<sub>8</sub>Si<sub>8</sub>O<sub>12</sub> (HT8) crystal. (b) White light transmission image of a crystal in the microscope. (c) Orientation of the crystal in the laboratory frame, defining the three Euler angles ( $\theta, \phi, \psi$ ) ( $E(\alpha)$  is an incident field polarization direction in the  $(X, Y)$  sample plane). (d) Raman spectrum of the crystal. The arrows point the resonances studied in this work ( $A_{1g}$  mode at  $\Omega_R = 2302 \text{ cm}^{-1}$ ;  $E_g$  mode at  $\Omega_R = 932 \text{ cm}^{-1}$ ; NR: nonresonant signal at  $1380 \text{ cm}^{-1}$ ).

fitting procedure consists of finding, for all polarization tuning configurations P, S and PS simultaneously, the couple  $(\psi, \rho_{\text{NR}})$  that minimizes the mean square error for the CARS intensities in the  $X$  ( $\mathcal{I}_X$ ) and  $Y$  ( $\mathcal{I}_Y$ ) directions, normalized by the maximum of the total intensity,  $\mathcal{I}_X + \mathcal{I}_Y$ . According to this definition, the mean square error function is given by:

$$\begin{aligned}
 \chi^2(\psi, \rho_{\text{NR}}) = & \\
 & \frac{1}{N_\alpha} \sum_i \left\{ [\mathcal{I}_X^{th}(\psi, \rho_{\text{NR}}, \alpha_p^i) - \mathcal{I}_X^{exp}(\alpha_p^i)]^2 + [\mathcal{I}_Y^{th}(\psi, \rho_{\text{NR}}, \alpha_p^i) - \mathcal{I}_Y^{exp}(\alpha_p^i)]^2 \right. \\
 & + [\mathcal{I}_X^{th}(\psi, \rho_{\text{NR}}, \alpha_s^i) - \mathcal{I}_X^{exp}(\alpha_s^i)]^2 + [\mathcal{I}_Y^{th}(\psi, \rho_{\text{NR}}, \alpha_s^i) - \mathcal{I}_Y^{exp}(\alpha_s^i)]^2 \\
 & \left. + [\mathcal{I}_X^{th}(\psi, \rho_{\text{NR}}, \alpha_{p,s}^i) - \mathcal{I}_X^{exp}(\alpha_{p,s}^i)]^2 + [\mathcal{I}_Y^{th}(\psi, \rho_{\text{NR}}, \alpha_{p,s}^i) - \mathcal{I}_Y^{exp}(\alpha_{p,s}^i)]^2 \right\}, \quad (4.12)
 \end{aligned}$$

where the sum runs over the different incident polarization angles  $\alpha^i$ . The first two terms in the sum correspond to the P polarization configuration, where  $\alpha_p$  rotates and  $\alpha_s = 0^\circ$ , which is pointed out by the subscript  $p$ . The following two terms correspond to the S polarization scheme ( $\alpha_s$  is tuned and  $\alpha_p = 0^\circ$ ), which is noted by the subscript  $s$ . Finally, in the last two terms, the subscript  $p, s$  stands for the PS polarization configuration, where  $\alpha_p = \alpha_s$  rotate from  $0^\circ$  to  $360^\circ$ . The superscript “*th*” denotes the theoretical intensity, calculated from Eq. (4.9), while “*exp*” corresponds to the CARS intensity acquired experimentally. Finally, the error function is normalized by the number of the incident polarization angles over which the sum is done, here  $N_\alpha = 73$ . The experimental polarization resolved nonresonant CARS intensities in the three polarization configurations, together with the best fits, are shown in Fig. (4.5).

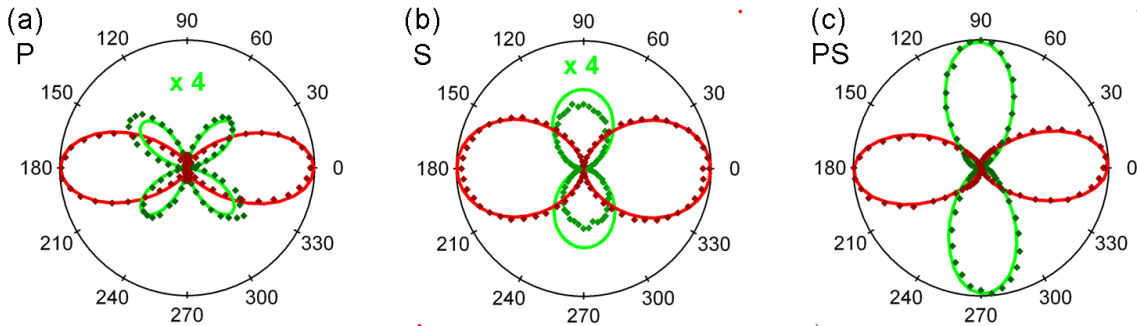


Figure 4.5: Polarization dependence of the nonresonant CARS signal ( $1380 \text{ cm}^{-1}$ ) analyzed along the  $X$  (red) or the  $Y$  (green) directions, depicted as a function of either  $\alpha_p$  and/or  $\alpha_s$ . Markers: experimental data; solid line: best fit according to Eq. (4.12). (a) P polarization configuration ( $\alpha_p$  rotates and  $\alpha_s = 0^\circ$ ); (b) S polarization scheme ( $\alpha_s$  rotates and  $\alpha_p = 0^\circ$ ) and (c) PS polarization configuration (both incident polarizations rotate simultaneously). Curves are normalized so that the maximum of the total intensity ( $\mathcal{I}_X + \mathcal{I}_Y$ ) is equal to 1.

Fig. (4.5) shows that the experimental results are in very good agreement with the crystal structure. In Fig. (4.6) we plot the cartography of the mean square error  $\chi^2$  for different values of the fitting parameters ( $\psi, \rho_{\text{NR}}$ ). We notice that the solution for the depolarization ratio is unique and corresponds to the value of  $\rho_{\text{NR}}$  where the mean square error  $\chi^2$  is minimum, which is  $\rho_{\text{NR}} = 0.38 \pm 0.05$ . However, the solution is not unique for the Euler angle  $\psi$ , for which a large range of possible values is observed in Fig. (4.6). This angle indetermination is most probably due to the present geometry which investigates a projection of a cubic object in the sample plane. Although the depolarization ratio expression resembles that from an isotropic medium, its value differs from the value measured in a pure water solution. If we apply the model developed in this chapter for a medium with cubic symmetry, to the experimental polarization resolved CARS responses of pure water, showed in Fig. (3.5), we obtain  $\rho_{\text{NR}} = 0.30 \pm 0.03$ , which is close to the

expected value of  $1/3$ , that was explained in chapter 3). This approach is thus able to quantify the deviation of the measured crystal symmetry from isotropy.

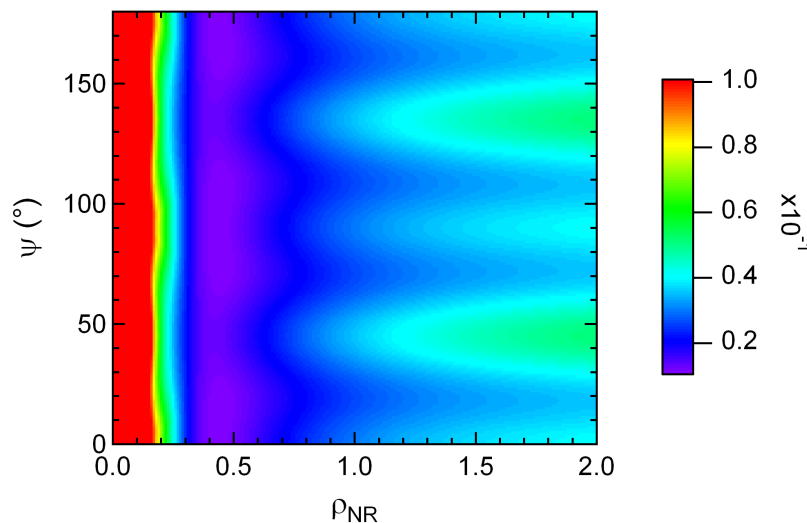


Figure 4.6:  $(\psi, \rho_{\text{NR}})$  cartography of the mean square error function defined in Eq. (4.12). The retained solution corresponds to the couple  $(\psi, \rho_{\text{NR}})$  that minimizes this function. There is no unique solution for the angle  $\psi$ , whereas a minimum is found for  $\rho_{\text{NR}} = 0.38 \pm 0.05$ .

#### 4.4.2 The resonant CARS responses of a totally symmetric vibrational mode

The resonant CARS polarization responses are first analyzed for the totally symmetric vibrational mode  $A_{1g}$ . These intensities are measured at the peak of the CARS spectrum, that is shown in Fig. (4.7), for different polarization configurations. These spectra do not present the wavelength dependence of a typical CARS spectrum, showed in Fig. (3.2), since no prominent dip is observed. This is due to the fact that the resonant signal dominates strongly the nonresonant contribution, because this is a very strong band, as can be seen in the spontaneous Raman spectrum of the HT8 crystal, in Fig. (4.4). In this case, the CARS and Raman spectra become very similar. The polarizations of the incident fields seem to play a major role on the peak intensities but no significant change is observed on the shapes of the bands, except for  $\alpha_p = \alpha_s = 0^\circ$  and  $\alpha_p = 90^\circ, \alpha_s = 0^\circ$ , in which cases the line widths become broader. This is probably due to the presence of a neighbor band at  $2296 \text{ cm}^{-1}$ , that corresponds to the degenerate  $T_{2g}$  vibrational mode [104], and has therefore a much more complex tensor structure than a totally symmetric vibration.

The experimental polarization resolved CARS intensities are depicted in Fig. (4.8a). These polar plots resemble slightly the nonresonant responses of Fig. (4.5). This is expected

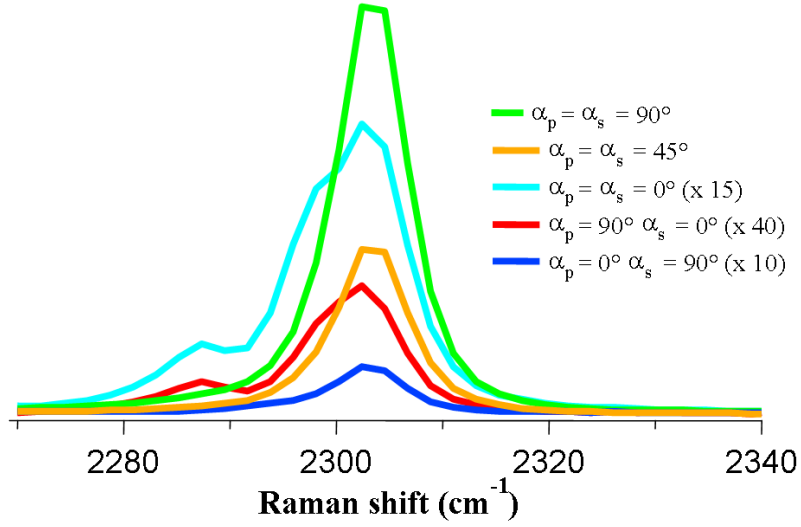


Figure 4.7: Experimental multiplex CARS spectra detected along the  $Y$  direction, around the totally symmetric vibrational mode  $A_{1g}$  of the HT8 crystal at  $2302 \text{ cm}^{-1}$ . Different spectra correspond to distinct polarization configurations. Curves in cyan, red and blue are enlarged for clarity.

since a totally symmetric vibrational mode  $A_{1g}$  exhibits a similar symmetry structure as the crystal point group [77]. The only difference between the nonresonant and totally symmetric resonant cases is the antisymmetric nature of the susceptibility tensor at resonance, due to the departure from Kleinman symmetry conditions, as we showed in Eq. (4.5). This property is visualized in the behavior of  $\mathcal{I}_Y(\alpha_s)$  that differs from the nonresonant response [Fig. (4.5b)].

Extending the approach developed in the previous section to this more complex resonant situation, the fit of the experimental data are performed according to Eq. (4.12), using the CARS intensities given in Eq. (4.9) with the microscopic susceptibility tensor described in Eq. (4.4). In the case of a totally symmetric vibration, three independent parameters are used in the fit: the depolarization ratios  $\rho_{A_1}^R$  and  $\rho_{A_2}^R$ , given in Eq. (4.6), and the Euler angle  $\psi$ , that remains undetermined from the nonresonant fit. The factor  $A$ , that measures the strength of the resonant over the nonresonant contributions is deduced from the CARS spectra showed in Fig. (4.7). For this measurement, we use the spectrum obtained at  $\alpha_p = \alpha_s = 45^\circ$ , in which case the incident polarizations are almost parallel to the in-plane orientation of the crystal ( $\phi = 49^\circ$  according to section 4.3). The vibrational band width  $\Gamma$  is measured in the spontaneous Raman spectrum of the HT8 crystal depicted in Fig. (4.4d).

The multiple-field polarization data fitting shows again that the  $\psi$  angle is not a crucial factor, with an angle range ( $\psi \leq 15^\circ$ ) providing acceptable solutions. A fit solution, depicted in Fig. (4.8b), shows a good agreement with the experimental data. The cartography of the mean square error between theory and experiment as a function of the two

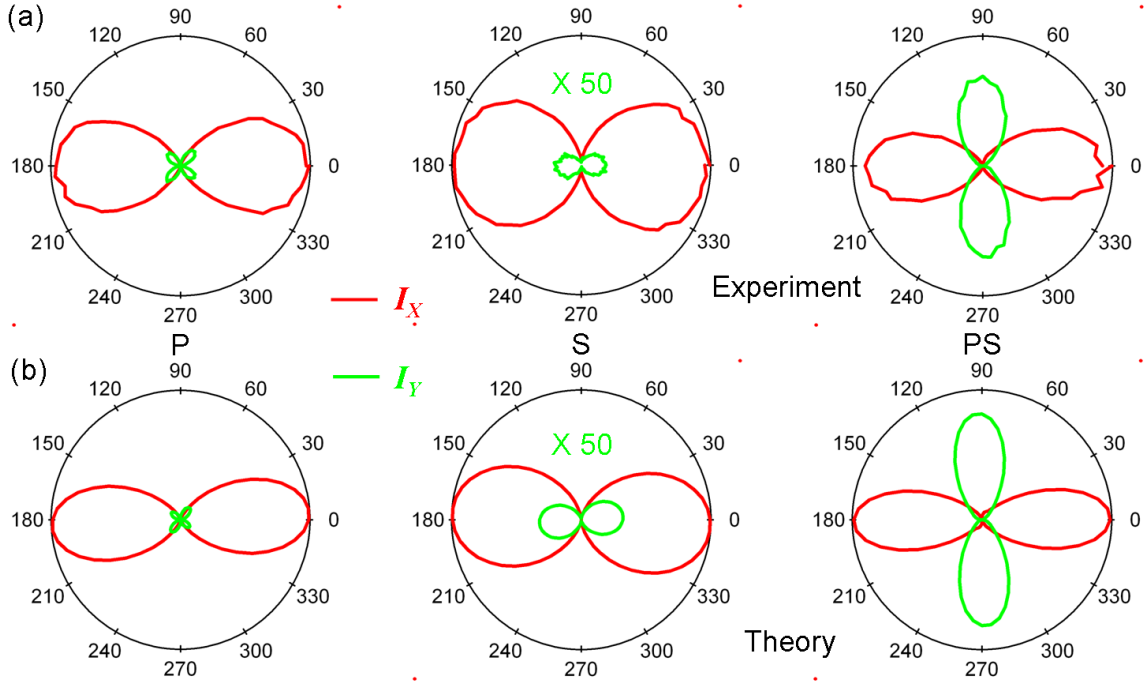


Figure 4.8: (a) Experimental polarization responses of the CARS signal analyzed along the  $X$  (red) and  $Y$  (green) directions of the  $A_{1g}$  vibrational mode at  $\Omega_R = 2302 \text{ cm}^{-1}$ . (b) Theoretical polar plots resulted from the fit, with fitting parameters  $\rho_{A_1}^R = 9.9$ ,  $\rho_{A_2}^R = 6.3$ ,  $\psi = 12^\circ$ . From left to right: P, S and PS polarization configurations. Curves are normalized so that the maximum of the total intensity ( $\mathcal{I}_X + \mathcal{I}_Y$ ) is equal to 1.

depolarization ratios  $\rho_{A_1}^R$  and  $\rho_{A_2}^R$  is shown in Fig. (4.9). The analysis of this map suggests a large range of reliable solutions, following a linear dependence of slope 0.53. This value is well below 1, which is the observed when Kleinman symmetry conditions apply, as in the nonresonant case. Consequently, this experiment, in addition to quantifying microscopic depolarization ratio relations for this vibrational band, provides also an estimation of Kleinman symmetry conditions departure at the specific wavelength of measurement.

Finally, we performed polarization resolved spontaneous Raman scattering measurements in the HT8 crystals. In these experiments, we rotate the incident polarization  $\alpha_p$  from  $0^\circ$  to  $180^\circ$  and we acquire the Raman spectra along the  $X$  and  $Y$  directions for each incident polarization. In the case of the  $A_{1g}$  mode, the intensities detected at the peak of the Raman band in function of  $\alpha_p$  are depicted in Fig. (4.10), together with the theoretical Raman intensities, calculated according to Eq. (4.11). In the theoretical curves, the incident field is corrected by the dichroism and ellipticity introduced by the experimental setup, following the procedure described in section 2.2.2. A good agreement is observed between the experiment and the theory, although the experimental curves are slightly tilted

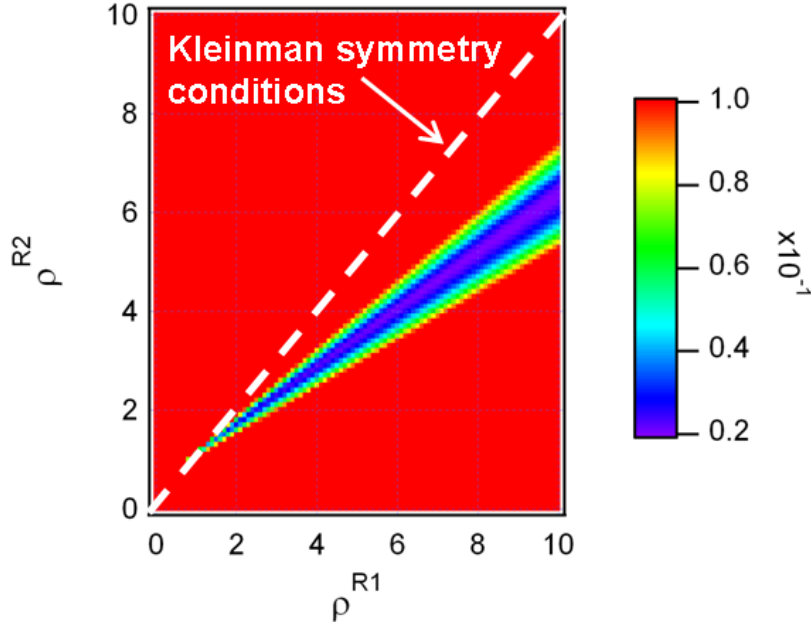


Figure 4.9:  $(\rho_{A1}^R, \rho_{A2}^R)$  cartography of the mean square error function defined in Eq. (4.12), for the totally symmetric vibrational mode at  $2302 \text{ cm}^{-1}$  of the HT8 crystal.

compared to the theoretical ones. This could be an effect of the birefringence of the sample, if its optical axis is not correctly aligned to the macroscopic frame, as we discussed in section 4.3. This is an experimental proof that spontaneous Raman spectroscopy can not differentiate cubic symmetry from isotropy. Therefore, nonlinear optical processes, such as CARS, are necessary to probe objects with high order symmetry.

#### 4.4.3 The resonant CARS responses of a nontotally symmetric vibrational mode

In this section, we investigate the degenerate vibrational mode  $E_g$ , at  $\Omega_R = 932 \text{ cm}^{-1}$ . The polarization responses at the peak of the CARS spectrum are shown in Fig. (4.11a) and they strongly differ from the nonresonant and totally symmetric vibration cases [Figs. (4.5) and (4.8), respectively]. In addition, the CARS spectrum itself is strongly dependent on the incident polarization settings, as we show in Fig. (4.12a), contrary to the  $A_{1g}$  vibrational mode. In the  $E_g$  resonance, the spectral positions of the peak and dip of the band as well as the intensity of the nonresonant contribution are very sensitive to the incident polarization arrangements. This is essentially due to the different tensorial structure of the  $E_g$  susceptibility in Eq. (4.7), as compared to the nonresonant CARS tensor in Eq. (4.2).

In order to include this spectral dimension in the CARS polarization data fit, we chose to fit principally the  $\mathcal{I}_X(\alpha_p)$  dependence, which is the most sensitive to wavelengths changes, at four spectral positions around the peak, depicted in Fig. (4.12a). All points are fitted

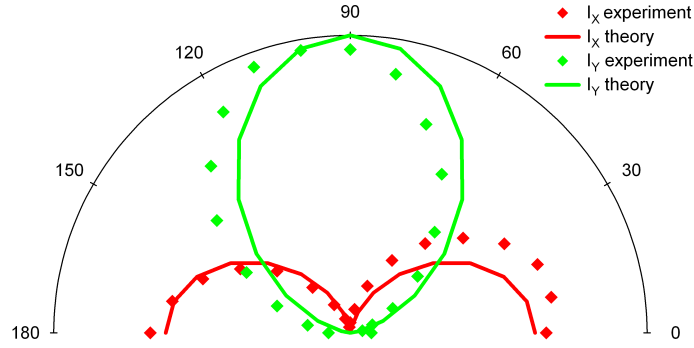


Figure 4.10: Polarization responses of the spontaneous Raman scattered intensities analyzed along the  $X$  (red) and  $Y$  (green) directions, for the  $A_{1g}$  vibrational mode at  $2302 \text{ cm}^{-1}$ . Light-color curves correspond to the experimental data, while dark-color curves depict the theoretical intensities. Curves are normalized so that the maximum of the total intensity ( $\mathcal{I}_X + \mathcal{I}_Y$ ) is equal to 1.

simultaneously, supposing in a first approximation that Kleinman symmetry conditions are valid. As mentioned previously, this crude assumption allows to reduce the number of free parameters in the fit. In this case, we chose  $\psi = 12^\circ$ , which is the same value used to build the theoretical polarimetric CARS responses of the totally symmetric vibrational mode, in Fig. (4.8b). The fitting parameters are therefore the three independent depolarization ratios defined in Eq. (4.8),  $\rho_{E1}^R$ ,  $\rho_{E2}^R$  and  $\rho_{E3}^R$ , and the mean square error function writes, following the same notation as in Eq. (4.12):

$$\begin{aligned}
 \chi^2(\rho_{E1}^R, \rho_{E2}^R, \rho_{E3}^R) = & \\
 & \frac{1}{N_\alpha} \sum_i \left\{ [\mathcal{I}_X^{th}(\rho_{E1}^R, \rho_{E2}^R, \rho_{E3}^R, \alpha_p^i, \delta\omega_A) - \mathcal{I}_X^{exp}(\alpha_p^i, \delta\omega_A)]^2 \right. \\
 & + [\mathcal{I}_X^{th}(\rho_{E1}^R, \rho_{E2}^R, \rho_{E3}^R, \alpha_p^i, \delta\omega_B) - \mathcal{I}_X^{exp}(\alpha_p^i, \delta\omega_B)]^2 \\
 & + [\mathcal{I}_X^{th}(\rho_{E1}^R, \rho_{E2}^R, \rho_{E3}^R, \alpha_p^i, \delta\omega_C) - \mathcal{I}_X^{exp}(\alpha_p^i, \delta\omega_C)]^2 \\
 & \left. + [\mathcal{I}_X^{th}(\rho_{E1}^R, \rho_{E2}^R, \rho_{E3}^R, \alpha_p^i, \delta\omega_D) - \mathcal{I}_X^{exp}(\alpha_p^i, \delta\omega_D)]^2 \right\}, \quad (4.13)
 \end{aligned}$$

where  $\delta\omega$  is the frequency shift  $\omega_p - \omega_s$  and the subscripts  $A$ ,  $B$ ,  $C$  and  $D$  correspond to the spectral positions depicted in Fig. (4.12). Each intensity  $\mathcal{I}_X$  is normalized by the maximum of the  $\mathcal{I}_X(\alpha_p)$  curve acquired at the peak of the CARS spectrum, in order to fit the shapes of the polar plots and also the relative intensities between the distinct spectral positions.

The best fit solutions obtained from Eq. (4.13), together with the experimental data, for the intensities along the  $X$  axis in the P polarization configuration at different spectral positions, are depicted in Fig. (4.12b). The theoretical curves show a good agreement

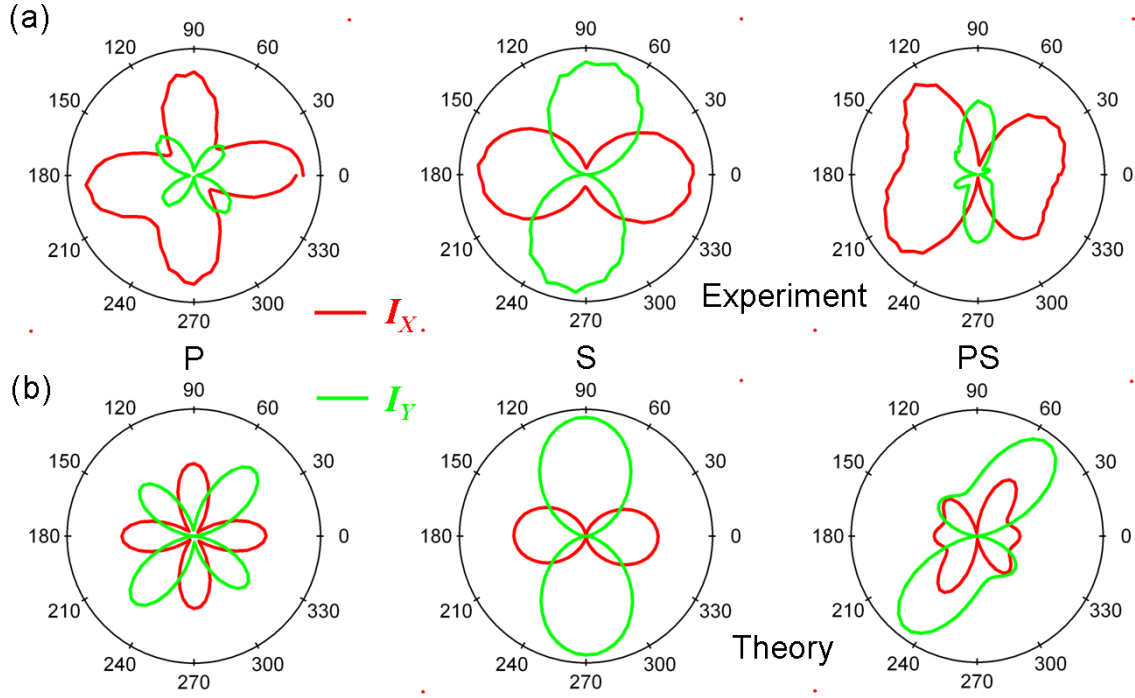


Figure 4.11: (a) Experimental polarization responses of the CARS signal at the peak of the CARS spectrum, analyzed along the  $X$  (red) and  $Y$  (green) directions, of the  $E_g$  vibrational mode ( $\Omega_R = 932 \text{ cm}^{-1}$ ). (b) Theoretical polar plots resulted from the fit. From left to right: P, S and PS polarization configurations. Curves are normalized so that the maximum of the total intensity ( $\mathcal{I}_X + \mathcal{I}_Y$ ) is equal to 1.

with the experimental data only in some spectral regions, in particular at the peak of the CARS spectrum where the other polarization tuning experiments (P, S and PS) also show a relatively good agreement with the model, as show in Fig. (4.11b). Between the peak and dip positions of the CARS spectrum [point  $C$  in Fig. (4.12)], no satisfactory solution can be found for any of the polarization tuning experiments, indicating essentially that Kleinman relations are not valid anymore. This is observed at the spectral region that corresponds to the maximum of the Raman vibrational band, that is shifted from the CARS peak, due to the presence of the nonresonant background in the CARS process (see section 3.1.3). By consequence, this spectral region is the most sensitive to resonance effects. The surrounding points  $A$  and  $D$  resemble typical nonresonant responses, although  $A$  is slightly perturbed by the appearance of another vibrational band in its vicinity, as can be seen in the CARS spectra in Fig. (4.12a). Overall, this analysis shows that the whole CARS spectral region around the  $E_g$  vibrational mode is strongly affected by its symmetry, characterized by the  $\chi^{(3)R}$  tensor structure in Eq. (4.7), with an additional

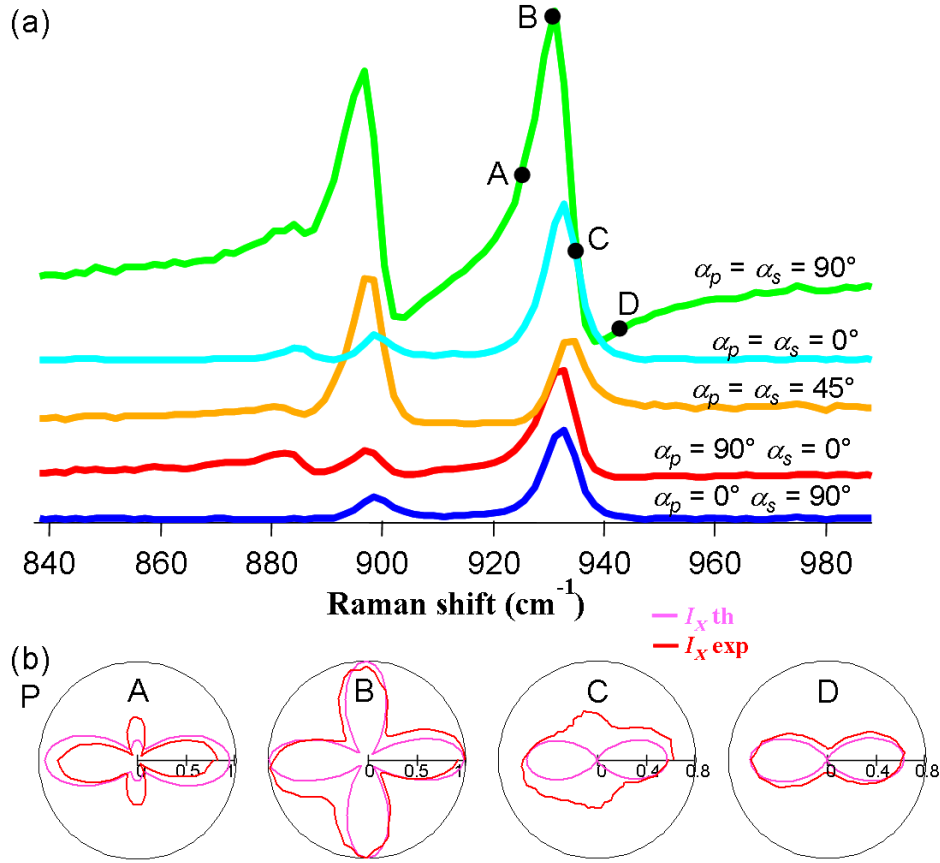


Figure 4.12: (a) Experimental multiplex CARS spectra detected along the  $Y$  direction, around the degenerate vibrational mode  $E_g$  of the HT8 crystal at  $932 \text{ cm}^{-1}$ , for different incident polarizations  $\alpha_p, \alpha_s$ . (b)  $\mathcal{I}_X(\alpha_p)$  CARS signal when tuning the pump polarization, at different spectral positions shown in the CARS spectrum: (A) before the CARS peak; (B), at the CARS peak; (C) around the minimum intensity of the CARS spectrum (dip); and (D) approaching the non-resonant signal. Red curves correspond to the experimental data and pink lines represent the best fit. In (b) the curves are normalized by the maximum of  $\mathcal{I}_X^B$ .

Kleinman deviation effect observed at the peak position of the spontaneous Raman band [point C, in Fig. (4.12)].

## 4.5 Conclusion

In this chapter, we have studied the polarization-resolved CARS signal of crystalline media with *a priori* known symmetry. In a first step, the analysis is done on the nonresonant CARS responses, which can provide information on the microscopic structure of the

nonresonant susceptibility tensor and also on the orientation of the crystal lattice in the macroscopic coordinate system. Depending on the crystal point group, the polarization-resolved nonresonant CARS signal allows to quantify the departure of the microscopic structure from isotropy. The second step consists of studying the resonant responses of the medium when a particular vibrational mode, with *a priori* known symmetry, is addressed. At resonance, the structure of the susceptibility tensor can be different from the nonresonant, unless the probed vibration is a totally symmetric mode. The analysis of the polarization-resolved CARS intensities can lead to the characterization of the microscopic tensor structure at resonance. Furthermore, it is possible to observe departure from Kleinman symmetry under resonant conditions, and even to quantify these deviations for certain vibrational modes.

The method developed in this chapter was applied to HT8 crystals, that have cubic symmetry and belong to the  $O_h$  crystallographic point group. In this case, the analysis of the nonresonant CARS signal allows to differentiate the crystal from an isotropic sample, which is not possible with lower-order optical processes, such as spontaneous Raman scattering. Two different resonances were also studied: a totally symmetric vibrational mode  $A_{1g}$  and a nontally symmetric degenerate vibration  $E_g$ . In the first, the polarization-resolved CARS analysis allowed to determine structural microscopic depolarization ratios, as well as to estimate Kleinman symmetry conditions departure at the peak of the CARS spectrum. In the  $E_g$  case, a spectral analysis together with the polarization measurements, showed that the CARS spectrum around the resonance is strongly affected by the structure of the microscopic resonant CARS tensor. Furthermore, evidence of Kleinman symmetry deviation is observed at the spectral position corresponding to the peak of the spontaneous Raman band.

The analysis developed in this chapter is restricted to media with cubic symmetry but it can be in principle extended to crystals belonging to any of the 32 crystallographic point groups. The only limitation in our method is that the used polarization configurations allow to probe up to 12 microscopic distinct tensor components. This is a consequence of the fact that three incident beams and one emitted field with linear polarizations projected along the  $X$  or  $Y$  axes can probe  $2^4 = 16$  distinct macroscopic tensor components. Since CARS is a degenerated optical process, with twice the pump field, the number of macroscopic tensor components that can be probed is reduced to  $2^4 - 2^2 = 12$ . Because the macroscopic and the microscopic elements of the susceptibility tensor are related through rotations of the Euler angles from one frame to another, the former are linear combinations of the latter. If the orientation of the crystal unit cell in the macroscopic frame is known, our method allows therefore to probe up to 12 microscopic tensor components. By consequence, crystals whose susceptibility tensor has more than 12 independent elements can not be totally characterized by this method. In the next chapter, we develop a method where no *a priori* information on the symmetry of the medium is necessary. This model is based on a statistical orientational distribution of the molecules and it allows to quantify molecular order and orientation, instead of individual microscopic tensor components.



---

---

## CHAPTER 5

---

# POLARIZATION RESOLVED CARS RESPONSES OF BIOMOLECULAR ASSEMBLIES

Type I collagen is a fibrillar collagen that is the most abundant in the body [12]. Changes in its fibrillar organization characterize different disease states and could be of great interest in early diagnostics. As fibrillar collagen is highly non-centrosymmetric, it generates a strong second harmonic generation (SHG) signal [9], whose polarization dependence provides information on fiber orientation and molecular organization. Previous works on polarization resolved SHG on collagen [45, 46, 14, 47, 48, 49, 50] have been able to retrieve individual microscopic second-order susceptibility tensor components, which can lead to the symmetry order of the molecular orientational distribution. The molecules probed in these cases are tightly packed amino-acids, responsible for the SHG response. A recent work has also shown the role of linking peptide bonds [106]. As SHG is a three wave-mixing process, it can probe up to the third order of symmetry of the molecular orientational distribution, as we showed in section 1.5.2. In addition, as most of the SHG investigations are nonresonant processes, only the odd-order symmetries can be addressed [107, 108]. The complementary even-order symmetries of the molecular orientational distribution can be probed by four wave mixing processes, such as CARS. Combining both methods could be a powerful way to retrieve the whole molecular angular distribution at microscopic scale (in a nonresonant regime, one would expect the same microscopic structures to be responsible for both SHG and CARS signals). A previous work on multimodal nonlinear optical imaging of collagen [109] has already shown qualitatively, that combining CARS and SHG provides complementary information on the submicrometric architecture of collagen arrays. However, in the cited work, no polarization measurements have been performed, which does not allow to extract any quantitative information.

In this chapter, we use polarization resolved nonresonant CARS to retrieve quantitative

information on molecular order and orientation in collagen fibers. As we are dealing with a nonresonant third-order nonlinear process, the correct denomination would be to say degenerate four-wave mixing process instead of CARS. However, in order to keep the consistency with the other chapters, we will use the term nonresonant CARS process, by malapropism. In the same way, we refer to the incident fields as the pump and Stokes beams, even if no vibrational resonance is addressed. In the first section, we use the model developed in section 1.5.2 to deduce the third-order nonresonant susceptibility tensor of collagen. Then, we present the experimental results and propose a fit procedure to quantify orientation and symmetry order of the molecular orientational distribution in collagen. Finally, we discuss how birefringence and the in-plane orientation of the fiber affect the expected results.

## 5.1 The nonresonant CARS susceptibility tensor of collagen

Biomolecular assemblies, such as collagen fibers, can be described as an assemblage of uniaxial molecules with a given statistical orientational distribution [12, 18, 84, 48, 50]. As we showed in section 1.5.2, this molecular angular distribution is defined by a normalized probability distribution function  $f(\Omega)$ , with  $\Omega = (\phi, \theta, \psi)$  the spherical angles characterizing the molecular orientation. As we are dealing with uniaxial molecules [Fig. (5.1)a], we can neglect the angle  $\psi$  in the calculations, which leads to  $\Omega = (\theta, \phi)$ . Moreover, the molecular hyperpolarizability has only one nonvanishing component in the molecular frame  $(u, v, w)$ , say  $\gamma_{www}^{(3)\text{NR}}$  (if it is oriented along the  $w$  axis). The molecular orientational distribution function is defined in the microscopic frame  $(x, y, z)$  by making its principal symmetry axis be parallel to the  $z$  axis. We can then assume that the main symmetry axis of the angular distribution is oriented along the direction of the collagen fiber, whose orientation in the macroscopic frame  $(X, Y, Z)$  is fixed and defined by the angles  $\Omega_0 = (\theta_0, \phi_0)$ , as we show in Fig. (5.1). Under these assumptions, the macroscopic nonresonant CARS susceptibility of the collagen fiber can be written from Eqs. (1.54) and (1.55), as:

$$\chi_{IJKL}^{(3)\text{NR}} = N \sum_{ijkl} [a_{Ii} a_{Jj} a_{Kk} a_{Ll}] (\Omega_0) \int \gamma_{www}^{(3)\text{NR}} [a_{iw} a_{jw} a_{kw} a_{lw}] (\Omega) f(\Omega) d\Omega. \quad (5.1)$$

where  $N$  is the number of molecules by unit volume and  $a_{ij}$  are the elements of the rotation matrix defining the Euler angles (with  $\psi = 0$ ), depicted in Eq. (1.50). The transformation from the molecular frame  $(u, v, w)$  to the microscopic frame  $(x, y, z)$  implies only the matrix elements in the third row of the transformation matrix (1.50).

We assume that the molecular orientational distribution function of the collagen fiber has cylindrical symmetry and by consequence, does not depend on  $\phi$ . This means that  $f(\theta)$  can be expanded in a series of the Legendre polynomials, according to:

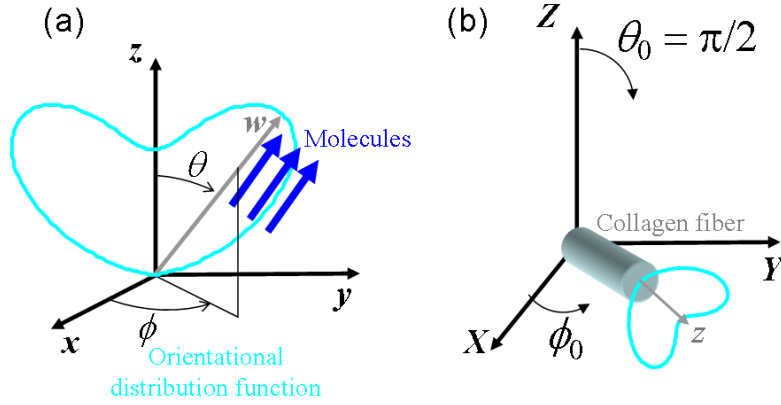


Figure 5.1: Definition of the molecular, microscopic and macroscopic frames. In (a) we identify the angles  $(\theta, \phi)$  that characterize the orientation of the molecular  $w$  axis in the microscopic  $(x, y, z)$  frame. We assume that the molecules are one-dimensional and oriented along the  $w$  axis. In (b) we show the orientation of the collagen fiber in the macroscopic frame  $(X, Y, Z)$ , defined by the Euler angles  $(\phi_0, \theta_0)$ .

$$f(\theta) = \sum_J f_J P_J(\cos \theta) \quad (5.2)$$

where  $P_J(\cos \theta)$  is a  $J$ -order polynomial on  $\cos \theta$ , with  $J \in \mathbb{N}$  accounting for the order of symmetry of the orientational distribution function. The coefficients  $f_J$  correspond to the weights of the function  $P_J$  in the decomposition and they are called order parameters [85]. They are equivalent to the coefficients  $f_m^J$  of the spherical harmonics expansion in Eq. (1.58) (see section 1.5.2). The Legendre polynomials are defined by [85]:

$$P_J(\cos \theta) = \frac{1}{2^J J!} \frac{d^J}{d(\cos \theta)^J} (\cos^2 \theta - 1)^J, \quad (5.3)$$

where  $\frac{d^J}{d(\cos \theta)^J}$  is the  $J^{\text{th}}$  derivative with respect to  $\cos \theta$ .

The first Legendre polynomials, until the fourth order ( $J = 4$ ) are:

$$P_0(\cos \theta) = 1 \quad (5.4a)$$

$$P_1(\cos \theta) = \cos \theta \quad (5.4b)$$

$$P_2(\cos \theta) = \frac{1}{2}(3 \cos^2 \theta - 1) \quad (5.4c)$$

$$P_3(\cos \theta) = \frac{1}{2}(5 \cos^3 \theta - 3 \cos \theta) \quad (5.4d)$$

$$P_4(\cos \theta) = \frac{1}{8}(35 \cos^4 \theta - 30 \cos^2 \theta + 3), \quad (5.4e)$$

with their graphical representations depicted in Fig. (5.2), which shows that the higher the order of the polynomials, the narrower they become in relation to  $\theta$ . An orientational distribution function that has only the zero-order term of the decomposition, does not depend on  $\theta$  and is therefore isotropic. In the other hand, the degree of order increases with the contribution of the higher-order terms of the Legendre polynomials in the distribution function decomposition.

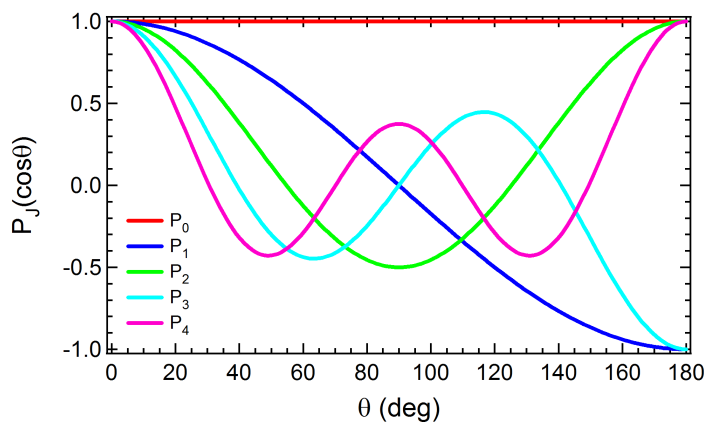


Figure 5.2: Graphical representation of the first Legendre polynomials  $P_J(\cos \theta)$  until the fourth order ( $J = 4$ ).

As the Legendre polynomials form a complete set of orthonormal functions, they verify the orthogonality property, as follows:

$$\int_0^\pi P_J(\cos \theta) P_K(\cos \theta) \sin(\theta) d\theta = \frac{2\delta_{JK}}{2J+1}, \quad (5.5)$$

where  $\delta_{JK}$  is the Kronecker delta, which is 1 when  $J = K$  and 0 otherwise.

In the case of nonresonant CARS process, we are dealing with a third-order nonlinear process, and by consequence, a fourth rank susceptibility tensor. According to section

1.5.2 it is thus possible to probe until the fourth order of symmetry of the orientational distribution function, corresponding to  $J = 4$ . Furthermore, only the even components of the decomposed distribution function can be read-out, in a nonresonant CARS process (section 1.5.2). Therefore, nonresonant CARS responses can provide complementary information in relation to three wave mixing processes, such as second harmonic generation. In the case of SHG, only the odd components of the orientational distribution function can be read, up to the third order of symmetry.

Finally, by replacing the even order Legendre polynomials into Eq. (5.1), the macroscopic nonresonant CARS susceptibility tensor writes:

$$\begin{aligned} \chi_{IJKL}^{(3)\text{NR}} &= N \sum_{ijkl} [a_{Ii} a_{Jj} a_{Kk} a_{Ll}] (\Omega_0) \int [a_{iw} a_{jw} a_{kw} a_{lw}] (\theta, \phi) \\ &\times [1 + f_2(3 \cos^2 \theta - 1) + f_4(35 \cos^4 \theta - 30 \cos^2 \theta + 3)] \sin \theta d\theta d\phi \quad (5.6) \end{aligned}$$

where  $f_2$  and  $f_4$  are the second and fourth order parameters, respectively. These coefficients are normalized by the weight  $f_0$  of the zeroth-order symmetry (isotropic distribution).  $f_2$  and  $f_4$  can assume any value under the condition that the distribution function  $f(\theta)$  is always positive and normalized. The macroscopic susceptibility tensor is normalized by  $\gamma_{www}$ .

### 5.1.1 The molecular orientational distribution function

The decomposition of the molecular orientational distribution function in a series of the Legendre polynomials corresponds to a multipolar expansion [107], for an one-dimensional structure with cylindric symmetry. The zeroth-order term  $J = 0$  is the monopole and corresponds to an isotropic distribution. When the coefficient  $f_2$  is zero, then the distribution is purely hexadecapolar, with fourth-order symmetry. In the same way, when  $f_4$  is zero, then the distribution is purely quadrupolar, with second-order symmetry ( $J = 2$ ). Fig. (5.3) shows the theoretical molecular angular distribution function  $f(\theta)$  projected into the plane  $xz$  as a function of  $\theta$ . In Fig. (5.3a), at least one of the two coefficients  $f_2$  or  $f_4$  is set equal to zero, whereas in (b) both coefficients are nonvanishing and can have either positive or negative values. Note that we do not plot the whole distribution function, but only its even terms, until the fourth-order.

When both coefficients  $f_2$  and  $f_4$  vanish the distribution is isotropic and no direction is privileged, as expected from the zeroth-order term of the multipolar expansion. When  $f_4 = 0$ , the distribution function has a two-lobe shape, that can be either along the  $z$  axis or in the plane perpendicular to it ( $xy$  plane), if the nonvanishing coefficient  $f_2$  is either positive or negative, respectively. In the other hand, when  $f_2 = 0$  the angular distribution function has a four-lobe shape, that characterizes the higher multipolar order. In this case also, the behavior of the function  $f(\theta)$  changes with the sign of the nonvanishing coefficient  $f_4$ . If  $f_4 > 0$  then the lobes are parallel to the axes  $x$  and  $z$ , whereas if  $f_4 < 0$ , the lobes are tilted in respect to these axes. When both coefficients are nonvanishing, the four-lobe

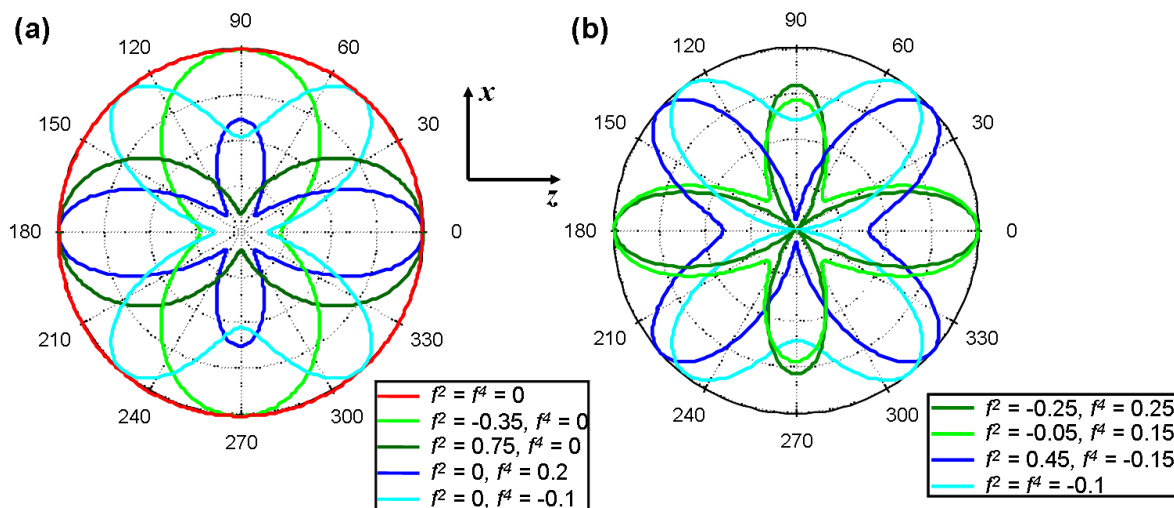


Figure 5.3: Molecular angular distribution function  $f(\theta)$  projected into the  $xz$  plane. (a) At least one of the two coefficients  $f_2$  or  $f_4$  vanishes. Green curves correspond to  $f_4 = 0$  whereas blue curves depict  $f_2 = 0$ . The red curve represents the isotropic distribution, for which  $f_2 = f_4 = 0$ . (b) Both coefficients  $f_2$  and  $f_4$  are nonvanishing.

pattern is always observed, as we show in Fig. (5.3b). Here, the orientation of the lobes follows the same behavior with the sign of  $f_4$  as in the case where  $f_2 = 0$ .

## 5.2 Experimental nonresonant CARS responses of collagen

### 5.2.1 Sample preparation

In this work we use collagen type I fibers, of about  $100 \mu\text{m}$  thick, extracted from rat tail and prepared in the group of Peter Winlove (University of Exeter, UK). To prepare the fibers, Adult Sprague Dawley rats were euthanased for purposes unconnected with the present research. Tails were removed and immediately snap frozen in liquid nitrogen cooled isopentane. At the time of use, the tissue was thawed and the tendon exposed. Individual fibers were teased out by microdissection and either examined immediately or stored frozen until required. Control Raman spectra were identical in either case, contained none of the peaks characteristic of proteoglycans, and were indistinguishable from those obtained from fibers purified by enzymatic extraction.

The sample is sandwiched between two glass coverslips glued together by a thickener double sided tape at the edge. This procedure prevents motion of the fibers during the measurements. The volume between the two coverslips is filled in with pure water. Record-

ing the nonresonant CARS signal emitted by the water allows to perform all the fine optical settings and alignments of the setup.

### 5.2.2 Experimental Protocol

The experimental protocol consists of the following steps: we first set both incident polarizations parallel to each other (either  $\alpha_p = \alpha_s = 0^\circ$  or  $\alpha_p = \alpha_s = 90^\circ$ ). Then, we acquire two Fwd-CARS images of the collagen fiber simultaneously, one along the  $X$  axis and the other along the  $Y$  axis. The images have  $40 \times 40 \mu\text{m}^2$  ( $101 \times 101$  pixels) and the pixel dwell time is 20 ms. The average powers of the pump and Stokes beams are 2 mW. In the first step, the focal plane is fixed at the bottom surface of the sample ( $Z = 0$ , according to Fig. (5.4a)). In this case, only the emitted anti-Stokes signal is affected by the fiber's birefringence. The next step consists of choosing different  $(X, Y)$  positions of the acquired image in order to perform the polarization resolved nonresonant CARS measurements, described earlier in section 2.1. Here, we focus on two polarization configurations out of the three depicted in section 2.1: either the P scheme (pump polarization is tuned while the Stokes polarization is fixed along the  $X$  axis) or the PS configuration (both incident polarizations are tuned simultaneously). These configurations are chosen for their high sensitivity to the sample symmetry and orientation. For each chosen point, we also record the polarization response of the input laser at frequency  $\omega_p$ , in order to characterize the local birefringence, which is nevertheless averaged over the whole thickness of the sample, as we discussed in section 2.3. We repeat the same procedure for another  $Z$  position of the sample [see Fig. (5.4b)], by focusing the incident beams deeper into the collagen fiber, at a distance  $Z = d$  from the bottom surface. In this case, both the incident pump and Stokes and emitted anti-Stokes beams are affected by birefringence. We are careful enough to perform the polarization measurements at the same in-plane  $(X, Y)$  positions at this different depth. As we are dealing with pure nonresonant CARS signals, the pump and Stokes wavelengths are set to  $\lambda_p = 724.49$  nm and  $\lambda_s = 856.99$  nm, respectively. The corresponding frequency shift is  $\delta\omega = \omega_p - \omega_s = 2134$   $\text{cm}^{-1}$ , which is far from any Raman active vibrational mode in the collagen spectrum.

### 5.2.3 Characterizing the orientation and symmetry order of the surface of the collagen fiber ( $Z = 0 \mu\text{m}$ )

The Fwd-CARS images of the collagen fibers, acquired at  $Z = 0 \mu\text{m}$ , are shown in Fig. (5.5). The three images correspond to different pieces of the fiber, away from each other more than a few millimeters. Direct observation of the images in Fig. (5.5), already shows that the orientation of the fiber is not the same for all three pieces. Here, we show the total nonresonant CARS intensity, obtained by the sum of the two images acquired along the  $X$  and  $Y$  axes simultaneously. Each image is normalized so that the maximum intensity is equal to 1. The three points depicted represent the  $(X, Y)$  spots chosen to make the polarimetric measurements.

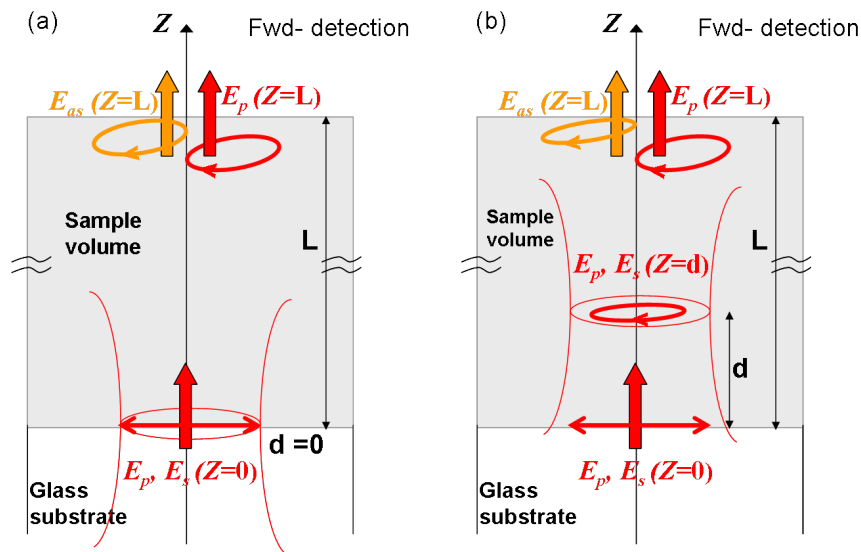


Figure 5.4: Fwd-detection scheme. The incident beams are linearly polarized and propagate along the  $Z$  axis. In (a) the pump and Stokes fields are focused at  $Z = 0$ , corresponding to the bottom surface of the sample. In this case, the polarization of the anti-Stokes signal emitted in the forward direction becomes elliptical after it crosses the whole thickness  $L$  of the sample. The birefringence of the collagen fiber can be estimated by measuring the ellipticity of the transmitted pump field. In (b) the incident fields are focused at a distance  $Z = d$  from the surface of the sample. In this case, they are elliptical at the excitation point. The anti-Stokes signal is emitted in the forward direction and it travels a distance  $Z = L - d$  in the sample.

The polarization responses of the nonresonant CARS signal allow to characterize the symmetry order of the molecular assemblies in the collagen fiber, as well as the mean orientation of the molecular distribution in the fiber, in respect to the macroscopic coordinate system (the laboratory frame). This can be done by fitting the theoretical model described in section 5.1 to the experimental data. The fit parameters are: (1) the order parameters  $f_2$  and  $f_4$ , corresponding to the weights of the terms of the probability distribution function expansion and (2) the angle  $\phi_0$ , characterizing the orientation of the molecular distribution in the  $XY$  plane. The other Euler angle  $\theta_0$ , that defines completely the orientation of the molecular distribution in the  $(X, Y, Z)$  coordinate system, is set to  $90^\circ$ , because the collagen fiber lies in the plane  $XY$ .

The fitting procedure consists of finding, for the two polarization configurations P and PS simultaneously, the set  $(f_2, f_4, \phi_0)$  that minimizes the mean square error function for the nonresonant CARS intensities in the  $X$  and  $Y$  directions, each one normalized by the maximum of the total intensity,  $\mathcal{I}_X + \mathcal{I}_Y$ . With such definitions, the mean square error function is given as following:

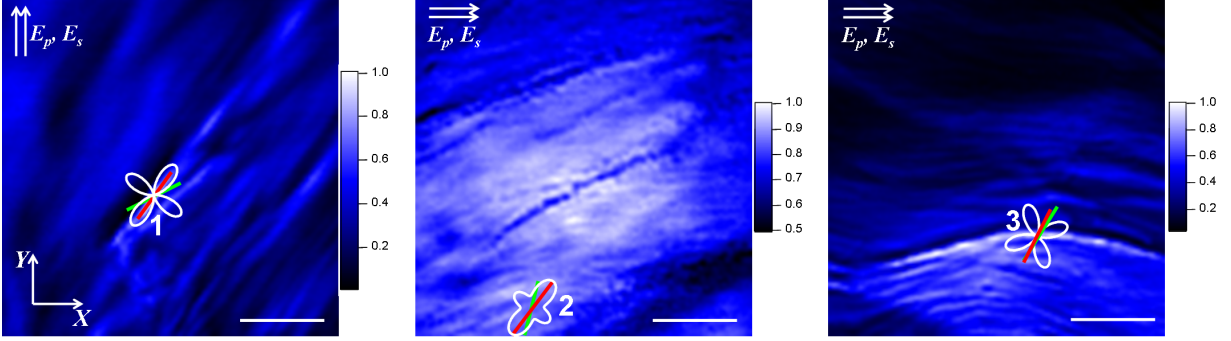


Figure 5.5: Fwd-nonresonant CARS images of collagen fibers, at different in-plane positions in the sample. The images show the total CARS intensity ( $\mathcal{I} = \mathcal{I}_X + \mathcal{I}_Y$ ) at  $Z = 0 \mu\text{m}$ . In the left, incident polarizations are set parallel to the  $Y$  axis, while in the other two images, input polarizations are along the  $X$  axis. Points 1, 2 and 3 correspond to the spots where the polarizations measurements take place. Red lines correspond to the orientation of the principal symmetry axis of the orientational distribution function in the  $XY$  plane,  $\phi_0$ , given by the best fit of the polarization resolved CARS intensities. The white curves show a section of the orientational distribution function, truncated to its orders 0, 2 and 4 and oriented in the macroscopic sample plane  $XY$ . Green lines represent the orientation of the fast optical axis of the fiber,  $\Theta_b$ , obtained by the fit of the intensity of the incident field  $\mathbf{E}(\alpha_p, \omega_p)$ . Scale bar:  $10 \mu\text{m}$ ; average powers: 2 mW; integration time: 20 ms; number of pixels:  $101 \times 101$ .

$$\begin{aligned}
 \chi^2(f_2, f_4, \phi_0) &= \frac{1}{N_\alpha} \sum_i \left\{ [\mathcal{I}_X^{th}(\alpha_p^i, f_2, f_4, \phi_0) - \mathcal{I}_X^{exp}(\alpha_p^i)]^2 \right. \\
 &+ [\mathcal{I}_Y^{th}(\alpha_p^i, f_2, f_4, \phi_0) - \mathcal{I}_Y^{exp}(\alpha_p^i)]^2 + [\mathcal{I}_X^{th}(\alpha_{p,s}^i, f_2, f_4, \phi_0) - \mathcal{I}_X^{exp}(\alpha_{p,s}^i)]^2 \\
 &\left. + [\mathcal{I}_Y^{th}(\alpha_{p,s}^i, f_2, f_4, \phi_0) - \mathcal{I}_Y^{exp}(\alpha_{p,s}^i)]^2 \right\}, \quad (5.7)
 \end{aligned}$$

where the sum runs over the different incident polarization angles  $\alpha^i$ . The first two terms in the sum correspond to the P polarization configuration, where  $\alpha_p$  rotates and  $\alpha_s = 0^\circ$ , which is pointed out by the subscript  $p$ . In the two last terms, the subscript  $p, s$  stands for the PS polarization configuration, where  $\alpha_p = \alpha_s$  rotate from  $0^\circ$  to  $360^\circ$ . The superscript “*th*” stands for the theoretical intensity, calculated as the modulus square of the CARS induced polarization, given by Eq. (1.3), with the CARS susceptibility obtained from Eq. 5.6. The superscript “*exp*” corresponds to the CARS intensity acquired experimentally. Finally, the error function is normalized by the number of the incident polarization angles over which the sum is done, here  $N_\alpha = 73$ .

Note that before fitting, the excitation and emitted field polarizations must be corrected by polarization distortions introduced by the optical setup and by birefringence of the sample, as described in section 2.3. However, we have shown in the same section that

only the emitted anti-Stokes field is affected by birefringence when the incident beams are focused at the bottom surface of the sample ( $Z = 0 \mu\text{m}$ ). In this way, the theoretical CARS field used in the fit equation (5.7) must account for the orientation of the optical axis  $\Theta_b$  and the dephasing  $\Phi_b$  between the fast and slow axes of the collagen fiber. As we saw in section 2.3, when the incident fields are affected by dichroism and ellipticity, the solution  $(\Phi_b, \Theta_b)$  is not unique. We will show in section 5.3, that the two independent solutions do not result in the same theoretical CARS intensities, for the same parameters  $(f_2, f_4, \phi_0)$ . Furthermore, solutions for which  $\Theta_b$  is related by a  $\pi/2$  periodicity, result in the same theoretical CARS intensities for the same parameters  $(f_2, f_4, \phi_0)$  only when  $Z = 0$  or  $Z = L$ , i.e., only when either the emitted CARS signal or the incident fields are affected by birefringence. The influence of the birefringence will be discussed in more detail in section 5.3. Here, we fit independently the parameters  $(f_2, f_4, \phi_0)$  for both birefringence solutions that are independent and we chose the couple  $(\Phi_b, \Theta_b)$  that gives the smallest mean square error  $\chi^2$ . Fig. (5.6) shows the experimental results and best fits for the three positions depicted in Fig. (5.5). The polar plots represent the nonresonant CARS intensities as a function of the incident polarization. Fig. (5.6a) corresponds to the P polarization configuration (only  $\alpha_p$  rotates) whereas Fig. (5.6b), shows the polarization resolved CARS responses in the PS scheme (both polarizations  $\alpha_p = \alpha_s$  rotate). The parameters found in this fit procedure are summarized in table 5.1.

Table 5.1: Set of parameters  $(f_2, f_4, \phi_0)$  obtained by the fit procedure, for different positions of the collagen fiber in the same  $XY$  plane for  $Z = 0 \mu\text{m}$ . Values of  $(\Phi_b, \Theta_b)$  are obtained by fitting the sample's birefringence.

Position	$f_2$	$f_4$	$\phi_0$ (deg)	$\Phi_b$ (deg)	$\Theta_b$ (deg)
1	-0.35	0.25	54	191	30
2	0.05	0.1	51	201	76
3	0.4	-0.2	63	179	58

Once the parameters  $f_2$  and  $f_4$  are fitted, it is possible to build the corresponding even terms of the orientational distribution functions in the microscopic frame. Their 3D plots in the microscopic frame  $(x, y, z)$  are shown in Fig. (5.7). In all three cases,  $f_4 \neq 0$ , which means that the angular distribution has a high-order symmetry (hexadecapolar) contribution. This explains the four-lobe shape depicted in the 3D plots. Position 2 (Fig. 5.7(b)) has the most isotropic molecular angular distribution. Positions 1 and 3 have more anisotropic distributions, in particular, positive values of  $f_4$  contribute to the appearance of the equatorial torus-like shape in the distribution, while negative values of  $f_4$  are responsible for the hollow shape of the distribution, as we have already shown in section 5.1.1. As we mentioned in section 1.5.2, a complete view of the orientational distribution function  $f(\theta)$ , until the fourth-order in the series expansion, would require the knowledge of the order parameters  $f_1$  and  $f_3$ . The latter could be probed by second harmonic generation resolved in polarization [110]. The diversity of shapes found in this sample could be most likely

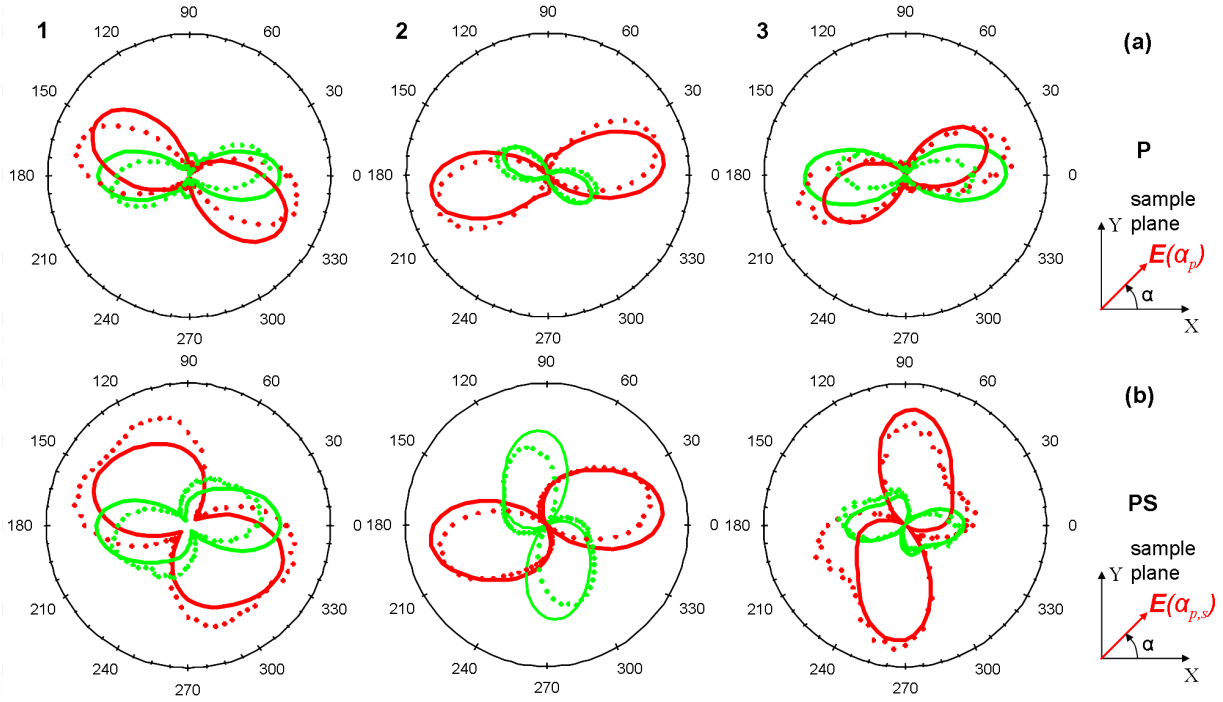


Figure 5.6: Nonresonant CARS intensities along  $X$  (red curves) or  $Y$  (green curves) as a function of the incident polarization. (a) P polarization configuration: the intensities vary as a function of  $\alpha_p$  for  $\alpha_s = 0^\circ$ . (b) Polarization scheme PS:  $\alpha_p$  and  $\alpha_s$  rotate simultaneously. The solid lines correspond to theoretical intensities given by the best fit, while markers depict the experimental data. From left to right, the polar plots correspond respectively to positions 1, 2 and 3, showed in Fig. (5.5). Data are acquired at  $Z = 0 \mu\text{m}$ .

due to the different arrangements of fibers depending on the sample location: indeed, we do not probe here single isolated crystalline collagen microfibrils, but rather a macroscopic organization of them in bundles, that constitute the tendon tissue.

In Fig. (5.5), the red lines superimposed to the nonresonant CARS images of the collagen, represent the fitted orientations of the molecular distribution  $\phi_0$ . The white curves are a projection in the  $xz$  plane of the 3D orientational distribution function (only the even terms up to the fourth order), oriented at  $\theta_0 = 90^\circ$  and the fitted  $\phi_0$  in the macroscopic frame. We can observe that the orientation of the collagen fiber, observed from the acquired images, agrees qualitatively with the molecular orientational distribution, for all the three studied positions. The fitted microscopic order parameters are therefore a good qualitative characterization of the macroscopic collagen fiber organization at localized positions.

The green lines in Fig. (5.5) correspond to the orientation of the fiber's fast optical axis  $\Theta_b$ , which should in principle coincide with the direction of the collagen fiber [111]. We can see however that this is not always observed in our measurements. In fact, the value of  $\Theta_b$  corresponds to the average orientation of the optical axis throughout the thickness of the

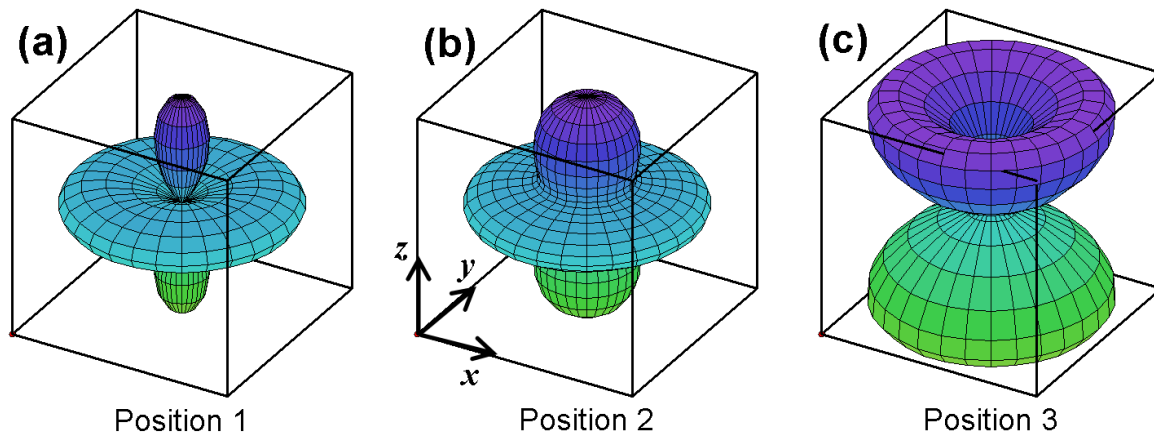


Figure 5.7: 3D plots of the even-order terms of the multipolar expansion of the molecular angular distribution functions, build from the fitted parameters  $f_2$  and  $f_4$ . Figures (a), (b) and (c) correspond respectively to positions 1, 2 and 3. The plots are in the microscopic frame  $(x, y, z)$ .

collagen fiber. It is therefore expected to find some discrepancies between the direction of the long axis of the fiber and its optical axis, specially when the orientation of the collagen fiber is very inhomogeneous along its thickness. The measured birefringence phase shift  $\Phi_b(L) \approx 190^\circ$ , can be used to deduce the approximate sample thickness  $L$  at the measured sample location. Assuming  $\Delta n \approx 0.003$  [111], between the long axis of the collagen fibers and its perpendicular direction, this measurement leads to  $L \approx 128 \mu\text{m}$ , which is reasonable in the studied sample.

In the next section we will study the influence of the sample's birefringence on the polarimetric CARS responses, that can be crucial when performing measurements at positions in the sample other than  $Z = 0 \mu\text{m}$ .

### 5.3 Influence of the sample's birefringence on the polarimetric CARS responses

If the collagen fiber is composed by fibrils that are all oriented in the same direction along  $Z$  and if it is not birefringent, then the polar plots obtained at different focal planes  $Z$  for the same position in the  $XY$  plane, should be the same. Fig. (5.8) shows that this is not observed in our experimental data. The polar plots depict the experimental nonresonant Fwd-CARS intensities acquired at a different depth in the sample,  $Z \approx 60 \mu\text{m}$ . A major change is observed at positions 1 and 3, specially for the intensity acquired along the  $X$  axis ( $\mathcal{I}_X$ ) when the polarization  $\alpha_p$  rotates. In this case, the two-lobe shape at the surface becomes a four-lobe pattern deeper in the fiber. Inhomogeneities and different orientations of the fibrils along  $Z$ , but also birefringence, could explain the changes observed. As

collagen is highly birefringent, the CARS signal is not the same when the incident fields are focused in the plane  $Z = 0 \mu\text{m}$  or in the plane  $Z = 60 \mu\text{m}$ . In the first case, only the emitted signal is affected by birefringence, while in the second situation, both the incident and emitted fields are depolarized by the effect of the fiber's anisotropy, as we explained in section 2.3.

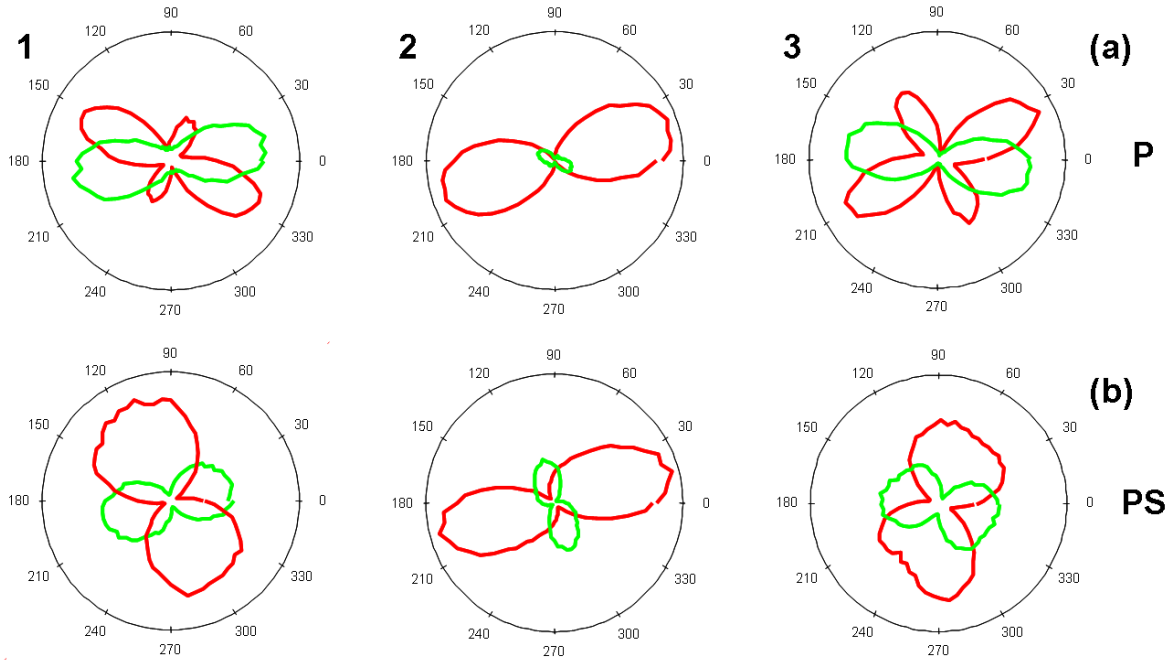


Figure 5.8: Experimental nonresonant CARS intensities, measured at  $Z \approx 60 \mu\text{m}$ , along  $X$  (red curves) or  $Y$  (green curves), as a function of the incident polarization. (a) P polarization configuration. (b) PS polarization configuration. From left to right, the polar plots correspond respectively to positions 1, 2 and 3.

In order to study the effects of birefringence on the nonresonant polarimetric CARS signal, we recall the approach adopted in section 2.3, in order to calculate the sample's anisotropy, defined by the parameters  $\Theta_b$  and  $\Phi_b$ . Fig. (5.9a) shows the intensities of the pump beam transmitted throughout the fiber and detected along the  $X$  and  $Y$  axes, as a function of  $\alpha_p$ , with the respective best fits, for position 3. The corresponding cartography of the mean square error as a function of  $(\Theta_b, \Phi_b)$  is depicted in Fig. (5.9b).

As we already showed in section 2.3, it is possible to identify four local minima, which proofs that the solution is not unique, in situations where the dichroic mirror already affects the input polarization. The four possible values for the set  $(\Theta_b, \Phi_b)$ , for position 3, are:  $(58^\circ, 179^\circ)_1$ ,  $(40^\circ, 228^\circ)_2$ ,  $(148^\circ, 181^\circ)_3$  and  $(130^\circ, 132^\circ)_4$ , the subscripts being used only to label the different possible results. Solutions 1 and 2 are independent and contribute to different theoretical polarization resolved CARS intensities. By consequence, using solution 1 or 2 in our fit procedure results in different values for the fitted parameters  $(f_2, f_4, \phi_0)$ . In

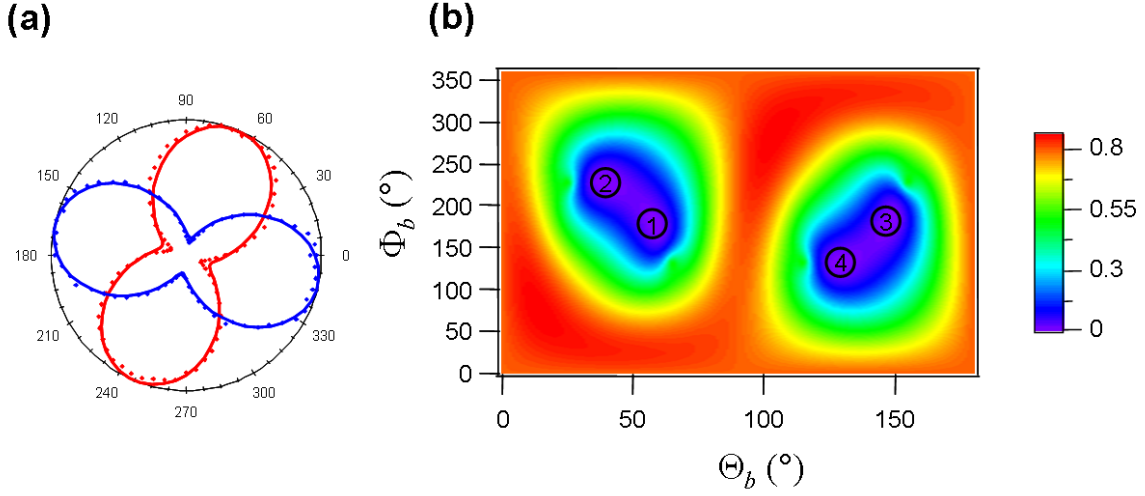


Figure 5.9: Fitting the birefringence of the collagen fiber. (a) Experimental laser intensities at frequency (dots) along  $X$  (red curves) and  $Y$  (blue curves), as a function of the incident polarization  $\alpha_p$ . Solid lines correspond to the respective best fits. (b)  $(\Phi_b, \Theta_b)$ -cartography of the mean square error.

the case of position 3, the best fits reported in table 5.1, are obtained with the birefringence of the fiber given by solution 1. In the following, we will therefore consider only solutions 1 and 3. The other two solutions, 3 and 4, are related to 1 and 2, respectively, by the  $\pi/2$ -periodicity on  $\Theta_b$  ( $\Theta_b^{3(4)} = \theta_b^{1(2)} + \pi/2$  and by consequence,  $\Phi_b^{3(4)} = 2\pi - \Phi_b^{1(2)}$ ).

When only the emitted CARS signal or the incident fields are affected by birefringence (corresponding respectively to focusing at  $Z = 0$  or  $Z = L$ , according to the scheme depicted in Fig. (5.4)), the two solutions where the optical axis is turned by  $90^\circ$  (i. e., related by the  $\pi/2$ -periodicity on  $\Theta_b$ ), give the same theoretical nonresonant CARS intensities. This is not observed when we focus in an intermediate position into the fiber ( $Z = d$ ,  $0 < d < L$ ). In this case, correcting the incident and emitted fields by  $(\Theta_b(d), \Phi_b(d))_1$  or  $(\Theta_b(d), \Phi_b(d))_3$  does not lead to the same polarimetric CARS responses, in both polarization configurations P and PS, as we show in Fig. (5.10). Therefore, in order to study the polarization responses of the CARS signal when both the incident and emitted fields are affected by birefringence, it is necessary to remove the ambiguity from the birefringence solution  $(\Theta_b, \Phi_b)$ . The same behavior is noticed in positions 1 and 2.

Fig. (5.10) shows the theoretical effect of the birefringence on the polarization-resolved CARS intensities, when the incident beams are focused at different  $Z$  into the fiber ( $d/L$  varies from 0 to 1, with a step of  $1/4$ ). As we stated in section 2.3, the incident and emitted fields are affected each one by an effective birefringence whose phase shift is given, respectively by  $\Phi_{b_{inc}} = \frac{d}{L}\Phi_b$  and  $\Phi_{b_{as}} = (1 - \frac{d}{L})\Phi_b$ . The theoretical CARS polar plots were built with the set of parameters  $(f_2, f_4, \phi_0)$  of position 3 and for both birefringence solutions

coupled by a  $\pi/2$ - periodicity,  $(\Theta_b, \Phi_b)_1$  and  $(\Theta_b, \Phi_b)_3$ . The results are highly sensitive to the birefringence parameters. In the case of the P polarization scheme (Fig. 5.10(c,d)), the four-lobe shape that appears in the experimental polar plots of the CARS intensities along  $X$  (Fig. 5.8) could be explained by the effect of birefringence. Indeed, when  $d/L \leq 0.5$  we observe this behavior in the theoretical polar plots of  $\mathcal{I}_X$  (Fig. 5.10(c,d)). Note that this effect is more prominent for  $\Theta_b = 148^\circ$  (solution 3). The theoretical behaviors of the polar plots in the PS polarization configuration, however, seem to agree very slightly (at least qualitatively) with the experimental results showed in Fig. (5.8). A suitable reason for this disagreement is the fact that the orientation  $\phi_0$  of the collagen fiber is not homogeneous along  $Z$ . In this case, the direction of the fast optical axis of the fiber  $\Theta_b$  can no longer be considered as a constant parameter throughout the whole thickness of the collagen fiber. The influence of  $\phi_0$  in the polarization responses of the nonresonant CARS intensities is discussed in the next section.

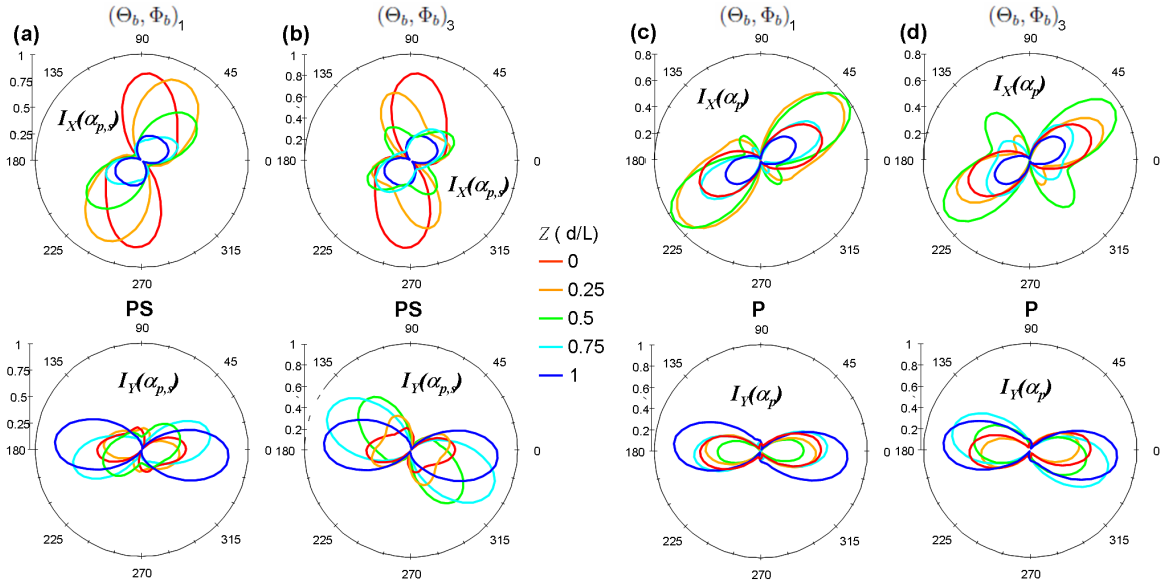


Figure 5.10: Theoretical nonresonant CARS intensities built from the fitted set of parameters  $(f_2, f_4, \phi_0)$  of position 3, when focusing at different  $Z = d$  into the fiber ( $d/L$  varies from 0 to 1 with a step of  $1/4$ ). (a,b) PS polarization scheme ( $\alpha_p$  and  $\alpha_s$  rotate simultaneously). (c,d) P polarization configuration ( $\alpha_p$  rotates while  $\alpha_s = 0^\circ$ ). (a,c)  $(\Theta_b, \Phi_b)_1 = (58^\circ, 179^\circ)$ ; (b,d)  $(\Theta_b, \Phi_b)_3 = (148^\circ, 181^\circ)$ . Red and blue curves correspond respectively to  $d/L = 0$  and  $d/L = 1$  and they are the same for both birefringence solutions.

## 5.4 Influence of the fiber's in-plane orientation on the polarimetric CARS responses

We showed in the previous section that only birefringence of the fiber is not sufficient to explain the quantitative behavior of the polarization responses of the CARS signal, when focusing at different depths  $Z$  into the sample. In this section, we study the effect of the in-plane orientation  $\phi_0$  of the collagen fiber on the nonresonant CARS intensities. First, we analyze the influence of  $\phi_0$  on the polarization responses of the CARS intensities at  $Z = 0 \mu\text{m}$ , where only the emitted anti-Stokes signal is affected by birefringence. Then, we try to find an orientation that matches both the experimental curves when focusing deeper into the fiber, for the fitted set of birefringence parameters,  $(\Theta_b, \Phi_b)$ .

The theoretical polarization responses of the nonresonant CARS intensities for different orientations of the collagen fiber in the  $XY$  plane at  $Z = 0 \mu\text{m}$  are drawn in Fig. (5.11). The polar plots are built with the parameters  $f_2, f_4, \Theta_b$  and  $\Phi_b$  given in table 5.1. Positions 1, 2 and 3 correspond to Figs. (5.11) (a), (b) and (c) respectively. For both polarization configurations P and PS, the shapes of the polar plots are highly sensitive to  $\phi_0$ , except for position 2. In this case, as we showed in section 5.2.3, the molecular angular distribution function is close to an isotropic distribution [see Fig. (5.7b)], which means that the CARS signal is not strongly dependent on the orientation of the fiber. Positions 1 and 3, in the contrary, are much dependent on  $\phi_0$ . In these cases, if the orientation of the fiber changes slightly with  $Z$ , then the polarization responses of the CARS signal can present very important variations. This fact can elucidate why only accounting for birefringence is not sufficient to explain the behavior of the CARS signal when focusing at different  $Z$  into the fiber.

The analysis developed in this section and in the previous one, concerning the influence of the sample's birefringence and in-plane orientation on the polarization-resolved CARS responses, shows that determining the local symmetry of the molecular orientational distribution function is a very delicate procedure, specially for a highly inhomogeneous medium. This is particularly true when the polarimetric measurements are carried out in different depths of the sample, other than its surfaces ( $Z = 0$  or  $Z = L$ ). At  $Z = 0 \mu\text{m}$ , only the emitted anti-Stokes signal is affected by birefringence, which can be measured throughout the whole thickness of the sample, by the method explained in section 2.3. By consequence, the ellipticity of the anti-Stokes polarization due to the anisotropy of the sample, can be corrected in the theoretical model, without affecting the determination of the order parameters and orientation of the molecular distribution. However, the local characterization of the orders of symmetry in a molecular statistical ensemble at  $Z = d \neq 0 \mu\text{m}$  can become a very complicated problem in inhomogeneous media, due to the sample's birefringence, since we can not measure  $(\Theta_b, \Phi_b)$  at  $Z = d$  (except if supposing a homogeneous medium). A complete fit including all the parameters  $(f_2, f_4, \phi_0, \Theta_b, \Phi_b)$  would not work even for a given  $Z$ , because it would involve too many parameters. In fact, for every value of the birefringence parameters  $(\Theta_b, \Phi_b)$ , it would be possible to find a different solution for  $(\phi_0, f_2, f_4)$ . It means that the local birefringence of the sample at different  $Z$ ,  $(\Theta_b(Z), \Phi_b(Z))$ , must be

#### 5.4. Influence of the fiber's in-plane orientation on the polarimetric CARS responses

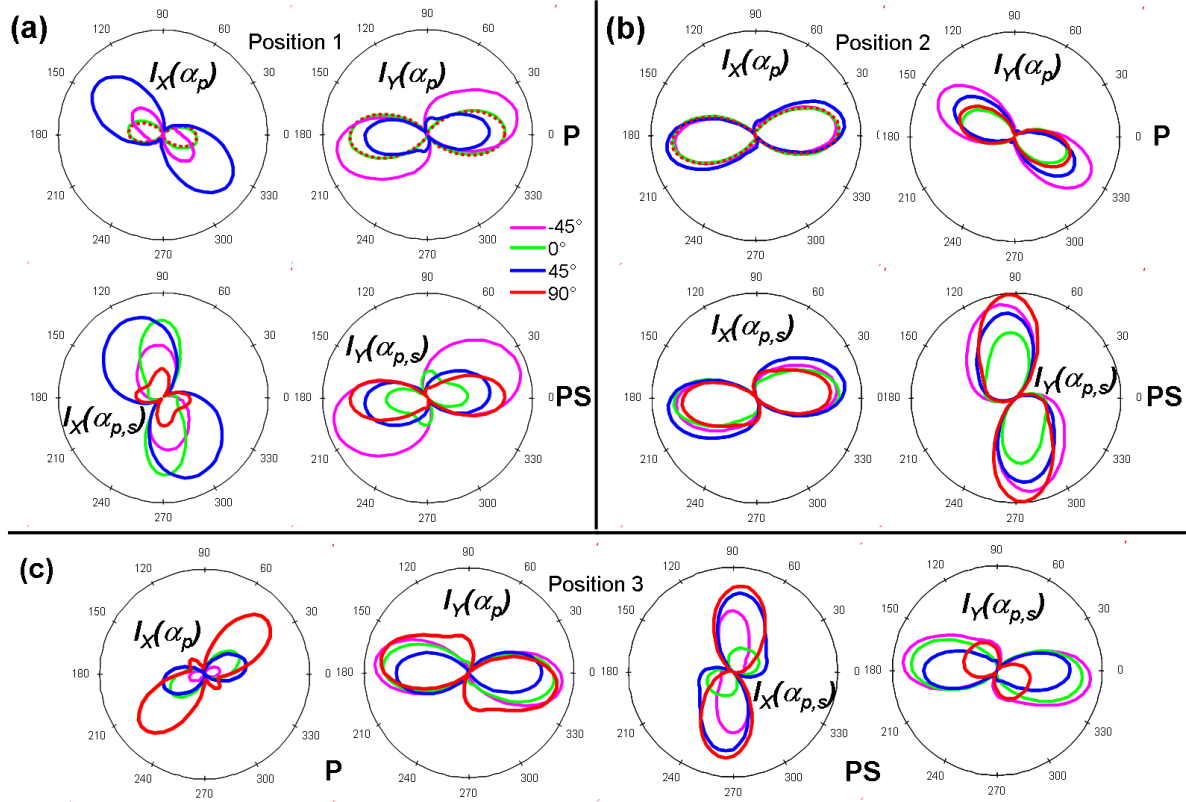


Figure 5.11: Theoretical CARS intensities for different orientations of the collagen fiber in the  $XY$  plane ( $\phi_0$ ). Figs. (a), (b) and (c) represent positions 1, 2 and 3, respectively. For each position, we depict separately the theoretical intensities along the  $X$  or the  $Y$  axes ( $I_X$  and  $I_Y$ , respectively). Both polarization schemes P ( $\alpha_p$ ) and PS ( $\alpha_{p,s}$ ) are shown in each case. Different curves correspond to the following in-plane orientation  $\phi_0$ : (1)  $-45^\circ$ , violet; (2)  $0^\circ$ , green; (3)  $45^\circ$ , blue and (4)  $90^\circ$ , red.

entered as *a priori* known parameters.

An iterative method should be employed in order to characterize the local molecular orientational distribution at intermediate depths in the sample. First, we characterize the fiber's birefringence, averaged throughout the thickness of the sample. Then, we measure the polarization-resolved CARS intensities  $\mathcal{I}_X$  and  $\mathcal{I}_Y$  at different depths  $Z_i = d$  in the sample, varying from  $Z_0 = 0$  to  $Z_n = L$ . Finally, for each position  $Z_i$  we fit a set of parameters ( $f_2, f_4, \phi_0, \Theta_b, \Phi_b$ ), by taking into account the results fitted in the previous measurement  $Z_{i-1}$ . With only two points throughout the whole thickness of the sample, it is not accurate to proceed to a rigorous fit at the intermediate depth, especially when it is highly inhomogeneous. This seems to be the case for positions 1 and 3, since the polarimetric nonresonant CARS intensities acquired at  $Z = 0 \mu\text{m}$  and  $Z = 60 \mu\text{m}$  do not present the same patterns, as can be seen in Figs. (5.6) and (5.8). For this reason, we do

not fit the experimental results at  $Z = 60 \mu\text{m}$  measured at positions 1 and 3. However, in the case of position 2, it is possible to find theoretical curves that match the experimental data showed in Fig. (5.8). This is a consequence of the fact that, at this particular  $XY$  position, the molecular angular distribution is close to isotropy. Therefore, the polarization-resolved CARS response does not depend strongly on the in-plane orientation  $\phi_0$  of the sample. We assume thus, that at this position, the fiber is homogeneous along  $Z$  and has consequently, the same molecular orientational distribution. In this way, we suppose that the fitted parameters  $f_2$  and  $f_4$  are the same at  $Z = 0 \mu\text{m}$  or  $Z = 60 \mu\text{m}$  and we try to find an orientation  $\phi_0$  that best fits the polarization-resolved CARS measurements showed in Fig. (5.8). The results are depicted in Fig. (5.12). For the fit, we used  $\Theta_b = 76^\circ$  and  $\Phi_b = 201^\circ$ . The fitted  $\phi_0$  is  $40^\circ$ , which is not far from the one found at the surface of the fiber.

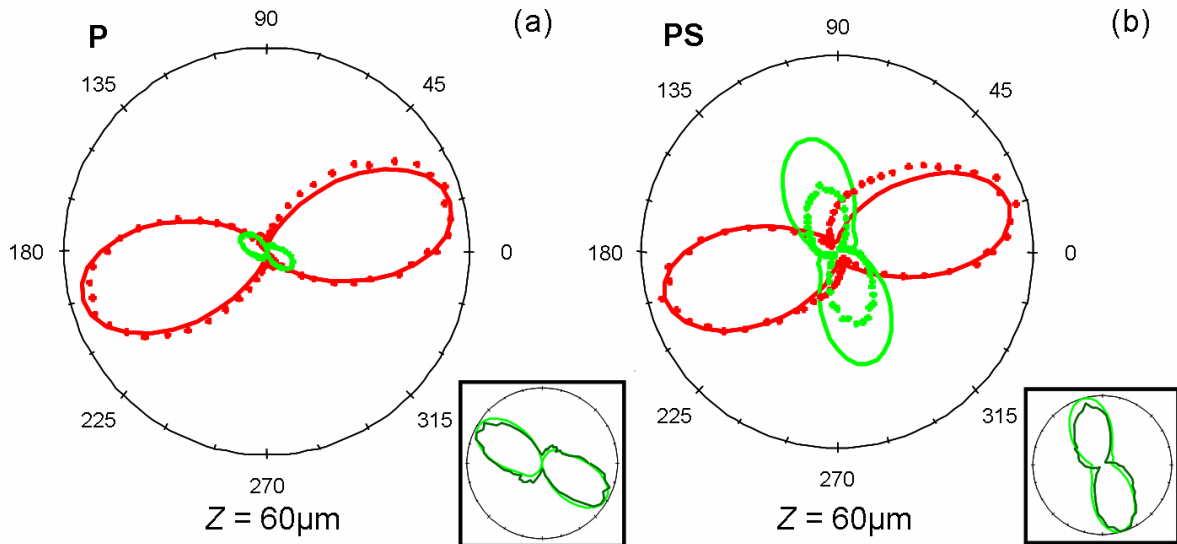


Figure 5.12: Experimental CARS intensities with their best fits at position 2 in the  $XY$  plane and  $Z = 60 \mu\text{m}$ . (a) P and (b) PS polarization configuration. Red and green curves correspond to the CARS intensities along the  $X$  and  $Y$  axes, respectively. Markers represent the experimental data and solid lines correspond to the best fits. Insets in (a) and (b) show in detail the fit  $\mathcal{I}_Y$ . In the case of (b), it is the intensity along  $Y$  normalized to 1 that is plotted in the polar graph.

## 5.5 Conclusion

In this chapter, we have shown that polarization resolved nonresonant CARS is a powerful technique to retrieve the even orders of symmetry up to the fourth order in a molecular statistical ensemble, such as collagen fibers. In particular, we propose a fitting procedure

that allows to estimate the microscopic molecular orientational distribution function and its orientation in the macroscopic frame. Careful analysis concerning the birefringence of the sample must be performed before fitting the experimental CARS signals, in order to avoid misunderstanding results. Note that the procedure of accounting for birefringence is made here delicate due to the dichroic mirror influence on the field polarization. This could be circumvented by correcting this effect before the microscope entrance (by a SLM controllable wave plate, for instance). The further extension of this technique to microscopy, enabling imaging of local symmetry orders and molecular organization, brings new possibilities for highcontrast structural spatial investigation with submicrometric resolution. Polarization resolved multimodal nonlinear microscopic can also be performed, by combining CARS with second-order nonlinear optical processes, such as SHG, in order to obtain complimentary information on the symmetry orders of the molecular distribution. Finally, this method can be widen to resonant polarization resolved CARS, by probing specific vibrational resonances of the molecular ensembles.



---

## CONCLUSION

This thesis has demonstrated the potential of polarization resolved four-wave mixing to read-out structural and vibrational symmetries in molecular media. Theoretical and experimental analyses were developed for three distinct samples: isotropic, crystalline and biomolecular assemblies. The third-order nonlinear optical process considered in this work was essentially coherent anti-Stokes Raman scattering (CARS), either at vibrational resonance or not. Stimulated Raman scattering (SRS) was also performed in isotropic media.

In a first step, we have set the theoretical basis of the tensorial approach of nonlinear optics, by demonstrating how the structures of the microscopic susceptibility tensors can be determined from symmetry considerations. In nonresonant processes, only spatial symmetries are involved, while at resonance, the symmetries of the vibrational modes play a major role in the characterization of the susceptibilities. In the case of third-order nonlinear optical processes, without any symmetry considerations, the susceptibility tensor has 81 nonvanishing and independent components (57 in the case of degenerate CARS process). This number can drop to only a few in highly symmetric media. In order to probe these microscopic information from polarimetric measurements, it is necessary to derive the macroscopic susceptibility tensors from the microscopic ones, either for crystalline media or molecular assemblies with statistical orientational distribution. Polarimetric measurements on crystals allow to retrieve the orientation and symmetry of the crystal unit cell. In the case of molecular assemblies, nonlinear polarimetry provides information on the symmetry order and orientation of the molecular distribution. As CARS is a third-order nonlinear optical process, it can probe symmetries up to the fourth-order.

Here, we have explored the full potential of CARS polarization analysis, by controlling and tuning independently the linear polarization states of the incident beams. The generated field is also analyzed along two distinct orthogonal directions. Precise control of the polarization in the experimental setup is essential for the accurate interpretation of the experimental results. We have then demonstrated the necessity of calibrating the polarization distortions in the optical setup in order to correctly interpret the experimental results.

Polarization resolved four-wave mixing measurements in media with distinct symmetries, such as isotropic, crystal and collagen, have achieved successful results. Polarimetric measurements at resonance were able to reveal the symmetry of the probed vibrational modes, either in isotropic media or in crystals with cubic symmetry. In isotropic samples, the symmetry of the vibrational resonance is characterized by the depolarization ratio, that could be measured from one single polarization configuration at two distinct spectral positions, in the case of CARS experiments. For SRS, it is possible to determine the depolarization ratio from one single polarization configuration at the peak of the spectrum. In cubic crystals, polarization responses of totally and nontotally symmetric vibrational modes showed completely different patterns, demonstrating the power of the technique in probing vibrational symmetries. Furthermore, we were able to characterize, and even quantify in totally symmetric vibrations, departure from Kleinman symmetry conditions.

Nonresonant four-wave mixing polarimetric measurements were able to probe departure from isotropy in crystals with cubic symmetry, which is not possible in lower-order optical processes, such as spontaneous Raman scattering. Furthermore, nonresonant measurements on collagen fiber provided quantitative information on the symmetry of the molecular orientational distribution, revealing the even terms of the multipolar expansion of the distribution function, up to the fourth order of symmetry.

Following the pioneer works developed in the 1970s, our study confirms the great potential of polarimetric four-wave mixing in revealing structural and vibrational symmetries in molecular media. It opens new prospective investigations based not only on chemical selectivity, but also structural imaging, dedicated to materials or biological diagnostics down to the nanoscale.

Polarimetric nonlinear optics is currently a very active field of research in the Mosaic group at Fresnel Institute, and the perspectives are very promising. Some of the directions to follow suggested by the studies developed in this thesis are:

- To perform polarimetric measurements combining different nonlinear optical processes, in order to get complimentary information on the sample's structural symmetry. It could be considered, for instance, to acquire polarimetric CARS and SHG images of the same sample simultaneously.
- To extended the nonresonant CARS measurements performed on collagen fibers to the resonant case. By consequence, additional information on the symmetry of the addressed vibrational modes could be obtained. For samples where the nonresonant signal is very strong, polarimetric measurements on SRS may be considered.
- To extend the application of the method to different samples with great interest in biology, including cell membranes, microtubules, chromosomes, protein aggregates and tissues.

---

---

# APPENDIX A

---

## SUSCEPTIBILITY TENSORS

Here we list the first-, second- and third-order susceptibility tensors, for all the 32 crystallographic point groups and also for isotropic media. This appendix is a reproduction of the Appendix 3 of reference [72] (pages 298 to 302). The tensor structures listed below are for arbitrary ratio of frequencies.

### A.1 First-order susceptibility tensor $\chi_{ij}^{(1)}(-\omega_\sigma; \omega_p)$

#### Triclinic system

Six independent nonvanishing components.

$$\begin{array}{ccc} \chi_{xx}^{(1)} & \chi_{yy}^{(1)} & \chi_{zz}^{(1)} \\ \chi_{xy}^{(1)} = \chi_{yx}^{(1)} & \chi_{zx}^{(1)} = \chi_{xz}^{(1)} & \chi_{yz}^{(1)} = \chi_{zy}^{(1)} \end{array}$$

#### Monoclinic system

Four independent nonvanishing components.

$$\begin{array}{ccc} \chi_{xx}^{(1)} & \chi_{yy}^{(1)} & \chi_{zz}^{(1)} \\ \chi_{zx}^{(1)} = \chi_{xz}^{(1)} & & \end{array}$$

#### Orthorhombic system

Three independent nonvanishing components.

$$\chi_{xx}^{(1)} \quad \chi_{yy}^{(1)} \quad \chi_{zz}^{(1)}$$

### Tetragonal, Trigonal and Hexagonal systems

Two independent nonvanishing components.

$$\chi_{xx}^{(1)} = \chi_{yy}^{(1)} \\ \chi_{zz}^{(1)}$$

### Cubic system and isotropic

One independent nonvanishing component.

$$\chi_{xx}^{(1)} = \chi_{yy}^{(1)} = \chi_{zz}^{(1)}$$

## A.2 Second-order susceptibility tensor $\chi_{ijk}^{(2)}(-\omega_\sigma; \omega_q, \omega_p)$

### Triclinic system

**Class  $C_1$**  All the 27 tensor components are independent and nonvanishing.

### Monoclinic system

**Class  $C_2$**  13 independent nonvanishing components.

$$\chi_{xyz}^{(2)} \quad \chi_{xzy}^{(2)} \quad \chi_{yzx}^{(2)} \quad \chi_{yxz}^{(2)} \quad \chi_{zxy}^{(2)} \quad \chi_{zyx}^{(2)} \\ \chi_{xxy}^{(2)} \quad \chi_{xyx}^{(2)} \quad \chi_{yxx}^{(2)} \\ \chi_{yyy}^{(2)} \\ \chi_{yzz}^{(2)} \quad \chi_{zyz}^{(2)} \quad \chi_{zzz}^{(2)}$$

**Class  $C_{1h}$**  14 independent nonvanishing components.

$$\chi_{xxx}^{(2)} \quad \chi_{xyy}^{(2)} \quad \chi_{xzz}^{(2)} \quad \chi_{xzx}^{(2)} \quad \chi_{xxz}^{(2)} \\ \chi_{yyz}^{(2)} \quad \chi_{yzy}^{(2)} \quad \chi_{yxy}^{(2)} \quad \chi_{yyx}^{(2)} \\ \chi_{zxx}^{(2)} \quad \chi_{zyy}^{(2)} \quad \chi_{zzz}^{(2)} \quad \chi_{zzx}^{(2)} \quad \chi_{zxx}^{(2)}$$

### Orthorhombic system

**Class  $D_2$**  Six independent nonvanishing components.

$$\begin{array}{cc} \chi_{xyz}^{(2)} & \chi_{xzy}^{(2)} \\ \chi_{yzx}^{(2)} & \chi_{yxz}^{(2)} \\ \chi_{zxy}^{(2)} & \chi_{zyx}^{(2)} \end{array}$$

**Class  $C_{2v}$**  Seven independent nonvanishing components.

$$\begin{array}{ccc} \chi_{xxz}^{(2)} & \chi_{xxz}^{(2)} & \\ \chi_{yyz}^{(2)} & \chi_{yyz}^{(2)} & \\ \chi_{zxx}^{(2)} & \chi_{zyy}^{(2)} & \chi_{zzz}^{(2)} \end{array}$$

### Tetragonal system

**Class  $C_4$**  Seven independent nonvanishing components.

$$\begin{array}{l} \chi_{xyz}^{(2)} = -\chi_{yxz}^{(2)} \\ \chi_{xzy}^{(2)} = -\chi_{yzx}^{(2)} \\ \chi_{xxz}^{(2)} = \chi_{yyz}^{(2)} \\ \chi_{xxz}^{(2)} = \chi_{yyz}^{(2)} \\ \chi_{zxx}^{(2)} = \chi_{zyy}^{(2)} \\ \chi_{zzz}^{(2)} \\ \chi_{zxy}^{(2)} = -\chi_{zyx}^{(2)} \end{array}$$

**Class  $S_4$**  Six independent nonvanishing components.

$$\begin{array}{l} \chi_{xyz}^{(2)} = \chi_{yxz}^{(2)} \\ \chi_{xzy}^{(2)} = \chi_{yzx}^{(2)} \\ \chi_{xxz}^{(2)} = -\chi_{yyz}^{(2)} \\ \chi_{xxz}^{(2)} = -\chi_{yyz}^{(2)} \\ \chi_{zxx}^{(2)} = -\chi_{zyy}^{(2)} \\ \chi_{zxy}^{(2)} = \chi_{zyx}^{(2)} \end{array}$$

**Class  $D_4$**  Three independent nonvanishing components.

$$\begin{aligned}\chi_{xyz}^{(2)} &= -\chi_{yxz}^{(2)} \\ \chi_{xzy}^{(2)} &= -\chi_{yzx}^{(2)} \\ \chi_{zxy}^{(2)} &= -\chi_{zyx}^{(2)}\end{aligned}$$

**Class  $C_{4v}$**  Four independent nonvanishing components.

$$\begin{aligned}\chi_{xzx}^{(2)} &= \chi_{yzy}^{(2)} \\ \chi_{xxz}^{(2)} &= \chi_{yyz}^{(2)} \\ \chi_{zxx}^{(2)} &= \chi_{zzy}^{(2)} \\ \chi_{zzz}^{(2)}\end{aligned}$$

**Class  $D_{2d}$**  Three independent nonvanishing components.

$$\begin{aligned}\chi_{xyz}^{(2)} &= \chi_{yxz}^{(2)} \\ \chi_{xzy}^{(2)} &= \chi_{yzx}^{(2)} \\ \chi_{zxy}^{(2)} &= \chi_{zyx}^{(2)}\end{aligned}$$

**Cubic system**

**Class  $O$**  One independent nonvanishing component.

$$\chi_{xyz}^{(2)} = \chi_{yzx}^{(2)} = \chi_{zxy}^{(2)} = -\chi_{xzy}^{(2)} = -\chi_{yxz}^{(2)} = -\chi_{zyx}^{(2)}$$

**Class  $T_d$**  One independent nonvanishing component.

$$\chi_{xyz}^{(2)} = \chi_{yzx}^{(2)} = \chi_{zxy}^{(2)} = \chi_{xzy}^{(2)} = \chi_{yxz}^{(2)} = \chi_{zyx}^{(2)}$$

**Class  $T$**  Two independent nonvanishing components.

$$\begin{aligned}\chi_{xyz}^{(2)} &= \chi_{yzx}^{(2)} = \chi_{zxy}^{(2)} \\ \chi_{xzy}^{(2)} &= \chi_{yxz}^{(2)} = \chi_{zyx}^{(2)}\end{aligned}$$

### Trigonal system

**Class  $C_3$**  Nine independent nonvanishing components.

$$\begin{aligned}
 \chi_{xxx}^{(2)} &= -\chi_{xyy}^{(2)} = -\chi_{yxy}^{(2)} = -\chi_{yyx}^{(2)} \\
 \chi_{xyz}^{(2)} &= -\chi_{yxz}^{(2)} \\
 \chi_{xzy}^{(2)} &= -\chi_{yzx}^{(2)} \\
 \chi_{xzx}^{(2)} &= \chi_{yzy}^{(2)} \\
 \chi_{xxz}^{(2)} &= \chi_{yyz}^{(2)} \\
 \chi_{yyy}^{(2)} &= -\chi_{yxx}^{(2)} = -\chi_{xyx}^{(2)} = -\chi_{xyx}^{(2)} \\
 \chi_{zxx}^{(2)} &= \chi_{zyy}^{(2)} \\
 \chi_{zzz}^{(2)} & \\
 \chi_{zxy}^{(2)} &= -\chi_{zyx}^{(2)}
 \end{aligned}$$

**Class  $D_3$**  Four independent nonvanishing components.

$$\begin{aligned}
 \chi_{xxx}^{(2)} &= -\chi_{xyy}^{(2)} = -\chi_{yxy}^{(2)} = -\chi_{yyx}^{(2)} \\
 \chi_{xyz}^{(2)} &= -\chi_{yxz}^{(2)} \\
 \chi_{xzy}^{(2)} &= -\chi_{yzx}^{(2)} \\
 \chi_{zxy}^{(2)} &= -\chi_{zyx}^{(2)}
 \end{aligned}$$

**Class  $C_{3v}$**  Five independent nonvanishing components.

$$\begin{aligned}
 \chi_{xzx}^{(2)} &= \chi_{yzy}^{(2)} \\
 \chi_{xxz}^{(2)} &= \chi_{yyz}^{(2)} \\
 \chi_{yyy}^{(2)} &= -\chi_{yxx}^{(2)} = -\chi_{xyx}^{(2)} = -\chi_{xyx}^{(2)} \\
 \chi_{zxx}^{(2)} &= \chi_{zyy}^{(2)} \\
 \chi_{zzz}^{(2)} &
 \end{aligned}$$

### Hexagonal system

**Class  $C_6$**  Seven independent nonvanishing components. The tensor structure is the same as for the class  $C_4$  of the tetragonal crystal system.

**Class  $C_{3h}$**  Two independent nonvanishing components.

$$\begin{aligned}\chi_{xxx}^{(2)} &= -\chi_{xyy}^{(2)} = -\chi_{yxy}^{(2)} = -\chi_{yyx}^{(2)} \\ \chi_{yyy}^{(2)} &= -\chi_{yxx}^{(2)} = -\chi_{xxy}^{(2)} = -\chi_{xyx}^{(2)}\end{aligned}$$

**Class  $D_6$**  Three independent nonvanishing components. The tensor structure is the same as for the class  $D_4$  of the tetragonal crystal system.

**Class  $C_{6v}$**  Four independent nonvanishing components. The tensor structure is the same as for the class  $C_{4v}$  of the tetragonal crystal system.

**Class  $D_{3h}$**  One independent nonvanishing component.

$$\chi_{yyy}^{(2)} = -\chi_{yxx}^{(2)} = -\chi_{xxy}^{(2)} = -\chi_{xyx}^{(2)}$$

### A.3 Third-order susceptibility tensor $\chi_{ijkl}^{(3)}(-\omega_\sigma; \omega_r, \omega_q, \omega_p)$

#### Triclinic system

For both classes  $C_1$  and  $C_i$ , all the 81 tensor components are independent and nonvanishing.

#### Monoclinic system

For all three classes ( $C_2$ ,  $C_{1h}$  and  $C_{2h}$ ), there are 41 independent nonvanishing tensor components, consisting of:

- 3 elements with suffixes all equal,
- 18 elements with suffixes equal in pairs,
- 12 elements with suffixes having two  $y$ s, one  $x$  and one  $z$ ,
- 4 elements with suffixes having three  $x$ s and one  $z$ ,
- 4 elements with suffixes having three  $z$ s and one  $x$ .

#### Orthorhombic system

For all three classes ( $D_2$ ,  $C_{2v}$  and  $D_{2h}$ ), there are 21 independent nonvanishing tensor components, consisting of:

- 3 elements with suffixes all equal,
- 18 elements with suffixes equal in pairs.

### Tetragonal system

For the three classes  $C_4$ ,  $S_4$  and  $C_{4h}$ , there are 41 nonvanishing tensor components of which only 21 are independent. They are:

$$\begin{array}{llll}
 \chi_{xxxx}^{(3)} = \chi_{yyyy}^{(3)} & \chi_{zzzz}^{(3)} & & \\
 \chi_{zzzx}^{(3)} = \chi_{zzyy}^{(3)} & \chi_{xyzz}^{(3)} = -\chi_{yxzz}^{(3)} & \chi_{xxyy}^{(3)} = \chi_{yyxx}^{(3)} & \chi_{xxxy}^{(3)} = -\chi_{yyyx}^{(3)} \\
 \chi_{xxzz}^{(3)} = \chi_{yyzz}^{(3)} & \chi_{zzxy}^{(3)} = -\chi_{zzyx}^{(3)} & \chi_{xyxy}^{(3)} = \chi_{yxyx}^{(3)} & \chi_{xxyx}^{(3)} = -\chi_{yyxy}^{(3)} \\
 \chi_{zxzx}^{(3)} = \chi_{zyzy}^{(3)} & \chi_{xzyz}^{(3)} = -\chi_{yzxz}^{(3)} & \chi_{xyyx}^{(3)} = \chi_{yxxy}^{(3)} & \chi_{xyxx}^{(3)} = -\chi_{yxxy}^{(3)} \\
 \chi_{xzxz}^{(3)} = \chi_{yzyz}^{(3)} & \chi_{zxzy}^{(3)} = -\chi_{zyzx}^{(3)} & & \chi_{yxxx}^{(3)} = -\chi_{xyyy}^{(3)} \\
 \chi_{zxzx}^{(3)} = \chi_{zyyz}^{(3)} & \chi_{zxyy}^{(3)} = -\chi_{zyxx}^{(3)} & & \\
 \chi_{xzxx}^{(3)} = \chi_{yzzz}^{(3)} & \chi_{xzyy}^{(3)} = -\chi_{yzxx}^{(3)} & & \\
 \chi_{xzzx}^{(3)} = \chi_{yzzz}^{(3)} & \chi_{xzyy}^{(3)} = -\chi_{yzxx}^{(3)} & & 
 \end{array}$$

For the four classes  $D_4$ ,  $C_{4v}$ ,  $D_{4h}$  and  $D_{2d}$ , there are 21 nonvanishing tensor components of which only 11 are independent. They are:

$$\begin{array}{llll}
 \chi_{xxxx}^{(3)} = \chi_{yyyy}^{(3)} & \chi_{zzzz}^{(3)} & & \\
 \chi_{yyzz}^{(3)} = \chi_{xxzz}^{(3)} & \chi_{yzzz}^{(3)} = \chi_{xzzz}^{(3)} & \chi_{xxyy}^{(3)} = \chi_{yyxx}^{(3)} & \\
 \chi_{zzyy}^{(3)} = \chi_{zzxx}^{(3)} & \chi_{yzzy}^{(3)} = \chi_{xzzz}^{(3)} & \chi_{xyxy}^{(3)} = \chi_{yxxy}^{(3)} & \\
 \chi_{zyyz}^{(3)} = \chi_{zxzx}^{(3)} & \chi_{zyzy}^{(3)} = \chi_{zxzx}^{(3)} & \chi_{xyyx}^{(3)} = \chi_{yxxy}^{(3)} & 
 \end{array}$$

### Cubic system

For the two classes  $T$  and  $T_h$ , there are 21 nonvanishing tensor components of which only seven are independent. They are:

$$\begin{array}{l}
 \chi_{xxxx}^{(3)} = \chi_{yyyy}^{(3)} = \chi_{zzzz}^{(3)} \\
 \chi_{yyzz}^{(3)} = \chi_{zzxx}^{(3)} = \chi_{xxyy}^{(3)} \\
 \chi_{zzyy}^{(3)} = \chi_{xxzz}^{(3)} = \chi_{yyxx}^{(3)} \\
 \chi_{yzyz}^{(3)} = \chi_{zxzx}^{(3)} = \chi_{xyxy}^{(3)} \\
 \chi_{zyzy}^{(3)} = \chi_{xzzz}^{(3)} = \chi_{yxxy}^{(3)} \\
 \chi_{yzzy}^{(3)} = \chi_{zxxz}^{(3)} = \chi_{xyyx}^{(3)} \\
 \chi_{zyyz}^{(3)} = \chi_{xzzz}^{(3)} = \chi_{yxxy}^{(3)}
 \end{array}$$

For the three classes  $O$ ,  $T_d$  and  $O_h$ , there are 21 nonvanishing tensor components of which only four are independent. They are:

$$\begin{array}{l}
 \chi_{xxxx}^{(3)} = \chi_{yyyy}^{(3)} = \chi_{zzzz}^{(3)} \\
 \chi_{yyzz}^{(3)} = \chi_{zzyy}^{(3)} = \chi_{zzxx}^{(3)} = \chi_{xxzz}^{(3)} = \chi_{xxyy}^{(3)} = \chi_{yyxx}^{(3)} \\
 \chi_{yzyz}^{(3)} = \chi_{zyzy}^{(3)} = \chi_{zxzx}^{(3)} = \chi_{xzzz}^{(3)} = \chi_{xyxy}^{(3)} = \chi_{yxxy}^{(3)} \\
 \chi_{yzzy}^{(3)} = \chi_{zyyz}^{(3)} = \chi_{zxxz}^{(3)} = \chi_{xzzz}^{(3)} = \chi_{xyyx}^{(3)} = \chi_{yxxy}^{(3)}
 \end{array}$$

**Trigonal system**

For the two classes  $C_3$  and  $S_6$ , there are 73 nonvanishing tensor components of which only 27 are independent. They are:

$$\begin{aligned}
 & \chi_{zzzz}^{(3)} \\
 \chi_{xxxx}^{(3)} = \chi_{yyyy}^{(3)} = \chi_{xxyy}^{(3)} + \chi_{xyyx}^{(3)} + \chi_{xyxy}^{(3)} & \left\{ \begin{array}{l} \chi_{xxyy}^{(3)} = \chi_{yyxx}^{(3)} \\ \chi_{xyyx}^{(3)} = \chi_{yxxxy}^{(3)} \\ \chi_{xyxy}^{(3)} = \chi_{yxyx}^{(3)} \end{array} \right. \\
 \chi_{yyyz}^{(3)} = \chi_{xxzz}^{(3)} & \quad \chi_{xyzz}^{(3)} = -\chi_{yxzz}^{(3)} \\
 \chi_{zzyy}^{(3)} = \chi_{zzxx}^{(3)} & \quad \chi_{zzxy}^{(3)} = -\chi_{zzyx}^{(3)} \\
 \chi_{zyyz}^{(3)} = \chi_{zxzx}^{(3)} & \quad \chi_{zxzy}^{(3)} = -\chi_{zyxz}^{(3)} \\
 \chi_{yzzy}^{(3)} = \chi_{xzxx}^{(3)} & \quad \chi_{xzzy}^{(3)} = -\chi_{yzzx}^{(3)} \\
 \chi_{yzyz}^{(3)} = \chi_{xzxx}^{(3)} & \quad \chi_{xzyz}^{(3)} = -\chi_{yzxz}^{(3)} \\
 \chi_{zyzy}^{(3)} = \chi_{zxzx}^{(3)} & \quad \chi_{zxyy}^{(3)} = -\chi_{zyzx}^{(3)} \\
 \chi_{xxxy}^{(3)} = -\chi_{yyyx}^{(3)} = \chi_{yyxy}^{(3)} + \chi_{yxyy}^{(3)} + \chi_{xyyy}^{(3)} & \left\{ \begin{array}{l} \chi_{yyxy}^{(3)} = -\chi_{xxyx}^{(3)} \\ \chi_{yxyy}^{(3)} = -\chi_{xyxx}^{(3)} \\ \chi_{xyyy}^{(3)} = -\chi_{yxxx}^{(3)} \end{array} \right. \\
 \chi_{yyyz}^{(3)} = -\chi_{yxxz}^{(3)} = -\chi_{xyxz}^{(3)} = -\chi_{xxyz}^{(3)} & \\
 \chi_{yyzy}^{(3)} = -\chi_{yxzx}^{(3)} = -\chi_{xyzx}^{(3)} = -\chi_{xzxzy}^{(3)} & \\
 \chi_{yzyy}^{(3)} = -\chi_{yzxx}^{(3)} = -\chi_{xzyx}^{(3)} = -\chi_{xzyy}^{(3)} & \\
 \chi_{zyyy}^{(3)} = -\chi_{zyxx}^{(3)} = -\chi_{zxyx}^{(3)} = -\chi_{zxxy}^{(3)} & \\
 \chi_{xxxx}^{(3)} = -\chi_{xyyz}^{(3)} = -\chi_{yxyx}^{(3)} = -\chi_{yyxz}^{(3)} & \\
 \chi_{xxzx}^{(3)} = -\chi_{xyzy}^{(3)} = -\chi_{yxzy}^{(3)} = -\chi_{yyzx}^{(3)} & \\
 \chi_{xzxz}^{(3)} = -\chi_{yzxy}^{(3)} = -\chi_{zyyx}^{(3)} = -\chi_{xzyy}^{(3)} & \\
 \chi_{zxxx}^{(3)} = -\chi_{zxxy}^{(3)} = -\chi_{zyxy}^{(3)} = -\chi_{zyyx}^{(3)} &
 \end{aligned}$$

For the three classes  $C_{3v}$ ,  $D_{3d}$  and  $D_3$  there are 37 nonvanishing tensor components of which only 14 are independent. They are:

$$\begin{aligned}
 & \chi_{zzzz}^{(3)} \\
 \chi_{xxxx}^{(3)} = \chi_{yyyy}^{(3)} = \chi_{xxyy}^{(3)} + \chi_{xyyx}^{(3)} + \chi_{xyxy}^{(3)} & \left\{ \begin{array}{l} \chi_{xxyy}^{(3)} = \chi_{yyxx}^{(3)} \\ \chi_{xyyx}^{(3)} = \chi_{yxyx}^{(3)} \\ \chi_{xyxy}^{(3)} = \chi_{yxyx}^{(3)} \end{array} \right. \\
 \chi_{yyzz}^{(3)} = \chi_{xxzz}^{(3)} & \quad \chi_{xxxz}^{(3)} = -\chi_{xyyz}^{(3)} = -\chi_{yxyz}^{(3)} = -\chi_{yyxz}^{(3)} \\
 \chi_{zzyy}^{(3)} = \chi_{zzxx}^{(3)} & \quad \chi_{xxzx}^{(3)} = -\chi_{xyzy}^{(3)} = -\chi_{yxzy}^{(3)} = -\chi_{yyzx}^{(3)} \\
 \chi_{zyyz}^{(3)} = \chi_{zxzx}^{(3)} & \quad \chi_{zxzx}^{(3)} = -\chi_{xzyy}^{(3)} = -\chi_{yzxy}^{(3)} = -\chi_{zyyx}^{(3)} \\
 \chi_{yzzz}^{(3)} = \chi_{xzzx}^{(3)} & \quad \chi_{zxzx}^{(3)} = -\chi_{zxxy}^{(3)} = -\chi_{zyxy}^{(3)} = -\chi_{zyyx}^{(3)} \\
 & \quad \chi_{yzyz}^{(3)} = \chi_{xzxz}^{(3)} \\
 & \quad \chi_{zyzy}^{(3)} = \chi_{zxzx}^{(3)}
 \end{aligned}$$

### Hexagonal system

For the three classes  $C_6$ ,  $C_{3h}$  and  $C_{6h}$ , there are 41 nonvanishing tensor components of which only 19 are independent. They are:

$$\begin{aligned}
 & \chi_{zzzz}^{(3)} \\
 \chi_{xxxx}^{(3)} = \chi_{yyyy}^{(3)} = \chi_{xxyy}^{(3)} + \chi_{xyyx}^{(3)} + \chi_{xyxy}^{(3)} & \left\{ \begin{array}{l} \chi_{xxyy}^{(3)} = \chi_{yyxx}^{(3)} \\ \chi_{xyyx}^{(3)} = \chi_{yxyx}^{(3)} \\ \chi_{xyxy}^{(3)} = \chi_{yxyx}^{(3)} \end{array} \right. \\
 \chi_{yyzz}^{(3)} = \chi_{xxzz}^{(3)} & \quad \chi_{xyzz}^{(3)} = -\chi_{yxzz}^{(3)} \\
 \chi_{zzyy}^{(3)} = \chi_{zzxx}^{(3)} & \quad \chi_{zzxy}^{(3)} = -\chi_{zzyx}^{(3)} \\
 \chi_{zyyz}^{(3)} = \chi_{zxzx}^{(3)} & \quad \chi_{zxzy}^{(3)} = -\chi_{zyxz}^{(3)} \\
 \chi_{yzzz}^{(3)} = \chi_{xzzx}^{(3)} & \quad \chi_{xzzz}^{(3)} = -\chi_{yzzz}^{(3)} \\
 \chi_{yzyz}^{(3)} = \chi_{xzxz}^{(3)} & \quad \chi_{xzyz}^{(3)} = -\chi_{yzxz}^{(3)} \\
 \chi_{zyzy}^{(3)} = \chi_{zxzx}^{(3)} & \quad \chi_{zxzy}^{(3)} = -\chi_{zyzx}^{(3)} \\
 \chi_{xxxy}^{(3)} = -\chi_{yyyx}^{(3)} = \chi_{yyxy}^{(3)} + \chi_{yxyy}^{(3)} + \chi_{xyyy}^{(3)} & \left\{ \begin{array}{l} \chi_{yyxy}^{(3)} = -\chi_{xxyx}^{(3)} \\ \chi_{yxyy}^{(3)} = -\chi_{xyxx}^{(3)} \\ \chi_{xyyy}^{(3)} = -\chi_{yxxx}^{(3)} \end{array} \right.
 \end{aligned}$$

For the four classes  $D_6$ ,  $C_{6v}$ ,  $D_{6h}$  and  $D_{3h}$ , there are 21 nonvanishing tensor components of which only 10 are independent. They are:

$$\chi_{zzzz}^{(3)}$$

$$\chi_{xxxx}^{(3)} = \chi_{yyyy}^{(3)} = \chi_{xxyy}^{(3)} + \chi_{xyyx}^{(3)} + \chi_{xyxy}^{(3)} \left\{ \begin{array}{l} \chi_{xxyy}^{(3)} = \chi_{yyxx}^{(3)} \\ \chi_{xyyx}^{(3)} = \chi_{yxyx}^{(3)} \\ \chi_{xyxy}^{(3)} = \chi_{yxxy}^{(3)} \end{array} \right.$$

$$\chi_{yyzz}^{(3)} = \chi_{xxzz}^{(3)}$$

$$\chi_{zzyy}^{(3)} = \chi_{zzxx}^{(3)}$$

$$\chi_{zyyz}^{(3)} = \chi_{zxzx}^{(3)}$$

$$\chi_{yzzy}^{(3)} = \chi_{zxzx}^{(3)}$$

$$\chi_{yzzy}^{(3)} = \chi_{zxzx}^{(3)}$$

$$\chi_{zyzy}^{(3)} = \chi_{zxzx}^{(3)}$$

### Isotropic

There are 21 nonvanishing tensor components of which only three are independent. They are:

$$\chi_{xxxx}^{(3)} = \chi_{yyyy}^{(3)} = \chi_{zzzz}^{(3)}$$

$$\chi_{yyzz}^{(3)} = \chi_{zzyy}^{(3)} = \chi_{zzxx}^{(3)} = \chi_{xxzz}^{(3)} = \chi_{xxyy}^{(3)} = \chi_{yyxx}^{(3)}$$

$$\chi_{yzzy}^{(3)} = \chi_{zyzy}^{(3)} = \chi_{zxzx}^{(3)} = \chi_{xzxz}^{(3)} = \chi_{xyxy}^{(3)} = \chi_{yxxy}^{(3)}$$

$$\chi_{yzzy}^{(3)} = \chi_{zyyz}^{(3)} = \chi_{zxzx}^{(3)} = \chi_{xzxz}^{(3)} = \chi_{xyyx}^{(3)} = \chi_{yxxy}^{(3)}$$

$$\chi_{xxxx}^{(3)} = \chi_{xxyy}^{(3)} + \chi_{xyxy}^{(3)} + \chi_{xyyx}^{(3)}$$

---

---

## APPENDIX B

---

# EXPANSION OF THE ORIENTATIONAL DISTRIBUTION FUNCTION IN A SERIES OF SPHERICAL HARMONICS: DETAILS OF THE CALCULATIONS FOR A THIRD-ORDER NONLINEAR OPTICAL PROCESS

We limit the analysis to a third-order nonlinear optical process ( $p = 4$ ) and we consider only molecules with cylindrical symmetry around their main symmetry axis. With this assumption, the orientation can be defined by only two Euler angles  $\Omega = (\theta, \phi)$  and it does not depend on  $\psi$ . The rotation matrix from the molecular  $(u, v, w)$  to the microscopic frame  $(i, j, k)$  can be written as a linear combination of the first-order spherical harmonics, according to:

$$a_{i\nu}(\theta, \phi) = \sum_{m=-1}^1 C_{m,J=1}^{u,i} Y_m^{J=1}(\theta, \phi) \quad (\text{B.1})$$

where  $a_{i\nu}$  is the element in the  $i^{\text{th}}$  column and  $\nu^{\text{th}}$  line of the rotation matrix by the angles  $(\theta, \phi)$  and  $C_{m,J}^{u,i}$  are the projection coefficients of this new basis decomposition. Therefore, the third-order hyperpolarizability in the microscopic frame writes:

$$\begin{aligned} \gamma_{ijkl}(\theta, \phi) &= \sum_{uvwv} a_{iu}a_{jv}a_{kw}a_{lv}(\theta, \phi)\gamma_{uvwv} = \sum_{uvwv} \gamma_{uvwv} \\ &\times \sum_{m_1 m_2 m_3 m_4} C_{m_1, J_1}^{u,i} C_{m_2, J_2}^{v,j} C_{m_3, J_3}^{w,k} C_{m_4, J_4}^{\nu,l} Y_{m_1}^{J_1}(\theta, \phi) Y_{m_2}^{J_2}(\theta, \phi) Y_{m_3}^{J_3}(\theta, \phi) Y_{m_4}^{J_4}(\theta, \phi), \end{aligned} \quad (\text{B.2})$$

with  $J_{1\dots 4} = 1$  and  $-1 \leq m_{1\dots 4} \leq 1$ .

As we have shown in chapter 1, the product of two spherical harmonics can be expressed by a linear combination of new spherical harmonics using the Wigner 3- $j$  symbols [86]:

$$\begin{aligned} Y_{m_1}^{J_1}(\theta, \phi) Y_{m_2}^{J_2}(\theta, \phi) &= \sum_{J, m} \sqrt{\frac{(2J_1 + 1)(2J_2 + 1)(2J + 1)}{4\pi}} \\ &\times \begin{pmatrix} J_1 & J_2 & J \\ m_1 & m_2 & m \end{pmatrix} \begin{pmatrix} J_1 & J_2 & J \\ 0 & 0 & 0 \end{pmatrix} (-1)^m Y_{-m}^J(\theta, \phi). \end{aligned} \quad (\text{B.3})$$

The Wigner 3- $j$  symbols can be calculated from the Racah formula [112]:

$$\begin{aligned} \begin{pmatrix} J_1 & J_2 & J \\ m_1 & m_2 & m \end{pmatrix} &= \delta_{m_1+m_2+m, 0} (-1)^{J_1-J_2-m} \\ &\times \sqrt{\frac{(J+J_1-J_2)!(J-J_1+J_2)!(-J+J_1+J_2)(J-m)!(J+m)!}{(J_1+J_2+J+1)!(J_1-m_1)!(J_1+m_1)!(J_2-m_2)!(J_2+m_2)!}} \\ &\times \sum_k \frac{(-1)^{k+J_2+m_2} (J_2+J+m_1-k)!(J_1-m_1+k)!}{(J-J_1+J_2-k)!(J-m-k)!(k+J_1-J_2+m)!}. \end{aligned}$$

The selection rules of the Wigner 3- $j$  symbols have been reported in chapter 1. Briefly, they must satisfy the triangular inequalities  $|J_1 - J_2| \leq J \leq |J_1 + J_2|$  and the parity rule, that establishes that  $J_1 + J_2 + J$  must be even so the product does not vanishes.

According to the multiplication rule for spherical harmonics, the product of two first-order spherical harmonics ( $J = 1$ ) can be simplified as:

$$Y_{m_1}^{J_1=1}(\theta, \phi) Y_{m_2}^{J_2=1}(\theta, \phi) = \sum_{J=0,2} \sum_{m=-J}^J \frac{3}{2} \sqrt{\frac{(2J+1)}{\pi}} A_{m_1, m_2}^{m, J} (-1)^m Y_{-m}^J \quad (\text{B.4})$$

where  $A_{m_1, m_2, m, J}$  is the coefficient containing the previous Wigner 3- $j$  symbols. From the triangular inequalities,  $(1 - 1) \leq J \leq (1 + 1)$  and from the parity rule,  $1 + 1 + J$  must be even, leading to  $J$  even. By consequence, the order of the resulting spherical harmonics can only be 0 or 2, this is the reason why the sum over  $J$  can only have these values. In the case of a third-order optical process, the rotation from the molecular frame to the microscopic frame implies the product of four first-order spherical harmonics, that writes:

$$Y_{m_1}^1 Y_{m_2}^1 Y_{m_3}^1 Y_{m_4}^1 = \sum_{JJ'mm'} \frac{9}{4\pi} \sqrt{(2J+1)(2J'+1)} A_{m_1, m_2}^{m, J} A_{m_3, m_4}^{m', J'} (-1)^{m+m'} Y_{-m}^J Y_{-m'}^{J'} \quad (\text{B.5})$$

where the angular arguments  $(\theta, \phi)$  were omitted in order to lighten the notation. From the rules above,  $J$  and  $J'$  must be even and between 0 and 4. The resulting spherical harmonics product in Eq. (B.5) can also be expressed in terms of the multiplication rule for spherical harmonics, leading to:

$$Y_{-m}^J Y_{-m'}^{J'} = \sum_{Kn} \sqrt{\frac{(2J+1)(2J'+1)(2K+1)}{4\pi}} \times \begin{pmatrix} J & J' & K \\ -m & -m' & n \end{pmatrix} \begin{pmatrix} J & J' & K \\ 0 & 0 & 0 \end{pmatrix} (-1)^n Y_{-n}^K \quad (\text{B.6})$$

By replacing Eq. (B.6) into Eq. (B.5), the product of four first-order spherical harmonics writes:

$$Y_{m_1}^1 Y_{m_2}^1 Y_{m_3}^1 Y_{m_4}^1 = \sum_{JJ'Kmm'n} \frac{9}{8\pi} \sqrt{\frac{(2K+1)}{\pi}} (2J+1)(2J'+1) \times A_{m_1, m_2}^{m, J} A_{m_3, m_4}^{m, J'} A_{-m, -m', n}^{J, J', K} (-1)^{m+m'+n} Y_{-n}^K \quad (\text{B.7})$$

with  $J + J' + K$  even, leading to  $K$  even and  $0 \leq K \leq 4$ , from the triangular inequalities. In conclusion,  $K = 0, 2, 4$  in the decomposition of the four spherical harmonics products. Finally, the molecular hyperpolarizability in the microscopic frame writes:

$$\gamma_{ijkl}(\theta, \phi) = \sum_{u,v,w,\nu} \gamma_{uvw\nu} \times \sum_{K,n} \sum_{\substack{m_1, m_2, m_3, m_4, \\ m, m', J, J'}} C_{m_1, J_1}^{u, i} C_{m_2, J_2}^{v, j} C_{m_3, J_3}^{w, k} C_{m_4, J_4}^{u, l} B_{m_1, m_2, m_3, m_4, m, n}^{J, J', K} Y_{-n}^K(\theta, \phi), \quad (\text{B.8})$$

where  $B = (-1)^{m+m'+n} 9 / (8\pi) [(2K+1)/\pi]^{1/2} (2J+1)(2J'+1) A_{m_1, m_2}^{m, J} A_{m_3, m_4}^{m, J'} A_{-m, -m', n}^{J, J', K}$ .

According to Eq. (1.54) in chapter 1, the microscopic susceptibility tensor component  $\chi_{ijkl}^{(3)}$  in the microscopic frame writes:

$$\chi_{ijkl}^{(3)} = N \int_0^{2\pi} \int_0^\pi \gamma_{ijkl}(\theta, \phi) f(\theta, \phi) \sin \theta d\theta d\phi \quad (\text{B.9})$$

where  $f(\theta, \phi)$  is an orientational distribution function, that can be expanded in a series of spherical harmonics, according to:

$$f(\theta, \phi) = \sum_{M,p} f_p^M Y_p^M(\theta, \phi) \quad (\text{B.10})$$

with  $-M \leq p \leq M$ . The final expression of the microscopic third-order susceptibility is then:

$$\begin{aligned} \chi_{ijkl}^{(3)} = & \sum_{u,v,w,\nu} \gamma_{uvw\nu} \sum_{K,M,n,p} \sum_{\substack{m_1,m_2,m_3,m_4, \\ m,m',J,J'}} C_{m_1,J_1}^{u,i} C_{m_2,J_2}^{v,j} C_{m_3,J_3}^{w,k} C_{m_4,J_4}^{\nu,l} \\ & \times B_{m_1,m_2,m_3,m_4,m,n}^{J,J',K} f_p^M \int_0^{2\pi} \int_0^\pi Y_{-n}^K(\theta, \phi) Y_p^M(\theta, \phi) \sin \theta d\theta d\phi. \end{aligned} \quad (\text{B.11})$$

The orthogonality property of the spherical harmonics [see Eq. (1.60) in chapter 1], states that:

$$\int_0^{2\pi} \int_0^\pi Y_{-n}^K(\theta, \phi) Y_p^M(\theta, \phi) \sin \theta d\theta d\phi = \delta_{-np} \delta_{KM}. \quad (\text{B.12})$$

Therefore Eq. (B.11) vanishes with  $M \neq K$ , which leads to  $M = 0, 2, 4$ . In conclusion, the theoretical third-order microscopic susceptibilities depend only on the terms of the orientational distribution function whose orders are  $M = 0, 2, 4$ . By consequence, third-order nonlinear polarimetric measurements can only read-out the even order terms of the distribution function, up to the fourth-order.

## List of publications originated from this work

---

- P. Schön, F. Munhoz, A. Gasecka, S. Brustlein and S. Brasselet, “Polarization distortion effects in polarimetric two-photon microscopy”, *Opt. Express*, **16**, (2008) 20891-20901.
- F. Munhoz, S. Brustlein, D. Gachet, F. Billard, S. Brasselet and H. Rigneault, “Raman depolarization ratio of liquids probed by linear polarization coherent anti-Stokes Raman spectroscopy”, *J. Raman Spectrosc.*, **40**, (2009) 775-780.
- D. Ait-Belkacem, A. Gasecka, F. Munhoz, S. Brustlein and S. Brasselet, “Influence of birefringence on polarization resolved nonlinear microscopy and collagen SHG structural imaging”, *Opt. Express*, **18**, (2010) 14859-14870.
- F. Munhoz, H. Rigneault, S. Brasselet, “High Order Symmetry Structural Properties of Vibrational Resonances Using Multiple-Field Polarization Coherent Anti-Stokes Raman Spectroscopy Microscopy”, *Phys. Rev. Lett.*, **105**, (2010) 123903.

EXPANSION OF THE ORIENTATIONAL DISTRIBUTION FUNCTION IN A SERIES OF  
SPHERICAL HARMONICS

---

---

## BIBLIOGRAPHY

- [1] P. A. Franken, A. E. Hill, C. W. Peters, and G. Weinreich, “Generation of Optical Harmonics,” *Physical Review Letters* **7**, 118–119 (1961).
- [2] J. A. Armstrong, N. Bloembergen, J. Ducuing, and P. S. Pershan, “Interactions between Light Waves in a Nonlinear Dielectric,” *Physical Review Online Archive (Prola)* **127**, 1918–1939 (1962).
- [3] N. Bloembergen and P. S. Pershan, “Light Waves at the Boundary of Nonlinear Media,” *Physical Review Online Archive (Prola)* **128**, 606–622 (1962).
- [4] N. Bloembergen and Y. R. Shen, “Quantum-Theoretical Comparison of Nonlinear Susceptibilities in Parametric Media, Lasers, and Raman Lasers,” *Physical Review Online Archive (Prola)* **133**, A37–A49 (1964).
- [5] S. A. Akhmanov and R. V. Khokhlov, “Concerning One Possibility of Amplification of Light Waves,” *Soviet Journal of Experimental and Theoretical Physics* **16** (1963).
- [6] S. A. Akhmanov and R. V. Khokhlov, *Problems of nonlinear optics* (Moscow, 1964).
- [7] R. Hellwarth and P. Christensen, “Nonlinear optical microscopic examination of structure in polycrystalline ZnSe,” *Optics Communications* **12**, 318–322 (1974).
- [8] J. N. Gannaway and C. J. R. Sheppard, “Second-harmonic imaging in the scanning optical microscope,” *Optical and Quantum Electronics* **10**, 435–439 (1978).
- [9] I. Freund and M. Deutsch, “Second-harmonic microscopy of biological tissue,” *Opt. Lett.* **11**, 94–96 (1986).
- [10] I. Freund, M. Deutsch, and A. Sprecher, “Connective tissue polarity. Optical second-harmonic microscopy, crossed-beam summation, and small-angle scattering in rat-tail tendon.” *Biophysical journal* **50**, 693–712 (1986).

## BIBLIOGRAPHY

---

- [11] P. J. Campagnola, A. C. Millard, M. Terasaki, P. E. Hoppe, C. J. Malone, and W. A. Mohler, “Three-dimensional high-resolution second-harmonic generation imaging of endogenous structural proteins in biological tissues.” *Biophysical journal* **82**, 493–508 (2002).
- [12] P. Stoller, K. M. Reiser, P. M. Celliers, and A. M. Rubenchik, “Polarization-Modulated Second Harmonic Generation in Collagen,” *Biophys J* **82**, 3330–3342 (2002).
- [13] G. Cox, E. Kable, A. Jones, I. Fraser, F. Manconi, and M. D. Gorrell, “3-dimensional imaging of collagen using second harmonic generation.” *Journal of structural biology* **141**, 53–62 (2003).
- [14] R. M. Williams, W. R. Zipfel, and W. W. Webb, “Interpreting Second-Harmonic Generation Images of Collagen I Fibrils,” *Biophys J* **88**, 1377–1386 (2005).
- [15] A. Zoumi, X. Lu, G. S. Kassab, and B. J. Tromberg, “Imaging Coronary Artery Microstructure Using Second-Harmonic and Two-Photon Fluorescence Microscopy,” *Biophys J* **87**, 2778–2786 (2004).
- [16] M. Both, M. Vogel, O. Friedrich, F. von Wegner, T. Künsting, R. H. A. Fink, and D. Uttenweiler, “Second harmonic imaging of intrinsic signals in muscle fibers in situ,” *Journal of Biomedical Optics* **9**, 882–892 (2004).
- [17] T. Boulesteix, E. Beaurepaire, M.-P. Sauviat, and M.-C. Schanne-Klein, “Second-harmonic microscopy of unstained living cardiacmyocytes: measurements of sarcomere length with 20-nm accuracy,” *Opt. Lett.* **29**, 2031–2033 (2004).
- [18] S. V. Plotnikov, A. C. Millard, P. J. Campagnola, and W. A. Mohler, “Characterization of the Myosin-Based Source for Second-Harmonic Generation from Muscle Sarcomeres,” *Biophys J* **90**, 693–703 (2006).
- [19] D. A. Dombeck, K. A. Kasischke, H. D. Vishwasrao, M. Ingelsson, B. T. Hyman, and W. W. Webb, “Uniform polarity microtubule assemblies imaged in native brain tissue by second-harmonic generation microscopy,” *Proceedings of the National Academy of Sciences of the United States of America* **100**, 7081–7086 (2003).
- [20] G. Cox, N. Moreno, and J. Feijó, “Second-harmonic imaging of plant polysaccharides.” *Journal of biomedical optics* **10** (2005).
- [21] M. Nuriya, J. Jiang, B. Nemet, K. B. Eisenthal, and R. Yuste, “Imaging membrane potential in dendritic spines,” *Proceedings of the National Academy of Sciences of the United States of America* **103**, 786–790 (2006).
- [22] J. Liu, M. Subir, K. Nguyen, and K. B. Eisenthal, “Second Harmonic Studies of Ions Crossing Liposome Membranes in Real Time,” *The Journal of Physical Chemistry B* **112**, 15263–15266 (2008).

- 
- [23] Y. Barad, H. Eisenberg, M. Horowitz, and Y. Silberberg, “Nonlinear scanning laser microscopy by third harmonic generation,” *Applied Physics Letters* **70**, 922+ (1997).
- [24] J. Squier, M. Muller, G. Brakenhoff, and K. R. Wilson, “Third harmonic generation microscopy,” *Opt. Express* **3**, 315–324 (1998).
- [25] D. Yelin and Y. Silberberg, “Laser scanning third-harmonic-generation microscopy in biology,” *Opt. Express* **5**, 169–175 (1999).
- [26] C.-K. K. Sun, S.-W. W. Chu, S.-Y. Y. Chen, T.-H. H. Tsai, T.-M. M. Liu, C.-Y. Y. Lin, and H.-J. J. Tsai, “Higher harmonic generation microscopy for developmental biology.” *Journal of structural biology* **147**, 19–30 (2004).
- [27] D. Debarre, W. Supatto, A.-M. Pena, A. Fabre, T. Tordjmann, L. Combettes, M.-C. Schanne-Klein, and E. Beaurepaire, “Imaging lipid bodies in cells and tissues using third-harmonic generation microscopy,” *Nature Methods* **3**, 47–53 (2006).
- [28] N. Olivier, M. A. Luengo-Oroz, L. Duloquin, E. Faure, T. Savy, I. Veilleux, X. Solinas, D. Debarre, P. Bourguine, A. Santos, N. Peyrieras, and E. Beaurepaire, “Cell Lineage Reconstruction of Early Zebrafish Embryos Using Label-Free Nonlinear Microscopy,” *Science* **329**, 967–971 (2010).
- [29] P. D. Maker and R. W. Terhune, “Study of Optical Effects Due to an Induced Polarization Third Order in the Electric Field Strength,” *Physical Review* **137**, A801–A818 (1965).
- [30] R. F. Begley, A. B. Harvey, and R. L. Byer, “Coherent anti-Stokes Raman spectroscopy,” *Applied Physics Letters* **25**, 387–390 (1974).
- [31] M. D. Duncan, J. Reintjes, and T. J. Manuccia, “Scanning coherent anti-Stokes Raman microscope,” *Opt. Lett.* **7**, 350–352 (1982).
- [32] A. Zumbusch, G. R. Holtom, and X. S. Xie, “Three-Dimensional Vibrational Imaging by Coherent Anti-Stokes Raman Scattering,” *Physical Review Letters* **82**, 4142–4145 (1999).
- [33] J.-X. X. Cheng, Y. K. Jia, G. Zheng, and X. S. Xie, “Laser-scanning coherent anti-Stokes Raman scattering microscopy and applications to cell biology.” *Biophysical journal* **83**, 502–509 (2002).
- [34] X. Nan, E. O. Potma, and X. S. Xie, “Nonperturbative chemical imaging of organelle transport in living cells with coherent anti-stokes Raman scattering microscopy.” *Biophysical journal* **91**, 728–735 (2006).
- [35] E. O. Potma and X. S. Xie, “Detection of single lipid bilayers with coherent anti-Stokes Raman scattering (CARS) microscopy,” *J. Raman Spectrosc.* **34**, 642–650 (2003).

## BIBLIOGRAPHY

---

- [36] E. O. Potma and X. S. Xie, “Direct visualization of lipid phase segregation in single lipid bilayers with coherent anti-Stokes Raman scattering microscopy.” *Chemphyschem : a European journal of chemical physics and physical chemistry* **6**, 77–79 (2005).
- [37] C. L. Evans, E. O. Potma, M. Puoris’haag, D. Côté, C. P. Lin, and X. S. Xie, “Chemical imaging of tissue in vivo with video-rate coherent anti-Stokes Raman scattering microscopy,” *Proceedings of the National Academy of Sciences of the United States of America* **102**, 16807–16812 (2005).
- [38] C. L. Evans, X. Xu, S. Kesari, X. S. Xie, S. T. C. Wong, and G. S. Young, “Chemically-selective imaging of brain structures with CARS microscopy,” *Opt. Express* **15**, 12076–12087 (2007).
- [39] P. Nandakumar, A. Kovalev, and A. Volkmer, “Vibrational imaging based on stimulated Raman scattering microscopy,” *New Journal of Physics* **11**, 033026+ (2009).
- [40] C. W. Freudiger, W. Min, B. G. Saar, S. Lu, G. R. Holtom, C. He, J. C. Tsai, J. X. Kang, and X. S. Xie, “Label-Free Biomedical Imaging with High Sensitivity by Stimulated Raman Scattering Microscopy,” *Science* **322**, 1857–1861 (2008).
- [41] Y. R. Shen, “Optical Second Harmonic Generation at Interfaces,” *Annual Review of Physical Chemistry* **40**, 327–350 (1989).
- [42] Y. R. Shen, “Surface properties probed by second-harmonic and sum-frequency generation,” *Nature* **337**, 519–525 (1989).
- [43] Y. Rao, M. Comstock, and K. B. Eisenthal, “Absolute Orientation of Molecules at Interfaces,” *The Journal of Physical Chemistry B* **110**, 1727–1732 (2006).
- [44] M. Sovago, E. Vartiainen, and M. Bonn, “Observation of buried water molecules in phospholipid membranes by surface sum-frequency generation spectroscopy.” *The Journal of chemical physics* **131** (2009).
- [45] P. C. Stoller, B.-M. Kim, A. M. Rubenchik, K. M. Reiser, and L. B. Da Silva, “Polarization-dependent optical second-harmonic imaging of rat-tail tendon,” *Journal of Biomedical Optics* **7**, 205–214 (2002).
- [46] T. Yasui, K. Sasaki, Y. Tohno, and T. Araki, “Tomographic Imaging of Collagen Fiber Orientation in Human Tissue Using Depth-Resolved Polarimetry of Second-Harmonic-Generation Light,” *Optical and Quantum Electronics* **37**, 1397–1408–1408 (2005).
- [47] Y. Sun, W.-L. Chen, S.-J. Lin, S.-H. Jee, Y.-F. Chen, L.-C. Lin, P. T. C. So, and C.-Y. Dong, “Investigating Mechanisms of Collagen Thermal Denaturation by High Resolution Second-Harmonic Generation Imaging,” *Biophys J* **91**, 2620–2625 (2006).

- 
- [48] F. Tiaho, G. Recher, and D. Rouède, “Estimation of helical angles of myosin and collagen by second harmonic generation imaging microscopy,” *Opt. Express* **15**, 12286–12295 (2007).
- [49] C. Odin, Y. Le Grand, A. Renault, L. Gailhouste, and G. Baffet, “Orientation fields of nonlinear biological fibrils by second harmonic generation microscopy,” *Journal of Microscopy* **229**, 32–38 (2008).
- [50] S. Psilodimitrakopoulos, S. I. C. O. Santos, I. A. Roldan, A. K. N. Thayil, D. Artigas, and P. L. Alvarez, “In vivo, pixel-resolution mapping of thick filaments’ orientation in nonfibrillar muscle using polarization-sensitive second harmonic generation microscopy,” *Journal of Biomedical Optics* **14**, 014001+ (2009).
- [51] S. Brasselet and J. Zyss, “Multipolar molecules and multipolar fields: probing and controlling the tensorial nature of nonlinear molecular media,” *J. Opt. Soc. Am. B* **15**, 257–288 (1998).
- [52] M. Florsheimer, M. Bosch, C. Brillert, M. Wierschem, and H. Fuchs, “Second-harmonic imaging of surface order and symmetry,” *Thin Solid Films* **327-329**, 241–246 (1998).
- [53] V. Le Floch, S. Brasselet, J.-F. Roch, and J. Zyss, “Monitoring of Orientation in Molecular Ensembles by Polarization Sensitive Nonlinear Microscopy,” *The Journal of Physical Chemistry B* **107**, 12403–12410 (2003).
- [54] C. Anceau, S. Brasselet, and J. Zyss, “Local orientational distribution of molecular monolayers probed by nonlinear microscopy,” *Chemical Physics Letters* **411**, 98–102 (2005).
- [55] J. Jiang, K. Eisenthal, and R. Yuste, “Second Harmonic Generation in Neurons: Electro-Optic Mechanism of Membrane Potential Sensitivity,” *Biophysical Journal* **93**, L26–L28 (2007).
- [56] D. Oron, D. Yelin, E. Tal, S. Raz, R. Fachima, and Y. Silberberg, “Depth-resolved structural imaging by third-harmonic generation microscopy,” *Journal of Structural Biology* **147**, 3–11 (2004).
- [57] N. Olivier, F. Aptel, K. Plamann, M.-C. Schanne-Klein, and E. Beaurepaire, “Harmonic microscopy of isotropic and anisotropic microstructure of the human cornea,” *Opt. Express* **18**, 5028–5040 (2010).
- [58] M. D. Levenson and N. Bloembergen, “Dispersion of the nonlinear optical susceptibility tensor in centrosymmetric media,” *Physical Review B* **10**, 4447–4463 (1974).
- [59] R. Lynch, “Experimental test for deviation from Kleinman’s symmetry in the third order susceptibility tensor,” *Physics Letters A* **50**, 61–62 (1974).

## BIBLIOGRAPHY

---

- [60] S. A. Akhmanov, A. F. Bunkin, S. G. Ivanov, and N. I. Koroteev, “Polarization active Raman spectroscopy and coherent Raman ellipsometry,” *Soviet Journal of Experimental and Theoretical Physics* **47** (1978).
- [61] M. D. Levenson, “Polarization techniques in coherent Raman spectroscopy,” *J. Raman Spectrosc.* **10**, 9–23 (1981).
- [62] J.-L. Oudar, R. W. Smith, and Y. R. Shen, “Polarization-sensitive coherent anti-Stokes Raman spectroscopy,” *Applied Physics Letters* **34**, 758–760 (1979).
- [63] C. Otto, A. Voroshilov, S. G. Kruglik, and J. Greve, “Vibrational bands of luminescent zinc(II)-octaethylporphyrin using a polarization-sensitive ‘microscopic’ multiplex CARS technique,” *J. Raman Spectrosc.* **32**, 495–501 (2001).
- [64] B. N. Toleutaev, T. Tahara, and H. Hamaguchi, “Broadband (1000 cm<sup>-1</sup>) multiplex CARS spectroscopy: Application to polarization sensitive and time-resolved measurements,” *Applied Physics B: Lasers and Optics* **59**, 369–375–375 (1994).
- [65] Y. Saito, T. Ishibashi, and H. Hamaguchi, “Polarization-resolved coherent anti-Stokes Raman scattering (CARS) spectroscopy: a new probe of molecular symmetry through accurate determination of the Raman depolarization ratio,” *J. Raman Spectrosc.* **31**, 725–730 (2000).
- [66] J.-X. Cheng, S. Pautot, D. A. Weitz, and X. S. Xie, “Ordering of water molecules between phospholipid bilayers visualized by coherent anti-Stokes Raman scattering microscopy,” *Proc. Nat. Ac. of Sc.* **100**, 9826–9830 (2003).
- [67] H. Wang, Y. Fu, P. Zickmund, R. Shi, and J.-X. Cheng, “Coherent Anti-Stokes Raman Scattering Imaging of Axonal Myelin in Live Spinal Tissues,” *Biophys. J.* **89**, 581–591 (2005).
- [68] M. Zimmerley, R. Younger, T. Valenton, D. C. Oertel, J. L. Ward, and E. O. Potma, “Molecular Orientation in Dry and Hydrated Cellulose Fibers: A Coherent Anti-Stokes Raman Scattering Microscopy Study,” *The Journal of Physical Chemistry B* **114**, 10200–10208 (2010).
- [69] A. V. Kachynski, A. N. Kuzmin, P. N. Prasad, and I. I. Smalyukh, “Realignment-enhanced coherent anti-Stokes Raman scattering and three-dimensional imaging in anisotropic fluids,” *Opt. Expr.* **16**, 10617–10632 (2008).
- [70] R. W. Boyd, *The elements of nonlinear optics* (Academic Press, 2008).
- [71] M. Joffre, *Optique non-linéaire en regime continu et femtoseconde* (Ecole Polytechnique, 2009).
- [72] P. N. Butcher and D. Cotter, *The elements of nonlinear optics* (Cambridge University Press, 1990).

- 
- [73] N. Bloembergen, "The Stimulated Raman Effect," *American Journal of Physics* **35**, 989–1023 (1967).
- [74] D. A. Kleinman, "Nonlinear Dielectric Polarization in Optical Media," *Physical Review Online Archive (Prola)* **126**, 1977–1979 (1962).
- [75] S. Popov, Y. Svirko, and N. N. Zheludev, *Susceptibility Tensors for Nonlinear Optics London, UK* (Institute of Physics Publishing, 1995).
- [76] E. Hartmann, *An introduction to crystal physics* (University College Cardiff Press, Cardiff, 1984).
- [77] J. H. Christie and D. J. Lockwood, "Selection Rules for Three- and Four-Photon Raman Interactions," *J. Chem. Phys.* **54**, 1141–1154 (1971).
- [78] M. Tinkham, *Group theory and quantum mechanics* (McGraw-Hill Book Company, 1964).
- [79] S.-H. Lee, J. Wang, S. Krimm, and Z. Chen, "Irreducible Representation and Projection Operator Application to Understanding Nonlinear Optical Phenomena: Hyper-Raman, Sum Frequency Generation, and Four-Wave Mixing Spectroscopy," *The Journal of Physical Chemistry A* **110**, 7035–7044 (2006).
- [80] R. L. Carter, *Molecular symmetry and group theory* (John Wiley & Sons, 1998).
- [81] B. Hudson, "Selection rules for coherent anti-Stokes Raman spectroscopy," *J. Chem. Phys.* **61**, 5461–5463 (1974).
- [82] Y. Kosmann-Schwarzbach, *Groupes et symétries* (Les éditions de l'Ecole Polytechnique, Palaiseau, 2005).
- [83] J. Zyss and J. L. Oudar, "Relations between microscopic and macroscopic lowest-order optical nonlinearities of molecular crystals with one- or two-dimensional units," *Physical Review A* **26**, 2028–2048 (1982).
- [84] I. Rocha-Mendoza, D. R. Yankelevich, M. Wang, K. M. Reiser, C. W. Frank, and A. Knoesen, "Sum Frequency Vibrational Spectroscopy: The Molecular Origins of the Optical Second-Order Nonlinearity of Collagen," *Biophys J* **93**, 4433–4444 (2007).
- [85] M. Gurf, "The use of rotation matrices in the mathematical description of molecular orientations in polymers," *Colloid and Polymer Science* **273**, 607–625 (1995).
- [86] A. Messiah, *Clebsch-Gordan Coefficients and 3j Symbols* (North Holland, Amsterdam, 1962), pp. 1054–1060.
- [87] P. D. Maker, "Spectral Broadening of Elastic Second-Harmonic Light Scattering in Liquids," *Physical Review A* **1**, 923–951 (1970).

## BIBLIOGRAPHY

---

- [88] P. Schön, M. Behrndt, D. A. Belkacem, H. Rigneault, and S. Brasselet, “Polarization and phase pulse shaping applied to structural contrast in nonlinear microscopy imaging,” *Physical Review A* **81**, 013809+ (2010).
- [89] P. Schön, “Phase and Polarization Pulse Shaping for Nonlinear Microscopy,” Ph.D. thesis, Université Aix-Marseille 3 (2010).
- [90] P. Schön, F. Munhoz, A. Gasecka, S. Brustlein, and S. Brasselet, “Polarization distortion effects in polarimetric two-photon microscopy,” *Opt. Express* **16**, 20891–20901 (2008).
- [91] K. Komorowska, S. Brasselet, G. Dutier, I. Ledoux, J. Zyss, L. Poulsen, M. Jazdyk, H. Egelhaaf, J. Gierschner, and M. Hanack, “Nanometric scale investigation of the nonlinear efficiency of perhydrotriphenylene inclusion compounds,” *Chemical Physics* **318**, 12–20 (2005).
- [92] D. Aït-Belkacem, A. Gasecka, F. Munhoz, S. Brustlein, and S. Brasselet, “Influence of birefringence on polarization resolved nonlinear microscopy and collagen SHG structural imaging,” *Opt. Express* **18**, 14859–14870 (2010).
- [93] J. J. Song, G. L. Eesley, and M. D. Levenson, “Background suppression in coherent Raman spectroscopy,” *Applied Physics Letters* **29**, 567+ (1976).
- [94] A. Voroshilov, C. Otto, and J. Greve, “Secondary Structure of Bovine Albumin as Studied by Polarization-Sensitive Multiplex CARS Spectroscopy,” *Appl. Spectrosc.* **50**, 78–85 (1996).
- [95] A. Voroshilov, G. W. Lucassen, C. Otto, and J. Greve, “Polarization-sensitive resonance CSRS of deoxy- and oxyhaemoglobin,” *J. Raman Spectrosc.* **26**, 443–450 (1995).
- [96] A. Voroshilov, C. Otto, and J. Greve, “On the coherent vibrational phase in polarization sensitive resonance CARS spectroscopy of copper tetraphenylporphyrin,” *The Journal of Chemical Physics* **106**, 2589+ (1997).
- [97] M. A. Yuratich and D. C. Hanna, “Coherent anti-Stokes Raman spectroscopy (CARS) – Selection rules, depolarization ratios and rotational structure,” *Molecular Physics: An International Journal at the Interface Between Chemistry and Physics* **33**, 671–682 (1977).
- [98] H. Lotem, R. T. Lynch, and N. Bloembergen, “Interference between Raman resonances in four-wave difference mixing,” *Physical Review A* **14**, 1748–1755 (1976).
- [99] F. Munhoz, S. Brustlein, D. Gachet, F. Billard, S. Brasselet, and H. Rigneault, “Raman depolarization ratio of liquids probed by linear polarization coherent anti-Stokes Raman spectroscopy,” *J. Raman Spectrosc.* **40**, 775–780 (2009).

- 
- [100] J. W. Fleming and C. S. Johnson, "A practical analysis for coherent anti-stokes Raman scattering (CARS) spectra," *J. Raman Spectrosc.* **8**, 284–290 (1979).
- [101] S. A. Kirillov, A. Morresi, and M. Paolantoni, "Recovery of the depolarization ratio of single lines from overlapping isotropic and anisotropic Raman profiles and assignment of molecular vibrations, with special reference to toluene and toluene-d8," *Journal of Raman Spectroscopy* **38**, 383–388.
- [102] F. A. Miller and H. R. Golob, "The infrared and Raman spectra of cyclohexane and cyclohexane-d12," *Spectrochimica Acta* **20**, 1517–1530 (1964).
- [103] F. Munhoz, H. Rigneault, and S. Brasselet, "High Order Symmetry Structural Properties of Vibrational Resonances Using Multiple-Field Polarization Coherent Anti-Stokes Raman Spectroscopy Microscopy," *Physical Review Letters* **105**, 123903+ (2010).
- [104] C. Marcolli, P. Laine, R. Buhler, G. Calzaferri, and J. Tomkinson, "Vibrations of H8Si8O12, D8Si8O12, and H10Si10O15 As Determined by INS, IR, and Raman Experiments," *J. Phys. Chem. B* **101**, 1171–1179 (1997).
- [105] T. Harada, T. Sato, and R. Kuroda, "Intrinsic birefringence of a chiral sodium chlorate crystal: Is cubic crystal truly optically neutral?" *Chemical Physics Letters* **413**, 445–449 (2005).
- [106] A. Deniset-Besseau, J. Duboisset, E. Benichou, F. Hache, P.-F. Brevet, and M.-C. Schanne-Klein, "Measurement of the Second-Order Hyperpolarizability of the Collagen Triple Helix and Determination of Its Physical Origin," *The Journal of Physical Chemistry B* **113**, 13437–13445 (2009).
- [107] J. Zyss, "Octupolar organic systems in quadratic nonlinear optics: molecules and materials," *Nonlinear optics* **1**, 3–18 (1991).
- [108] J. Zyss, "Molecular engineering implications of rotational invariance in quadratic nonlinear optics: From dipolar to octupolar molecules and materials," *J. Chem. Phys.* **98**, 6583–6599 (1993).
- [109] C. P. Pfeffer, B. R. Olsen, F. Ganikhanov, and F. Légaré, "Multimodal nonlinear optical imaging of collagen arrays." *Journal of structural biology* **164**, 140–145 (2008).
- [110] S. Brasselet and J. Zyss, "Nonlinear polarimetry of molecular crystals down to the nanoscale," *Comptes Rendus Physique* **8**, 165–179 (2007).
- [111] F. P. Bolin, L. E. Preuss, R. C. Taylor, and R. J. Ference, "Refractive index of some mammalian tissues using a fiber optic cladding method," *Appl. Opt.* **28**, 2297–2303 (1989).
- [112] W. J. Thompson, *Appendix 3: Tables of formulas* (John Willey and Sons, 1994).

## Abstract

One of the greatest challenges in nonlinear optics microscopy is the search for new contrast mechanisms. This is one of the reasons of the increasing interest in polarimetric nonlinear optics in the last couple of decades. In this work we have explored the potential of four-wave mixing in probing vibrational and structural symmetries in molecular media. In particular, we have been concerned with coherent Raman scattering (CRS), either at resonance or not. We have developed a theoretical model allowing to determine the structures of the susceptibility tensors from symmetry considerations, involving both the spatial structure of the medium and the vibration of specific molecular modes. Experimental results on isotropic sample, crystals and biomolecular assemblies were successfully achieved. Polarimetric measurements at resonance provide information on the symmetry of the addressed vibrational modes and on departure from Kleinman symmetry conditions. Nonresonant polarimetric measurements are able to reveal departure from isotropy in cubic crystals and the symmetry order and orientation of molecular distribution in biomolecular assemblies, such as collagen fibers. In particular, we have shown that higher-order molecular symmetries can only be probed by high-order nonlinear optical processes. Finally, this work has demonstrated the great potential of polarimetric four-wave mixing as a powerful contrast mechanism, providing structural selectivity in microscopy imaging. When it is further associated with a resonant process (such as CRS), it provides also chemical selectivity, allowing a complete description of the sample, involving both structural and vibrational symmetries.

**Keywords :** four-wave mixing, coherent Raman scattering, polarization, structural symmetry, vibrational symmetry, microscopy

---

## Résumé

Un des plus grands défis de la microscopie optique non linéaire est la recherche de nouveaux mécanismes de contraste. Ceci explique l'intérêt croissant pour l'optique non-linéaire polarimétrique ces dernières décennies. Dans ce travail de thèse, nous utilisons le mélange à quatre ondes résolu en polarisation pour sonder les symétries structurales et vibrationnelles dans les milieux moléculaires. En particulier, nous nous sommes intéressés à la diffusion cohérente Raman (CRS, pour l'acronyme en anglais), à-et-hors résonance. Nous avons développé un modèle théorique qui permet de déterminer les structures des tenseurs de susceptibilité à partir des considérations de symétrie qui impliquent aussi bien la structure spatiale du milieu que les vibrations des modes moléculaires spécifiques. Des résultats expérimentaux sur des échantillons isotropes, cristaux et assemblages biomoléculaires ont été accompli avec succès. Les mesures polarimétriques à résonance fournissent des informations concernant la symétrie des modes de vibration considérés et l'écart aux conditions de la symétrie de Kleinman. Les mesures polarimétriques hors résonance permettent de révéler l'écart de l'isotropie dans les cristaux à symétrie cubique et l'ordre de symétrie et orientation de la distribution moléculaire dans les milieux biomoléculaires, comme les fibres de collagène. En particulier, nous avons montré que les symétries moléculaires d'ordre supérieur ne peuvent être sondées que par les processus optiques non linéaires d'ordre élevé. Enfin, ce travail a démontré que le mélange à quatre ondes résolu en polarisation peut être utilisé comme puissant mécanisme de contraste, permettant une sélectivité structurale en imagerie microscopique. Associé à un processus résonant (comme CRS, par exemple), il est possible d'obtenir une sélectivité chimique, ce qui permet de décrire complètement l'échantillon, à partir des symétries structurales et vibrationnelles.

**Mots clefs :** mélange à quatre ondes, diffusion Raman cohérente, polarisation, symétrie structurale, symétrie vibrationnelle, microscopie